PhD manuscript

prepared in the framework of a cotutela/cotutelle agreement between the

Università degli Studi di Udine

Corso di dottorato di ricerca in Scienze dell'Ingegneria Energetica e Ambientale

XXXV Ciclo

and the

Aix-Marseille Université

Discipline : Sciences pour l'Ingénieur, **Spécialité :** Mécanique et physique des fluides

École doctorale 353 Sciences pour l'ingenieur : Mécanique, Physique, Micro et Nanoélectronique

by

Davide DI GIUSTO

with title

Dynamics of fibres in viscous and turbulent flows : an experimental and numerical study

To be defended on the XX April 2023 in front of the following PhD Committee :

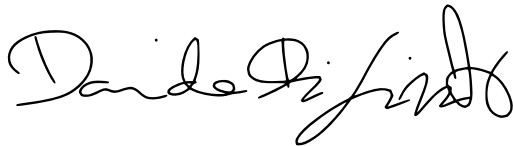|	
Prof. Ivana VINKOVIC (Université Claude Bernard Lyon)	Referee and President
Prof. Fredric LUNDELL (KTH Royal Institute of Technology)	Referee
Prof. Laurence BERGOUGNOUX (Aix-Marseille Université)	PhD Supervisor
Prof. Cristian MARCHIOLI (Università degli Studi di Udine)	PhD Supervisor
Prof. Gautier VERHILLE (Aix-Marseille Université)	Examiner
Prof. Alfredo SOLDATI (T.U. Wien)	Examiner
Prof. Élisabeth GUAZZELLI (Université Paris Cité)	Invited

Affidavit

I, undersigned, Davide Di Giusto, hereby declare that the work presented in this manuscript is my own work, carried out under the scientific supervision of Prof. Cristian Marchioli (Università di Udine) and Prof. Laurence Bergougnoux (Aix-Marseille Université) , in accordance with the principles of honesty, integrity and responsibility inherent to the research mission. The research work and the writing of this manuscript have been carried out in compliance with both the french national charter for Research Integrity and the Aix-Marseille University charter on the fight against plagiarism.

Udine, 31/01/2023

List of publications and conferences

List of publications prepared in the framework of this research :

1. **D. Di Giusto** and C. Marchioli, Turbulence Modulation by Slender Fibers, *Fluids*, 7(8), 255, 2022

2. **D. Di Giusto**, L. Bergougnoux, C. Marchioli and É. Guazzelli, Influence of small ineria on Jeffery orbis, *In preparation for Journal of Fluid Mechanics*, 2023

List of attended conferences :

1. **D. Di Giusto**[†], L. Bergougnoux, C. Marchioli and É. Guazzelli, Poster : Axisymmetric particle rotations in shear flow, 18th *Multiphase Flow Conference & Short Course*, Dresden (Deu), 08-12 November 2021(Online) ;

2. **D. Di Giusto**[†], L. Bergougnoux, C. Marchioli and É. Guazzelli, Axisymmetric particle rotations in shear flow, *APS-DFD Annual Meeting*, Phoenix (USA), 21-23 November, 2021 ;

3. **D. Di Giusto**[†], and C. Marchioli, Turbulence modulation by slender flexible fibres in channel flow, 6th *international conference on Turbulence and Interactions*, Elba Island (IT), 15-20 May 2022 ;

4. **D. Di Giusto**[†] and C. Marchioli, Turbulence modulation by slender flexible fibers in channel flow, *DLES13 - Direct and Large Eddy Simulation ERCOFTAC Workshop*, Udine (IT), 25-28 October 2022 ;

5. **D. Di Giusto**[†], L. Bergougnoux, C. Marchioli and É. Guazzelli, Influence of inertia on the rotation of axisymmetric particles in shear flow, *APS-DFD Annual Meeting*, Indianapolis (USA), 20-22 November, 2022 ;

6. **D. Di Giusto**[†] and C. Marchioli, Turbulence modulation by slender fibers in a channel flow, *APS-DFD Annual Meeting*, Indianapolis (USA), 20-22 November, 2022 ;

[†] Presentation Speaker.

Abstract

In this thesis, the influence of inertia and flexibility on the dynamics of elongated particles in fluid flows has been investigated. In particular, original experiments have been designed and performed to understand the small-inertia effects on the rotational dynamics of neutrally-buoyant axisymmetric particles in a viscous shear flow, while accurate simulations have been conducted to examine the effect of flexibility in a wall-bounded turbulent flow. Being very rich in physics, the physical problem considered in this work is far-reaching from a fundamental point of view, but it has also a practical importance being relevant to several environmental and engineering processes.

In the first part of this manuscript, we present an experimental study examining the influence of small-inertia on the rotational dynamics of axisymmetric particles suspended in a simple shear flow. A custom-built shearing cell and a multi-view shape-reconstruction method are used to obtain direct measurements of the orientation and period of rotation of cylindrical and ellipsoidal particles of varying aspect ratios. By systematically changing the viscosity of the fluid, we examine the effect of inertia on the dynamical behaviour of these suspended particles up to particle Reynolds number of approximately one. While no significant effect on the period of rotation is found in this small-inertia regime, a systematic drift among several rotations toward limiting stable orbits is observed. Prolate particles are seen to drift towards the tumbling orbit in the plane of shear, whereas oblate particles of any particle aspect ratio are driven either to the tumbling or to the vorticity-aligned spinning orbits, depending on their initial orientation. These results are compared to recent small-inertia asymptotic theories.

The second part of the manuscript focuses on the numerical study, which was conducted by means an Eulerian-Lagrangian computational approach based on DNS of turbulence coupled with LPT of elongated and flexible fibres dispersed in channel flow. Particles are modelled as chains of constrained sub-Kolmogorov rods that extend well in the inertial range of turbulence and are naturally prone to bending. Statistics are presented at shear Reynolds number $Re_\tau = 300$, highlighting the complex interaction between fibres and turbulence, while evaluating the influence of bending stiffness and inertia. In the bulk of the flow flexible fibres are seen to orient and rotate as if they were rigid particles suspended in Homogeneous Isotropic Turbulence, whereas the same particles orient with the mean flow and experience stronger tumbling rates when they move to the walls. By looking at the deformation of the particles, we find that the most probable configuration for long flexible fibres in wall turbulence is a stretched one. The dynamics of particle deformation are discussed, giving some

insight into its relation to small-scales turbulence activity. Finally, we discuss the effectiveness of long and slender fibres as drag reducing agents in turbulent channel flows at $Re_\tau = 150, 300$. The presence of the particles determines a Non-Newtonian stress in the axial momentum balance of the turbulent channel flow, influencing the first and second-order moments of the fluid velocity. The analysis of the spectra and the budget of turbulent kinetic energy provides more insight into the mechanism responsible for drag reduction.

Keywords: shear flow, axisymmetrical particles, inertia, flexibility, turbulence, drag reduction

Résumé

Dans cette thèse, l'influence de l'inertie et de la flexibilité sur la dynamique des particules allongées dans les écoulements a été étudiée. En particulier, des expériences originales ont été conçues et réalisées pour comprendre les effets de la petite inertie sur la dynamique rotationnelle de particules individuelles axisymétriques à flottabilité neutre dans un écoulement de cisaillement, tandis que des simulations précises ont été menées pour examiner l'effet de la flexibilité dans un écoulement turbulent d'une suspension de fibres limité par des parois. Très riche en physique, le problème considéré dans ce travail est d'une grande portée d'un point de vue fondamental, mais il a également une importance pratique car il est pertinent pour plusieurs processus environnementaux et d'ingénierie.

Dans la première partie de ce manuscrit, nous présentons l'étude expérimentale examinant l'influence de la petite inertie sur la dynamique de rotation de une seule particule axisymétrique en suspension dans un écoulement à cisaillement simple. Une cellule de cisaillement sur mesure et une méthode de reconstruction de forme multi-vues sont utilisées pour obtenir des mesures directes de l'orientation et de la période de rotation de particules cylindriques et ellipsoïdales de différents rapports d'aspect. En modifiant systématiquement la viscosité du fluide, nous examinons l'effet de l'inertie sur le comportement dynamique de ces particules en suspension jusqu'à un nombre de Reynolds d'environ un. Alors qu'aucun effet significatif sur la période de rotation n'est trouvé dans ce régime à faible inertie, une dérive systématique parmi plusieurs rotations vers des orbites stables limites est observée. Les particules 'prolate' dérivent vers l'orbite de culbute dans le plan de cisaillement, tandis que les particules 'oblate', quel que soit leur rapport d'aspect, sont entraînées soit vers l'orbite de culbute, soit vers l'orbite de rotation alignée avec la vorticité, en fonction de leur orientation initiale. Ces résultats sont comparés aux récentes théories asymptotiques en regime de petite inertie.

La deuxième partie du manuscrit se concentre sur l'étude numérique, qui a été menée au moyen d'une approche de calcul eulérienne-lagrangienne basée sur la DNS de la turbulence couplée à la LPT de fibres allongées et flexibles dispersées dans un écoulement en canal. Les particules sont modélisées comme des chaînes de tiges sub-Kolmogorov contraintes qui s'étendent bien dans la plage inertielle de la turbulence et sont naturellement enclines à la flexion. Les statistiques sont présentées au nombre de Reynolds de cisaillement $Re_\tau = 300$, mettant en évidence l'interaction complexe entre les fibres et la turbulence, tout en évaluant l'influence de la rigidité de flexion et de l'inertie. Dans le coeur de l'ècoulement, les fibres flexibles s'orientent

et tournent comme s'il s'agissait de particules rigides dans une turbulence isotrope homogène, alors que les mêmes particules s'orientent avec l'écoulement moyen et connaissent des taux de rotation plus élevés lorsqu'elles se déplacent vers les parois. En examinant la déformation des particules, nous constatons que la configuration la plus probable pour les longues fibres flexibles dans la turbulence de paroi est une configuration étirée. La dynamique de la déformation des particules est discutée, donnant un aperçu de sa relation avec l'activité de la turbulence à petites échelles. Enfin, nous discutons de l'efficacité des fibres longues et minces comme agents de réduction de la traînée dans les écoulements turbulents de canaux à $Re_\tau = 150, 300$. La présence des particules détermine une contrainte non-newtonienne dans l'équilibre du moment axial de l'écoulement turbulent en canal, influençant les moments de premier et de second ordre de la vitesse du fluide. L'analyse des spectres et du bilan de l'énergie cinétique turbulente permet de comprendre le mécanisme responsable de la réduction de la traînée.

Mots clés: écoulement de cisaillement, particules axisymétriques, inertie, flexibilité, turbulence, réduction de la traînée

Acknowledgements

Contents

List of Figures

List of Tables

Nomenclature

$\bar{\mathbf{I}}$ Identity Matrix

$\bar{\mathbf{J}}_n$ Inertia tensor of a rod element

$\dot{\gamma}$ Shear rate of the viscous shear flow

ℓ Half-length of an axisymmetrical particle

ϵ_R Regularization time scale of the ERPP method

λ Projected polar angle of the Jeffery orbits

$\mathbb{B}$ Viscous-elasto number of the chain of rods

$\mathbb{M}$ Mass load of the turbulent channel flow

$\omega = (\omega_x, \omega_y, \omega_z)$ Rotational velocity of a rod

$\mathbf{B} = (B_x, B_y, B_z)$ Axes-Aligned Bounding Box vector

$\mathbf{F}_n^D$ Drag Force experienced by the n_{th} rod element

$\mathbf{F}_{2w}$ Two-way coupling Eulerian force

$\mathbf{H}_n^D$ Hydrodynamic torque on the n_{th} rod element due to the flow velocity gradient

$\mathbf{n}$ Orientation vector of an axisymmetrical particle

$\mathbf{o} = (o_x, o_y, o_z)$ Rod element orientation vector

$\mathbf{p} = (p_x, p_y, p_z)$ Rod element position vector

$\mathbf{T}_n^D$ Hydrodynamic torque on the n_{th} rod element due to the to the relative spin between the particle and flow

$\mathbf{u} = (u, v, w)$ Flow velocity vector

$\mathbf{v} = (v_x, v_y, v_z)$ Rod element linear velocity

$\mathbf{x} = (x, y, z)$ Eulerian coordinate vector in the absolute frame of reference

$\mathbf{X}_n$ Constrain force between the $n-1_{th}$ and the n_{th} rod elements of any chain

$\mathbf{Y}_n$ Constrain torque between the $n-1_{th}$ and the n_{th} rod elements of any chain

μ Fluid dynamic viscosity

∇ Gradient

ν	Fluid kinematic viscosity
∂	Partial Derivative
Φ	Volume fraction of the fibres in the turbulent channel flow
ϕ	Azimuth angle of the Jeffery orbits
ρ	Fluid density
ρ_p	Particle density
σ_R	Regularization length scale of the ERPP method
τ_w	Characteristic response time of the flow at the wall
$\tau_{p,n}$	Response time of any rod element
θ	Polar angle of the Jeffery orbits
a	Radius of an axisymmetrical particle
d_x, d_y	Grid spacing in the homogeneous directions
dt	time-step
dz_{max}	Maximum grid spacing in the non-homogeneous direction
dz_{min}	Minimum grid spacing in the non-homogeneous direction
E_Y	Young's Modulus of the chain of rods
g	Gaussian function of the ERPP method
h	Half-height of the turbulent channel flow
L_0	Length of a chain of rods
L_i	Length of the domain over the i_{tj} direction
m_n	Mass of a rod element
n_x, n_y, n_z	Number of Eulerian grid-points in the three coordinates (x,y,z)
n_{rod}	Number of rods in a chain
N_{tot}	Total number of dispersed rods in the turbulent channel flow
P	Equivalent pressure gradient
r	Aspect ratio of an axisymmetrical particle
r_{eq}	Equivalent aspect ratio of an axisymmetrical particle
r_{tot}	Aspect ratio of a chain of rods
Re	Reynolds number of a flow
Re_p	Particle Reynolds number

Re_τ	Shear Reynolds number
rms	Root Mean Square of a variable
St	Stokes number
T	Period of the Jeffery orbits of an axisymmetrical particle
t	time variable
u_τ	Shear velocity of the Turbulent Channel Flow
u'	Fluctuating velocity component
AABB	Axes-Aligned Bounding Box
DNS	Direct Numerical Simulation
DR	Drag Reduction
ERPP	Exact Regularized Point Particle
HIT	Homogeneous Isotropic Turbulence
LPT	Lagrangian Particle Tracking
TKE	Turbulent Kinetic Energy

1. Introduction

This thesis is focused on the study of the dynamics of fibres in viscous and turbulent flows. Given the broad range of intents, two specialities have been combined in the framework of a co-supervision agreement between the Università degli Studi di Udine and the Aix-Marseille Université. This has determined a mixed methodology. On one side, experiments have been performed at the Laboratoire IUSTI of the Aix-Marseille Université to study the influence of inertia on the rotations of axisymmetrical particles suspended in a viscous shear flow. This line of research represents a unique opportunity to study a natural dynamical system produced by the interaction between an isolated particle and the viscous flow. Moreover, it aims at finding an answer to recent theoretical efforts (Dabade et al., 2016; Einarsson, Candelier, et al., 2015b), which included inertial effects to lift the indeterminacy of the Jeffery orbits (Jeffery, 1922). On the other side, the theory of Jeffery has become the foundation for highly accurate simulations of the dynamics of fibres in wall turbulence, performed at the Multiphase Flow Laboratory of the Università degli Studi di Udine. These calculations intend to characterise the dynamics and deformations of long and flexible fibres suspended in a turbulent channel flow, relating their phenomenology to the fundamental properties of turbulence.

We reckon that this multi-scale investigation of fibres in flows will be more profitable if we first recall some general concepts. Therefore, we start by looking into natural and industrial processes to understand where suspensions of fibres are a relevant physical system in Section 1.1. In a second moment, a brief introduction to turbulence is provided in Section 1.2, as it represent the flow condition of highest interest for particle-laden flows. At this point, we begin the discussion of the dynamics of axisymmetrical particles in flows. The first step is manifest and concerns the rotation of axisymmetrical particles suspended in a viscous shear flow in Section 1.3.1. Afterwards, turbulence is recovered as we look at how this complex flow condition influences the orientation and tumbling rate of suspended disks and fibres in Section 1.3.2. This multi-scale system is of particular interest as many parameters, such as particle inertia and flexibility, interplay in influencing the flow-particle interaction. Finally, our discussing culminates into the analysis of drag reduction in Section 1.4, a macroscopic manifestation of the modulation of turbulence that fibres determine when carried by a flow.
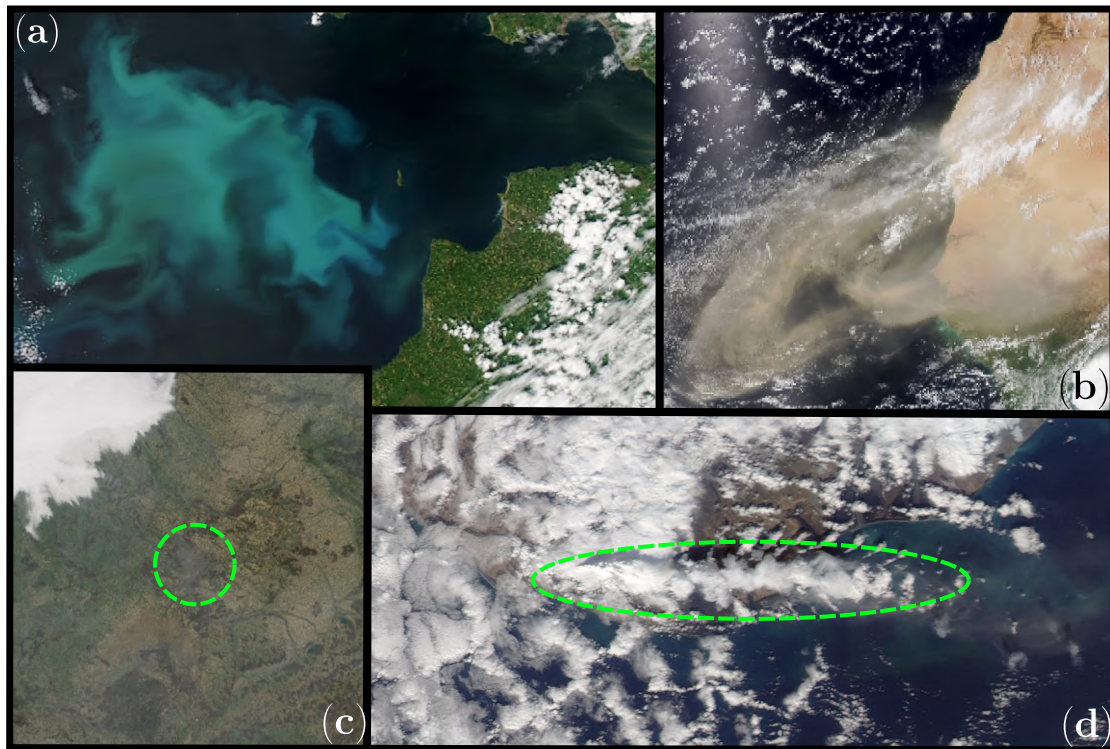
Figure 1.1. – Examples of suspensions of particles in nature: a) abundances of phyto-plankton not far from Bristol (UK), whose swirls and shapes in the bloom trace the movement of sea currents, in early summer of 2022. These plant-like organisms play an important role in the absorption of carbon dioxide by oceans (NASA, 2022b); b) Sarah Desert sand carried by a storm far off the African coast towards South America. It is estimated that 100 tons of dust are dispersed from the Sarah Desert every year, representing an important fertilizer for lands and seas downwind, but with deep consequences on climate as well (NASA, 2022a); c) haze over the city of Paris, completely covered by a gray cloud of $PM_{2,5}$ during a stagnant spring air in 2014 (NASA, 2014) ; d) the plume caused by the eruption of Iceland Eyjafjallajökull, winding down by April 12, 2010 (NASA, 2010)

1.1. Context of the thesis

A suspension is a multi-phase physical system where particles (the carried phase) are dispersed in a fluid (the carrier phase). Once we accept this definition, it is clear that suspensions are ubiquitous, and their understanding is of absolute interest for humanity. A spectacular example is the eruption of the Iceland's volcano Eyjafjallaj okull in April 2010, when large amounts of small rocks, minerals (especially silica) and glass particles with typical size below 2 mm were suspended in the atmosphere of Europe up to 6000 meters of altitude (W. R. Chen and L. R. Zhao, 2015), as captured by NASA in Figure 1.1, panel (d). Given the risk of engine failure that volcanic ash

determines when is encountered by a plane, thousands of flights were cancelled in the days following the eruption, with an estimated economical damage of 2 billion dollars.

A more down-to-hearth suspension is that of particulate matter, which have been correlated to a considerably high number of deaths in the main European cities (Khomenko et al., 2021) and can be seen as a grey haze, like the one covering Paris in Figure 1.1, panel (c). In this case, we are talking about smaller particles ($PM_{2,5}$) emitted by combustion engines, coal power plants and factories, whose size is below $2.5 \mu m$ but which are visible as a gray cloud lying above the urban landscape and, despite recent improvements, still represent the fifth greatest risk factor for global mortality (Burnett et al., 2018).

Suspensions can also sparkle life, like the phytoplankton early summer bloom captured by NASA around Bristol (UK), displayed in Figure 1.1, panel (a). These microscopic plant-like organisms play an important role for the marine ecosystem as well as in the global carbon cycle so that recent studies have looked at the impact of global warming on their concentration in the Norther seas, of great importance for the local food chain (McQuatters-Gollop et al., 2019). Indeed, these and other micro-planktons passively drift within the oceans whiles their sensing, metabolism, locomotion and sexual reproduction strongly depend on their orientation, modelled as that of an axisymmetrical object (Guasto et al., 2012; Basterretxea et al., 2020).

As a matter of fact, one should not be surprised to find out that suspensions play a major role in Earth's climate and biological systems. It is estimated that winds pick up approximately 100 million tons of dust from the Sahara desert each year, during events like the one captured by NASA and displayed in Figure 1.1, panel (b). Once airborne, the particles alter the amount of solar energy reaching the surface and affect the formation of clouds and storms too. Winter and spring seasonal winds often push dust higher into the atmosphere, so that it can reach the Caribbean, the Gulf of Mexico and the Amazon rain forest carried by high-level winds, fertilising these ecosystems as well as the oceans in between.

Modelling such complex physical systems usually requires to specify the shape of the suspended particles. The simplest approximation would be to treat them as spheres, and try to estimate the hydro-dynamical coupling between the carrier and carried phases in order to produce a mathematical description of the dispersed flow that would be useful for practical applications. This is exactly what has been done to produce social distancing rules during the still ongoing COVID pandemic, by treating saliva droplets as small falling spheres whose diameter varies between $1 \mu m$ and $1 mm$ while they are carried by the air flow produced by human speech or respiratory events (C.D.C.P., 2020; J. Wang et al., 2022). Scientists are also looking into solutions to model and prevent fluxes of sand in the lower atmosphere, a major issue for human infrastructures near desert zones. In this regard sphere-laden simulations of the atmospheric turbulent boundary layer are a powerful tool to gain insights into the saltation and deposition of sand around obstacles (Le Ribault et al., 2021).

Plenty of industrial processes take advantage of axisymmetrical particles such as cylinders and ellipsoids, i.e. particles whose shape is not spherical but it is obtained
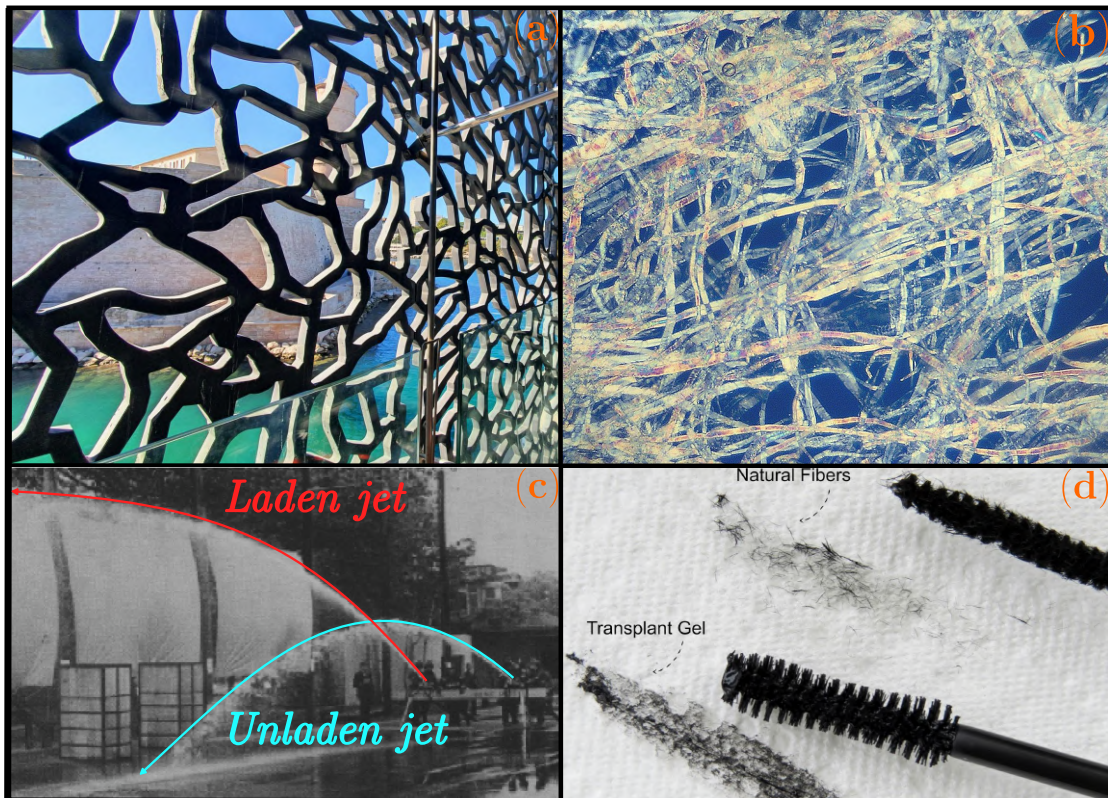
Figure 1.2. – Examples of suspensions of particles in industrial processes. Panels: (a) High Performance Fibre-reinforced Concrete structures of the Mucem, Marseille (FR) (copyright: www.marseille-tourisme.com); (b) Cellulose fibres of a paper bag, enlarged by 200 times. Scale: $800 \times 600 \ \mu m$ (copyright: Jan Homann, Wikipedia); (c) Polymer-laden vs. unladen jets: additives like polymers and fibres are well known Drag Reducing agents (source: Karpikov, 2005); (d) Fibre-laden natural mascara vs. regular mascara. Natural mascara better lengthens eyelashes and is less nocive (copyright: 3D Silk Fiber Mascara, Milky Spoon).

from the rotation of a rectangle or an ellipse around one of its axes of symmetry. Differently from spheres, this kind of particles expresses an orientation within a flow, which determines an anisotropic hydro-dynamical interaction (Voth and Soldati, 2017). As a consequence, the qualities of final products such as high performance fibre-reinforced concrete and paper, displayed in panels (a) and (b) of Figure 1.2 respectively, strongly depend on the micro-structure that the embedded particles determine while flowing as a suspension during production (Lundell et al., 2011). Fibres are also known to be Drag Reducing agents and, despite less effective than polymers, whose positive increment of water flow-rate is shown in in panel (c) of Figure 1.2, these particles have been deployed in flooded motors and oil pipelines (Hoyt, 1972). In addition, fibre-like particles are appearing in daily-life applications, where they are used to produce natural cosmetics, such as the fibre-reinforced mascara displayed in panel

21

(d) of Figure 1.2.

Axisymmetrical suspended particles are also an effective way of representing microplastics and better understand the cycle of these global contaminants, first dispersed in domestic and industrial waste-waters but now contaminating the entirety of the oceans on planet Earth (Ross et al., 2021). Finally, axisymmetrical particles can be a simplified model to study the hydro-dynamical stresses determined by red blood cells on the walls of human veins, as well as phenomena of cell adhesion, important in hemostasis and thrombosis (Goldsmith, 1996). Indeed, the dynamical behaviour of these objects is of great interest, determined by the interplay of viscosity and elasticity of their surface, combined with a shape memory (Dupire et al., 2012).

1.2. A brief description of turbulent flows

Having looked at the importance of suspensions of axisymmetrical particles, we now focus on a qualitative understanding of suspension motion in turbulence, as it represents the most common condition where these physical systems are encountered, both in nature and in industrial processes. The flow of a fluid is described by the Reynolds number:

$$Re = \frac{\rho U L}{\mu} \, , \tag{1.1}$$

where ρ and μ are respectively the density and the dynamic viscosity of the fluid, and U and L are the characteristic velocity and dimension of the flow. The Reynolds number appears in the Navier-Stokes equations which, together with the continuity equation, describe the conservation of mass and momentum of a physical system where a fluid is flowing in a finite volume:

$$\nabla \cdot \mathbf{u} = 0 \, , \tag{1.2a}$$

$$\frac{\partial \mathbf{u}}{\partial t} + (\mathbf{u} \cdot \nabla)\mathbf{u} = -\nabla P + \frac{1}{Re}\nabla^2 \mathbf{u} \, , \tag{1.2b}$$

where $\mathbf{u}$ indicates the generic velocity vector and P is the pressure gradient that is driving the flow. Examples of flow in the viscous regime, when the Reynolds number is particularly small, are common in the field of biology and cell dynamics, like the experiments with single red blood cells given in figure 1.3, panel (a). From equation 1.2b, we can appreciate how, for increasing Reynolds number, the relative importance of the viscous term $\nabla^2 \mathbf{u}$ will be eclipsed by the convective terms $\frac{\partial \mathbf{u}}{\partial t} + (\mathbf{u} \cdot \nabla)\mathbf{u}$. Such transition between regimes can be found in the circulatory system, an interesting example of a multi-scale system, where flow regimes spawn from the viscous one of capillary veins to a preliminary turbulent flow in the largest aortas (Verzicco, 2022). Then, as the Reynolds number becomes sufficiently large, the flow completely evolves from the laminar to the turbulent regime and inertia now dominates over viscosity. This enhances the transport of heat and momentum within, at the price of an unstable
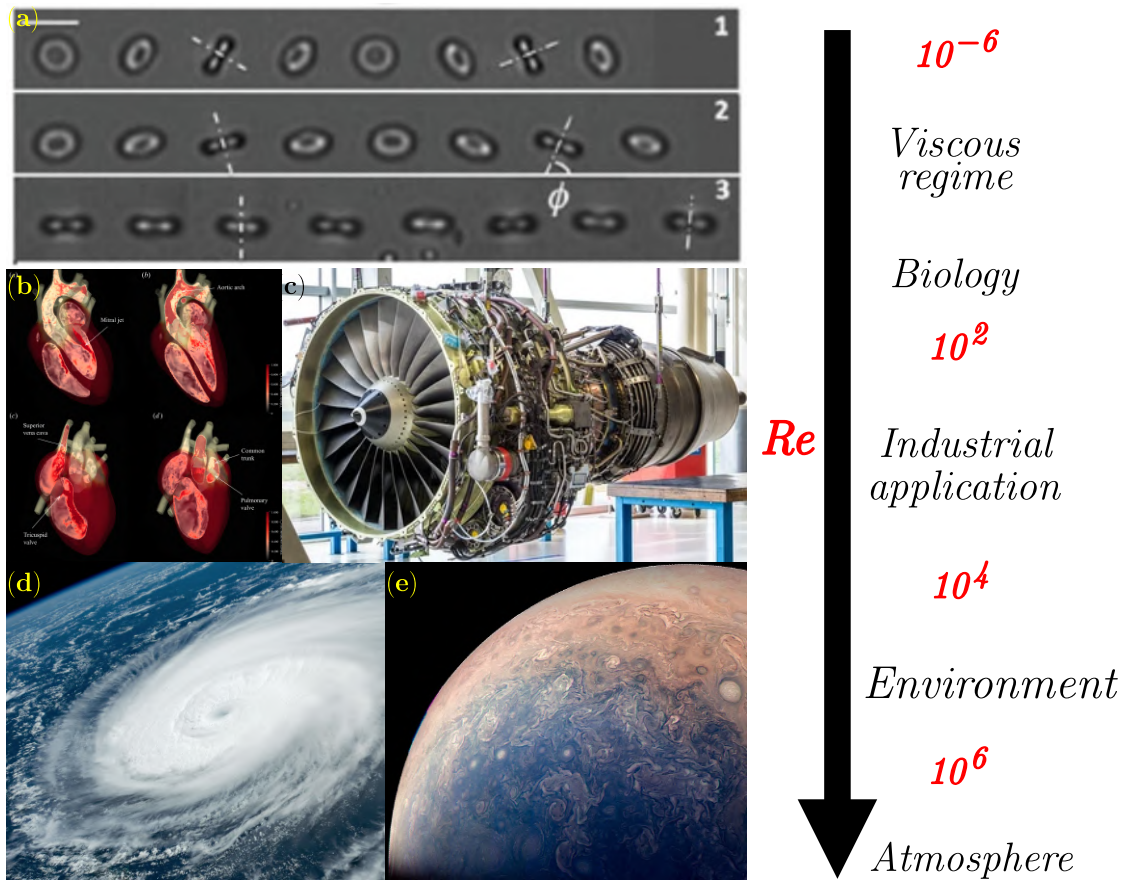
Figure 1.3. – Examples of flows across scales and regimes. Panels: (a)Single red blood cell dynamics experiments in the viscous regime $Re << 1$ (Viallat and Abkarian, 2014); (b) Human blood flow is typically laminar but can peak up to $Re = 10^4$ in the largest aortas. Simulation of the flow in the heart during the cardiac cycle, coloured according to the velocity magnitude (Verzicco, 2022).; (c) jet engine down for maintenance. The typical Reynolds number is $\sim \mathbb{O}(10^4; 10^5)$; (d) the typhoon Hinnamnor in Aug. 2022 in the Western Pacific Ocean. Higher than average sea temperatures feed these kind of storms, which are suggestive examples of turbulent eddies (NASA, 2022c); (e) one of poles of Jupiter, as seen by the NASA's Juno spacecraft in Dec. 2016. It is possible to admire a transition from a zone of organized turbulence around the equator (top) to a cluster of filament structures at the pole (bottom) (NASA, 2017).

and unpredictable phenomenology as well as increased drag losses (Pope, 2000).

Industrial processes are a typical example of turbulent flows, like the jet engine displayed in panel (c) of Figure 1.3. In general, the aircraft performance critically depends on the control of the boundary layer developing around the wings as well as on the flow regime within the engine (Marusic, 2009). Nevertheless, no known solution satisfies the two criteria of existence and smoothness for the Navier-Stokes equations,

therefore physicists and engineers have been forced to model turbulence for a long time. One of the most significant contributions dates back to 1920 when L. F. Richardson pictured the multi-scale nature of turbulent flows by describing an atmospheric boundary layer composed by eddies, i.e. structures of locally coherent turbulent motion (Richardson, 1920). According to the English scientist, the largest eddies are comparable to the scale of the flow, L_0, but are not stable and eventually break up, transferring their energy to generate smaller ones. This mechanism replicates through the intermediate eddies, which correspond to the inertial range of turbulence, in a sort of energy cascade that eventually generates such small eddies, at scale L_D, that their motion is stabilized by the molecular viscosity, which dissipates all their excess energy. Satellites can help in understanding this multi-scale description: for example, by looking at a picture of Jupiter's atmosphere, displayed in panel (e) of Figure 1.3, we appreciate a smooth transition from large coherent structures around the equator of the planet to small filament eddies at the pole. Multi-scale turbulent structures are also found in more familiar places, such as the Hinnamnor storm, displayed in panel (d) of Figure 1.3.

The theory of Richardson introduced the fundamental concept of scale separation and energy cascade within a turbulent flow. Because of its importance, the Russian mathematician A. Kolmogoroff used it as a starting point to describe the structure of Homogeneous Isotropic Turbulence (HIT hereinafter), presented in his famous AK41 (Kolmogorov, 1941), published in 1941 but translated to English and discussed only after the World War Two by Batchelor (Batchelor, 1947).

According to the Russian, for high enough Reynolds number flows, small scales are statistically isotropic and uniquely determined by the interaction between viscosity μ and dissipation ϵ, which is nothing but a degradation of mechanical energy due to shear stress action. The Kolmogorov length, time and velocity scales are consequently defined:

$$\eta \sim \left(\frac{\nu^3}{\epsilon}\right)^{1/4} , \tag{1.3a}$$

$$\tau_\eta \sim \left(\frac{\nu}{\epsilon}\right)^{1/2} , \tag{1.3b}$$

$$u_\eta \sim (\nu\epsilon)^{1/4} . \tag{1.3c}$$

Using the Kolmogoroff scales, it is possible to deduce the range of length scales that a turbulent flow expresses, which is given by the following expression:

$$\frac{L_0}{L_D} \sim Re^{3/4}, \tag{1.4}$$

so that this ratio increases with the Reynolds number at the point that high *Re* flows present a wide range of eddies that are much smaller than the flow characteristic scale L_0 and much larger than the viscous scale L_D, also known as the inertial sub-range, whose statistical motion is hypothesized to be universal.

Having characterised the ratio of scales in a turbulent flow, the Russian scientist
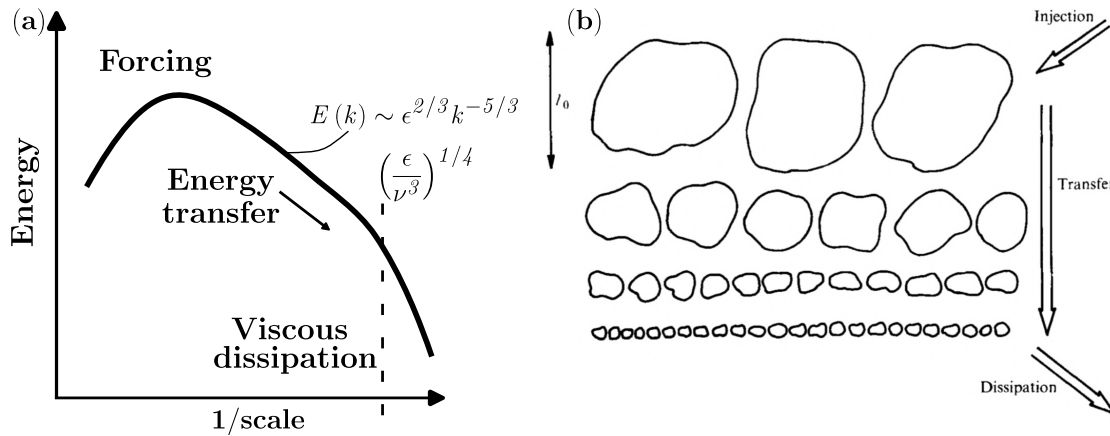
Figure 1.4. – Panels: (a) turbulent energy against eddies length-scale. Energy is emitted into the system at large scale (left) by a forcing term, i.e. a pressure gradient, to be transferred along the cascade to less and less inertial eddies until reaching the smallest scales, where viscous dissipation takes care of all the remaining energy. (b) Representation of the energy cascade. Eddies are space-filling at every step. Image taken from Frisch et al., 1978.

investigated the structure functions of turbulence, in order to determine how kinetic energy is distributed among eddies of different sizes. He found that, in the limit of an infinite Reynolds number, such distribution is determined only by the interplay between dissipation and the given length scale, and energy is flowing from larger to smaller scales. When that is the case, the power spectrum of the turbulent kinetic energy will exhibit a power-law scaling in the intermediate inertial range:

$$E(\kappa) = C\epsilon^{2/3}\kappa^{-5/3} \; , \tag{1.5}$$

as visualized in Figure 1.4. The influence of Kolmogorov's theory of turbulence is such that still nowadays it represents the base for any novel approach to the subject. Anyhow, the discussion has been lively since its publication. Indeed, small-scale activity was soon found to be intermittent, in the sense that eddies in the inertial and, even more, in the dissipating range are not filling the space homogeneously, as predicted by the AK41, but emerge as sudden energy-containing bursts surrounded by quiescent regions (Batchelor and Townsend, 1949). Consequently, this has deep consequences on the structure of the cascade and determines a modification of the universal scaling of the moments of the velocity increment.

Recalling the seminal work of Richardson, one detail was lost up to this point, which is the fact that the British framed the atmospheric boundary layer as the archetype of turbulent flow. Indeed, in the real world is common to see turbulence developing around a body or being confined within bodies, whereas the HIT configuration is a sort of ideal scenario, suitable for mathematical analysis. Because of this, the study of wall turbulence is a matter of great importance and the focus of an intense investigation and will be dealt with for the rest of this manuscript. The main consequence
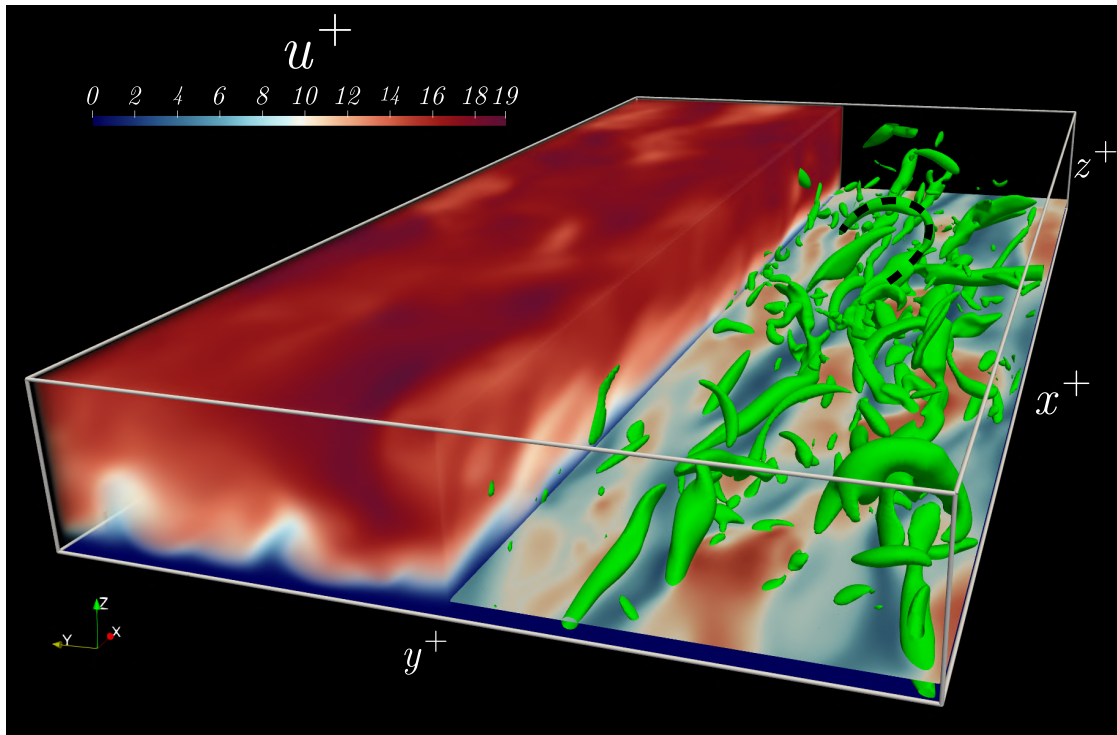
Figure 1.5. – Visualisation of a section of volume ($L_x^+ = \pi Re_\tau, L_y^+ = \pi/2 Re_\tau, L_z^+ = \frac{2}{3} Re_\tau$) of a turbulent channel flow at shear Reynolds number $Re_\tau = 150$. The simulation was developed in-house during the preparation of this manuscript as detailed in 3. The left-side volume rendering of the dimensionless stream-wise velocity u^+ clearly shows the coherence of the bulk of the flow, from which fast-speed streaks burst towards the wall determining, due to mass conservation, the eruption of slow-speed streaks of fluid from the wall to the bulk, especially visible in the front. This is particularly evident in the right-side horizontal panel, displaying the dimensionless stream-wise velocity u^+ at $z^+ = 10$, where the irregular alternation of fast-slow fluid zones is clearly visible. This interplay between slow and fast fluid generates eddies, here rendered as iso-surfaces of the second invariant Q of the fluid velocity gradient tensor (the selected value is Q = 0.04, corresponding to one-fifth of the maximum value of Q obtained in the simulations). It is possible to appreciate how eddies detach from the wall to ultimately reach the typical hairpin shape (black dashed line).

of having introduced a wall in our turbulent flows is the generation of a turbulent boundary layer, which breaks the statistical homogeneity of the wall-normal direction. Macroscopically, this corresponds to a dramatic increase of drag and heat transfer on the surface of any vehicle: for example, 50% of the total drag in commercial aircraft is determined by the development of a turbulent boundary layer (Marusic, 2009).

Microscopically, it has some peculiar consequences, as eddies now scale with the distance to the wall, rendering dissipation largely localized near the wall (Jiménez, 2012). Not only, but a mechanism is also generated, where eddies lift slow fluid from the wall and replace it with fast fluid from above, as displayed in figure 1.5. In this way, layers of fluid start to roll up while being stretched, finally resulting in vortexes that are long but, in some sense, still attached to the wall, whose shape reminds that of a hairpin (Perry and Chong, 1982), as suggested by the black dashed line over one turbulent structure in figure 1.5. These structures are believed to be fundamental in the transition to turbulence of a laminar boundary layer, and still represent a matter of ongoing research.

1.3. Suspensions of axisymmetrical particles

After having provided a brief description of the phenomenology of turbulence, we now introduce axisymmetrical particles in the picture. First, we focus on their dynamics in viscous flows, providing a quick resume of the experimental, theoretical and numerical efforts that were produced in order to understand how these objects rotate within a simple shear flow. This will give us the opportunity to focus on relevant research matters, such as the influence of inertia on particle dynamics. Second, we will move to turbulent flows laden with axisymmetrical particles, especially fibres as they represent the most studied shape in this multi-phase system. A complete picture of the influence of turbulence on the rotation rate of these particles will be then provided. The discussion will also focus on the main sources of bias for this multiphase system: inertia, determined by the relative length of the particles within the flow and by a density mismatch between the carried and carrying phases. Finally, we will mention the influence of particle flexibility on the dynamics of axisymmetrical particles in viscous and turbulent flows. Given the complexity of the matter, we will limit our selves to fibres, looking into their rich deformation dynamics and how these modify their orientation and rotation trends.

1.3.1. Suspensions in viscous flow

Given the complexity of the subject, the modelling of suspensions of axisymmetrical particles is a matter of ongoing research (Voth and Soldati, 2017). In these physical systems hydrodynamic interactions are entangled to the relative orientation of the particles, so that their collective behaviour can differ from what observed for spherical objects even in relative simple scenarios like particle sedimentation (Metzger, Guazzelli, et al., 2005). Then, a small contribution by fluid inertia will deeply affect the orientation and concentration of sedimenting axisymmetrical particles (Lopez and Guazzelli, 2017), which, for a turbulent flow, depends on the relative importance between convective and velocity-gradient torques in determining preferential alignment or orthogonality with the gravity force (Sheikh et al., 2020). The relative orientation within suspended axisymmetrical particles is also responsible for the non-Newtonian

properties exhibited by these systems when they are sheared (Snook et al., 2014).

At this point, we should be convinced that the modelling of suspensions of axisymmetrical particles depends primarily on the way these particles orient within a flow. Neglecting gravitational effects, this depends solely on the way an object reacts to a deformation imposed by the flow, at a given shear rate ($\dot{\gamma}$). Then, among the numerous parameters that play an important role in determining this system, the most important is certainly the particle aspect ratio r . This given by the ratio between the length of the particle along its symmetry axis, 2ℓ, and its diameter, $2a$:

$$r = \frac{2\ell}{2a} \, , \tag{1.6}$$

equal to one for a sphere, greater than one for prolate objects and lower for oblate shapes. As we shall see, the particle aspect ratio alone has already an important influence on the orientation of axisymmetrical particles in viscous and turbulent flows.

Besides the particle aspect ratio, other parameters act as sources of bias. Among these, we find the possibility for axisymmetrical particles to deform (Forgacs and Mason, 1959; Żuk et al., 2021) but also their inertia (Mao and Alexeev, 2014). This is usually determined by inertial effects of the flow on the particle rotation and by the inertia of the particle alone, the former quantified by the particle Reynolds number and the latter by the particle Stokes number:

$$Re_p = \frac{\rho \dot{\gamma} \ell^2}{\mu} \, , \tag{1.7a}$$

$$St = \frac{\rho_p}{\rho} \cdot Re_p = \frac{\rho_p \dot{\gamma} \ell^2}{\mu} \, , \tag{1.7b}$$

where ρ_p is the density of the particle and $\dot{\gamma}$ is the shear rate that the object is feeling within the flow. Weakly inertial particles will follow the flow stream and are therefore called tracers, whereas as inertia becomes more and more relevant, determined by a relevant density ratio ρ_p/ρ or an important particle size 2ℓ, particles will develop a ballistic behaviour and strongly sediment. One must not forget that turbulence is usually in the bargain, giving also raise to phenomena of particle resuspension (Le Ribault et al., 2021).

Therefore, in his seminal work Jeffery, 1922 strongly simplified the physical system in order to be able to obtain a theory for the orientation of axisymmetrical particles suspended in a viscous shear flow. Indeed, the author considered a linear shear flow, i.e., a good local approximation of a pressure-imposed turbulent flow, in the viscous regime, i.e., for vanishing particle Reynolds number, where a rigid ellipsoidal particle is suspended, being its density equal to that of the fluid. In the absence of inertial and Brownian forces, Jeffery found that the axis of revolution of the axisymmetric particle rotates along one of an infinite one-parameter family of closed periodic orbits, known as Jeffery orbits, rendered as dotted spherical ellipses in figure 1.6 for an ellipsoid with
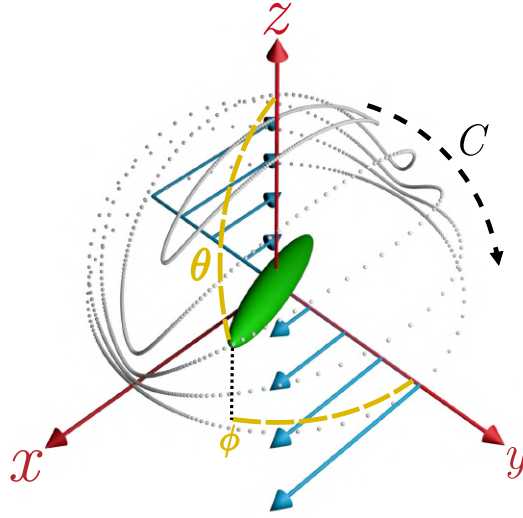
Figure 1.6. – Rendering of five different Jeffery orbits for an ellipsoid of aspect ratio $r = 10$ in the limit of a viscous shear flow ($Re_p = 0$). The azimuthal and polar angles, ϕ and θ, are defined in yellow. The trajectories of one extremity of the particle are obtained by integrating equation 1.8 in time from different initial conditions, and are displayed as dotted lines on the surface of a sphere of radius ℓ. The orbit constant C increases among the represented orbits following the dashed arrow, from $C = 0$ in the z axis-aligned rolling orbit to $C = \infty$ in the tumbling orbit in the x, z plane.

particle aspect ratio $r = 10$. The time change in orientation is given by the equation for the unit vector $\mathbf{n}$ parallel to the axis of revolution of the ellipsoid:

$$\dot{\mathbf{n}} = \Omega \cdot \mathbf{n} + \frac{r^2 - 1}{r^2 + 1} \left[\mathbf{E} \cdot \mathbf{n} - \mathbf{n} \left(\mathbf{n} \cdot \mathbf{E} \cdot \mathbf{n} \right) \right] \ . \tag{1.8}$$

The orientation rotates fully with the rate of rotation of the flow, Ω, and only a fraction $(r^2 - 1)/(r^2 + 1)$ of the rate of strain of the flow, $\mathbf{E}$. Note that the seemingly non-linear term at the end of the right-hand side of equation (1.8) is just meant to keep $|\mathbf{n}| = 1$. Considering the uniform shearing motion defined by $(\dot{\gamma} y, 0, 0)$ where $\dot{\gamma}$ is the flow shear rate, the orientation of the particle axis of revolution is described by the azimuthal and polar angle, ϕ and θ, shown in Figure 1.6. The Jeffery orbits are of the form (with $t = 0$ when $\phi = 0$):

$$\tan \phi = \frac{1}{r} \tan \left[\frac{\dot{\gamma} t}{r + (1/r)} \right] \ , \tag{1.9a}$$

$$\tan \theta = \frac{Cr}{(\cos^2 \phi + r^2 \sin^2 \phi)^{1/2}} \ , \tag{1.9b}$$

where the constant of integration C is known as the orbit constant. The period of rotation is $T_{Jeffery} = 2\pi(r + 1/r)/\dot{\gamma}$. The rotational motions consist of infinitely

many possible spherical ellipses, limited by a tumbling orbit in the (x, y) plane on the equator of the sphere ($C = \infty$) and a spinning orbit aligned with the vorticity z-axis on the pole of the sphere ($C = 0$).

Since their formulation, many experimental studies have reported Jeffery orbits for ellipsoids as well as for other axisymmetrical particles such as fibres ($r > 1$) and disks ($r < 1$) (Taylor, 1923; Binder, 1939; Forgacs and Mason, 1959; Goldsmith and Mason, 1962b; Karnis et al., 1966; Einarsson, Mihiretie, et al., 2016). Forgacs and Mason, 1959 looked at flexible fibres, mentioning that permanently bent particles express a shorter period of rotation than straight ones. Some other experiments reported Jeffery orbits for particles suspended in a Poiseuille flow configuration (Goldsmith and Mason, 1962b; Karnis et al., 1966). A late effort by Moses et al., 2001 investigated experimentally particle rotations in a confined shear flow, finding that, as long as the fibres are located at a distance from the wall greater than 2ℓ, they would still describe Jeffery orbits.

Interestingly, fibres were observed to rotate with a period comparable to that of ellipsoids with a lower aspect ratio, as displayed in figure 1.7. This would suggest an equivalence of shape between the physical cylindrical aspect ratio r and the equivalent ellipsoidal aspect ratio r_{eq}, that would extend the theory of Jeffery to cylindrical shapes. Following experiments with disks (Goldsmith and Mason, 1962a) and high-aspect ratio fibres (Anczurowski and Mason, 1968a), allowed a more and more precise estimation of a general expression for this equivalence of shape between ellipsoidal and cylindrical particles, moving from a linear proportionality ($r_{eq} = 0.74\,r$) (Burgers, 1938; Trevelyan and Mason, 1951) to a semi-empirical asymptotic theory ($r_{eq} = 1.24\,r/\sqrt{\log r}$) (Cox, 1971) to a final data-driven formula ($r_{eq} = 1.14\,r/r^{0.156}$) (Harris and Pittman, 1975).

Anyway, differently from a suspension of spheres (Einstein, 1906), the first modification to the viscosity of a suspension of ellipsoids is indeterminate in the limit of the derivation of Jeffery, 1922, as the particles exist in a dynamical state depending only on their initial orientation and without steady-state preferential orientation. To solve this indeterminacy, Jeffery himself was the first to suggest that ellipsoids would eventually align with the local vorticity, driven by the terms neglected in his calculations, namely flow and particle inertia.

In the first place, Taylor, 1923 experimentally confirmed the suggestion of Jeffery, 1922 that ellipsoidal particles would align in the spinning orbit, just to be later disproved by the analysis of Saffman, 1956. In the following years, few experiments explored the influence of inertia on Jeffery orbits. Preliminary efforts characterised the phenomenon in terms of a slow variation of orbit constant C among consecutive rotations for negligible particle Reynolds number (Goldsmith and Mason, 1962a; Stover and C. Cohen, 1990). Karnis et al., 1963 found that fibres and disks suspended in circular tubes at $Re_p \mathbb{O}(10^{-4})$ would eventually rotate in the tumbling ($C = \infty$) and spinning ($C = 0$) orbits respectively. Yet, to the best of our knowledge, no experimental study has produced a rigorous characterisation of the influence of inertia on the Jeffery orbits of these rigid objects.

Instead, weak inertial effects have been thoroughly addressed in the recent theoretical efforts of Subramanian and Koch, 2005; Subramanian and Koch, 2006; Dabade et
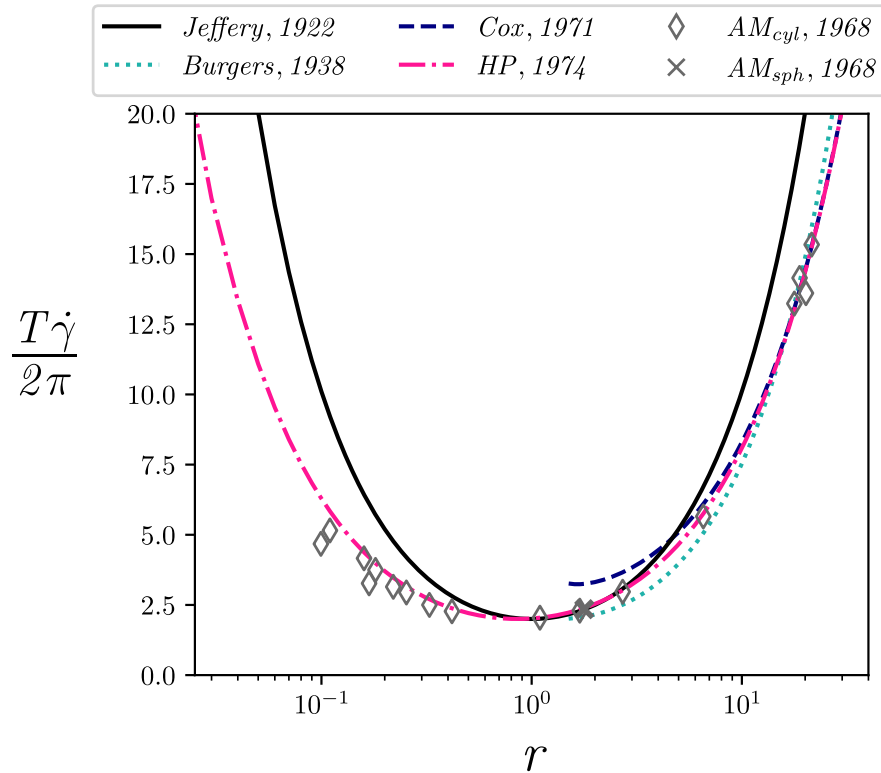
Figure 1.7. – Period of rotation, T, of the axisymmetrical particles against the particle aspect ratio r. The period is made dimensionless using the shear rate $\dot{\gamma}$ and normalized by a factor 2π. The theories of Jeffery, 1922 and Burgers, 1938, the semi-empirical correlation of Cox, 1971, and the empirical expression of Harris and Pittman, 1975 are displayed as a solid black line, a dotted cyan line, a dashed blue line and a dash-dotted pink line, respectively. The experiments of Anczurowski and Mason, 1968b are displayed as empty grey diamonds (cylinders) and one solid x (ellipsoid), clearly showing the equivalence of shapes between the two shapes.

al., 2016; Marath and Subramanian, 2017; Marath and Subramanian, 2018 and Einarsson, Candelier, et al., 2015a; Einarsson, Candelier, et al., 2015b, who independently reached similar conclusions: the first effect of fluid and/or particle inertia is to lift the degeneracy of the infinitely many stable Jeffery orbits since the ellipsoidal particles are then driven towards a limiting stable orbit through consecutive rotations as displayed in figure 1.8. Prolate ellipsoids are pushed towards the tumbling orbit ($C = \infty$). The situation is more complex for oblate ellipsoids which are attracted to either the sole spinning orbit ($C = 0$) or both the vorticity-aligned ($C = 0$) and the tumbling ($C = \infty$) orbits, depending on whether their aspect ratio is larger or smaller than a critical value of approximately 0.14 (Dabade et al., 2016; Einarsson, Candelier, et al., 2015a). Interestingly, Marath and Subramanian, 2017 also suggested a second-order effect of inertia on the period of rotation, while Rosén, Einarsson, et al., 2015 discussed the
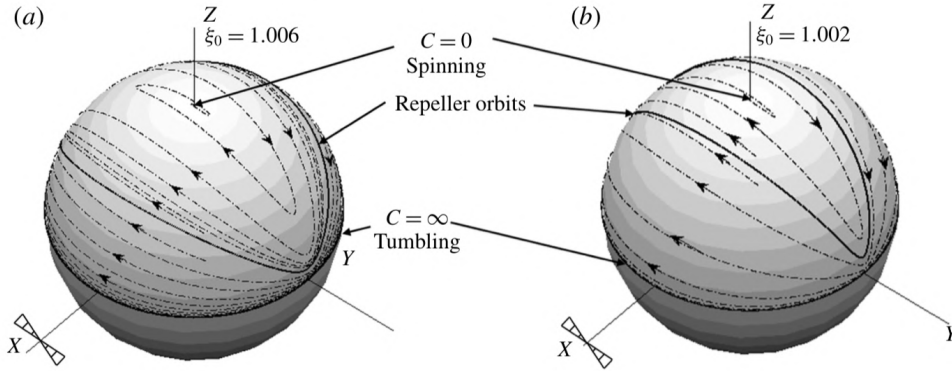
Figure 1.8. – Effect of particle inertia ($St = 0.8$) on the Jeffery orbits as calculated by Dabade et al., 2016. The Jeffery orbits are not closed spherical ellipses but instead describe a spiralling trajectory towards one of the two stable attracting cycles. Two different oblate particles are considered among the left and the right panel, showing the precise location of the cycle separating between the tumbling and spinning basins of attraction.

influence of flow confinement over the stability of the tumbling and spinning orbits.

The problem has been also tackled numerically. Several studies based on the Lattice-Boltzmann method have considered prolate and oblate ellipsoids in the near-sphere limit (Qi and Luo, 2003; Huang et al., 2012; Mao and Alexeev, 2014), with the advantage of easily separating between fluid and particle inertia. By exploring a wide parameter space ($0 < Re_p < 300$ and $0 < St < 1200$) for ellipsoids with moderate aspect ratio $2 \leq r \leq 6$, these authors found a good agreement with the theoretical efforts of Dabade et al., 2016; Einarsson, Candelier, et al., 2015a at $Re_p \mathbb{O}(10^1)$, but also the emerging of other stable rotation states (spinning, inclined spinning, inclined tumbling or kayaking) for different combinations of increasing particle and flow inertia (Rosén, Einarsson, et al., 2015). Interestingly, these simulations and previous experiments by Zettner and Yoda, 2001 reported an increase of the period of rotation with flow inertia, proportional to $(Re_{p,cr} - Re_p)^{-0.5}$, where $Re_{p,cr}$ is a critical particle Reynolds number above which the considered particles were observed to stop rotating.

1.3.2. Suspensions in turbulent flows

An axisymmetrical particle suspended in a viscous shear flow behaves as a periodic dynamical system, while a small inertial effect ($Re_p << 1$) supposedly modifies the stability of the Jeffery orbits driving the object towards preferential limiting cycles. This phenomenology dramatically changes when axisymmetrical particles are carried by a turbulent flow. It is of interest to look at how the particles react to the multi-scale flow structures and re-orient due to the intermittent velocity gradients. Therefore, the natural observable becomes the particle rotation rate. For a a sub-Kolmogorov fibre

this is predicted by the theory of Jeffery as following:

$$\dot{n}_i = \Omega_{i,j} n_j + \frac{r^2 - 1}{r^2 + 1} \left(E_{i,j} n_j - n_i n_k E_{k,l} n_l \right), \tag{1.10}$$

determined by the interplay of the flow rate of rotation, i.e. its vorticity $\Omega_{i,j}$ and the flow rate of strain $S_{i,j}$ (Ni et al., 2015). As displayed in panel (a) of Figure 1.9, the phenomenology of the rotation rate of a fibre suspended in turbulence becomes very intermittent, as rotations 30 times stronger than the mean suddenly burst (Parsa, Calzavarini, et al., 2012).

Numerical simulations and experiments have lead to insights into the rotations of axisymmetrical particles in turbulence, especially fibres. Parsa, Calzavarini, et al., 2012 obtained experimental measurements of the tumbling rate of tracer rods suspended in HIT. Nevertheless, in agreement with previous numerical HIT simulations by Shin and Koch, 2005, they reported a mean squared tumbling rate up to 3 times smaller than what was predicted for randomly oriented particles through the theory of Jeffery, 1922.

An explanation for this must be sought in the preferential alignment that these particles express within a turbulent flow. Indeed, the orientation of short rods is strongly correlated with the vorticity vector as well as the first two eigenvectors of strain rate tensor Pumir and Wilkinson, 2011; Ni et al., 2015. This alignment is determined by the fluid stretching, which is known to follow the intermediate eigenvector, while conservation of angular momentum causes vorticity to preferentially follow this direction too (Voth and Soldati, 2017). Therefore, as short rods align with the local strain, their strong correlation with the vorticity will determine a remarkable spinning motion around their symmetry axis. On the other hand, small disks experience a complementary behaviour, aligning their axis with the third eigenvector of the strain rate, in an orthogonal tumbling motion driven by local vorticity. In the end, tumbling and spinning are complementary effects when comparing rods and disks, adding up to determine an almost shape-independent variance of the angular velocity Byron et al., 2015, as displayed in panel (b) of Figure 1.9.

Several other mechanisms come into play when the size of the axisymmetrical particles becomes larger, as fluid inertia must be accounted for ($Re_p >> 0$) while the flow sampling happens at a length-scale proportional to their largest dimension, filtering out contributions by smaller eddies Shin and Koch, 2005. Therefore, fibres in the inertial range will experience a reduced mean squared tumbling rate, well predicted by a $(2\ell)^{-4/3}$ power law scaling observed both experimentally and numerically in the HIT configuration(Parsa and Voth, 2014; Pujara et al., 2019).

Simulations disclosed that fibres in the inertial range of HIT still align with the extensional eigenvectors of the perceived strain-rate tensor (Pujara et al., 2019; Olivieri, Mazzino, et al., 2022). Therefore, the negative power law scaling is explicable only by the filtering effect due to the extended particle size (Shin and Koch, 2005). As the fibres size is further increased ($2\ell >> 2a > \eta_k$), the characteristic spinning time-scale becomes important too, as these particles will spin much more than tumble, trapped
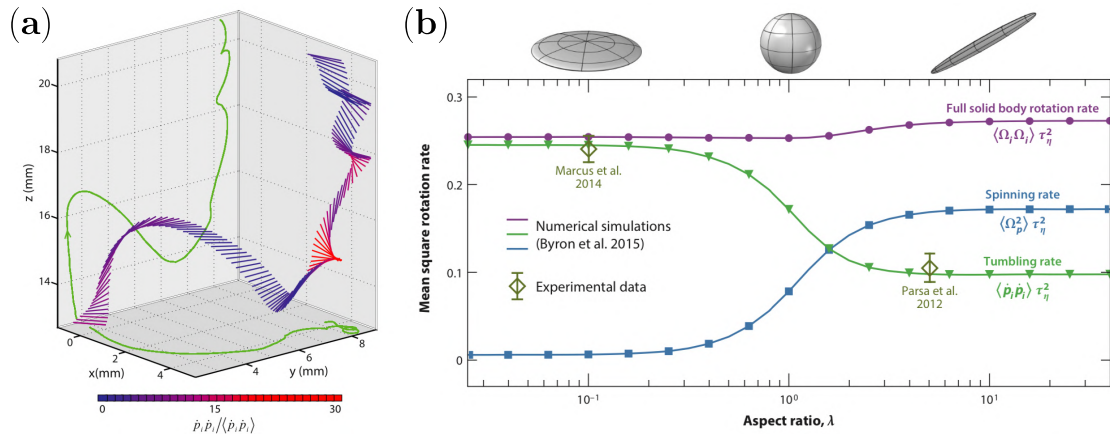
Figure 1.9. – Panels : (a) Three-dimensional reconstruction of the trajectory of a rod with aspect ratio $r = 5$ in a HIT configuration at $Re_\lambda = 214$. The projected trajectories of the center of the rod are also displayed as green lines onto the x, y and y, z planes. The rod color shows its rotation rate. Image taken from Parsa, Calzavarini, et al., 2012. (b) Mean square tumbling, spinning and rotation rates against the particle aspect ratio for tracer axisymmetrical particles in HIT as measured in the simulations of Byron et al., 2015 and in the experiments of Parsa, Calzavarini, et al., 2012; Marcus et al., 2014. Image taken from Voth and Soldati, 2017.

within elongated coherent structures, while once again a $-4/3$ power law scaling for the variance of the spinning rate was experimentally found (Oehmke et al., 2021).

The described phenomenology changes when we move from HIT to wall turbulence, as turbophoresis comes into play. As described by Soldati and Marchioli, 2009, this mechanism entangles small spheres inside flow sweeps that cluster them in a near-wall accumulation region, where they will either gently diffuse to the wall or be puked back into the buffer layer by flow ejection phenomena. Simulations showed that short ellipsoids follow the same fate, segregating towards the wall in low-speed streaks proportionally with their particle aspect ratio r, where they will recover a Jeffery-like dynamical behaviour (Mortensen et al., 2008; Marchioli, Fantoni, et al., 2010). This implies that short rods (resp. disks) near the wall will be preferentially aligned to the mean flow (resp. wall-normal direction) while describing a tumbling motion (Hoseini and Andersson, 2015; Capone and Romano, 2015; Voth and Soldati, 2017).

Actually, as numerically shown by L. Zhao and Andersson, 2016, sub-Kolmogorov rods (resp. disks) are still aligning with the local flow stretching (resp. compression) across the whole section of a turbulent channel flow, similar to what is observed in HIT, but with the main difference that, in the near wall region, vorticity becomes perpendicular to the direction of maximum stretching, therefore determining an increased tumbling rate for these particles. On the other hand, as the vorticity-stretching alignment is restored in the bulk of the wall-bounded flow, a HIT scenario is recovered, where short rods will cluster in low vorticity regions and express a lower tumbling rate

(Jie et al., 2019).

When longer fibres are considered in wall turbulence, experiments by Shaik et al., 2020 have shown that they will accumulate in high-speed streaks, while the extended particle length will determine interaction with larger and more energetic turbulent structures so that the tumbling rate of longer fibres could even become higher.

Another source of bias is given by particle inertia ($St >> 0$), determined by the different density of the carried phase, which will in the first place reduce the fibre alignment with the local stretching and vorticity (Olivieri, Mazzino, et al., 2022). Consequently, this will induce a higher tumbling rate for intermediate values of St, which will saturate and decrease as fibres become more and more ballistic (Kuperman et al., 2019). As shown by Bounoua et al., 2018 in HIT, the $-4/3$ power law scaling is extendable to include particle inertia effects on the tumbling rate of fibres, having normalised it by the characteristic rotational response time. In wall turbulence, instead, inertia strengthens wall segregation as well as the thickness of the region where axisymmetrical particles will feel the influence of the wall, while particle orientation becomes more isotropic in the bulk of the flow (L. Zhao, Challabotla, et al., 2015; L. Zhao, Challabotla, et al., 2019). Another consequence of particle inertia is the preferential sampling of the flow by prolate ellipsoids, which is expected to have deep consequences for their acceleration and tumbling rate (Ouchene et al., 2018).

1.3.3. Deformation of fibres in flows

What seen until now is valid for rigid fibres in viscous and turbulent flows. Anyway, in several biological and industrial applications, fibres are flexible and will deform within the flow (Du Roure et al., 2019). Flexibility modifies the way an axisymmetrical particle will sample flow rotation and strain, where viscous and elastic forces compete to determine the following dimensionless number, known as the visco-elastic number, defined here for a viscous shear:

$$\mathbb{B} = \frac{8\pi\mu\dot{\gamma}\ell^4}{E_Y\pi/4a^4} \,, \tag{1.11}$$

being E_Y is the Young's modulus of the material.

As $\mathbb{B}$ increases, a flexible fibre suspended in a viscous shear flow will struggle to rotate as a whole, transitioning to a snaking motion and undergoing events of extreme deformation (buckling) (Forgacs and Mason, 1959; Delmotte et al., 2015). Flexibility also influences the way a fibre sediments in a viscous flow, as different equilibrium shapes are attained depending on the elasticity of the particle, which can optimise the drag experienced by the particle (Marchetti et al., 2018). In slightly more complex scenarios, such as a viscous cellular flow, fibres buckling depends on the particles' configuration when they approach stagnation points, determining the following dynamics more chaotic (Quennouz et al., 2015).

Coming to turbulence, a stiff fibre will be deformed only by large strain, rapidly restoring its fully stretched shape afterwards Rosti et al., 2018. On the other hand,
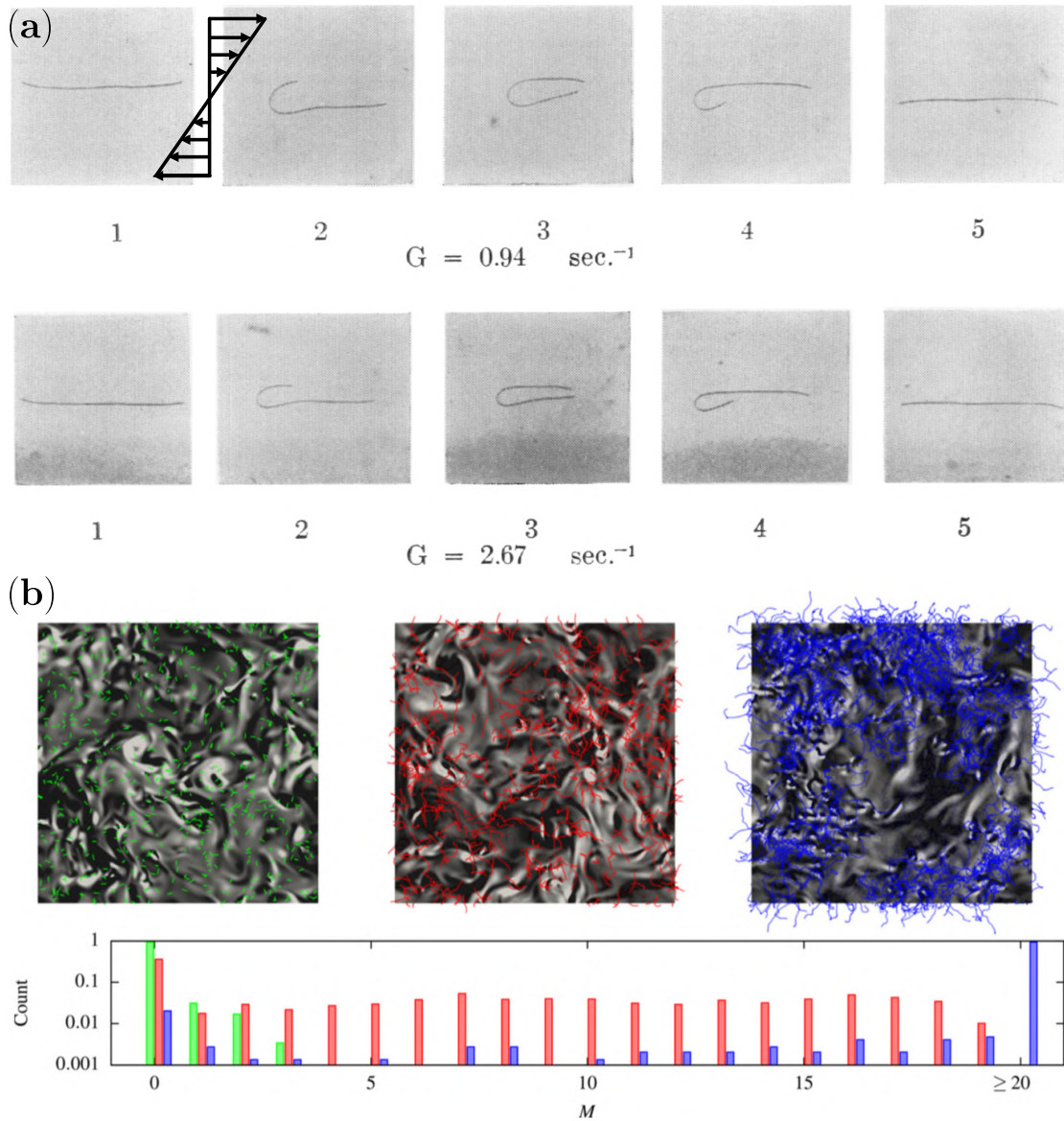
Figure 1.10. – Panels : (a) Left-to-right time sequence of an elastomer filament in viscous shear flow undergoing buckling deformation. *G* is the estimated shear rate (Forgacs and Mason, 1959). (b) (Top) DNS of 1000 inertial fibres dispersed in HIT for three different particle lengths (short in green, intermediate in red, long in blue). The grey-scale panels display the normal component of the vorticity (negative in white, positive in black). (Bottom) Histogram of the inflexion of the fibres from straight (left) to 20 inflexion points (M) along the particle (right). Image taken from Olivieri, Mazzino, et al., 2021.

a stiff-less fibre will be enslaved to turbulent fluctuations (Andrić et al., 2013). This means that sub-Kolmogorov flexible fibres suspended in HIT will be fully stretched

for most of the time, undergoing buckling instability when they tumble and meet a suddenly strong flow compression (Allende et al., 2018).

Indeed, experiments and scaling laws suggest that particle flexibility is negligible for fibres shorter than a critical length, determined by the interaction between turbulence intensity, bending stiffness and particle length (Brouzet et al., 2014; Verhille and Bartoli, 2016). Then, it should be of no surprise to see stiff-less and long fibres being stretched inside vortical regions of comparable size, as observed numerically for flexible bead-spring chains in HIT by Picardo et al., 2020. In the end, these features seem to indicate that the bending stiffness has a moderate influence on alignment statistics (Olivieri, Mazzino, et al., 2022).

Few studies considered flexible fibres in wall turbulence. There, long and stiff-less fibres will be stretched by the strong mean shear in the near wall region, reaching a steady-state elongation regardless of their location within the channel flow, i.e., their relative ratio to the local scales of the flow (Dotto, Soldati, et al., 2020). Anyway, to the best of our knowledge no study has explored the alignment and the rotation of long and flexible fibres in wall turbulence, which will be discussed in this thesis.

1.4. Turbulence modulation and Drag Reduction

We have seen that axisymmetrical particles preferentially orient within a turbulent flow, consequently experiencing modified rotation rates. Anyway, it is known that these particles, if dispersed in sufficient concentration, will also modulate the turbulence, with consequences that culminate in a macroscopic phenomenology known as Drag Reduction (hereinafter DR) (Voth and Soldati, 2017).

DR is ubiquitously pursued in nature. Form DR is the most common, a typical example being the sword of swordfishes or the skin of the sharks (Bushnell and Moore, 1991). On the other hand, many industrial processes are more suitable for a different kind of phenomenology: DR by additives. This manifests when a flow, driven by an imposed pressure gradient, will produce a higher flow rate due to the interaction between the fluid and a carried phase, as displayed in figure 1.11, panel (b) (Lumley, 1969).

The first experimental observations of DR date back to the pioneering works of Forrest and Grierson, 1931 on wood pulp fibre suspensions and of Toms, 1949 on dispersed polymers in pipes. Here, polymers are some macro molecules of small size, usually shorter than the Kolmogorov length scale of the carrier flow, which can coil and, therefore, accumulate energy. Fibres, instead, remain bigger objects, comparable to the Kolmogorov length scale and characterized by a stretched equilibrium shape. Differently from polymers, fibres cannot store energy and therefore will interact with the flow in a purely hydrodynamic way, resulting in lower drag-reduction effectiveness, together with the risk of pipeline plugging. On the bright side, fibres exhibit chemical and mechanical stability over a wider range of stresses and temperatures when compared to polymers (Y. Wang et al., 2011). Panel (c) of figure 1.11 displays the differences between these two DR agents.
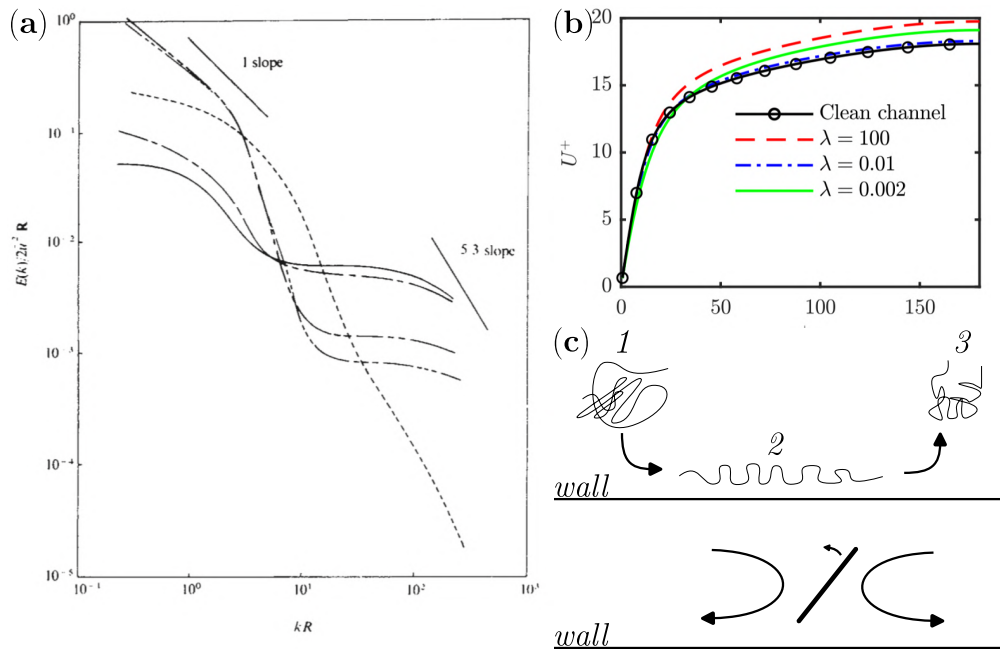
Figure 1.11. – Panels: (a) Experimentally measured turbulent kinetic energy spectra against the wavenumbers of a turbulent channel flow dispersed with asbestos fibres ($r \mathbb{O}(10^4)$) at 300 p.p.m. The dashed line represents the unladen spectrum, whereas the other lines represent different experimental runs where fibres are dispersed in the flow. It is possible to appreciate the kinked shape of the spectra, feeding energy from the intermediate scales to redistribute it to the smallest ones. Some spectra show a typical resonance at the largest scales, associated with the DR (McComb and Chan, 1981); (b) Dimensionless mean velocity profiles against the wall-normal coordinate of a turbulent channel flow at shear Reynolds $Re_\tau = 180$, laden with slender prolate ellipsoids (red dashed line), thin (blue dash-dotted) and extremely thin (green solid) oblate ellipsoids (Z. Wang et al., 2021). It is possible to appreciate a higher mean velocity profile over all the section of the channel when compared to the unladen case (black solid line with circles), sign of DR. (c) Top: polymers naturally exist in a coiled state within the flow (1) and, as they move to the near-wall region, they will be stretched and consequently store elastic energy (2). This energy will be later released as the polymers coil back (3), determining local visco-elastic effects that generate the overall DR. Bottom: as fibres are typically much larger than polymers and interact with the flow in a purely hydrodynamic way, they weaken the near-wall quasi stream-wise eddies proportionally with their particle aspect ratio(Paschkewitz et al., 2004). After these flow structures rearrange, DR is obtained.

Many experimental studies followed these two seminal works so that a large qualitative characterisation of drag reduction was produced, both by polymers (Metzner and Park, 1964; Gadd, 1965) and by fibres, especially in the limit of very high aspect ratio ($r \sim [1000; 10000]$) (Hoyt, 1972; Sharma, 1981). The common picture is that the DR agents would introduce some extra stresses of non-Newtonian nature within the flow, even at low concentrations of a few hundred PPM in weight. More in detail, polymers would reduce the coupling between axial and wall-normal turbulent components by being continuously stretched from their coiled state, especially in the near-wall region, where this would interfere with the turbulent bursts directed towards the bulk of the flow(Virk, 1975). On an intimate level, this was theoretically found to determine a visco-elastic behaviour of the suspension. According to the viscous theory of DR by Lumley, 1973, when sheared, a polymer-laden flow will express significant extensional viscosity in those regions where turbulent stretching is particularly strong. Instead, in the vision of De Gennes, 1990, DR occurs because polymers determine elastic stresses comparable to the turbulent stresses of the flow. In any case, this would correspond to a small-scale interaction, thickening the viscous sub-layer without affecting the turbulent core of the flow (Voth and Soldati, 2017), therefore treatable as an additional effective viscosity (Benzi et al., 2008).

Numerical simulations explored DR by fibres. Studies were limited to near-Kolmogorov rods with a moderate particle aspect ratio ($r = 100$), adopting a probabilistic closure model to resolve the orientation of the particles in a purely Eulerian approach at first (Paschkewitz et al., 2004; Gillissen et al., 2008), to later directly calculate the particle dynamics in the framework of two-way coupled Euler-Lagrangian simulations (Moosaie and Manhart, 2013; Z. Wang et al., 2021). It was found that the dispersed fibres indeed reduce the axial to wall-normal momentum exchange by weakening the quasi-streamwise eddies, but also determine a new axial to wall-normal term that penalizes the possible drag reduction by replacing the missing amount of Reynolds stress (Z. Wang et al., 2021). Indeed, as fibres tend to be macroscopic objects, their action is less effective in the near-wall region as they do not directly determine an effective viscosity like polymers, but instead will impose external constraints on the near-wall eddies, forcing them to restructure (Marchioli and Campolo, 2021).

On the other hand, fibres have been shown to interact on a wide range of turbulent scales, feeding energy from intermediate scales of the turbulent flow to re-distribute it at smaller ones, in an effect known as spectral shortcut (Olivieri, Brandt, et al., 2020). The intensity of this phenomenon is directly related to the mass loading of the suspension, i.e. to the density ratio between the fibres and the flow, and also depends on the relative length of the particles as well as on their aspect ratio, while particle deformability is a less relevant parameter (Olivieri, Mazzino, et al., 2022). Extremely slender fibres in a pressure-imposed flow were also observed to resonate, distributing energy to the largest scales of turbulence, determining a phenomenology associated with prominent drag reduction (McComb and Chan, 1981).

1.5. General aim of this manuscript

As this brief introduction tried to summarise, the study of suspensions of axisymmetrical particles is a matter of intense ongoing research. Many fundamental questions still remain unanswered, depending on the interaction between these particles and the carrying flows in a complex and multi-scale manner. Because of this, we were inspired to develop a multi-method approach, combining simple laboratory experiments with cutting-edge numerical simulations and exploring suspensions of fibres across multiple scales. This was possible by establishing a co-supervision agreement between the Università di Udine and the Aix-Marseille Université, and with the patronage of the Università Italo-Francese through the 'Bando Vinci 2021'. In the end, this has lead to the investigation of three fundamental aspects.

First, despite the recent theoretical and numerical efforts, a fundamental question still remains open in the study of suspensions of axisymmetrical particles:

- ◦ **What is the influence of inertia on the Jeffery orbits?**

To finally close this matter, an experimental investigation was prepared and executed at the Laboratoire IUSTI of the Aix-Marseille Université. The experimental set-up is described in detail in Chapter 2, together with the experimental protocols and the post-processing methods for the particle segregation and pose estimation. Results are then presented in Section 2.4, looking at Jeffery orbits of ellipsoidal and cylindrical particles in the weakly-inertial regime ($Re_p \leq 1$) and comparing with the recent theories of Dabade et al., 2016; Einarsson, Candelier, et al., 2015b.

Second, a numerical tool was developed at the Università di Udine in order to simulate a fibre-laden turbulent channel flow by an Euler-Lagrangian approach. The implementation is described in Chapter 3. Especially, we will focus on the modelling of the fibres, obtained through the Rod-Chain model by Yamamoto and Matsuoka, 1993; Lindström and Uesaka, 2007, as well as on the implementation of the two-way coupling in the Navier-Stokes equations, performed through the Exact Regularized Point Particle method by Gualtieri et al., 2015 to emulate the otherwise neglected boundary conditions imposed by the particles on the flow. As we will see, the hydrodynamical foundation of this implementation will permit to validate our software against the experimental results. Time will be also spent discussing the High-Performance Computing solutions deployed to implement this software for large-scale execution.

Then, the results of fibre-laden turbulent channel flow simulations at shear Reynolds number $Re_\tau = 150$ and $Re_\tau = 300$ will be presented in Section 3.8. We will first focus on the deformation of long fibres in wall turbulence at shear Reynolds $Re_\tau = 300$ in Section 3.8.1, exploring the influence of particle length, inertia and bending stiffness on their dynamics and their shape to answer the following question:

- ◦ **How do long fibres deform in wall turbulence?**

As simulations are performed in the two-way coupling regime, the feedback force determined by the slender fibres on the fluid will be evaluated, consequently determining the modulation of turbulence. Results of a wide numerical investigation will be presented in Section 3.8.6 at shear Reynolds $Re_\tau = 150$ and $Re_\tau = 300$, trying to answer to the third fundamental question of this manuscript

○ **Can long slender fibres be Drag Reducing agents?**

Given the broad range of our research, we anticipate that a combined methodology is the only possible solution. Indeed, experiments in the viscous regime are a powerful tool that allowed for an immediate answer to the influence of inertia on Jeffery orbits. On the other end, experimentally validated numerical simulations are the best option for the study of fibre-laden turbulent flows, exploring a vast parameter space defined by particle inertia and bending stiffness while looking at the mutual influence between the carried and carrier phases. In conclusion, it is clear that the two approaches strongly complemented each other and will lead to a multi-scale investigation of suspensions of fibres.

2. Experiments on the influence of small-inertia on the Jeffery orbits of axisymmetrical particles

In this chapter, the experimental campaign conducted to study the influence of small inertia on the Jeffery orbits of axisymmetrical particles is presented. At first, we look at the experimental methods, focusing on the preparation of the particles and the shear cell. Details about the particle detection method are then given, as well as a description of the data-driven approach to the multi-view object orientation estimation. Afterwards, the experimental results are discussed. Typical experiments are presented, highlighting the differences among Jeffery orbits for negligible and appreciable inertia. Then, we thoroughly characterise the equivalence of shape between ellipsoidal and cylindrical particles. Finally, we look into the influence of inertia on the period of rotation and the orbit constant of the experimentally observed Jeffery orbits. Results are also compared with the most recent small-inertia theories.

2.1. Experimental methods

2.1.1. Fabrication and characterization of axisymmetrical particles

The first problem faced in this thesis was to find particles of cylindrical and ellipsoidal shapes having a typical size of few mm and a density easily equated with a transparent and viscous fluid.

2.1.1.1. Fabrication

Custom axisymmetrical particles are fabricated for the preparation of this thesis. The shapes of interest are those of cylinders and of ellipsoids, as detailed in table 2.1 and visualised in figure 2.1. Whereas there exists a large literature describing experimental studies with cylindrical particles, i.e., fibres and disks (Trevelyan and

Code Name	shape	r	ℓ (mm)	a (mm)	Batch
ELL02	oblate ellipsoid	0.20 ± 0.01	0.58 ± 0.02	2.91 ± 0.01	I
ELL06	oblate ellipsoid	0.56 ± 0.01	1.27 ± 0.01	2.28 ± 0.01	I
ELL2	prolate ellipsoid	1.72 ± 0.02	1.78 ± 0.01	1.04 ± 0.01	I
ELL3	prolate ellipsoid	2.67 ± 0.06	2.53 ± 0.01	0.95 ± 0.02	I
ELL5	prolate ellipsoid	5.1 ± 0.1	2.64 ± 0.01	0.52 ± 0.01	I
ELL9	prolate ellipsoid	9.0 ± 0.1	2.62 ± 0.01	0.29 ± 0.01	I
ELL13	prolate ellipsoid	13 ± 1	4.7 ± 0.2	0.36 ± 0.02	I
CYL005	oblate cylinder	0.05 ± 0.01	0.14 ± 0.01	2.58 ± 0.06	III
CYL009	oblate cylinder	0.10 ± 0.01	0.15 ± 0.02	1.51 ± 0.01	III
CYL01	oblate cylinder	0.11 ± 0.01	0.31 ± 0.01	2.90 ± 0.04	III
CYL02	oblate cylinder	0.20 ± 0.01	0.31 ± 0.01	1.56 ± 0.02	III
CYL06	oblate cylinder	0.56 ± 0.01	1.03 ± 0.01	1.85 ± 0.02	III
CYL2	prolate cylinder	1.33 ± 0.02	1.78 ± 0.02	1.34 ± 0.01	I
CYL10	prolate cylinder	9.0 ± 0.2	2.59 ± 0.01	0.29 ± 0.01	I
CYL15	prolate cylinder	15.4 ± 0.2	3.48 ± 0.01	0.23 ± 0.01	II
CYL20	prolate cylinder	20.5 ± 0.7	4.54 ± 0.01	0.22 ± 0.01	II

Table 2.1. – Characteristics of all the particles used in the experiments: code name, mean aspect ratio r, half-length ℓ, radius a and identification of the production method.

Mason, 1951; Anczurowski and Mason, 1968b; Alipour, De Paoli, Ghaemi, et al., 2021; Verhille, 2022; Baker and Coletti, 2022), efforts with ellipsoids are rare, given the embedded difficulty in accurately producing such shape (Anczurowski and Mason, 1968b; Will et al., 2021). In addition, a strong constraint is enforced as we want to avoid confinement effects in order to better compare our results with theoretical efforts, typically derived for single objects suspended in an infinite viscous shear flow (Jeffery, 1922; Dabade et al., 2016; Einarsson, Candelier, et al., 2015a). This means that the typical size of the considered particles must be in general less than 1 *cm*.

Three different production methods are selected to fabricate our axisymmetrical objects. The first one (producing the particles identified as Batch II) is practically inexpensive and consists in cutting short segments from long fishing lines and is particularly suitable to produce slender fibres. The other two methods are somewhat more complex, involve basic knowledge of three-dimensional modeling and rapid prototyping, and require specialized and expensive machines. One procedure is based on the Laser cutting of Plexiglas sheets (Batch III). The Laser cutter is an Epilog Laser model, with a resolution of 1200 DPI, capable of cutting two-dimensional shapes and engraving a finite thickness of the material. Therefore, it is particularly suitable for the production of oblate cylinders, drawn in Adobe Illustrator, a commercial vector-based graphics software.

The other approach relies on the polymerization of a photo-sensitive resin (Batch I).

The resin printer is an Anycubic Photon Mono X model, with a resolution of 50 microns. Particles are generated from '.stl' files, produced in Blender, an open-source software for three-dimensional rendering. Therefore, this method is helpful in producing some fibres as well as both oblate and prolate ellipsoids. Finally, all particles except the fibres are polished at the end of their fabrication. Disks are manually smoothed between two sandpaper sheets. Ellipsoids are shaken by a mechanical agitator at 1000 rpm inside a small plastic box, partially filled with sand and whose internal walls are covered in sandpaper. Both methods improve the smoothness of the particles' surface as well as their overall shape.

2.1.1.2. Characterization

The shape of the produced particles is measured by a Hirox RH-2000 digital microscope. This allows taking multiple pictures with different perspectives of a given object, at a typical resolution of 221 pixels per mm. Then, at least 10 measurements of the particle shape are taken, in order to produce a statistical characterization of their length, 2ℓ, and their diameter, $2a$, and consequently of their particle aspect ratio r. These are produced using the open-source imaging software ImageJ (Abràmoff et al., 2004), which offers two functions to manually measure rotated rectangles and ellipses. The latter is deployed to characterize both the side and the top view, where the particle's axis is perpendicular to the plane of the image, of disks and ellipsoids, as shown in the panels (a) to (f) of figure 2.1 for an oblate ellipsoid with $r = 0.6$ (ELL06). The former is used to measure the fibres by solely looking at their side view, with the particle's axis lying in the plane of the image, as done in the panels (g) to (i) of figure 2.1 for a fibre with aspect ratio $r = 9.0$ (CYL10). Disks are also measured by fitting a rectangle on their top (panel (l), CYL005) and side views (panel (m) for CYL01 and (n) for CYL009). Indeed, we can appreciate the quality of the fabrication method from the fitted contours, especially in determining a realistic ellipsoid (panels (a) to (c)) with a circular mid-section (panels (d) to (f)). This is quite impressive considering the typical size of the objects, given by the scale reported in panel (c). Moreover, having repeated the measurements for different sides of the object, not only we check the symmetry of the particles but also collect enough data for a statistically sound characterization of their two sizes. In the end, we are able to produce and characterize 7 ellipsoids and 9 cylinders, whose aspect ratio and sizes are reported in columns 3 to 5 of table 2.1.

A comment is in order about the surface roughness of our particles, which in some cases appear not so smooth, like in panel (l) of figure 2.1. Anyway, from a detailed observation of the produced objects, we estimate the shape deviations to be not so relevant to their rotational dynamics, being always small when compared to their smallest size.

Finally, since the typical values of the Young modulus E_Y of the three materials are of the order of few gigapascals, we assume the particles to be perfectly rigid. Therefore, as the ratio between viscous and elastic forces will be vanishingly small, the particles are not expected to deform within the flow (Du Roure et al., 2019).
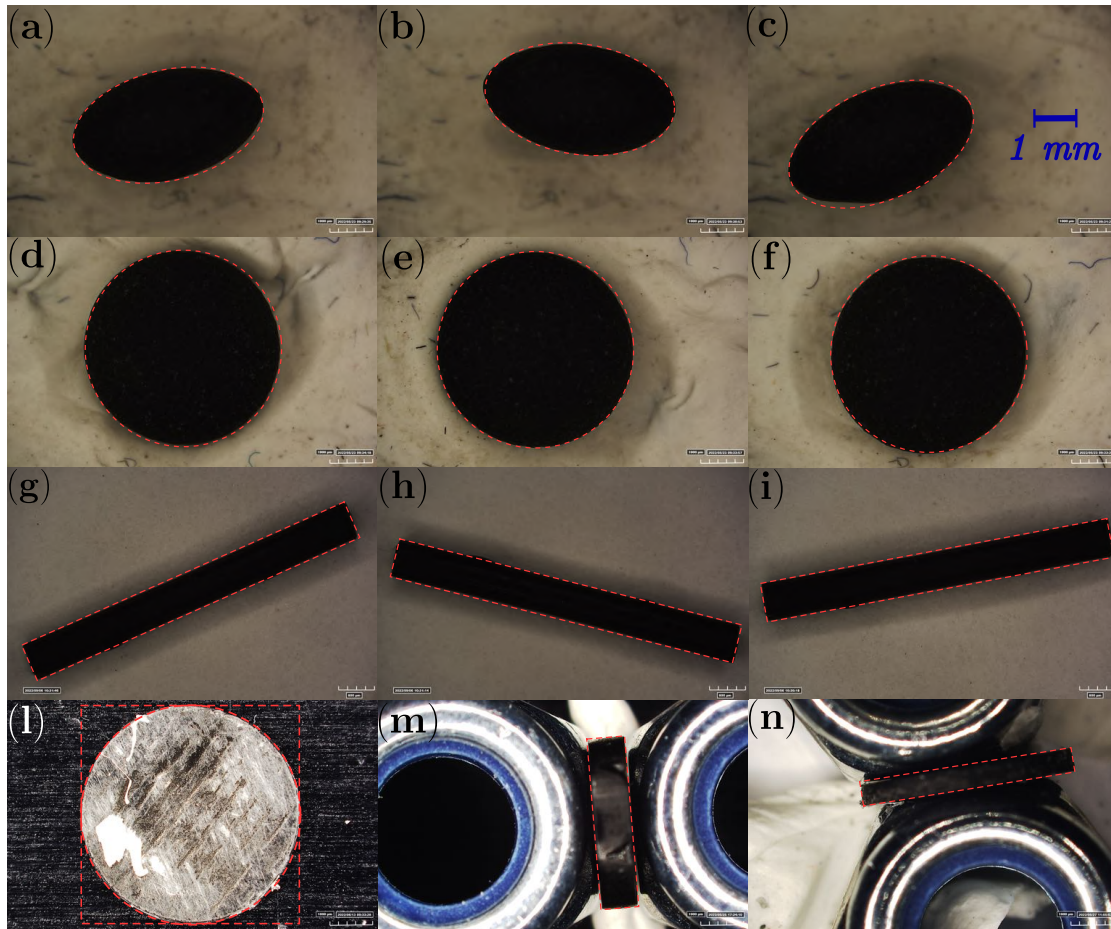
Figure 2.1. – Typical images for the characterization of some of the particles used in our experiments taken by the digital microscope. Panels: (a), (b) and (c): side view of the oblate ellipsoid ELL06 ($r = 0.6$), where the symmetry axis lies in the plane of the image; (d), (e) and (f): top view of the same oblate ellipsoid ELL06 ($r = 0.6$), where the symmetry axis is perpendicular to the plane of the image; (g), (h), (i): side view of the prolate cylinder CYL10 ($r = 9.0$); (l): top view of the oblate cylinder CYL005 ($r = 0.05$); (m): side view of the oblate cylinder CYL01 ($r = 0.11$); (m): side view of the oblate cylinder CYL009 ($r = 0.1$). The global scale is also reported in blue in panels (c).

2.1.2. Preparation of density-matched suspensions

The theory of Jeffery describes the rotation of axisymmetrical particles *suspended* in a *viscous* shear flow. Having described the protocol to prepare and measure axisymmetrical particles, we now focus on the experimental fluids, which will need to match the density of the given particles in order to nullify gravitational effects on their dynamics as well as be comfortably adjustable in their viscosity. For this reason, we found it convenient to prepare solutions of pure water, Ucon oil (Oil 75-H-90,000 Dow
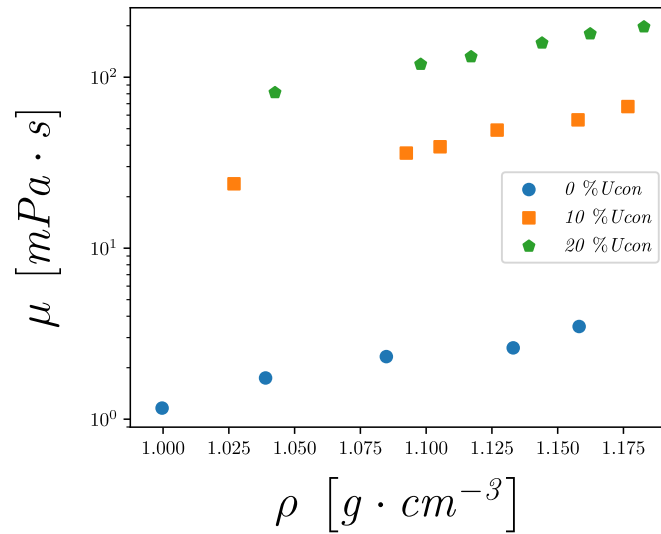
Figure 2.2. – Density-viscosity map for the water-citric acid-Ucon oil solution at three different concentrations of Ucon oil, namely $(0, 10, 20\%)$.

(www.dow.com)) and citric acid. Ucon oil is a particular oil which is deployed as a lubricant in solution with pure water, allowing it to increase its viscosity up to 40000 times that of the original fluid. Instead, the citric acid is mixed with water to increase the density of the resulting solution proportionally with its concentration, up to 1.3 times that of the original fluid.

Therefore, experimental fluids were prepared by first imposing the Ucon oil concentration and roughly fixing the viscosity of the final solution to later adjust its density to that of the given particle by finely tuning the citric acid concentration. An example is given in figure 2.2, where three solutions at $0, 10, 20\%$ concentration in mass are displayed (circles, squares and pentagons respectively), while the citric acid concentration is increased from left to right of the graph.

Viscosity measurements were made using an Anton Paar Physica MCR 501 rotational rheometer, with an error of $0.001 Pa \cdot s$ fully taking into account the real uncertainties. A comment is in order about the properties of a solution of pure water, citric acid and Ucon oil, whose viscosity is particularly sensitive to the temperature. Because of this, all experiments and rheological measurements were performed in a room at a controlled temperature of $23 \pm 1°$.

Given the typical size of the particles, it was not possible to directly estimate their density. Therefore, particles were suspended in a viscous fluid ($\mu \sim \mathbb{O}(10) mPas$) inside a thin 100 ml graduated beaker. Then, the density of the fluid was adjusted by small ($\sim 1g$) additions of citric acid or dilutions with pure water, until the settling/rising velocity of the particle was in the order of $\mathbb{O}10^{-6} m/s$, calculated between consecutive pictures over a time extent of several minutes. At that moment, the density of the fluid was measured by means of an Anton Paar Handheld density meter, estimating a maximum error of $4 \frac{kg}{m^3}$ to fully take into account uncertainties for all our samples. This measurement was also used to estimate the density of the given particles, setting

their value for the experimental fluids at all viscosity.

2.1.3. Experimental set-up

Viscous shear flows have been experimentally studied for one century now since the first experimental observation of Jeffery orbits (Taylor, 1923). Indeed, the simplicity of this configuration is a powerful advantage, allowing us to study more or less complex suspensions and directly compare them with the corresponding theory. Nevertheless, an embedded limitation is given by the fact that, contrary to theoretical modelling, the experimental realisation of a shear flow requires the confinement of the fluid, which must be handled with care in order to avoid undesired effects (Zettner and Yoda, 2001).

Viscous shear flows are typically produced in two different configurations: a cylindrical shear cell (Taylor, 1923; Trevelyan and Mason, 1951; Anczurowski and Mason, 1968b; Mason and Manley, 1956) and a linear shear cell (Moses et al., 2001; Zettner and Yoda, 2001; Metzger and Butler, 2012). The former offers the advantage of comfortably controlling the zero-velocity central line by adjusting the relative rotational velocity between the two counter-rotating concentric cylinders that shear the fluid. Nevertheless, the produced velocity gradient does not have a perfect linear variation, which must be taken into account (Trevelyan and Mason, 1951). On the other hand, linear shear cells produce a constant velocity gradient but present tougher technological challenges and can especially suffer from confinement effects and secondary flows (Zettner and Yoda, 2001). To solve this issue, double linear shear cells represent an expensive and complicated alternative (Moses et al., 2001).

A linear shear cell is deployed for the preparation of this thesis, illustrated in figure 2.3. The setup comes from the work of Metzger and Butler, 2012 and is similar to that of Zettner and Yoda, 2001. It consists of a small metal tank (1) 500 mm long, 40 mm wide, and 90 mm deep with 10 mm thick glass walls on its long sides. The tank is covered by a hollow lid (2), from which two metallic cylinders of diameter 20 mm hang, both equipped with polylactic acid (PLA) cylindrical supports to increase their diameter to 27 mm, which corresponds to the extent of the shear L_y. One cylinder is free to rotate (3), being coupled to a transmission shaft (4) through a rolling bearing. The other one is fixed to the lid (5) but allows it to re-adjust its position along the long side of the tank. In this way, a 0.1 mm thick transparent plastic belt (6) made of Mylar is kept under tension between the two. Small rectangular holes are cut on the top side of the belt, to ensure its coupling with a gear wheel that is glued to the rotating cylinder (not visualized for the sake of simplicity). The belt is 70 mm tall, extending from nearly the bottom to the top of the shear cell. An analog rotating motor is deployed for the experiments, powered by a Laboratory DC power supply and operating at an imposed current of 0.2 A and imposed tension of 24 V to ensure a stabilized Direct Current output voltage, manually adjusted between 5 and 9 V. This is connected to the transmission shaft by means of a drive belt and will rotate it at constant velocity. Therefore, the gear glued on the connected cylinder will grip the transparent belt and drive it in an infinite loop, shearing the fluid confined within at a
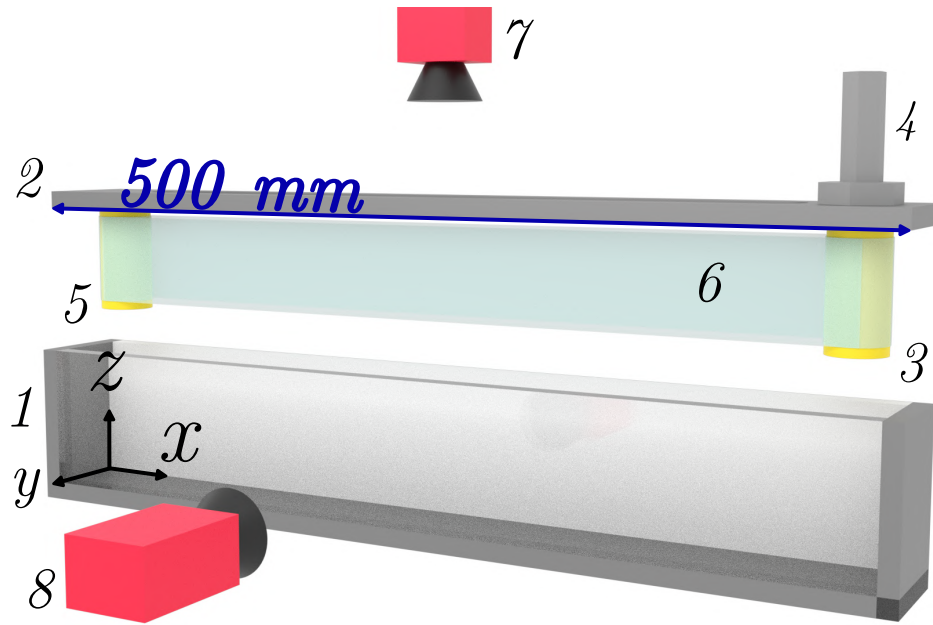
Figure 2.3. – Realistic rendering of the linear shear cell deployed during this thesis. The small tank is displayed (1), together with its lid (2), from which the two cylinders hang. The first is free to rotate (3), being coupled to a transmission shaft (4) through a rolling bearing. The second is fixed (5). Between them, a transparent plastic belt made of Mylar is kept under tension (6). Neither the laser-cut holes in the belt nor the gear glued on the rotating cylinder is visualized for sake of simplicity. The two cameras are also portrayed: one looking at the flow-gradient (x, y) plane (7), and the other focused on the flow-vorticity (x, z) plane (8). The scale is also reported in blue.

constant rate.

As displayed in figure 2.3, we define the absolute system of reference where x is the flow direction, y is the gradient direction and z is the vorticity direction, opposite to the gravity. In our experiments, one single particle at a time will be sheared in an iso-density fluid, having initially placed it by hand between the two sides of the transparent plastic belt. Given their inner distance of $27 mm$, we understand the importance of producing typically small particles in order to avoid confinement effects.

2.1.4. Characterisation of the flow

2.1.4.1. Particle Image Velocimetry

Particle Image Velocimetry (PIV) measurements are performed to characterize the viscous shear flow. For this purpose a 500 mW Class 4 laser is combined with a prism to shed a homogeneous 250 μm thick layer of light onto a flow-gradient x, y plane as rendered in panel (a) of figure 2.4. The wavelength of the chosen laser is of 532
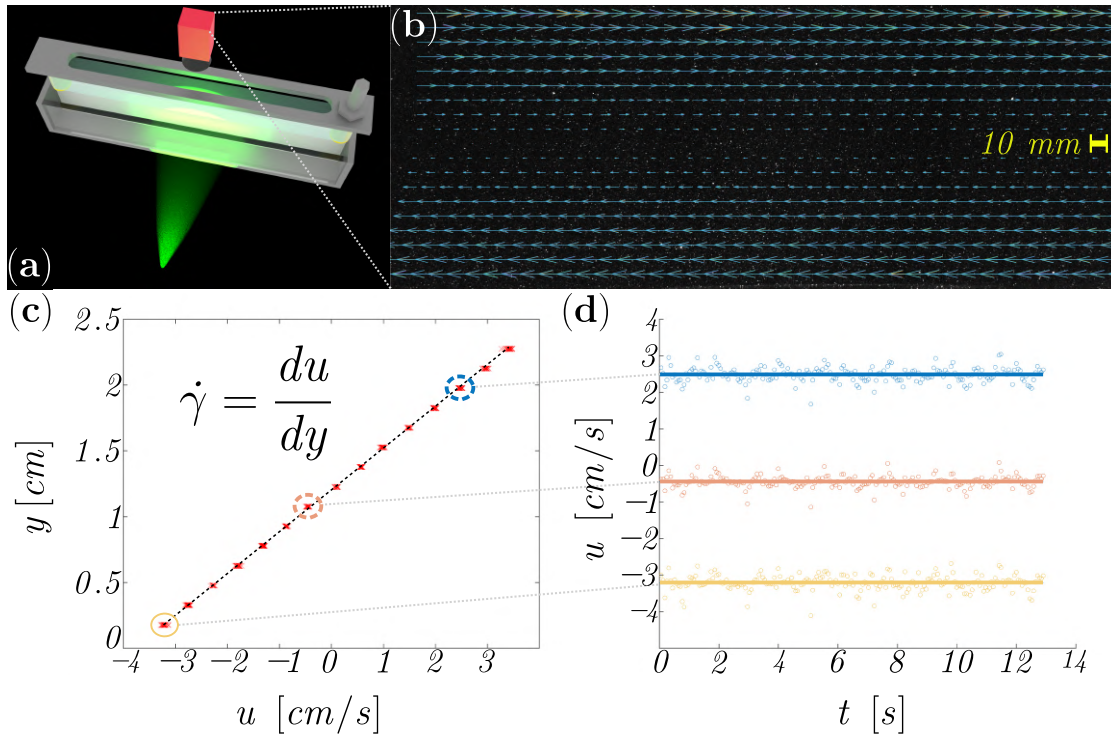
Figure 2.4. – Panels: (a) rendering of the set-up for the PIV measurements, where the side camera is replaced by the laser beam; (b) typical PIV field with arrows showing the result of one measurement averaged over 200 couples of images at 39 mm from the bottom of the tank. The scale is also reported; (c) collapse of the flow-direction velocity u for the $y = const$ lines of points, averaged in time. The black dashed line indicates the linear fitting to measure the mean shear. For these measurements, the viscosity is $\mu = 0.05 Pas$ and the tension imposed on the rotating stage is of $9V$, returning a shear rate of 3.16 ± 0.03 $1/s$. (d) Scattering of the velocity measurements in time at three different positions along the gradient direction y. The shear Reynolds number is $Re = \frac{\rho \dot{\gamma} (L_y)^2}{\mu} = 55$, where the shear length $L_y = 27$ mm is given by the imposed distance between the two sides of the transparent plastic belt.

nm, corresponding to the sensitivity peak of the top camera, while the side view is not considered for these measurements. Then, micro-spheres of glass covered with silver are chosen as tracers to seed the fluid. These particles have an estimated batch diameter of 15 μm and a density of 1.4 g/cm^3 (Dantec Measurement Technology). Given their characteristics, we can estimate a very low particle response time, therefore the particles are expected to act as tracers ($St \sim \mathbb{O}(10^{-5})$) and follow the flow without developing an inertial behaviour. The solid phase volume fraction is very small so particle-particle interactions are negligible.

When the laser beam is pointed from one of the long sides, we obtain a clear visu-

alization of the flow generated by the motion of the transparent belt by the contrast between the shiny particles, which diffuse the laser light, and the dark background. A typical PIV image is displayed in panel (b) of figure 2.4, with the result of the measurement drawn as blue arrows. Then, two consecutive pictures of the illuminated flow-gradient plane are taken with the top camera at a frame rate of 1/30 s. An Eulerian approach is chosen to analyse the sequence of images in order to measure the flow around 48×19 points of the flow-gradient plane. The following routine is implemented in the program DPIVSoft (Meunier and Leweke, 2003). Centred around each point, a square interrogation window from the first frame is correlated to its twin from the second frame, the latter being also displaced around its centre in the two dimensions by a finite distance. The typical size of the interrogation window is 32 pixels. Correlation is calculated among the Fourier transforms of the two interrogation windows, whose peak will indicate the average displacement of the glass beads in that region of the flow.

A comment is in order about the delay between the two images, which must be adjusted according to the intensity of the shear and the size of the interrogation window to avoid losing track of the tracers. Nevertheless, a viscous shear flow with a typical size like the one considered in our experiments does not express such strong velocity gradients and the given parameters represented an optimal configuration during the whole preparation of this manuscript.

2.1.4.2. Characteristics of the Viscous shear flow

PIVs are usually performed averaging over 200 couples of images, with a delay of 1 s between each. Measurements are repeated at three different heights above the bottom of the channel (28, 39 and 56 mm), in order to obtain information on a flow window deep enough ($\sim 30 mm$) to comfortably perform the experiments, but also well separated from the floor of the tank and the free surface of the fluid, typically recorded at $\sim$ 65 mm. The typical resolution for the intermediate depth is of $\sim$ 7 pixels/mm.

The mean shear rate is $\dot{\gamma} = du/dx$ and is measured by linearly fitting the mean velocity profile in the flow direction x against the gradient coordinate y, as shown in panel (c) of figure 2.4. Errors are calculated by taking the mean value of the standard deviation calculated at each $y = const$ line of points in time and in space. In panel (d) of figure 2.4 the time-evolution of the flow velocity u is displayed for three measurement points at different values of the gradient coordinate y. We can appreciate a nice collapse of the scattered points around the mean values, displayed as solid lines. These fluctuations are due to the random oscillation of the transparent plastic belt as well as to the presence of the secondary flows, determined by the two rotating and static cylinders. Anyway, the quality of our results leads us to estimate their impact as negligible on the mean shear along the whole width of the camera field, which corresponds to $\sim 14 cm$ where to perform experiments.

Finally, PIV measurements are repeated at low ($0.05 Pas$) and high ($0.4 Pas$) viscosity values for two different values of the tension imposed on the rotating stage. In this

Table 2.2. – Shear rate measurements for two different viscosity values. Averages are performed in time over 200 couples of frames, and in space along the flow direction x. PIV measurements are repeated at different depths to ensure a constant shear region whose estimated depth is $\sim 30mm$.

Viscosity [$Pa\ s$]	Voltage [V]	$\dot{\gamma}$ [$1/s$]
0.4	5	2.07 ± 0.03
0.4	9	3.64 ± 0.05
0.05	5	1.97 ± 0.03
0.05	9	3.16 ± 0.03

way, shear rate values will be estimated by linear interpolation on the actual viscosity of the experimental fluids during the experiments, allowing us not to repeat a PIV measurement for each experimental session, which would be highly time-consuming and very unpractical. The measured shear rates are reported in table 2.2. It is possible to appreciate a slight decrease in the effective shear rate with the viscosity of the experimental fluid.

2.1.5. Particle detection and methods for the pose estimation

2.1.5.1. Image recording

We now discuss the methods for the recording of the experiments, the detection of the particles and the reconstruction of their three-dimensional orientation. As displayed in figure 2.5, two cameras are placed, their axes perpendicular in a virtual (y, z) plane, to get two complementary views of the shear cell. The top camera looks at the flow-gradient (x, y) plane, while the side camera looks at the flow-vorticity (x, z) plane. Both cameras are focused on a three-dimensional region of interest which is 14 cm long in the flow direction, while its extent in the gradient direction is limited to the distance between the two sides of the transparent plastic belt, fixed to 27 mm. Finally, the depth of this region of interest is limited to 3 cm, corresponding to the typical vertical spread of the PIV measurements, and starts 1 cm below the free surface of the fluid.

The cameras are two Allied Prosilica GX1910, with a resolution of 1890×1080 pixels. Both cameras are equipped with a Nikon micro nikkor 55mm 2.8 objectif. Being placed at a distance of less than half a meter from the shear cell, they record images with a resolution of ~ 20 pixels per mm for each view. Moreover, the objectives' exposition is constantly reduced to the bare minimum in order to enhance the depth of focus, estimated to be approximately 3 cm, yet without compromising the images' contrast. Distortion effects are assumed to be negligible, especially considered the distance between the cameras and the shear-cell. Nevertheless, this is verified manually by measuring a check-board inclined pattern placed in the camera fields inside the small tank for both perspectives. Also, this allows to exclude phenomena of diffraction at the interfaces, especially crucial for the side view.
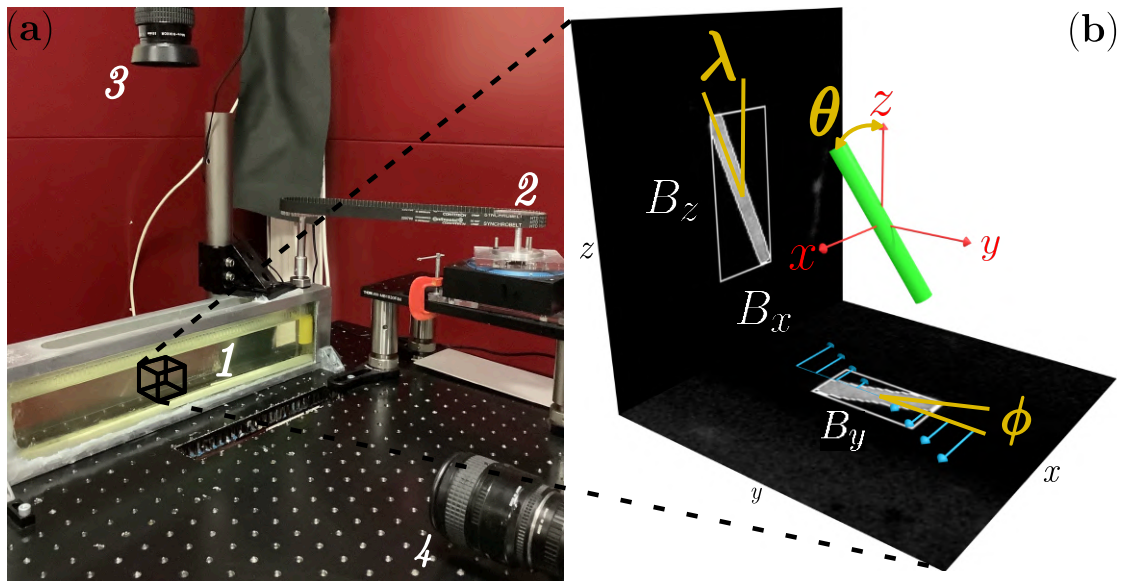
Figure 2.5. – Panels: (a) Picture of the experimental setup, where the tank filled with fluid between the two sides of the transparent plastic belt is visible (1), together with the motion transmission system (2) and the two cameras, looking at the (x, y) flow-gradient plane (3) and at the (x, z), flow-vorticity plane (4). (b) Sketch of the output given by the dual-camera video-recording system. The reference frame is defined at the centre of the particle. The azimuth and polar angles, ϕ and θ, as well as the projected angle, λ, and the three components of the Axes-Aligned Bounding Box, B, are also represented. The two recorded frames are displayed on the corresponding (x, y) flow-gradient and (x, z) flow-vorticity planes, to appreciate the contrast between the particle projections and the background as well as the detected particle contours and Axes-Aligned Bounding Boxes.

The cameras are connected by Ethernet cable to one computer each and controlled by a Matlab script developed In-house. The script allows to take single images, multiple images or videos at a given frame-rate in the range $[3.5 - 30]$ fps. Videos of the experiments with a single particle suspended in a viscous shear flow are recorded as following. First, the shear flow is activated. Second, the particle is manually placed as close as possible to the neutral zero-velocity line. Third, having waited for a short time in order for the particle to forget the influence of its positioning of the initial condition, the video-recording for both cameras is started. At this point, both videos are synchronized by a luminous signal. Then, the video-recording is stopped after a satisfying number of rotations has been observed or before the particle is to leave the camera fields in the flow direction. A typical result is displayed in figure 2.6, where the chrono-photography of a fibre with particle aspect ratio $r = 5.5$ is displayed combining the frames recorded by the top (panel (a)) and bottom (panel (b)) cameras.
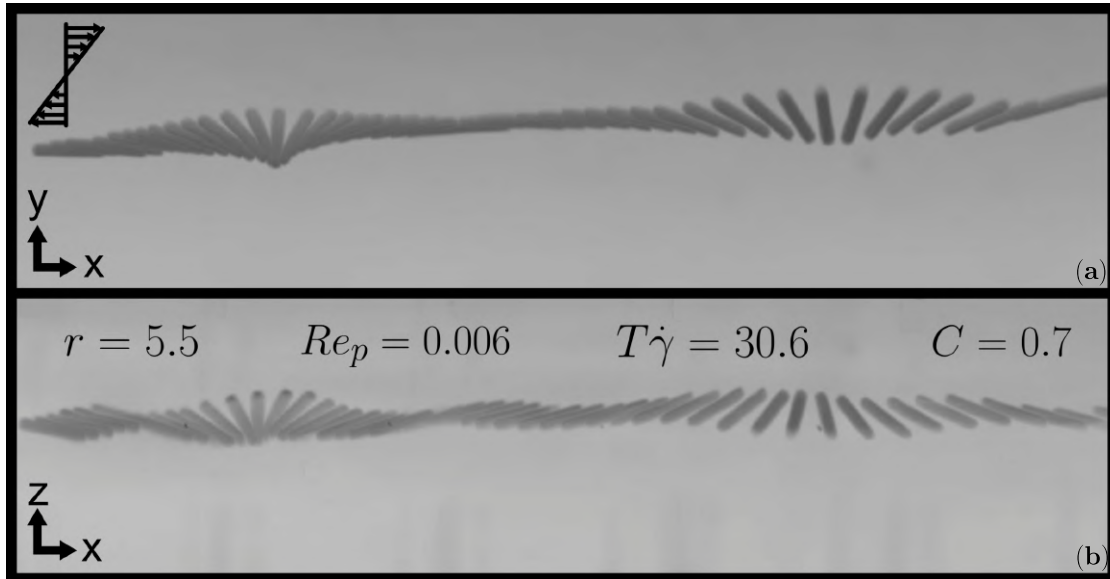
Figure 2.6. – Left-to-right chrono-photography of a fibre with $r = 5.5$ in viscous shear flow, obtained by taking the minimum intensity of one frame every 10. The aspect ratio r, the particle Reynolds number Re_p, the dimensionless period of rotation $\dot{\gamma}T$ and the fitted orbit constant C are also reported. Panels: (a) top view of the flow-gradient x, y plane; (b) side view of the flow-vorticity x, z plane.

2.1.5.2. Particle segmentation

The processing of the two videos of one experiment starts with the manual identification of the first synchronized frame, given by the luminous signal, as well as of the particle's initial position. Both parameters are manually measured using the software ImageJ, and represent the input for a Python script for the automatic detection of the particle, developed during the preparation of this thesis. We'd like to stress on the fundamental importance of automatising as much as possible this procedure, given the large amount of experiments that have been recorded.

In order to automatically detect the particle in the recordings of our experiments, the computer must be able to separate it as a whole from the background and other surfaces or objects, which could include imperfections in the transparent plastic belt or in the glass side of the tank, small bubbles or other particles that accidentally contaminated the experimental fluid (dust, hair, dirt). In other words, the computer must be capable of a task usually identified as image segmentation, a fundamental operation since the rise of Computer Vision with important applications in medical image analysis, video surveillance and autonomous vehicles (Minaee et al., 2021).

A typical image segregation algorithm partitions the image into coherent regions classified according to a fundamental property, such as pixel intensity, in order to be able to assign them a proper label, i.e., identify their nature as a coherent object (Pham et al., 2000). Classical approaches include the image thresholding (Otsu, 1979) or the
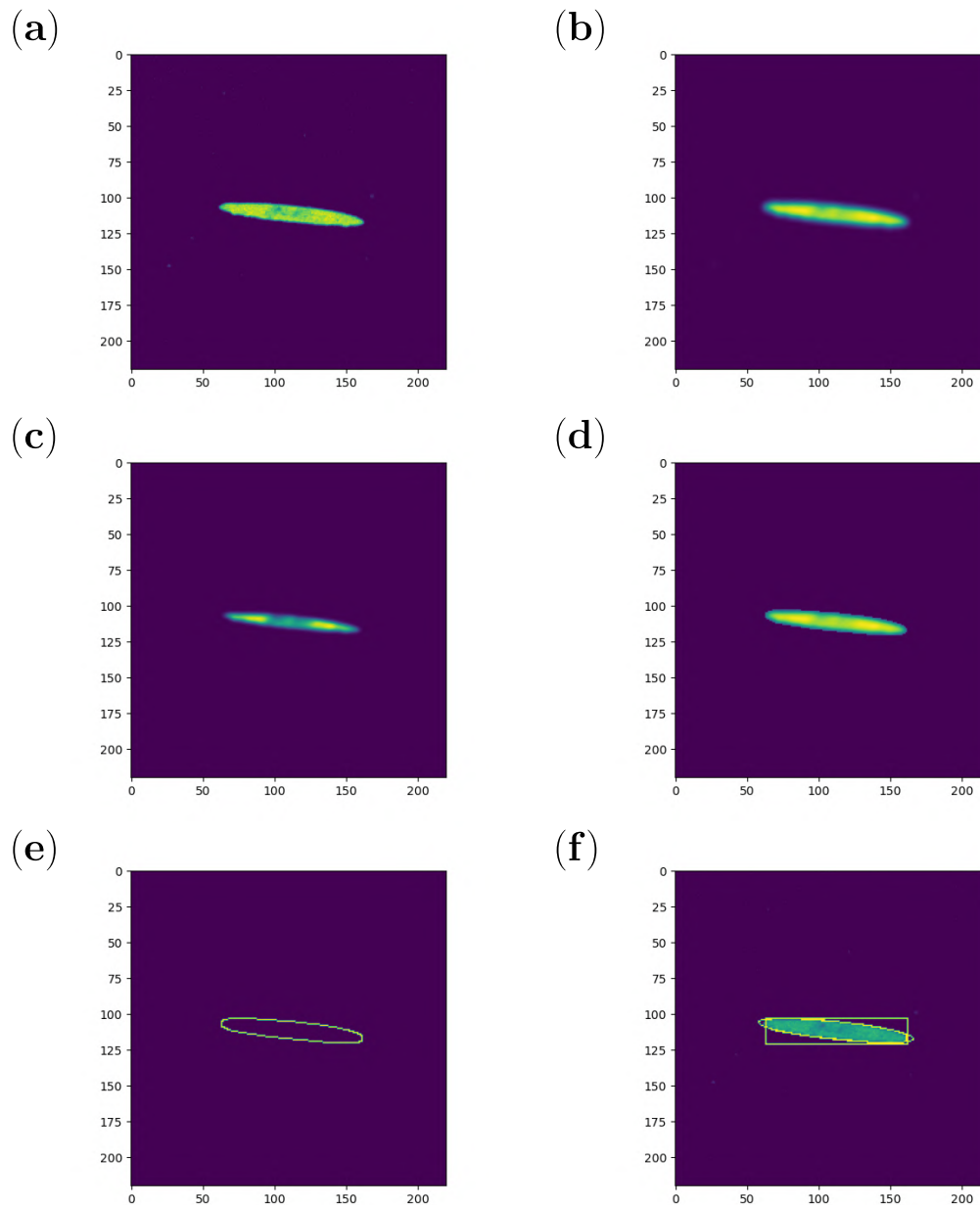
Figure 2.7. – Steps of the Particle detection method for one typical frame. Panels: (a) original frame zoomed on the particle; (b) blurred frame to reduce noise; (c) square power of the original frame to increase the contrast between the particle and the background; (d) threshold filter to segregate the particle; (e) detection of the contour based on the Canny-edge method; (f) contour fitting to measure its orientation (fitEllipse) and its Axis Aligned Bounding Box (boundingRect).

watershed method (Najman and Schmitt, 1994) among many. The former has been the foundation of many successful studies with rigid and flexible fibres suspended in

viscous or turbulent flows (Brouzet et al., 2014; Einarsson, Mihiretie, et al., 2016; Will et al., 2021; Alipour, De Paoli, Ghaemi, et al., 2021). Instead, data-driven approaches based on Deep Learning models have rapidly taken over in the past years, because of their superior performance and accuracy (Minaee et al., 2021). Nevertheless, their popularity in the field of fluid mechanics could be limited by the difficoulties in producing reliable data-sets for training.

A threshold approach was chosen for the particle detection script, combined with the Canny, 1986 contour detection method and implemented in Python using the OpenCv library (Bradski, 2000). The script completes a simple detection routine for all the frames of a video-recording of one experiment as illustrated in figure 2.7. First, a background subtraction operation is performed using a particle-less image of the tank. Second, the frame is reduced to a focused region of size $4\max(\ell; a)$ around the particle centre (panel (a)), having manually measured the scaling on the particle's smallest size by ImageJ. For the most slender objects, this corresponds to ~ 10 pixels over the smallest size of the particle. At this point, the following operations are performed on the image:

— a Gaussian filter is applied to reduce the noise (panel (b));
— the square power of the image is calculated a stored in a second array (panel (c)). This operation results in an increased separation between the intensity of the pixels belonging to the particle (high) and to the background (low);
— a Threshold filter is applied to the image according to its previously calculated squared values, erasing to zero all the pixels whose intensity lies below a fraction of the mean intensity of the picture. This fraction intuitively depends on the aspect ratio of the particle, as more slender images fill a lower part of the frame (panel (d)).

At this stage, the image is ready for the detection of the particle's edges, which is performed by the Canny method (panel (e)). This algorithm allows the recognition of contours within an image by measuring its pixel intensity gradients and reconstructing the shapes through hierarchical threshold (Canny, 1986). Finally, if the detected contour satisfies some geometrical constraints given by the known-a-priori particle shape, measurements of the projected particle are taken. First, the orientation angle of the contour is recorded. This is done through the fitEllipse function of the OpenCv library, which performs a least-squared optimization method to fit an ellipse to the measured contour and estimate its orientation.

The method was always successful for prolate shapes, whereas the returned angles would not be the actual ones in the case of disks or oblate ellipsoids, despite maintaining a consistent time-evolution. Second, the two-dimensional Axis Aligned Bounding Box is measured (AABB hereinafter). By Axis-Aligned Bounding Box (AABB hereinafter) we mean the smallest rectangle (parallelepiped when generalizing to three dimensions) that is tangent to the particle projection (particle in three dimensions), and is obtained from the boundingRect function of the OpenCv library. Finally, both measurements are stored before advancing to the next frame, which will be centered around the latest measured centre of the particle, also given by the fitEllipse method. In the end, the described routine will produce long lists of the time-evolution of the

(a)

(b)
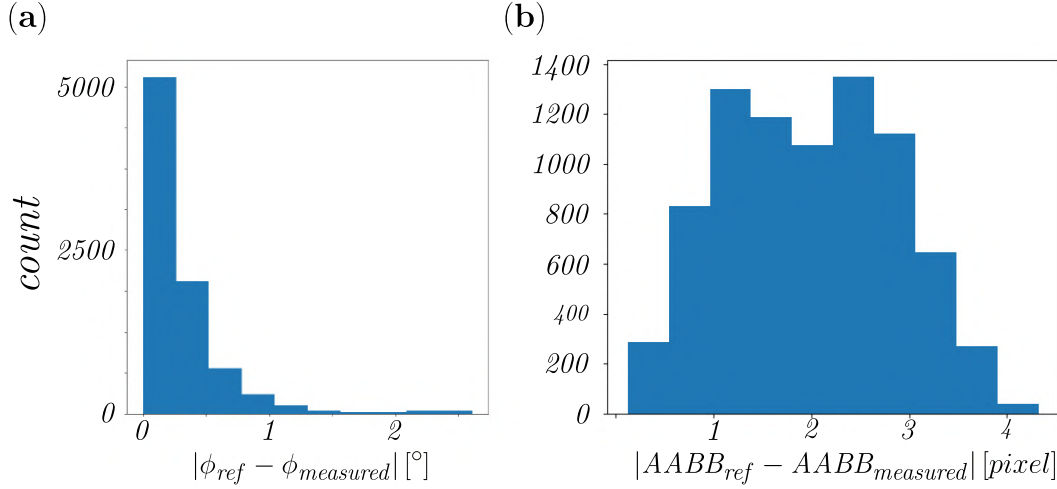
Figure 2.8. – Evaluation of the accuracy of the proposed particle detection method. Panels: (a) absolute error between the reference and measured values of the particle contour orientation angle for a fibre of aspect ratio 10; (b) Euclideian norm error between the reference and measured values of the particle AABB for a disk of aspect ratio 0.1 and diameter 490 pixels.

centre, orientation and AABB of the particle projection for each recorded video.

The accuracy of the post-processing script is evaluated in figure 2.8 against 8100 virtual images of randomly oriented disks and fibres. These images are generated using the open-source software Blender, covering all possible orientations in the first quadrant of a three-dimensional reference system in optimal light conditions. Also, a resolution of 7 pixels over the particle's smallest dimension, comparable to the one available in the experiments. As we can appreciate from panel (a) of figure 2.8, the error on the angle is typically below 2°. The error on the Axes-Aligned Bounding Box is also small, being limited to few pixels for a particle with perimeter equal to 490 pixels.

2.1.5.3. Pose estimation

Having described how to obtain the time-evolution of the position, orientation and AABB components of the projections of the particles onto the flow-gradient and flow-vorticity planes for one experiment, we now discuss the methods to estimate their three-dimensional orientation. The procedure is non-trivial, therefore we find it convenient to introduce a polar reference system that returns the three components of the particle orientation vector **n** as following:

$$\mathbf{n} = (\sin\phi\sin\theta, \cos\phi\sin\theta, \cos\theta),\qquad(2.1)$$

where ϕ and θ are the azimuth and polar angles respectively, graphically introduced in panel (b) of figure 2.5 or in figure 1.6. Note that the Euclidean norm of **n** is always one by definition.

From the experiments of Trevelyan and Mason, 1951 with fibres suspended in a

viscous shear flow we know that, whereas the particle projection in the flow-gradient (x, y) plane provides a direct measurement of the azimuth angle ϕ, that in the flow-vorticity (x, z) plane determines a projected polar angle λ, which corresponds to the real polar angle θ only in the flow-aligned particle orientations. Since, most of the experimental studies aiming at estimating the three-dimensional orientation of rigid fibres in viscous and turbulent flows relied on a projection-based approach (Stover and C. Cohen, 1990; Baker and Coletti, 2022). The main advantage of this method is the fact that a simple direct calculation of the particle orientation is performed from its projected lengths. Anyway, its two main drawbacks are the following. First, the projection-based approach naturally requires a high resolution on the particle in order to be accurate. Second, this method is particularly efficient for slender particles, being more error prone as the particle aspect ratio decreases and becoming useless for ellipsoidal objects.

A remarkable alternative is the pattern-recognition approach described in the work of Will et al., 2021, who measured the orientation of ellipsoids rising in a still fluid. This method is based on correlating experimental observations and computer-generated images of ellipsoidal particles to estimate the rotation of the former from the latter, having painted a corresponding pattern on both real and virtual particles. Finally, if provided with enough computational resources and training data, one could also look into Neural Networks for the direct pose estimation from one or two images, taking advantage of pre-trained models to rapidly adapt them to our task (Redmon et al., 2016).

Two issues have emerged during this study that motivated a novel approach to the orientation estimation of axisymmetrical particles suspended in a viscous shear flow. First, the resolution on the particle sizes is not sufficient to successfully deploy a projection-based approach. Second, we intend to estimate the pose of ellipsoidal particles from their projections only, as their typical size would not allow to mark them and follow the pattern-recognition method of Will et al., 2021.

Therefore, we found convenient to look at the relation between the particle orientation vector **n** and the length of the particle projection along the three-axis of the Cartesian reference system, i.e., its three-dimensional Axes Aligned Bounding Box **B**. This is a non-linear expression and known is a closed form only for the inverse transformation, allowing to recover the projections of cylindrical and ellipsoidal particles by having previously imposed their orientation. Such operation is straightforward for a cylinder, whose axes aligned projected lengths correspond to the sum of a line of size 2ℓ and two oriented capping circles of diameter $2a$ (Quilez, 2016). By defining the eccentricity e of these rotated circles as follows:

$$e = a \cdot \sqrt{1 - \mathbf{n} \cdot \mathbf{n}}\,, \tag{2.2}$$

given their center points $\mathbf{p_a}$ and $\mathbf{p_b}$, the Axes-Aligned Bounding Box **B** is given by maximizing the only two possible orientation extensions:

$$\mathbf{B} = \max\big((\mathbf{p_a} + e), (\mathbf{p_b} + e)\big) - \min\big((\mathbf{p_a} - e), (\mathbf{p_b} - e)\big)\,. \tag{2.3}$$

A similar calculation is slightly more complex for ellipsoidal particles, considering their natural lack of sharp edges. A generic ellipsoid oriented with the z axis ($\mathbf{n} = (0,0,1)$) is presented in its quadric form as following:

$$\overline{\mathbf{O}} = \begin{bmatrix} a^{-2} & 0 & 0 \\ 0 & a^{-2} & 0 \\ 0 & 0 & (a \cdot r)^{-2} \end{bmatrix} \tag{2.4}$$

It is straightforward to build a generic rotation matrix $\overline{\mathbf{R}}$ that aligns the original orientation of the quadric, $(0,0,1)$, to any generic orientation given by the two polar angles as in equation 2.1. Therefore, the quadric itself will be rotated to the new orientation by the following:

$$\overline{\mathbf{Q}} = \overline{\mathbf{R}} \cdot \overline{\mathbf{O}} \cdot \overline{\mathbf{R}}^T . \tag{2.5}$$

Given the matrix $\overline{\mathbf{Q}}$, it is possible to demonstrate that the square roots of the first three components of the diagonal of its inverse are the halved sides of the AABB:

$$\mathbf{B}_i = 2 \cdot \sqrt{\overline{\mathbf{Q_{i,i}}}^{-1}} . \tag{2.6}$$

Demonstration for this statement is provided in Appendix A.

We now posses all the information to estimate the orientation of the given axisymmetrical particles. Indeed, by a suitable re-scaling of the two-dimensional AABBs measured in the flow-gradient and flow-vorticity planes, it is possible to obtain an experimental observation of the time evolution of the three-dimensional Axes-Aligned Bounding Box. On the other hand, having fixed the particle aspect ratio r, equations 2.3 or 2.6 can be iterated over all the possible orientations of a three-dimensional Cartesian system, reducing it to the first quadrant due to the symmetries of the system. This was done by Python scripting over $360 \times 360 = 129600$ possible combinations of ϕ, θ in the range $[0; 90]$ resulting in long lists of geometrically calculated three-dimensional AABBs with resolution of $0.25°$ over each angular variable. Finally, the time evolution of the particle orientation vector $\mathbf{n}$ is regressed by minimizing each AABB experimental measurement over the virtually generated list of geometrically calculated AABB for the given geometry. Note that this approach does not allow us to measure the spin of the particles.

2.1.5.4. Multi-variate minimization by Deep Learning

The minimization of the experimentally measured AABB over the virtually generated list of AABBs to regress the particle orientation represents an optimisation problem in three variables (B_x, B_y, B_z). This type of calculation can be especially time consuming even when implemented using specialized optimization libraries such as Scipy. Therefore, given the abundance of synthetic three-dimensional AABBs, a data-driven approach was chosen instead, based on a simple Deep Learning model implemented using Tensorflow (Abadi et al., 2015). A Deep Learning model, or Neural Network, is a collection of parameters, or weights, which respond to a determinate input according

to a non-linear activation function. These models can by trained over labeled data, i.e., data where input and output are related in a known way, to automatically learn features. This is done by minimizing a loss-function, which calculates the difference between the predicted and true output in response to a given input value. After trained, complex and non-linear functions can be comfortably solved for novel data by the Neural Network, as long as one possesses sufficient training data and computational power.

Therefore, we choose to build a simple Deep Learning model to estimate the pose of the given axisymmetrical particle from its Axes-Aligned Bounding Box. The model is trained on synthetic data, i.e., the geometrically deduced lists of AABBs and **n**, prepared following equations 2.3 and 2.6 as described in the previous section. The model takes the three components of the AABB as input and returns the corresponding orientation vector **n**, both of size 3. A Gaussian noise layer with 0.1 standard deviation is attached to the input layer, which will randomly corrupt the AABBs values in order to avoid overfitting and strengthen the general predicion of the model. Then, hidden dense layers are placed inbetween, made of 256 fully connected weights, being 'relu' their activation function. We observed that one hidden layer is typically sufficient for the regression of the most slender prolate shapes, but three seem preferable to deal with oblate and nearly spherical objects. Finally, a dedicated Lambda layer ensures the normalization of the Euclidean norm of the model output. The model is compiled and trained over at least 20 epochs by minimizing a custom loss function, which calculates the Euclidean norm of the difference between the true and predicted values of the orientation vector **o**:

$$loss = \sqrt{\sum_{i=1}^{3} \left(\mathbf{n}_{true,i} - \mathbf{n}_{pred,i} \right)^2} \ . \tag{2.7}$$

In addition to that, the custom loss function strongly penalizes any prediction whose value would be lower than zero, as such orientation vector components are not possible. The chosen optimization method is the 'Adam', which is a randomized batched Gradient Descent method. A random 20% splitting of the data-set between training and testing samples is picked for the evaluation of trained model. The result of the testing phase is visualized in figure 2.9, where the predicted values of the particle orientation vector **n** are displayed against the true solution for a fibre with aspect ratio $r = 9.0$ (CYL10). We can appreciate the great accuracy of the proposed method, as the Neural Network clearly succeeded in learning the geometrical function that takes the particle Axes-Aligned Bounding Box **B** as input and returns the the particle orientation vector **n**.

A comment is in order about the dependence of the proposed method on the particle shape, as the model must be recompiled and trained for every different particle geometry or particle aspect ratio. We expect that a general model for all axisymmetrical particles could be built and trained, but for sake of simplicity and lack of knowledge an attempt towards such solution was not made during the preparation of this manuscript.
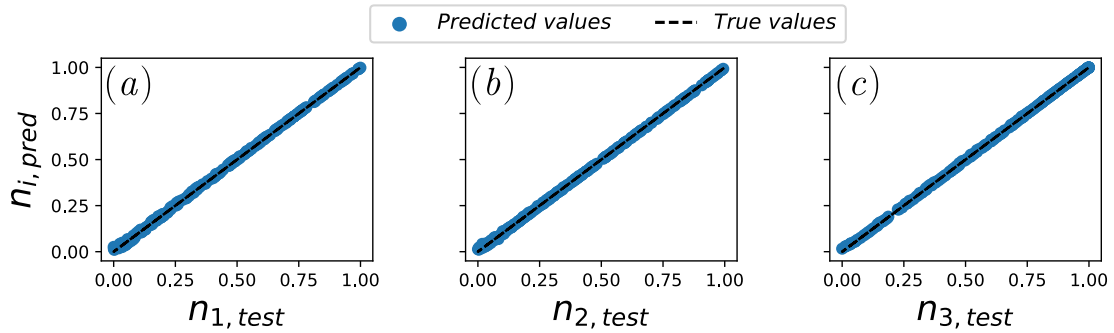
Figure 2.9. – Predicted values against true values of the orientation vector **n** obtained by training and testing the described Deep Learning over the geometrically calculated synthetic data for a fibre with aspect ratio $r = 9.0$ (CYL10): (a) n_1 along x, (b) n_2 along y, (c) n_3 along z.

2.1.6. Analysis of the experiments

2.1.6.1. Projected angles and period of rotation

By taking full advantage of the described methodology, we can perform experiments with a given particle sheared in an iso-density flow that last up to several rotations. Then, experiments will be repeated approximately 10 times for a given particle Reynolds number, trying to sample as many as possible different initial conditions. A report of the performed experiments with the given particles is given in table 2.3.

Typical results consist of long time series of the evolution of the two measured angles ϕ and λ, as well as the coordinates of the centres of the particle's projections in the flow-gradient and flow-vorticity planes together with the components of the two Axes-Aligned Bounding Boxes.

We focus at first on the analysis of the projected angles in order to obtain some insight into the period of rotation of the considered axisymmetrical particles. As an example, one complete experimental run with an oblate ellipsoid (ELL06) with particle aspect ratio $r = 0.6$ is presented. Anyway, the methodology and the approach to the analysis of the data will be the same for all the particles considered for the preparation of this thesis. During this run, 11 experiments are performed at constant shear rate $\dot{\gamma} = 3.15 \ 1/s$, being $\rho = 1.23 \ g/cm^3$ the density and $\mu = 46 \ mPa \ s$ the viscosity of the experimental fluid. The particle Reynolds number is $Re_p = 0.44$ and the shear Reynolds number is $Re = 15$.

The time-evolution of ϕ and λ are displayed in panels (a) and (b) of figure 2.10 for all the experiments. The profiles of the angle ϕ show a clearly periodic evolution, describing multiple passages between 0° and 360°, each corresponding to one Jeffery orbit. Instead, the projected polar angle λ shows a less intelligible behaviour, oscillating between ±90°.

Clearly, both angles can be interpreted as time series and characterised by Fourier analysis. This is done by calculating the Fourier transform of the two signals, whose power spectra are displayed in panels (c) and (d) of figure 2.10 respectively. The

60

Code Name	N. of experiments	Range of Re_p
ELL02	10	0.04 - 0.05
ELL06	32	0.01 - 1.04
ELL2	77	0.03 - 0.38
ELL3	13	0.5 - 1.3
ELL5	40	0.008 - 0.291
ELL9	50	0.007 - 0.642
ELL13	5	0.18
CYL005	56	0.03 - 0.78
CYL009	36	0.01 - 0.34
CYL01	30	0.04 - 1.32
CYL02	10	0.005 - 0.009
CYL06	20	0.04 - 0.25
CYL2	50	0.002 - 0.336
CYL10	153	0.007 - 0.986
CYL15	5	0.059
CYL20	5	0.100

Table 2.3. – Number of experiments and range of particle Reynolds number for each considered particle.

calculations are done in Python using the Fast Fourier Transform implementation of the Numpy library. We can appreciate a clear resonance of the signal power around the characteristic frequencies of the system. This is also highlighted in the inserts, where the dispersion of the frequencies of the maximum power around its mean is illustrated. Therefore, the period of rotation of the given particle is estimated as the inverse of the mean of these frequencies, where a minimum squared error criterion is applied to choose between the signals of ϕ and λ. Uncertainties are calculated as standard deviation errors over all the available measurements. We argue that differences between the two angles arise from particular inclinations of the particle within the flow, which render the detection of one of the two impossible, like when attempting the detection of the angle ϕ of an oblate ellipsoid aligned with the vorticity axis.

Once the mean period of rotation T_m has been measured, we can invert the formula of Jeffery, 1922 to estimate the equivalent particle aspect ratio r_{eq} by resolving the following second order equation:

$$r_{eq}^2 - \frac{T_m \dot{\gamma}}{2\pi} r_{eq} + 1 = 0 \, . \tag{2.8}$$

This operation returns the aspect ratio of the ellipsoid that corresponds to the experimentally observed particle. Previous studies have shown that fibres and disks express an equivalence of shape, as they always tend to rotate at the same time as less slender

61
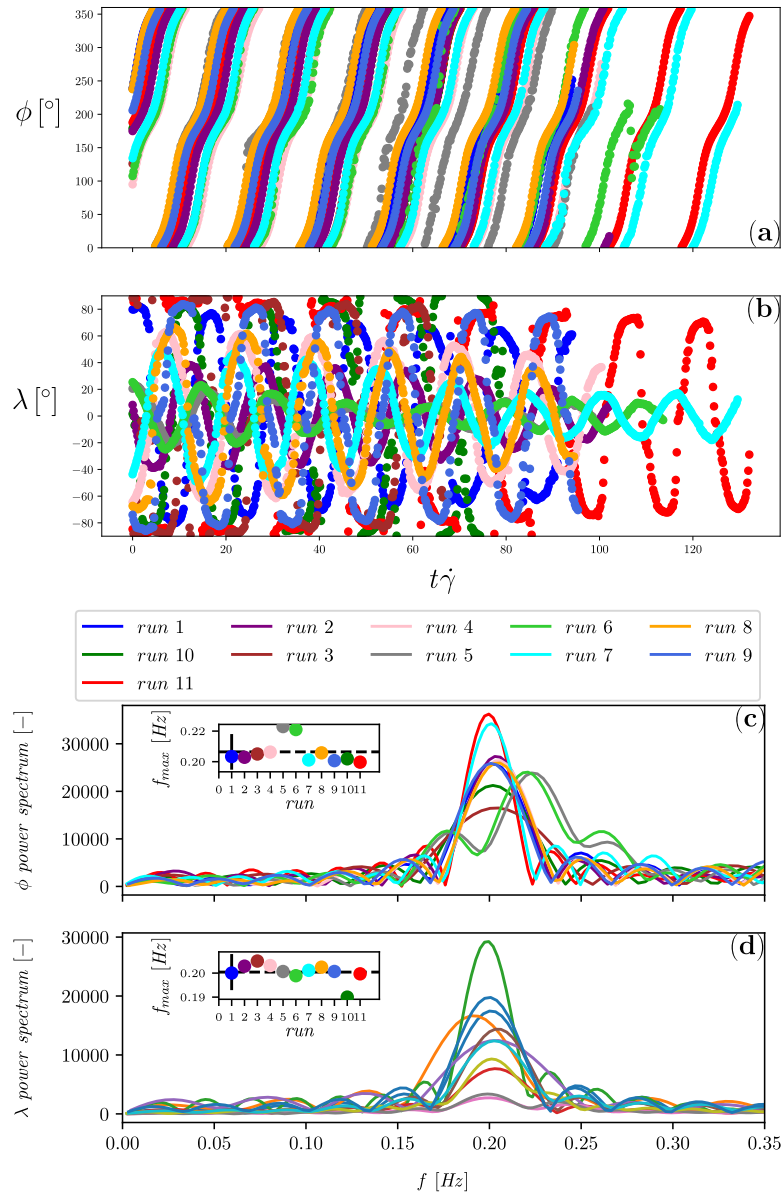
Figure 2.10. – Characterisation of the measured angles ϕ and λ during 11 experimental runs with an ellipsoid of aspect ratio $r = 0.6$ at particle Reynolds number $Re_p = 0.44$ and $T\dot{\gamma} = 15.67$. Panels: (a) azimuthal angle ϕ against the dimensionless time $t\dot{\gamma}$; (b) projected polar angle λ against the dimensionless time $t\dot{\gamma}$; (c) power-spectra of the azimuthal angle ϕ; (d) power-spectra of the projected polar angle λ. The inserts in panels (c) and (d) show the dispersion around the mean of the maximum frequencies of the power spectra.

ellipsoids. (Trevelyan and Mason, 1951; Anczurowski and Mason, 1968b; Harris and Pittman, 1975).

Burgers, 1938 analytically showed that the disturbance caused by a cylinder of

axis ratio r will be reproduced by an ellipsoid of $r_{eq} = 0.74 r$. (Trevelyan and Mason, 1951) experimentally found a good agreement at intermediate prolate aspect ratios ($10 \lesssim r \lesssim 20$). Later on, Cox, 1971 derived a semi-empirical asymptotic expression for the equivalence of shape of slender cylinders, which he fitted on the data of Anczurowski and Mason, 1968b to find that $r_{eq} = 1.24 r / \sqrt{\log r}$. Finally, Harris and Pittman, 1975 found that Cox's equivalence was slightly overestimating their measurements at high particle aspect ratios ($r > 200$), suggesting an alternative data-driven power-law expression to determine the equivalent ellipsoids at $r_{eq} = 1.14 r / r^{0.156}$ for both disks and fibres. Given the long-standing efforts in finding the correct shape equivalence between cylinders and ellipsoids, we expect our measurements of the period of rotation to be particularly insightful during our experiments.

2.1.6.2. Particle orientation vector and Jeffery orbits

The two projected AABBs are recombined by a suitable re-scaling, having manually measured the number of pixels over the particle diameter by ImageJ. Then, the Deep Learning model is trained over the geometry of the particle and deployed to obtain the time-evolution of the particle orientation vector **n** during the experiments. Finally, a mono-dimensional Gaussian filter is applied to reduce measurement noise.

We now consider the same oblate ellipsoid but with a different experimental fluid, being $\rho = 1.23$ its density and $\mu = 1.2 \ Pa \ s$ its viscosity. The estimated shear rate is $\dot{\gamma} = 3.64 \ 1/s$, determining a low particle Reynolds number $Re_p = 0.02$ and shear Reynolds number $Re = 0.69$. Only one experiment of the given session is discussed in figure 2.11, but the methodology is the same for all runs with any of the considered particles.

The time-evolution of the three components of the particle orientation **n** is displayed in panel (a) of figure 2.11. We appreciate an excellent agreement between our data (green dots) and the theory of Jeffery (solid black line), obtained integrating equation 1.8 in time from the first flow-aligned position of the particle during the experiment. The three components can be recombined to render the experimental Jeffery orbits in the three-dimensional space, as done in panel (b) of figure 2.11. Once again we can appreciate the nice agreement between the experiment and the theory, as the Jeffery orbits of the considered oblate ellipsoid appears like a slightly spherical ellipse on the surface of a sphere of radius 1.

Finally, we are just left with the task of measuring the orbit constant C during our experiments. At this scope, we can directly measure the real polar angle $\theta = \arccos(n_3)$ and fit its definition according to the theory of Jeffery

$$\theta = \arctan\left(\frac{C \cdot r}{\sqrt{r^2 cos(\phi)^2 + sin(\phi)^2}}\right) \tag{2.9}$$

where $\phi = \arctan(n_1/n_2)$ is the azimuth angle and the equivalent aspect ratio $r = r_{eq}$ must be imposed to correctly estimate C. This is done graphically in figure 2.12, where
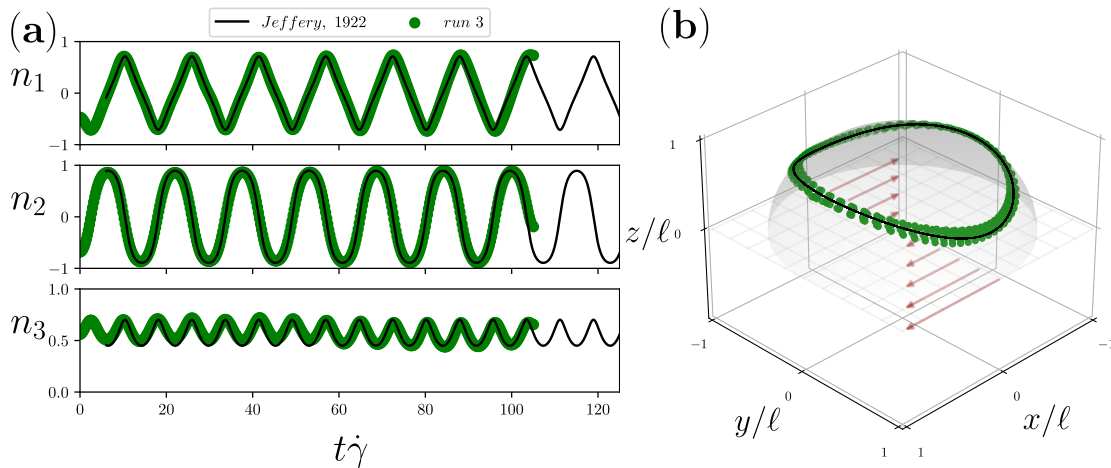
Figure 2.11. – Visualization of the experimentally measured particle orientation vector $\mathbf{n} = (n_1, n_2, n_3)$ for an oblate ellipsoid with aspect ratio $r = 0.6$ (ELL06). The shear rate is $\dot{\gamma} = 3.64\ 1/s$ and the viscosity is $\mu = 1.2\ Pas$, determining a particle Reynolds number equal to $Re_p = 0.02$. Panels: (a)time-evolution of the three components of the particle orientation vector; (b)Three-dimensional reconstruction of the Jeffery orbits. The theory of Jeffery is also displayed in the panels as a solid black line.

the experimentally measured values of θ are plotted as empty black dots together with the values returned by equation 2.9 using the fitted orbit constants C displayed in the legend. Whereas in the viscous regime ($Re_p \sim 0$) we know that the orbit constant will not vary in time, allowing us to fit the whole experiment for one value, this is not expected to be the case when considering experiments at relevant particle Reynolds number (Dabade et al., 2016). Therefore, it is preferable to measure the orbit constant every half-rotation, fitting equation 2.9 over a short window of size $0.8 \cdot T_m$. This operation will produce two discrete measurements for each period of rotation, which will be differentiated with the corresponding points at the next rotation as following:

$$\Delta C_i = \frac{C_{i+2} - C_i}{T_m} \ . \tag{2.10}$$

In figure 2.12 it is possible to appreciate a contained variation of the orbit constant among consecutive rotations as expected, given the small value of the particle Reynolds number that was considered in this experiment.

2.2. Dimensional analysis

The rotation of axisymmetrical particles suspended in a viscous shear flow is characterized by seven quantities:

— the shear rate $\dot{\gamma}\ \left[s^{-1} \right]$;
— the fluid dynamic viscosity $\mu\ \left[kg\ m^{-1}\ s^{-1} \right]$;
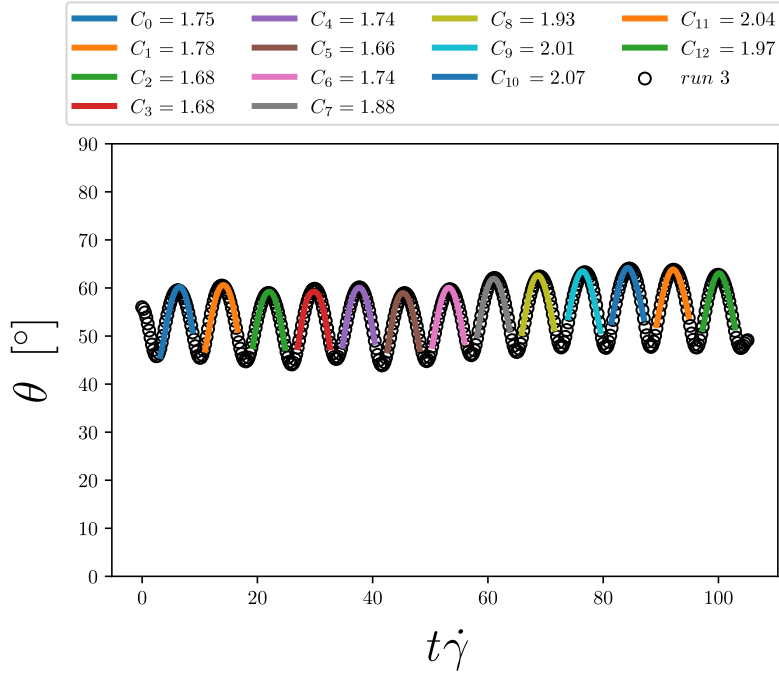
Figure 2.12. – Time-evolution of the experimentally measured polar angle θ (black empty circles) and least-square fitting of the theory of Jeffery over each half-period (coloured lines). $Re_p = 0.02$.

— the density of the fluid ρ $\left[kg\ m^{-3}\right]$;
— the density of the particle ρ_p $\left[kg\ m^{-3}\right]$;
— the length of the particle 2ℓ $[m]$;
— the diameter of the particle $2a$ $[m]$;
— the length of the shear L_y $[m]$.

Following the Π theorem (Buckingham, 1914), we find $7 - 3 = 4$ dimensionless numbers that describe the physical system:

○ the particle aspect ratio $r = \frac{2\ell}{2a}$. This dimensionless number quantifies the slenderness of the axisymmetrical particles, i.e., the way they preferentially sample strain and vorticity in the flow. Once the shear rate $\dot{\gamma}$ is specified, the temporal extent of the Jeffery orbits purely depends on the particle aspect ratio, being the dimensionless period:

$$T\dot{\gamma} = 2\pi \left(r + \frac{1}{r}\right). \tag{2.11}$$

During the preparation of this thesis, we worked with not particularly slender cylinders and ellipsoids, exploring the range $r \in [0.05; 20.1]$.

○ the particle confinement ratio $\kappa = \max(2a, 2\ell)/L_y$. This dimensionless number quantifies confinement effects over particle dynamics. Its importance on the flow and on the particles was evaluated by Zettner and Yoda, 2001. Great care was taken during the fabrication of our axisymmetrical particles so that their

major size would always determine a confinement ratio κ lower than 0.2 during the experiment with small but finite particle Reynolds number, and $\kappa \leq 0.35$ for the most slender prolate particles (ELL13 and CYL20);

○ the particle Reynolds number $Re_p = \frac{\rho \dot{\gamma} \max(a,\ell)^2}{\mu}$. This dimensionless number measures the ratio between the inertial effects induced by the flow on the particle dynamics and the viscous forces and it is of crucial importance in the considered physical system. In our experiments, its range is limited by the following factors. First, the density of the flow is fixed to match that of the particles and nullify gravitational contributions to their dynamics. Second, the largest size of the particle is typically kept small in order to minimize confinement effects to better compare experiments and theoretical efforts. Third, the shear rate of the system is limited by the characteristics of the rotating stage. Therefore, flow inertia is controlled by modifying the viscosity μ of the experimental fluids, to explore the following range: $Re_p \in \left[\mathbb{O}(10^{-3}); \mathbb{O}(10^0)\right]$. The particle Reynolds number Re_p and the confinement ratio κ combine to determine the shear Reynolds number $Re = \frac{\rho \dot{\gamma}(L_y/2)^2}{\mu}$, which evaluates the ratio between the inertial and viscous forces of the shear flow. Its influence on the stability of the particle dynamics was evaluated in the work of Zettner and Yoda, 2001. In our experiments, the shear Reynolds number will be varied in the range $Re \in [0.2; 37]$;

○ the particle Stokes number $St = \rho_p/\rho Re_p = \rho_p \dot{\gamma} \max(a,\ell)^2/\mu$, which measures the ratio between the inertia of the particle and the viscous forces. Simulations and theoretical efforts have explored its influence over the Jeffery orbits (Rosén, Lundell, et al., 2014; Einarsson, Candelier, et al., 2015b; Dabade et al., 2016). Nevertheless, it is impossible to separate between fluid and particle inertia in our experiments, as the density of the fluid and that of the suspended object are supposedly matched, which means that $Re_p = St$ at all times. The theory of Dabade et al., 2016 has quantified the relative importance between the contributions of fluid and particle inertia in determining the instability of the Jeffery orbits. As we will discuss in Section 2.3, the former will always dominate the latter in intensity for both prolate and an oblate particles.

2.3. Small-inertia theories

Einarsson, Candelier, et al., 2015b and Dabade et al., 2016 presented two theoretical derivations of the hydrodynamic torque acting on an ellipsoid suspended in a viscous shear flow based on the reciprocal theorem. In this way, these authors could model the influence of small-inertia on the Jeffery orbits to order Re_p, both finding that the first effect is a modification of their stability.

Einarsson, Candelier, et al., 2015a presented their results as an equation of motion
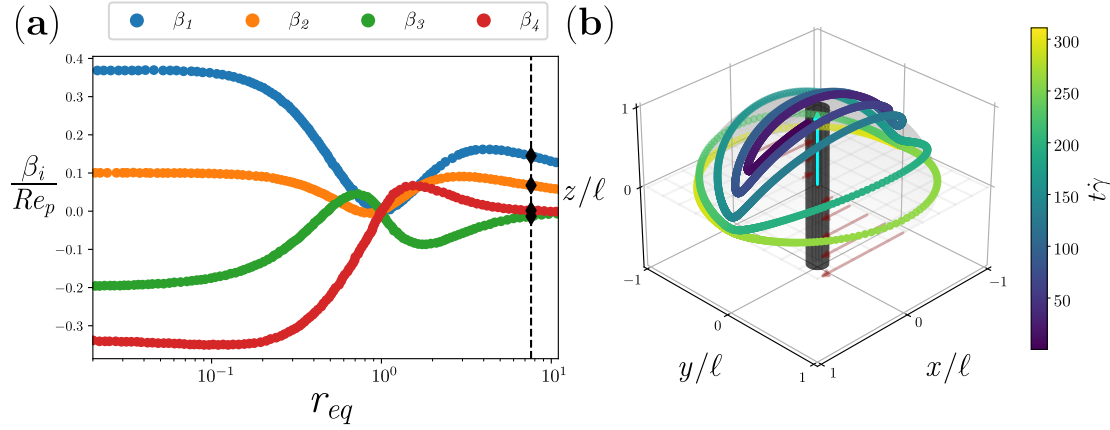
Figure 2.13. – Panels: (a) β_i coefficients of equation 2.12 as given in Figure 2 of Einarsson, Candelier, et al., 2015a. As an example, for the fibre CYL10 with $r = 9.0$, the coefficients β_i are chosen at the intersection between the dotted vertical line at $r_{eq} = 7.4$ with the respective curves; (b) Three-dimensional reconstruction of the Jeffery orbits of a fibre with aspect ratio $r = 9$ at particle Reynolds number $Re_p = 0.5$ obtained by integration equation 2.12 in time, using the β_i coefficients calculated graphically in panel (a). The colour scale indicates the dimensionless time and is reported in the colour-bar.

for the particle orientation vector **n** as follows:

$$
\begin{aligned}
\dot{\mathbf{n}} \;=\; & \boldsymbol{\Omega}\cdot\mathbf{n} + \frac{r^2-1}{r^2+1}\left[\mathbf{E}\cdot\mathbf{n} - \mathbf{n}\left(\mathbf{n}\cdot\mathbf{E}\cdot\mathbf{n}\right)\right] \\
& + \beta_1\left(\mathbf{n}\cdot\mathbf{E}\cdot\mathbf{n}\right)\mathbb{P}(\mathbf{E}\cdot\mathbf{n}) + \beta_2\left(\mathbf{n}\cdot\mathbf{E}\cdot\mathbf{n}\right)\boldsymbol{\Omega}\cdot\mathbf{n} + \beta_3\mathbb{P}(\boldsymbol{\Omega}\cdot\mathbf{E}\cdot\mathbf{n}) + \beta_4\mathbb{P}(\mathbf{E}\cdot\mathbf{E}\cdot\mathbf{n})
\end{aligned}
\tag{2.12}
$$

where $\mathbb{P}(\mathbf{x}) = \mathbf{x} - (\mathbf{n}\cdot\mathbf{x})\,\mathbf{n}$ is an operator that projects out components in the **n**-direction. The right-hand side of the first row corresponds to the equation of Jeffery while the second row contains the additional terms. The scalar coefficients β_i are functions of the particle aspect ratio, combining to determine the preferential response of the ellipsoid to the influence of strain and vorticity in the small inertia regime. They were provided graphically in figure 2 of Einarsson, Candelier, et al., 2015a for $Re_p = St$ and are reported here in panel (a) of figure 2.13, where the equivalent aspect ratio is used when considering a cylinder with $r = 10$.

Equation 2.12 shows that for small but finite Re_p an ellipsoidal particle will continue to rotate periodically where its period of rotation T is still given by the theory of Jeffery, 1922. Anyway, inertial effects arise proportionally to the particle Reynolds number and affect the stability of the Jeffery orbits. This will determine a slow drift through consecutive rotations depending on the particle aspect ratio, as displayed in panel (b) of figure 2.13. Prolate ellipsoids will drift towards the stable $C = \infty$ Jeffery orbit in the flow-gradient (x, y) plane where they will adopt a pure tumbling motion. Instead, oblate ellipsoids in the near-sphere limit will drift to the stable $C = 0$ spinning orbit

along the vorticity axis z. Nevertheless, oblate ellipsoids below a critical aspect ratio $r^* \sim 0.14$ display a peculiar behaviour, feeling two stable orbits in both the spinning and the tumbling limiting cycles. Therefore, slender oblate particles below the critical aspect ratio will drift to either the spinning or the tumbling orbit depending on their initial orientation.

Dabade et al., 2016 reached similar conclusions on the influence of inertia on the Jeffery orbits, giving a precise estimation of the separation between the two basins of attraction for the oblates, which moderately raises from the tumbling orbit ($C = \infty$) as the slenderness increases. These authors characterised the inertial effect as a drift through consecutive rotations by means of a discrete variation of orbit constant ΔC in a single Jeffery period. To understand such a formulation, we must discuss Jeffery orbits as a periodic dynamical system. To this purpose, it is convenient to recall the formulation of Leal and Hinch, 1971, who introduced the orbit time τ and the orbit phase (or constant) C to describe the two-dimensional parameter space of the Jeffery orbits. Hence, following a classical textbook on the subject (Glendinning, 1994), the time-dependence of the system can be dropped in order to look at variations ΔC of its phase C through dynamical states, where the intensity and the sign of the variations will characterise the stability of the corresponding Jeffery orbit.

Dabade et al., 2016 provide closed expressions for the drift due to particle and fluid inertia separately. For particle inertia, this is given in their equation (5.19) in terms of the eccentricity: $\xi_0 = \sqrt{1/(1 - 1/r^2)}$ for the prolate and $\xi_0 = \sqrt{1/(1 - r^2)}$ for the oblate particles. The eccentricity parameter ξ_0 is calculated using the physical particle aspect ratio, r, for the ellipsoids and the equivalent particle aspect ratio, r_{eq}, for the cylinders. Then, the integrals I_i, J_i are provided in their Appendix C, while the prolate F_i^p, G_i^p coefficients come from their equations (5.7-5.12). Following Dabade et al., 2016 to obtain the oblate coefficients, one needs first to multiply the prolate coefficients by the squared length-scale to obtain their dimensional form. Then the transformation prolate-to-oblate must be applied ($\xi_0 < - > i \left(\xi_0^2 - 1\right)^{0.5}$), before returning to dimensionless variables by dividing by the squared length-scale, as described below equation (5.12) of Dabade et al., 2016. The fluid-inertia drift is still obtained from equation (5.19), where St is replaced by Re_p and the F_i^f, G_i^f coefficients are given in equations (6.1-6.8).

The normalized orbit constant variations are displayed in figure 2.14 for a prolate (panel (a)) and an oblate (panel (b)) ellipsoid against the normalized orbit constant. The contributions are normalized by the squared particle eccentricity to keep the drift finite in the near sphere limit. The positive sign of the curve shows that prolate particles tend to the tumbling cycle as the orbit instability peaks at intermediate orientations before relaxing in the (x, y) plane ($C/(C+1) = 1$). On the other hand, the oblate shape is pushed towards the spinning orbit, as its ΔC is mostly negative. Nevertheless, a tiny region of positive orbit constant variations is visible in correspondence with the tumbling orbit ($C/(C+1) = 1$), highlighting the existence of a double basin of attraction for this oblate spheroid. A comment is in order about the relative importance of particle and fluid inertia, as the former is clearly dominated by the latter for both

Figure 2.14. – Normalized orbit constant variation ΔC against the normalized orbit constant C. The variations are scaled in the near sphere limit, normalizing by the squared particle eccentricity ξ_0^2. Blue lines display the fluid inertia contribution while pink lines report the particle inertia contribution. Panels: (a) prolate ellipsoid, $r = 10$; (b) oblate ellipsoid, $r = 0.1$. The dotted black lines show the neutral stability line.

shapes. Also, orbit constant variations are plainly larger for the oblate particle.

In the following of this chapter, the results of an experimental campaign observing the influence of inertia on the Jeffery orbits will be presented and compared to the two theoretical efforts of Einarsson, Candelier, et al., 2015b and Dabade et al., 2016. First, we will look at the time-evolution of meaningful experiments against equation 2.12 of Einarsson, Candelier, et al., 2015b for both prolate and oblate shapes. The equation was integrated in time using the 'odeint' function of the Scipy Python Library from the first flow-aligned orientation of the given experimental run. Then, we will measure variations ΔC of orbit constant C by discretely differentiating over the experimentally measured orbit constants, in order to directly compare our results to the stability maps of Dabade et al., 2016.

2.4. Experimental results and comparison with the small-inertia theories

2.4.1. Jeffery orbits

Typical experimental Jeffery orbits for a disk with aspect ratio $r = 0.05$ and a disk with aspect ratio $r = 0.11$ are shown in figure 2.15, (a),(b) and (c),(d) respectively. In addition, we display the experimental Jeffery orbits observed for an ellipsoid with aspect ratio $r = 0.6$ and a fibre with aspect ratio $r = 9.0$ in figure 2.16, (a),(b) and (c),(d) respectively. In these two figures, the coloured symbols represent the intersection

Figure 2.15. – Three experimental Jeffery orbits for the disk CYL005 with $r = 0.05$ and $r_{eq} = 0.09$ (top-row panels) and the disk CYL01 with $r = 0.1$ and $r_{eq} = 0.18$ (bottom-row panels): (a) Disk, $r = 0.05$, $Re_p = 0.24$; (b) Disk, $r = 0.05$, $Re_p = 0.8$; (c) Disk, $r = 0.11$, $Re_p = 0.05$; (d) Disk, $r = 0.11$, $Re_p = 1.32$. The particles considered in this figure are rendered in the vorticity-aligned position with their orientation vector **n** highlighted in cyan. The coloured dots represent the intersection of the axis given by the orientation vector **n** with the half sphere of radius a for the oblate. The corresponding Jeffery orbits are also displayed as solid black lines and were obtained using the experimentally measured equivalent aspect ratio r_{eq} by integrating equation (1.8) from an initial condition given by the first flow-aligned orientation of each experiment.

Figure 2.16. – Three experimental Jeffery orbits for the ellipsoid ELL06 with $r = 0.6$ (top-row panels) and the fibre CYL10 with $r = 9.0$ (bottom-row panels): (a) Ellipsoid, $r = 0.6$, $Re_p = 0.02$; (b) Ellipsoid, $r = 0.6$, $Re_p = 0.43$; (c) Fibre, $r = 9.0$, $Re_p = 0.08$; (d) Fibre, $r = 9.0$, $Re_p = 1.0$. The particles considered in this figure are rendered in the vorticity-aligned position with their orientation vector **n** highlighted in cyan. The coloured dots represent the intersection of the axis given by the orientation vector **n** with the half sphere of radius a for the oblate. The corresponding Jeffery orbits are also displayed as solid black lines and were obtained using the experimentally measured equivalent aspect ratio r_{eq} by integrating equation (1.8) from an initial condition given by the first flow-aligned orientation of each experiment

of the axis given by the orientation vector **n** with the half sphere of radius ℓ for the prolate particles and a for the oblate particles, respectively. The corresponding Jeffery orbits at zero inertia are also displayed as solid black lines. These were obtained upon integration of equation (1.8) using the first flow-aligned orientation of each experimental run as initial condition.

At low inertia, i.e., for the disk CYL01 at $Re_p = 0.05$ of panel (c) in figure 2.15 as well as the ellipsoid ELL06 at $Re_p = 0.02$ of panel (a) and the fibre F10 at $Re_p = 0.08$ of panel (c) of figure 2.16 , there is no significant change between the successive rotations for runs with different initial conditions, i.e. different orbit constants. The experimental orbits are in good agreement with the theoretical Jeffery orbits, represented by the solid black spherical ellipses.

As inertia becomes finite, i.e. for the disk CYL005 at $Re_p = 0.24$ in panel (a) and at $Re_p = 0.8$ in panel (b) and the disk CYL01 at $Re_p = 1.32$ of panel (d) in figure 2.15 as well as the ellipsoid ELL06 at $Re_p 0.43$ of panel (b) and the fibre CYL10 at $Re_p = 1$ of panel (d) in figure 2.16, the picture slightly changes. The experimental orbits are still spherical ellipses, but they depart from the zero-inertia orbits as their shapes evolve between successive rotations. For the fibre of panel (d) of figure 2.16, the orbits are expanding towards the tumbling orbit ($C = \infty$) on the equator of the sphere, i.e. in the (x, y) flow-gradient plane. It is worth mentioning that the orbits are not equally unstable as the fibre experiences a stronger drift when describing intermediate orbits (brown dots) than when close to the rolling (pink pentagons) and tumbling (green hexagons) cycles.

The oblate particles are also drifting through consecutive orbits, but their behaviour is more complex as two limiting stable orbits clearly exist. As shown in panels (a),(b) and (d) of figure 2.15 and panel (b) of figure 2.16, the disks and the ellipsoid can either maintain a tumbling orbit ($C = \infty$) in the plane of shear or drift to a spinning orbit ($C = 0$), i.e. aligning its orientation vector with the direction of vorticity, z.

Focusing on panel (a) of figure 2.15, it is interesting to note that for a slender disk with $r = 0.05$ at $Re_p = 0.24$ the two orbits closer to the pole of the half sphere (blue dots and red pentagons) are attracted toward the spinning orbit ($C = 0$) while the other orbit, which is starting with a much larger orbit constant (pink hexagons), is drawn toward the tumbling orbit ($C = \infty$) on the equator of the half sphere. This is also clearly visible for the oblate ellipsoid with $r = 0.6$ at $Re_p = 0.43$, where the initial conditions of the tumbling orbit (green dots) and the orbit drifting to the vorticity (orange pentagons) are even more close to each other.

2.4.2. Period of rotation

The dimensionless period of rotation, $T\dot{\gamma}/2\pi$, of the axisymmetric particles is displayed against particle aspect ratio, r, in figure 2.17. The main panel (a) shows all the results obtained for both prolate and oblate particles, while the two smaller panels distinguish between (b) prolate and (c) oblate shapes and focus on the asymptotic limits. The data are obtained by averaging over all the available experiments for all particle Reynolds number ($Re_p \lesssim 1$), meaning that we choose in these plots not to
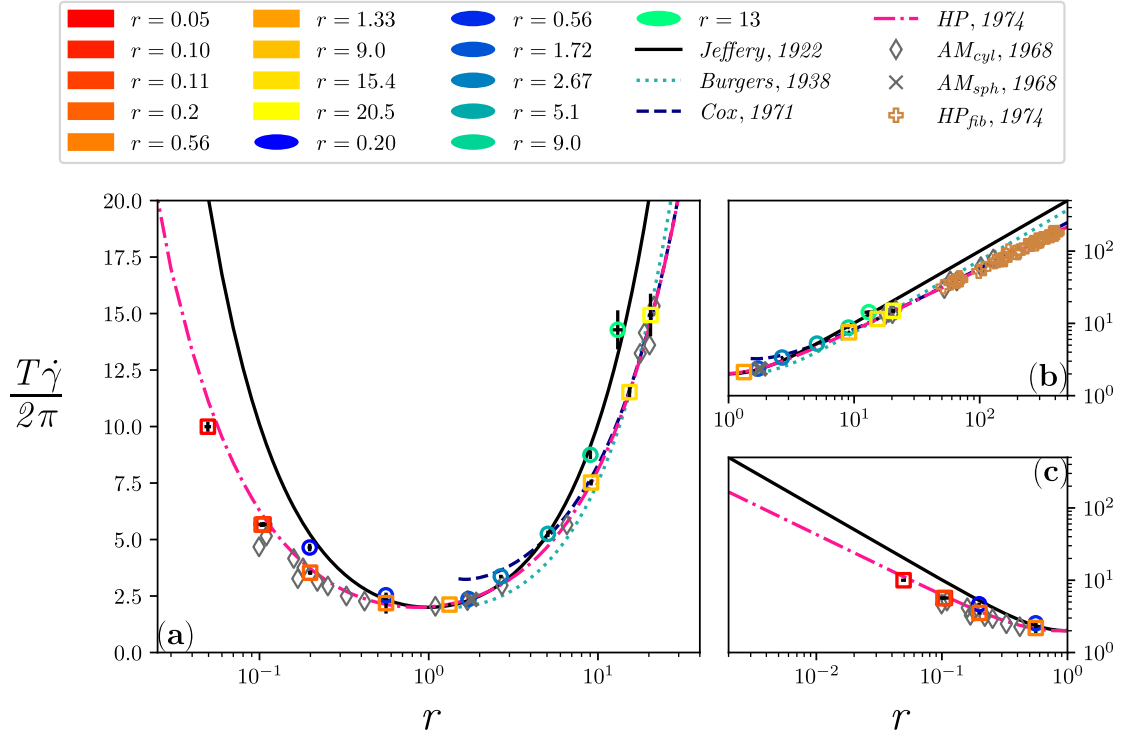
Figure 2.17. – Period of rotation, T, of the axisymmetrical particles against the particle aspect ratio r. The period is made dimensionless using the shear rate $\dot{\gamma}$ and normalized by a factor 2π. Panels: (a) both prolate and oblate, (b) prolate, and (c) oblate particles. The experimental values are displayed as coloured rectangles (cylindrical particles) and circles (ellipsoidal particles). Each point is the average over all the available experiments for all particle Reynolds numbers ($Re_p \lesssim 1$). The theories of Jeffery, 1922 and Burgers, 1938, the semi-empirical correlation of Cox, 1971, and the empirical expression of Harris and Pittman, 1975 are displayed as a solid black line, a dotted cyan line, a dashed blue line and a dash-dotted pink line, respectively. The experiments of Anczurowski and Mason, 1968b are displayed as empty grey diamonds (cylinders) and one solid x (ellipsoid), while the data of Harris and Pittman, 1975 correspond to empty brown plus symbols.

take into account any possible influence of inertia on the period of rotation. Such influence will be addressed later at the end of this section. These data are displayed as empty rectangles for cylindrical particles and circles for ellipsoidal particles and explore a moderate range of aspect ratios ($0.05 \lesssim r \lesssim 21$). They complement the previous experimental results of Anczurowski and Mason, 1968b for disks and fibres (empty grey diamonds) as well as one prolate ellipsoid (solid grey x), and those of Harris and Pittman, 1975 for fibres with higher aspect ratio (empty brown pluses), also reported in the figure. Note that the present measurements for the period of ellipsoidal

particles span over two decades of r around $r = 1$, extending the experimental dataset of Anczurowski and Mason, 1968b.

The agreement with the theory of Jeffery, 1922, $T\dot{\gamma}/2\pi = r + 1/r$, displayed as a solid black curve, is excellent for the ellipsoids. In contrast, the measured period of cylindrical particles systematically lies below Jeffery's curve, meaning that the period of a cylinder is always smaller than that of the corresponding ellipsoid at the same r. This difference is minimal around $r = 1$ and increases with increasing slenderness or flatness. These data are in good agreement with those available in the literature (Anczurowski and Mason, 1968b; Harris and Pittman, 1975).

Since the work of Trevelyan and Mason, 1951, it has been suggested that an equivalent aspect ratio, r_{eq}, can be found for cylindrical particles to recover the Jeffery period. In particular, r_{eq} can be computed from $T\dot{\gamma} = 2\pi(r_{eq} + 1/r_{eq})$ using the measured period of rotation for T, as described in Section 2.1.6.1 Different expressions have been proposed for r_{eq}. In an earlier work for the case of fibres, Burgers, 1938 showed that the disturbance caused by a cylinder of axis ratio r will be reproduced by an ellipsoid of $r_{eq} = 0.74 \, r$, an expression which would eventually diverge at high r as well as underestimate the period of rotation in the near-sphere limit. Our measurements for $10 \lesssim r \lesssim 20$ show good agreement with the proposed equivalence. Later on, by fitting his asymptotic theory to the measurements of Anczurowski and Mason, 1968b, Cox, 1971 provided an expression for slender cylinders as $r_{eq} = 1.24 \, r/\sqrt{\log r}$. Our data are in good agreement with this formula for $r > 5$. Then, Harris and Pittman, 1975 proposed an unweighted least square log-log fit over their measurements for slender rods leading to $r_{eq} = 1.14 \, r/r^{0.156}$. They found that Cox's semi-empirical prediction was an overestimate in the asymptotic limit and their power-law function of r showed an excellent agreement with all the considered experimental measurements available at that time. This empirical correlation provides an excellent match with our present data for both prolate and oblate cylinders. It is even accurately predicting the additional measurements with the thinnest disk (CYL005, red rectangles in figure 2.17).

Finally, we move to the influence of inertia on the period of rotation. Figure 2.18 shows the period of rotation, T, normalised by the Jeffery period, $2\pi(r_{eq} + 1/r_{eq})/\dot{\gamma}$, against the particle Reynolds number, Re_p. The data are now averaged over experimental runs at the same Re_p for each particle. While r_{eq} is equal to the aspect ratio r for the ellipsoidal particles, its value for the cylindrical particles is determined by solving $T\dot{\gamma} = 2\pi(r_{eq} + 1/r_{eq})$ using their measured period of rotation, T, at each Re_p. For both prolate and oblate particles, there is a good collapse of the data around unity, corresponding to the Jeffery period. The data are scattered within $\pm 20\%$ but do not indicate any systematic trend with increasing inertia. We can conclude that inertia does not affect significantly the period of rotation, T, for $Re_p \lesssim 1$.

2.4.3. Drift

Having previously looked at the general behaviours of the Jeffery orbits in figures 2.15 and 2.16, we now examine more in detail the influence of inertia on the time
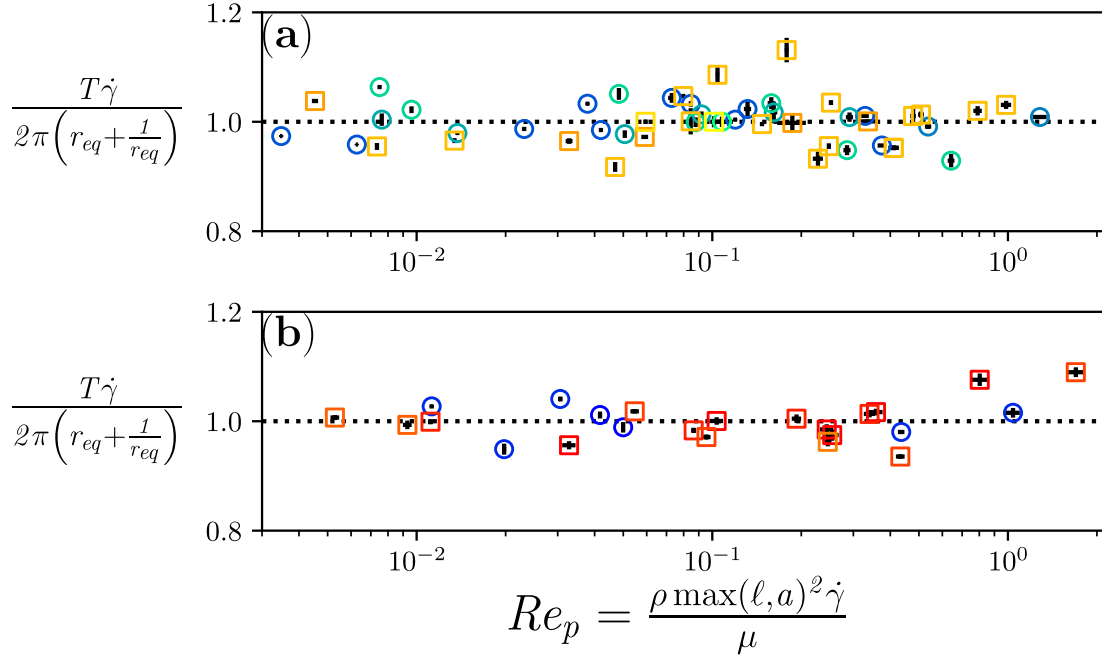
Figure 2.18. – Experimentally measured period of rotation, T, of axisymmetrical particles against the particle Reynolds number, Re_p: (a) Prolate particles and (b) oblate particles. The period is now normalised by the Jeffery period, $2\pi(r_{eq} + 1/r_{eq})/\dot{\gamma}$. The dotted black line corresponds thus to the Jeffery period within this normalisation. The experiments are displayed as coloured rectangles (cylindrical particles) and circles (ellipsoidal particles) with the same colour code as in figure 2.17.

evolution of each component of the orientation vector **n**. Figures 2.19 and 2.20 display the three components of **n** in the flow (n_1), gradient (n_2), and vorticity (n_3) directions against the dimensionless time, $t\dot{\gamma}$, respectively projecting the panels (a) and (d) of figure 2.15 and the panels (b) and (d) of figure 2.16. In this way, we focus the discussion on a subset of three runs for the most slender disk with $r = 0.05$ at moderate $Re_p = 0.24$ (CYL005 in panel (a) of figure 2.19), a less slender disk with $r = 0.1$ at much intense $Re_p = 1.32$ (CYL01 in panel (b) of figure 2.19), the oblate ellipsoid with $r = 0.6$ again at moderate $Re_p = 0.43$ (ELL06 in panel (a) of figure 2.20) and, at last, the fibre with $r = 9.0$ at $Re_p = 1.0$ (CYL10 in panel (b) of figure 2.20). We also compare our results with the asymptotic model of Einarsson, Candelier, et al., 2015a as detailed in Section,2.3. It is important to stress that, while the model considers an unbounded shear flow, there is some degree of confinement in the experiments ($\kappa \leq 0.19$) which may affect the stability of the orbits (Rosén, Einarsson, et al., 2015).

Let us first examine the influence of inertia on the dynamics of the disk with aspect ratio $r = 0.05$ in panel (a) of figure 2.19. The general tendency is that the disk either drifts away from the flow-vorticity (x, y) plane towards the vorticity-aligned spinning orbit (runs 1 and 2), either aligns itself in the tumbling orbit in the plane of shear (run 5).
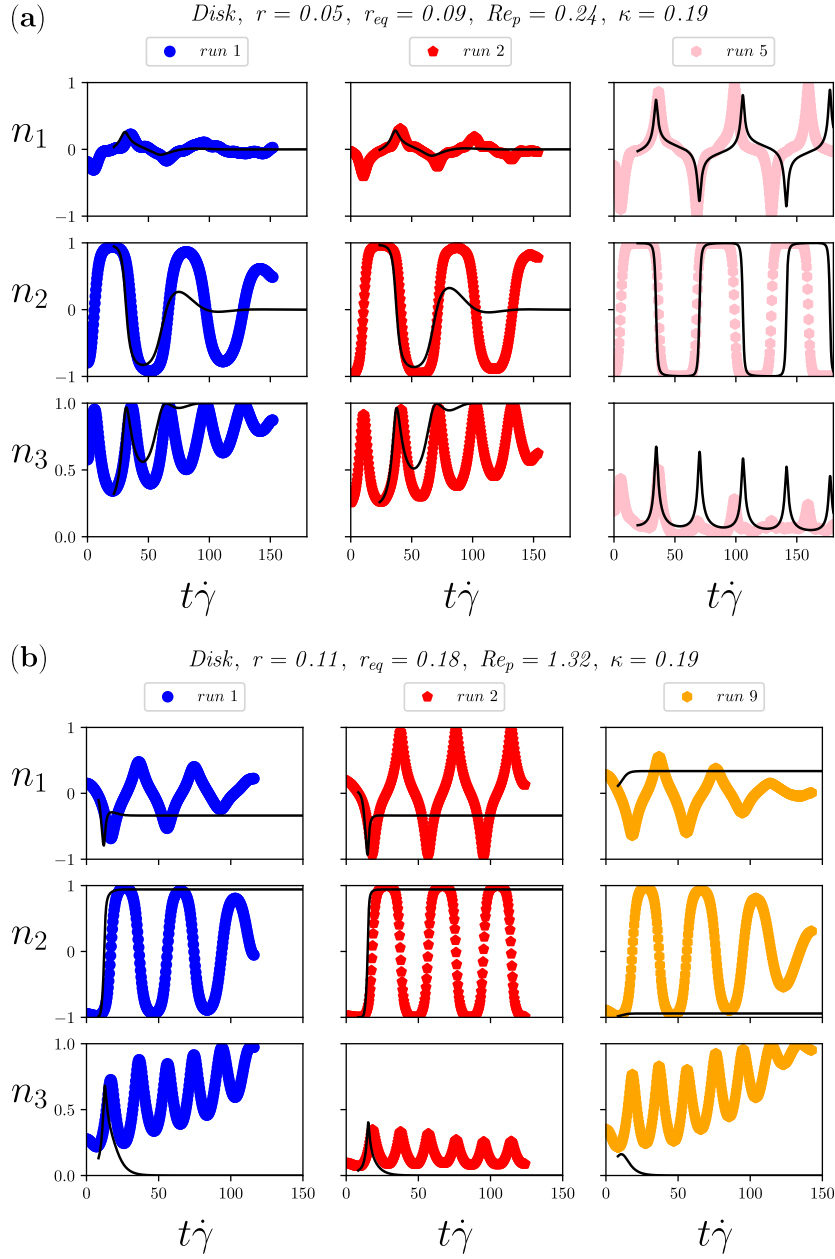
Figure 2.19. – Evolution of the components of the orientation vector **n**, displayed as vertically aligned panels for 3 typical runs against the dimensionless time $t\dot\gamma$. Panels: (a) disk CYL005 with aspect ratio $r = 0.05$ and confinement ratio $\kappa = 0.19$ at $Re_p = 0.24$; (a) disk CYL01 with aspect ratio $r = 0.11$ and confinement ratio $\kappa = 0.19$ at $Re_p = 1.32$. Comparison with the model of Einarsson, Candelier, et al., 2015a, presented in § 2.3 is also given as black dashed lines.

This is evinced by the systematic increase or decrease of n_3 with successive oscillations. The described dynamics are observed also for the disk with $r = 0.1$ in panel (b) of
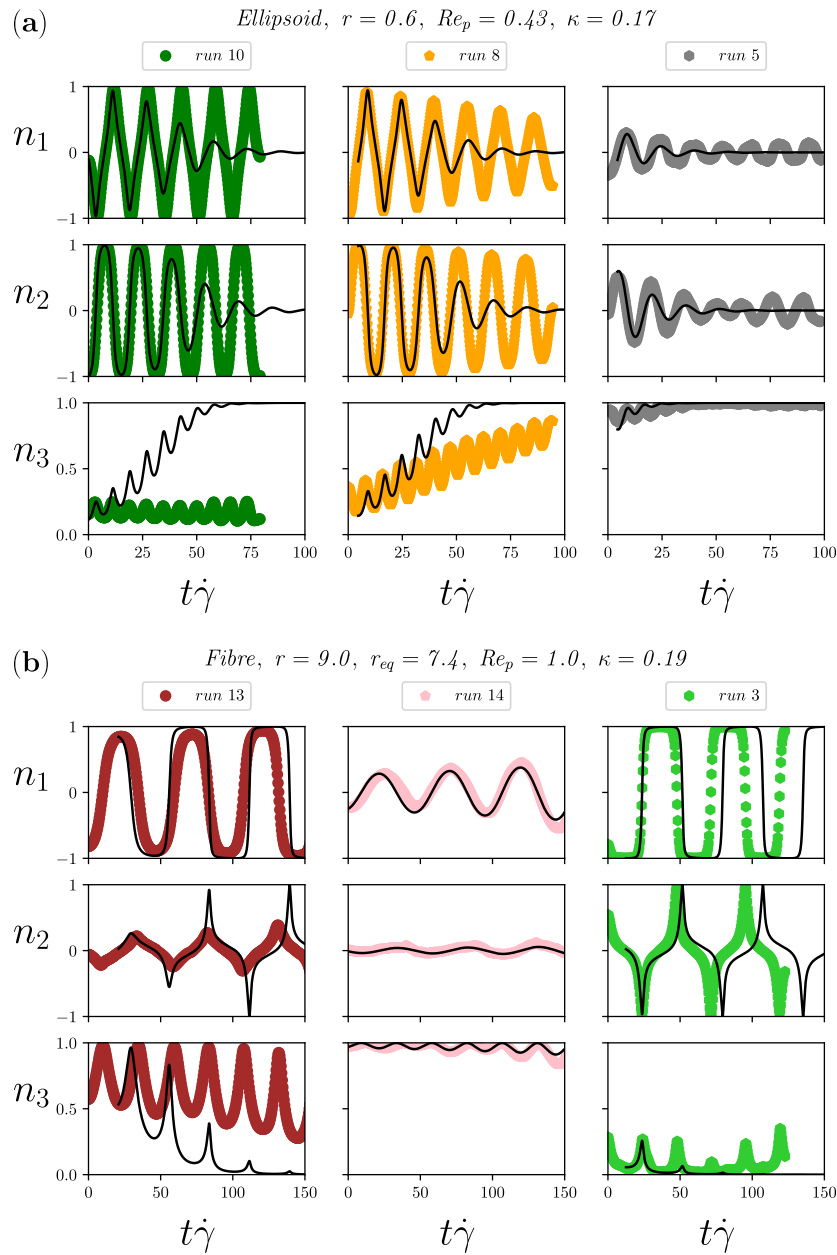
Figure 2.20. – Evolution of the components of the orientation vector **n**, displayed as vertically aligned panels for 3 typical runs against the dimensionless time $t\dot\gamma$. Panels: (a) Ellipsoid ELL06 with aspect ratio $r = 0.6$ and confinement ratio $\kappa = 0.17$ at $Re_p = 0.43$; (a) fibre CYL10 with aspect ratio $r = 0.9$ and confinement ratio $\kappa = 0.19$ at $Re_p = 1.0$. Comparison with the model of Einarsson, Candelier, et al., 2015a, presented in § 2.3 is also given as black dashed lines.

figure 2.19, where, again, the particle will either drift to the vorticity orbit (runs 1 and 9), or just tumble towards the tumbling orbit (run 2). A qualitative agreement between

the model of Einarsson, Candelier, et al., 2015a and the experiments is observed for the disk CYL005 at small $Re_p = 0.24$ in panel (a), despite the theory predicts a faster drift towards the spinning orbit. Instead, the disk CYL01 at much higher $Re_p = 1.32$ shows a clear discrepancy between the experiments and the model, which predicts a rapid degeneration of the Jeffery orbits to an inclined flow-aligned configuration.

The discussion is now repeated for the oblate ellipsoid with $r = 0.6$ in panel (a) of figure 2.20 at moderate $Re_p = 0.43$. Again, this oblate particle exhibits a dual dynamical behaviour, drifting to the vorticity-aligned, spinning orbit (runs 8 and 5), but also adopting a tumbling motion in the plane of shear (run10). The agreement with the model of Einarsson, Candelier, et al., 2015a is improved for this particle, as the drift intensities are more comparable than before. Anyway, the theory fails to predict the tumbling motion observed when this particle starts its rotation with its orientation vector oriented in the plane of shear.

Finally, we conclude the analysis by looking at the fibre with $r = 9.0$ in panel (b) of figure 2.20 at a considerable $Re_p = 1.0$. The influence of inertia forces the particle to drift out of the spinning orbit towards the tumbling one in the flow-gradient plane. Moreover, the drift intensity is stronger at intermediate orientations (run 13), while the prolate cylinder lazily leaves the vorticity-aligned cycles (run14). In general, there is a good agreement between the experiments and the model of Einarsson, Candelier, et al., 2015a and the experiments, despite the theory again overestimates the drift intensity for the intermediate orientations (run 13).

In conclusion, our results indicate that prolate particles will always be driven towards the sole limiting tumbling orbit, whereas oblate shapes can drift towards two different limiting cycles, the spinning or the tumbling orbits, depending upon their initial orientations. Whereas the model of Einarsson, Candelier, et al., 2015a successfully predicts the existence of two limiting orbits, it gives a much stronger overestimation of the drift through consecutive orbits in the oblate case than in the prolate case, especially for more slender shapes.

As previously mentioned in introduction of this manuscript, the separation between the two limiting orbits for the oblate particles should depend on their initial orientations but also on their aspect ratio (Einarsson, Candelier, et al., 2015a; Dabade et al., 2016). To examine this difference in drift more closely, we calculate the change in the orbit constant in a single Jeffery period as done in Dabade et al., 2016. As detailed in Section 2.1.6.2, this implies the fitting of our experimental measurements to estimate the local values of the orbit constant C before taking discrete differences ΔC over each period of rotation. The results are shown in figure 2.21, where the normalised change in the orbit constant in a single period, $Re_p^{-1}\Delta C/(C^2 + 1)$, is plotted against the normalised orbit constant $C/(C+1)$ for all the experiments. Measurements referring to different values of Re_p are identified by different colours. The values $C/(C + 1) = 0$ and $C/(C + 1) = 1$ correspond to the spinning and tumbling modes, respectively. Following Dabade et al., 2016, to keep the drift finite in the near-sphere limit, the normalisation for ΔC also uses a factor depending on the particle eccentricity: $\xi_0 = \sqrt{1/(1 - 1/r^2)}$ for the prolate particles and $\xi_0 = \sqrt{1/(1 - r^2)}$ for the oblate particles.

Figure 2.21 displays results for the following cases: the thinnest disk CYL005 with
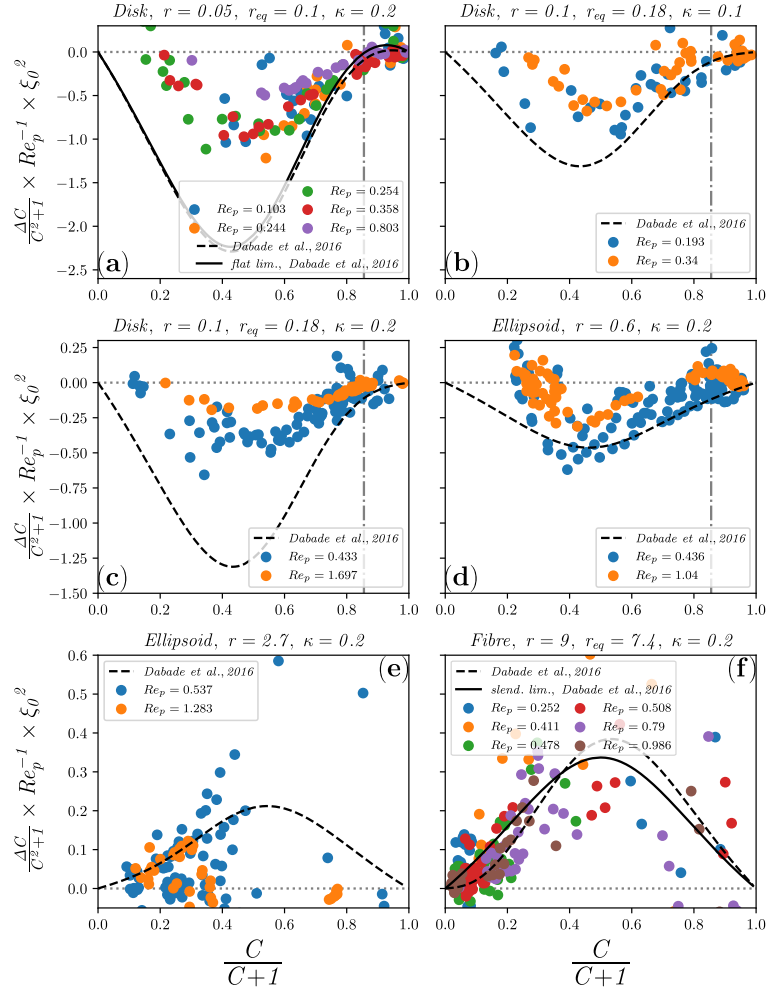
Figure 2.21. – Discrete variation of the orbit constant over one period, ΔC, against the orbit constant C at varying Re_p. Results refer to the following particle types (characterized by different colours): (a) disk CYL005 ($r = 0.05$ and $\kappa = 0.19$); (b) disk CYL009 ($r = 0.1$ and $\kappa = 0.11$); (c) disk CYL01, ($r = 0.11$ and $\kappa = 0.21$); (d) ellipsoid ELL06, $r = 0.56$ and $\kappa = 0.17$); (e) ellipsoid ELL3, ($r = 2.67$ and $\kappa = 0.19$); (f) fibre CYL10, ($r = 9.01$ and $\kappa = 0.19$). The drift is normalized to keep its value finite in the near-sphere limit as in Dabade et al., 2016, thus allowing for a better comparison with their model (black dashed line and black solid line in the slender limit). The critical orbit constant $C^* \gtrsim \sqrt{35}$ ($C/(C+1) \gtrsim 0.86$) separating the basins of attraction in the slender disk limit is also displayed as a dash-dotted grey line (Dabade et al., 2016). Data are collected over all the available experiments at a given Re_p (up to 10 runs), measuring the orbit constant and its variation as described in Section 2.1.6.2.

$r = 0.05$ in panel (a), two disks having similar r but two different confinement ratios in panels (b) (CYL009 with $r = 0.1, \kappa = 0.1$) and (c) CYL01 with ($r = 0.11, \kappa = 0.2$), a

thicker oblate ellipsoid EYLL06 with $r = 0.6$ in panel (d). Also included are the results for two prolate particles, a prolate ellipsoid with $r = 2.7$ in panel (e) and a slender fibre with $r = 9$ in panel (f). These data are compared to the theoretical prediction of Dabade et al., 2016 considering both particle and fluid inertia ($St = Re_p$ in the present neutrally-buoyant case) as detailed in Section 2.3.

Despite the rather large scatter of the data, there are some clear trends and qualitative agreements with theoretical predictions. Prolate particles experience positive increments of the orbit constant, which drive them towards tumbling motion ($C = \infty$, i.e. $C/(C + 1) = 1$), while oblate particles experience negative variations as they are mostly attracted to the vorticity-aligned orbit ($C = 0$, i.e. $C/(C + 1) = 0$). Moreover, as revealed from the scales of the ordinate axes, the drift intensity ΔC increases with the particle aspect ratio r, as more slender objects experience stronger variations of C. The oblate particles not only drift towards the spinning orbit but also to the tumbling orbit as evidenced by the clustering of points around zero and slightly above for orbit constants $C \gtrsim \sqrt{35}$, i.e. $C/(C + 1) \gtrsim 0.86$, as computed by Dabade et al., 2016, see panels (a) to (c). This is in stark contrast with the strong incline taken by the fibre of aspect ratio $r = 9$ in panel (f) when leaving the spinning orbit ($C/(C + 1) = 0$) which is unstable for this prolate particle.

An interesting behaviour is observed in panel (d) for the oblate spheroid with $r = 0.6$, which is an aspect ratio well above the predicted critical aspect ratio of approximately 0.14, for which only the drift towards the spinning motion is expected (Dabade et al., 2016). Anyway, this particle is still describing stable tumbling and spinning orbits, in contradiction with theoretical predictions. The critical orbit constant seems also to have moved as positive increments of orbit constant are observed at $C \lesssim \sqrt{35}$, i.e. $C/C + 1 \lesssim 0.86$, in particular for the higher Re_p. Similar behaviour is observed for the disk with $r_{eq} = 0.18$ in panels (b) and (c), which correspond to different confinements. This may suggest a wider region of attraction for the tumbling mode at aspect ratios above the critical one ($r^* \sim 0.14$). The influence of confinement is clearly visible between panels (b) and (c), where are shown two disks at a comparable $r \approx 0.1$ but differing confinement ratios, $\kappa = 0.11$ and $\kappa = 0.21$. The smaller disk is in better agreement with the theory than the large disk having a twofold increase of confinement ratio, where the drift is much less intense than that predicted by Dabade et al., 2016 for an unconfined viscous shear flow.

Finally, we address the scaling of the drift intensity with the particle Reynolds number. Clearly, experiments at higher particle Reynolds number ($Re_p \approx 1$) do not collapse with those at smaller Re_p. Despite the large scatters, this is particularly evidenced in panels (a),(c),(d) for oblate objects, where the intensity of the drift is weaken for the larger Re_p. This suggests a saturation effect above a certain inertial threshold.

2.5. Conclusions

We have examined the rotation of axisymmetrical particles suspended in a simple shear flow when inertia is progressively increased up to particle Reynolds number $Re_p \simeq 1$. A custom-built shearing cell and a multi-view reconstruction method have been used to obtain direct measurements of the orientation and period of rotation of ideal objects such as ellipsoids but also shapes of practical interest such as cylinders with varying aspect ratios. This system is rather flexible and is amenable to study the alignment of small objects of other shape in simple shearing flows.

The first important result is that the axisymmetric particles still rotate with the Jeffery period in this small-inertia regime. Our results also complement the data available in the literature (Anczurowski and Mason, 1968b; Harris and Pittman, 1975), showing that the period of rotation of a cylinder is smaller than that of an ellipsoid with the same aspect ratio. An equivalent aspect ratio can be inferred to recover the Jeffery period in the case of cylinders. Our results show that the empirical expression of Harris and Pittman, 1975 still remains the best prediction for this equivalent aspect ratio, which we were able to validate over one further decade of slender oblate particles compared to available literature results.

The second major finding is that we observe an irreversible drift across Jeffery orbits towards attracting limiting cycles. This drift is due to weak inertial effects, and its occurrence confirms, at least qualitatively, the asymptotic theories of Einarsson, Candelier, et al., 2015a and Dabade et al., 2016. Our measurements indicate that prolate particles are uniquely driven towards a tumbling motion in the flow-gradient plane regardless of their initial orientation and aspect ratio. For small but finite Re_p (up to $\mathcal{O}(10^{-1})$ in our experiments), there is a good quantitative agreement with the theories. For larger Re_p (up to $\mathcal{O}(1)$ in our experiments) a saturation of the phenomenon is observed and the asymptotic theories predict a faster drift toward the tumbling orbit, indicating that their limit of validity may have been trespassed. In stark contrast to prolate particles, which only possess a single attracting orbit, oblate particles are observed to drift towards two different orbits, the spinning orbit or the tumbling orbit, depending upon their initial orientation. Whereas the asymptotic models of Einarsson, Candelier, et al., 2015a and Dabade et al., 2016 do predict the existence of two limiting orbits, there is some notable discrepancy between predictions and experiments.

First, the theories provide an overestimation of the drift through consecutive orbits, which is even more severe when Re_p approaches unity. We remark here that part of the observed overestimation may be ascribed to unavoidable confinement effects, which tend to lower the drift intensity and thus introduce a small bias in the experimental measurements. Second, we do not observe the bifurcation toward a single stable spinning orbit above a critical aspect ratio of approximately 0.14 as predicted by the theories. The experiments seem to suggest a wider basin of attraction for the tumbling mode. The existence of two stable limiting cycles for oblate particles may not be attributed to confinement, as disks with values of κ down to 0.1 still exhibit both rotation modes despite their equivalent aspect ratio being larger than the critical

value.

Overall, our results indicate that fluid and particle inertia play a significant role in breaking the indeterminacy of the Jeffery orbits. This finding has major consequences for the steady-state rheology of suspensions of axisymmetrical particles in a viscous dilute regime, i.e. when particle-particle interactions are negligible. Indeed, prolate particles will eventually drift toward the tumbling orbit, aligning asymptotically with the mean flow direction. Conversely, the effective viscosity of a suspension of oblate particles will always depend on their initial orientation and regardless of their aspect ratio, i.e., not only in the lower near-sphere limit ($0.14 < r < 1$) as predicted by Dabade et al., 2016.

A final comment is in order about the importance of including the effect of both the fluid and particle inertia in the numerical calculation of the rotational dynamics of axisymmetric particles suspended in complex flows, e.g. turbulent flows. In a turbulent flow, the modified rotation rate (see equation 2.12) might affect the distribution of particle orientations (Sheikh et al., 2020). In homogeneous isotropic turbulence, axisymmetric prolate (*resp.* oblate) particles were seen to align with (*resp.* perpendicular to) the local vorticity vector, following the local flow stretching in a mostly spinning (*resp.* tumbling) rotational state (Ni et al., 2015; Byron et al., 2015). Accounting for the inertial torques would strengthen the influence of the local stretching, even if one might argue under which conditions the inertial contribution becomes relevant given the intermittent nature of the flow.

The picture is even more complex in bounded turbulence, where the strong near-wall shear causes axisymmetric particles to follow the local flow stretching but aligns the vorticity vector in the spanwise direction (L. Zhao and Andersson, 2016). In this case, inertial torques could especially modify the orientation statistics of oblate particles, which tend to align normal to the wall, with possible consequences for drag reduction (Z. Wang et al., 2021).

3. Numerical simulations of fibre-laden turbulent channel flows

In this chapter we present a numerical investigation carried out to study the dynamics of long and flexible fibres suspended in a turbulent channel flow. After having detailed the physical problem, the governing equations are introduced. Then, the numerical methodology for the Direct Numerical Simulation of a fibre-laden turbulent channel flow is presented, as well as its implementation for the execution on accelerated and distributed computing architectures. Then, we validate the novel software against typical literature results, discussing the importance of the particle-induced flow acceleration in recovering the correct shape equivalence for fibres suspended in a viscous shear flow. Finally, results are presented, focusing on the orientation, rotation and deformation of flexible fibres in a turbulent channel flow at shear Reynolds number $Re_\tau = 300$, while evaluating the influence of the particle length, particle inertia and particle bending stiffness. At last, we discuss the turbulence modulation by the fibres and its consequences for drag reduction.

3.1. Physical problem

In the previous chapter we briefly discussed the lattice Boltzmann method as a tool for exploring the influence of inertia on the Jeffery orbits of ellipsoidal particles (Rosén, Lundell, et al., 2014). This method is appropriate when a single ellipsoid in a viscous flow is considered, but, as we have seen in the introduction of this manuscript, typical suspensions a axisymmetrical particles include millions of them and are flowing in the turbulent regime. The description of such a physical problem is clearly more complex and difficult, because one should solve the Navier-Stokes equations imposing a no-slip boundary condition at the surface of each particle, which is impossible.

As a matter of fact, the system could be greatly simplified if we assumed that the ellipsoids are shorter than the smallest relevant flow scale, i.e. the Kolmogorov's length-scale. Then, particles could be accurately modelled as zero-volume point-wise objects, feeling only the Stokes drag force (Happel and Brenner, 1983) and the Jeffery
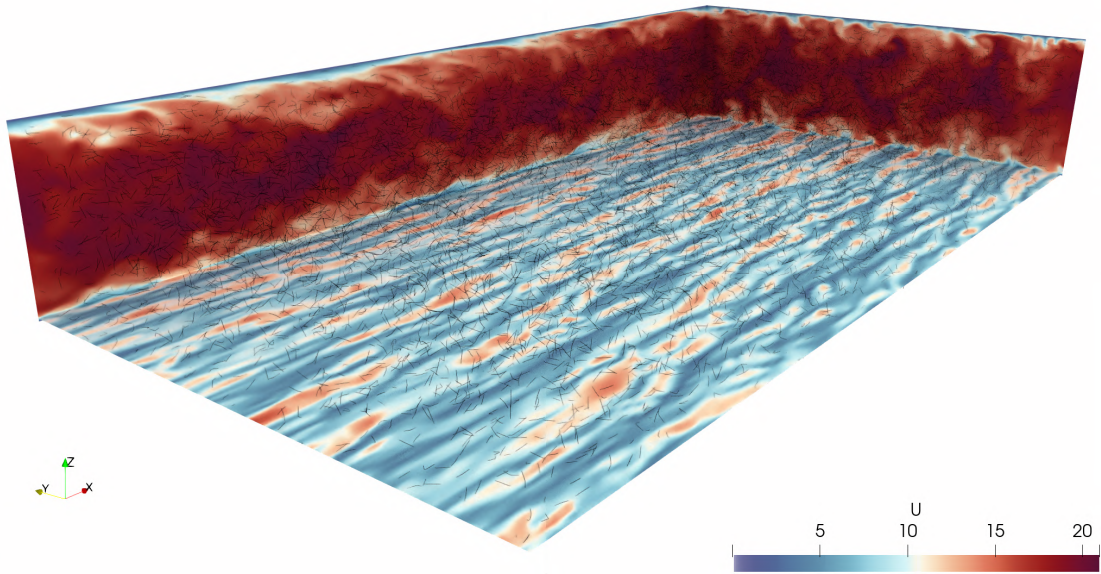
Figure 3.1. – Visualization of a turbulent channel flow at shear Reynolds number $Re_\tau = 300$, laden with 125.000 stiff ($E_Y^+ = 10^4$) tracer-like fibres of total length $L_\Xi^+ = 35.81$ and aspect ratio $r = 100$. The panels display the stream-wise component of the velocity. The bottom panel is cut at $z^+ = 10$ from the wall. The upper wall is transparent for visualisation porpuses.

torque (Jeffery, 1922). In addition, in the limit of dilute suspensions, we would gladly neglect the hydrodynamic disturbance that the particles determine on the flow and on each other. These are the principles of the **Lagrangian Particle Tracking** (LPT), which, despite the drastic approximations, has lead to great insight into the dynamics of short axisymmetrical particles in turbulence (Marchioli, Fantoni, et al., 2010; L. Zhao, Challabotla, et al., 2015; L. Zhao, Challabotla, et al., 2019).

Solution to extend prolate particles across the flow scales was found in the work of Yamamoto and Matsuoka, 1993, who were the first to use several sub-Kolmogorov's spheres to form longer chains, where two consecutive elements would be entangled by a *no-slip* condition at their contact point. This method rapidly evolved as Lindström and Uesaka, 2007 replaced the spherical constitutive elements with ellipsoids, reducing the computational cost and improving the stability of the model. Then, Andrić et al., 2013 presented the final formulation of what is known as the **Rod-Chain** model, where a bending resistance was taken into account to keep to constrained rods aligned within the turbulent flow. A remarkable variation on theme is that proposed in the work Delmotte et al., 2015, who built their fibres as chains of spheres held together by a *free slip* constraint.

A more sophisticated approach is that illustrated in the work of Picano et al., 2015, who performed Direct Numerical Simulations with a direct-forcing Immerse Boundary Method to account for the presence of spheres and, in a following study, rigid oblate particles (Ardekani et al., 2017). Despite the more intense computational cost,

which limits the number of dispersed particles, this method is especially accurate for particles of non-negligible size. Moreover, as the particles' boundary conditions are naturally restored, it is a natural framework for the observation of turbulence modulation by finite particles. Nevertheless, the approach naturally tends to particles in the near-sphere limit and without sharp edges, making the simulation of cylindrical shapes very challenging.

On the other hand, Lindström and Uesaka, 2007 had already shown the importance of taking into account the particle-induced acceleration of the surrounding flow to recover the correct shape equivalence when simulating a fibre suspended in a viscous shear flow. In the case of point-wise particle simulations, this is done by a two-way coupling scheme, among which we find the Particle-In-Cell method (Squires and Eaton, 1990) or the more advanced Exact Regularised Point Particle method (Gualtieri et al., 2015). Interestingly, turbulence modulation and drag reduction are recovered even for point-wise axisymmetrical particle simulations in the two-way coupling regime, as long as sufficiently high volume fractions are considered (Z. Wang et al., 2021).

During the preparation of this manuscript, we have studied the of long, slender and flexible fibres suspended in wall turbulence. The canonical configuration of the turbulent channel flow is chosen (J. Kim et al., 1987), and the Rod-Chain model is deployed (Andrić et al., 2013) together with the Exact Regularized Point Particle two-way coupling method (Gualtieri et al., 2015).

3.2. Governing Equations

3.2.1. The flow

The carrier phase is an incompressible Newtonian fluid, driven by an imposed pressure gradient between two smooth, parallel walls of a plane channel. This Poiseuille flow conserves mass and momentum, therefore it is described by the coupled system of continuity and Navier-Stokes equations, here reported in dimensional vector form:

$$\nabla \cdot \mathbf{u} = 0 \tag{3.1a}$$

$$\rho \left[\frac{\partial \mathbf{u}}{\partial t} + (\mathbf{u} \cdot \nabla)\mathbf{u} \right] = -\nabla P + \mu \nabla^2 \mathbf{u} + \mathbf{F}_{2w}, \tag{3.1b}$$

where $\mathbf{u} = (u, v, w)$ is the velocity vector corresponding to the position $\mathbf{x} = (x, y, z)$ referred to the absolute system of reference, $-\nabla P$ is the equivalent pressure gradient that drives the flow and the fluid is identified by its two properties: the density ρ and the viscosity μ. Finally, the last term $\mathbf{F}_{2w}$ represents two-way coupling momentum term that the carried phase determines on the flow, which will be presented in detail later on.

As displayed in figure 3.2, this flat channel geometry is periodic in the stream-wise x and span-wise y directions, while it is bounded by the two walls in the wall-normal z one, at a distance of $2h$ from each other. Usually, a factor of π is introduced for the

span-wise extension of the channel, and another factor of 2 will scale the stream-wise length so that the total volume of the channel is $L_x \times L_y \times L_z = 4\pi h \times 2\pi h \times 2h$. The nondimensionalization procedure starts by identifying the Newtonian fluid, which is supposed to be iso-thermal and is, therefore, determined by two properties: the density ρ and the viscosity μ. The reference velocity for this kind of flow is the friction velocity $u_\tau = \sqrt{\tau_w/\rho}$, where τ_w is the shear stress exerted by the flow at the wall. We can identify the characteristic length-scale of the flow as such given by the channel half-height h. It follows that the reference time-scale is given by $\frac{h}{u_\tau}$. Therefore, coordinates, velocities and time can be made dimensionless to give the traditionally named outer units:

$$\mathbf{x}^- = \frac{\mathbf{x}}{h}, \quad \mathbf{u}^- = \frac{\mathbf{u}}{u_\tau}, \quad t^- = \frac{u_\tau}{h}t. \tag{3.2}$$
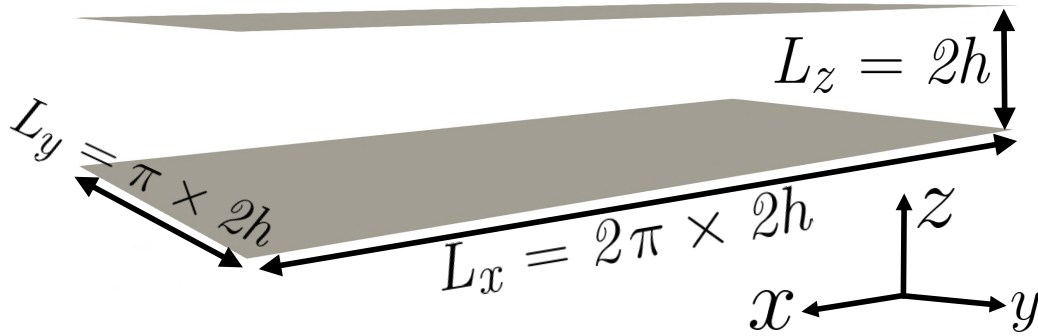
Figure 3.2. – Sketch of the turbulent channel flow. Solid walls are rendered are grey surfaces. The absolute system of reference is also represented. Note that the origin is usually set in the bottom left corner of the system.

At this point, we introduce the shear Reynolds number, which is given by the ratio between inertial and viscous forces and will be the fundamental phenomenological parameter that determines the simulated flow:

$$Re_\tau = \frac{\rho u_\tau h}{\mu}. \tag{3.3}$$

To complete, we will also present the outer form of the pressure and the two-way coupling force:

$$P^- = \frac{P}{\rho u_\tau^2}, \quad \mathbf{F}_{2w}^- = \mathbf{F}_{2w}\frac{h}{\rho u_\tau}. \tag{3.4}$$
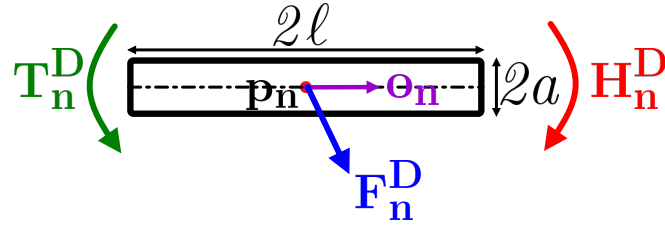
Figure 3.3. – Representation of a point-wise rod element with the drag force (blue), the hydrodynamic torque due to the relative spin (green) and that due to the fluid velocity gradients (red). The rods' length is 2ℓ while its diameter is $2a$. The position of its centre of mass is given by the vector $\mathbf{p}_n$, while its orientation by the vector $\mathbf{o}_n$, whose Euclidean norm must be one at all times.

Then, the two governing equations 3.1 become:

$$\nabla \cdot \mathbf{u}^- = 0 \tag{3.5a}$$

$$\frac{\partial \mathbf{u}^-}{\partial t^-} + (\mathbf{u}^- \cdot \nabla)\mathbf{u}^- = -\nabla P^- + \frac{1}{Re_\tau}\nabla^2 \mathbf{u}^- + \mathbf{F}_{2w}^-, \tag{3.5b}$$

where the $-$ apex indicates the dimensionless quantities in outer units.

3.2.2. The fibres

The fundamental concept of the rod-chain model is to treat the $n - th$ rod element of any fibre as a point-wise object in order to calculate its translation and rotational dynamics, as displayed in figure 3.3. Its position will be indicated as $\mathbf{p}_n$ while its orientation will be given by a unity norm vector $\mathbf{o}_n$. Then, its linear and angular velocities will be reported as $\mathbf{v}_n$ and $\boldsymbol{\omega}_n$. The mass of this cylindrical object is $m_n = \rho_n 2\pi r a^3$, where ρ_n is its density, a its radius and $r = \ell/a$ its aspect ratio, defined as the ratio between the rod half length ℓ and cross-sectional radius a. Dynamic and kinematic equations for linear and angular motion are given by the following system:

$$m_n \frac{d\mathbf{v}_n}{dt} = \mathbf{F}_n^D + \mathbf{X}_{n+1} - \mathbf{X}_n, \tag{3.6a}$$

$$\frac{d\bar{\mathbf{J}}\boldsymbol{\omega}_n}{dt} = \mathbf{T}_n^D + \mathbf{H}_n^D + \ell\mathbf{o}_n \times (\mathbf{X}_{n+1} + \mathbf{X}_n) + (\mathbf{Y}_{n+1,b} - \mathbf{Y}_{n,b}), \tag{3.6b}$$

$$\frac{d\mathbf{p}_n}{dt} = \mathbf{v}_n, \tag{3.6c}$$

$$\frac{d\mathbf{o}_n}{dt} = \boldsymbol{\omega}_n \times \mathbf{o}_n, \tag{3.6d}$$

where $\mathbf{F}_n^D$ is the hydrodynamic drag force exerted by the fluid on the element, $\bar{\mathbf{J}} = \frac{m_n a^2}{12}[(4r^2 + 3)(\bar{\mathbf{I}} - \mathbf{o}_n\mathbf{o}_n^T) + 6\mathbf{o}_n\mathbf{o}_n^T]$ is the inertia tensor of the element in the absolute
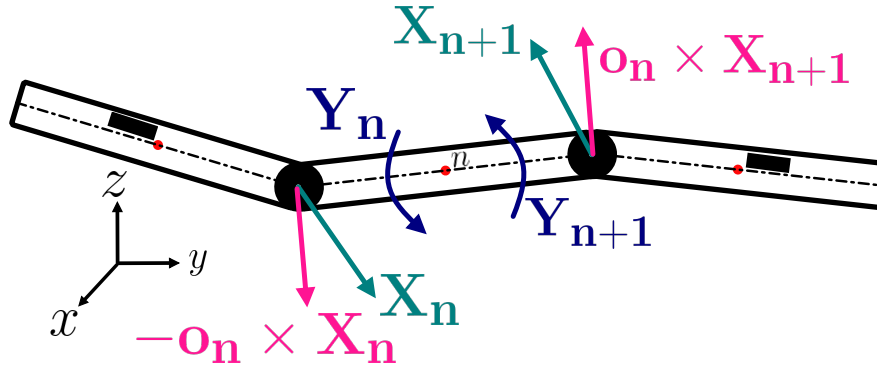
Figure 3.4. – Representation of three constrained point-wise rod elements with the constraint forces (purple), constraint torques (pink) and bending torques (blue).

frame of reference, with $\bar{\mathbf{I}}$ the identity matrix. Instead, the term $\mathbf{T}_n^D$ is the hydrodynamic torque due to the relative spin between fluid and rod element and $\mathbf{H}_n^D$ is the hydrodynamic torque due to the fluid velocity gradients' action of the rod.

Finally, the extra terms $\mathbf{X}$ and $\mathbf{Y}$ represent the constraint forces and moments that consecutive rods of one chain exert on each other, as displayed in figure 3.4. They arise by the enforcement of a no-slip constraint between consecutive point-wise cylinders, which is given by the following equation:

$$\mathbf{p}_n + \ell_n \mathbf{o}_n - (\mathbf{p}_{n+1} - \ell_{n+1}\mathbf{o}_{n+1}) = 0. \tag{3.7}$$

In the meantime, the bending resistance torque appearing in equation 3.6b is modelled following Lindström and Uesaka, 2007:

$$\mathbf{Y}_r^b = -k_b \alpha_r^b \mathbf{e}_r^b, \tag{3.8}$$

where $k_b = E_Y(J + J)/(4\ell_r) = \pi E_y a^3/(8r)$ is a constant parameter, determined by the Young modulus E_Y of the rod element. The torque is calculated as the product between the solid angle α_r^b between two consecutive elements and their relative curvature:

$$\mathbf{Y}_r^b = -\frac{\pi E_Y a^3}{8r}\cos^{-1}(\mathbf{o}_r \cdot \mathbf{o}_{n-1})\frac{\mathbf{o}_r \times \mathbf{o}_{n-1}}{|\mathbf{o}_r \times \mathbf{o}_{n-1}|}. \tag{3.9}$$

Therefore, the constraint forces $\mathbf{X}$ alone would be sufficient to keep the chains of rods together, while the role of the moments $\mathbf{Y}$ is just to maintain the rod elements aligned in a minimal energy configuration.

The equations for the carried phase are made dimensionless in terms of wall units, indicated as $^+$ units. The purpose is now to scale the particles according to the relevant turbulence scales at the wall, and not as done before, in the centre of the channel. Here, the reference length scale is determined by the viscosity: $\mu/(\rho u_\tau)$. In this way, the radius of one rod becomes $a^+ = \frac{a\rho u_\tau}{\mu}$. Then, the reference time-scale is given

by $\mu/(u_\tau^2 \rho)$, so that $t^+ = \frac{t u_\tau^2 \rho}{\mu}$; finally, the reference velocity is u_τ, so that $\mathbf{u}_r^+ = \mathbf{u_r}/u_\tau$. Therefore, angular velocities will be made dimensionless as $\omega_r^+ = \frac{\omega \mu}{\rho u_\tau^2}$, constraint forces as $\mathbf{X}_r^+ = \frac{\mathbf{X}_r \rho}{\mu^2}$ and the Young Modulus will become $E_Y^+ = \frac{E_Y}{u_\tau^2 \rho}$.

3.2.2.1. Two-way coupling

The point-wise modelling of the dispersed rods neglects the boundary condition that actual fibres would impose on the flow. This is clearly necessary as we will simulate up to 25 million elements (Prosperetti, 2015). Anyway, we can recover the particle's back reaction of the fluid as the Newtonian reaction to the experienced drag force $\mathbf{F}_n^D$. Intuitively, each particle will then contribute within a finite volume of the flow, so that the sum of all reaction forces determines a normalized force $\mathbf{F}_{2w}$ that appears in the Navier-Stokes equation 3.1. This method is known as the Particle In Cell method, and it was proposed in the work of Squires and Eaton, 1990 and has been largely deployed since, due to its simplicity. Anyway, it requires a large number of particles within every small portion of flow volume over which the two-way coupling force is normalized in order not to diverge, and in the past, this would make the accurate calculation of particle stresses on turbulent flows unfeasible (Gillissen et al., 2007).

Therefore, for this work at not particularly large particle concentrations another method of more recent derivation is deployed: that is the Exact Regularized Point Particle method, presented for the first time by Gualtieri et al., 2015 and then generalized to wall-bounded turbulent flows by Battista et al., 2019, whose details we know briefly describe.

The method provides a rigorous derivation based on the unsteady Stokes flow around a small, spherical, rigid particle, whose interaction with the flow is physically regularized by viscous diffusion, that slowly propagates the generated vorticity field from the particle's boundary to the computational grid. This means that the method introduces a delayed time-scale ϵ_R, below which the particle's disturbance has yet to interact with the flow and can be neglected without incurring in large errors. The resolution of such time-scale imposes a length-scale σ_R that the computational grid needs to discretise, as displayed in figure 3.5:

$$\sigma_R = \sqrt{2\nu\epsilon_R} \tag{3.10}$$

where ν indicates the fluid viscosity. In the end, each particle delayed hydrodynamic force will be the one calculated at a slightly previous time-step $t-\epsilon_R$, when the particle was at the position $\mathbf{x}_p(t-\epsilon_R)$, regularized by means of a Gaussian $g[\mathbf{x}-\mathbf{x}_p(t-\epsilon_R),\epsilon_R]$ whose variance is indeed σ_R. The summation of the contribution of all particles gives:

$$\mathbf{F}_{2w} = \sum_n^{N_p} \mathbf{F}_n^D(t-\epsilon_R) \cdot g[\mathbf{x}-\mathbf{p}_n(t-\epsilon_R),\epsilon_R], \tag{3.11}$$

where N_p is the total number of simulated rods and the Gaussian corresponds to the
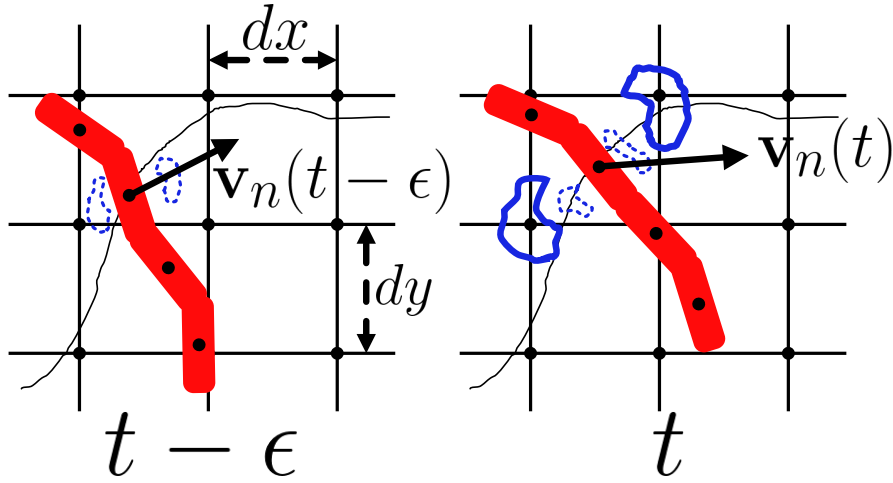
Figure 3.5. – Representation of the two-way coupling according to the ERPP method. Panels: $(t-\epsilon)$ the disturbance generated by the n-th element moving with velocity $\mathbf{v}_n(t)$ at the time-step $t-\epsilon$ has yet to diffuse to the computational grid, whose spacing is indicated by dx and dy. (t) the n-th element has now moved along its trajectory while the previously generated disturbance has diffused enough to reach the computational grid with delay ϵ. Image freely inspired from Gualtieri et al., 2015.

following expression:

$$g[\mathbf{x}-\mathbf{p}_n(t-\epsilon_R),\epsilon_R] = \frac{1}{[4\pi\nu\epsilon_R]^{3/2}} \cdot exp(-\frac{||\mathbf{x}-\mathbf{p}_n(t-\epsilon_R)||^2}{4\nu\epsilon_R}), \qquad (3.12)$$

The dimensionless forms for the regularization time-scale and length-scale given by equation 3.10 are:

$$\epsilon_R = \frac{\epsilon_R^- \cdot h}{u_\tau} = \frac{\epsilon_R^+ \cdot \nu}{u_\tau^2} \,, \qquad (3.13a)$$

$$\sigma_R = \sigma_R^- \cdot h = \frac{\sigma_R^+ \cdot \nu}{u_\tau} \,. \qquad (3.13b)$$

The two-way coupling term given by equation 3.11 has units $\frac{N}{m^3}$. Indeed the Gaussian form is the inverse of a volume, which gives:

$$g = \frac{g^-}{h^3} = \frac{g^+}{(\frac{\nu}{u_\tau})^3} \,. \qquad (3.14)$$

For the drag force, instead, we have:

$$\mathbf{F}^D = \mathbf{F}^{D-} \cdot \rho u_\tau^2 h^2 = \frac{\mathbf{F}^{D+} \cdot \mu^2}{\rho} \,. \qquad (3.15)$$

In the end, the two-way coupling term will be calculated in plus units, as the rest of the particle solver, to be converted to minus units before being added to the convective terms of the Navier-Stokes equation as follows, in simplified notation:

$$\mathbf{F}_{2w} = \sum_{n}^{N_p} \mathbf{F}_n^{D-} \cdot g^- = \sum_{n}^{N_p} \mathbf{F}_n^{D+} \cdot g^+ \cdot Re_\tau . \tag{3.16}$$

3.3. Numerical methodology

3.3.1. The flow

The flow is resolved in down to the smallest scale (Direct Numerical Simulation) on an Eulerian grid. The numerical method follows a classical pseudo-spectral algorithm, where all the calculations are performed in modal space, except for the convective terms $(\mathbf{u} \cdot \nabla)\mathbf{u}$, which are resolved in physical space and then re-transformed back (Canuto et al., 2007).

Some treatment is necessary to obtain the dimensionless equations 3.5: splitting the pressure gradient between mean $\frac{d\bar{P}}{dx^-}$ and fluctuating $\frac{\partial p}{\partial x^-}$ one allows us to collect the source terms $\mathbf{S}$ as following, where we will start to drop the $-$ apex for the sake of brevity:

$$\frac{\partial \mathbf{u}}{\partial t} = \mathbf{S} + \frac{1}{Re_\tau}\nabla^2\mathbf{u} - \frac{\partial \mathbf{p}}{\partial \mathbf{x}}. \tag{3.17}$$

Note that the two-way coupling force (equation 3.11) is collected inside the source term too. The velocity-vorticity formulation is adopted to solve the flow field. The curl of the Navier-Stokes equation produces a second-order equation for the wall-normal component of the vorticity:

$$\nabla \times \frac{\partial \mathbf{u}}{\partial t} = \nabla \times \mathbf{S} + \frac{1}{Re_\tau}\nabla \times \nabla^2\mathbf{u} - \nabla \times \nabla p, \tag{3.18}$$

where the last term is identically zero. From the definition of vorticity $\omega = \nabla x\mathbf{u}$, it follows that

$$\frac{\partial \omega}{\partial t} = \nabla \times \mathbf{S} + \frac{1}{Re_\tau}\nabla^2\omega, \tag{3.19}$$

which is nothing but the equation describing the transport of vorticity.

Taking again the curl operator on our last result, 3.19 produces the following Helmholtz fourth-order equation:

$$\frac{\partial(\nabla^2\mathbf{u}}{\partial t} = \nabla^2\mathbf{S} - \nabla(\nabla \cdot \mathbf{S}) + \frac{1}{Re_\tau} \cdot \nabla^4\mathbf{u}. \tag{3.20}$$

Finally, the equations 3.19 and 3.20 are projected in the wall-normal direction, to solve for ω_z and w, in order to use the definitions of continuity and vorticity to calculate the

two other velocity components u, v, so that the final system of equations to be solved corresponds to:

$$\nabla \cdot \mathbf{u} = 0, \tag{3.21a}$$

$$\omega \cdot \mathbf{n}_z = (\nabla \times \mathbf{u}) \cdot \mathbf{n}_z, \tag{3.21b}$$

$$\frac{\partial(\nabla^2 \mathbf{u})}{\partial t} \cdot \mathbf{n}_z = [\nabla^2 \mathbf{S} - \nabla(\nabla \cdot \mathbf{S}) + \frac{1}{Re_\tau} \nabla^4 \mathbf{u}] \cdot \mathbf{n}_z, \tag{3.21c}$$

$$\frac{\partial \omega}{\partial t} \cdot \mathbf{n}_z = (\nabla \times \mathbf{S} + \frac{1}{Re_\tau} \nabla^2 \omega) \cdot \mathbf{n}_z. \tag{3.21d}$$

This method comes from the already classical algorithm developed by J. Kim et al., 1987.

3.3.2. Pseudo-spectral discretization

The dimensionless system of equations is discretized on an Eulerian grid in space following a pseudo-spectral approach. Fourier discretization is applied in the streamwise and spanwise directions x and y, implicitly imposing periodic boundary conditions for those coordinates as they are assumed to be statistically homogeneous. Chebyshev polynomials are adopted for the wall-normal direction instead. The main advantage is that Chebyshev-Gauss-Lobatto points lead to a much finer discretization close to the walls as visualised in figure 3.6. Indeed, this is the critical region of the turbulent channel flow, where the scales are smaller and require a much finer resolution J. Kim et al., 1987. The main advantage of adopting such a pseudo-spectral method is the high accuracy of spatial derivatives when calculated in modal space: indeed, truncating infinite Fourier and Chebyshev series produces extremely small errors.

The computational grid that will resolve all the Eulerian flow variables corresponds to the following coordinates in the three physical dimensions:

$$x_i = (i-1)\frac{L_x}{N_x - 1} i = 1, ..., N_x, \tag{3.22a}$$

$$y_j = (j-1)\frac{L_y}{N_y - 1} j = 1, ..., N_y, \tag{3.22b}$$

$$z_k = cos(\frac{k-1}{N_z - 1}\pi) k = 1, ..., N_z, \tag{3.22c}$$

where L_x, L_y are the domain lengths in the stream-wise and span-wise directions, whereas the channel always extends from -1 to +1 in z, and N_x, N_y, N_z represent the number of total points for the grid in each dimension.

A generic velocity signal u in physical space will be represented in modal space as the result of consecutive Fourier and Chebyshev transforms:

$$u(x, y, z, t) = \sum_{i=0}^{N_x/2} \sum_{j=-N_y/2+1}^{N_y/2} \sum_{k=0}^{N_z-1} \hat{u}\left(k_{x,i}, k_{y,j}, k, t\right) T_k(z) e^{\iota(k_{x,i} x + k_{y,j} y)} \tag{3.23}$$
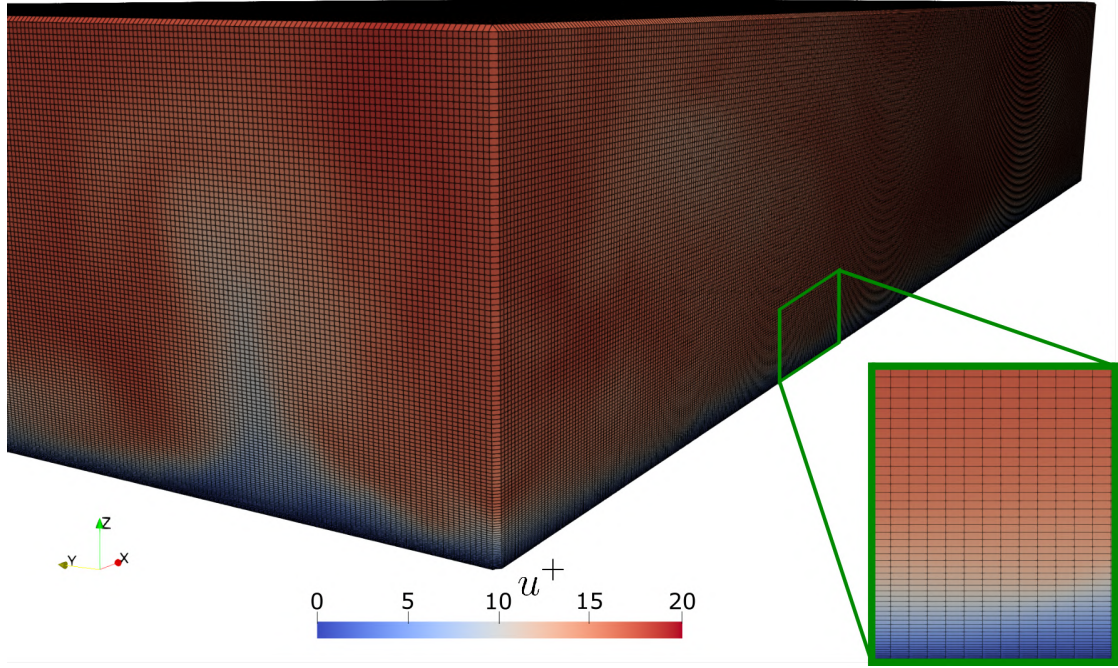
Figure 3.6. – Visualization of the Eulerian grid over half of the channel height at shear Reynolds number $Re_\tau = 150$. The grid is made of $n_x = 1024 \times n_y = 512 \times n_z = 257$ grid-points, which are located at the intersection between black lines. The grid spacing in the stream-wise x and span-wise y coordinates is uniform, and is simply determined by the chosen number of points ($dx^+ = L_x^+/n_x = dy^+ = L_y^+/n_y$), being $L_x^+ = 4\pi Re_\tau = 2 \times L_y^+$. Chebyshev polynomials, calculated according to equation 3.22c, allow to obtain a much finer grid discretization close to the wall, as we can appreciate from the small insert.

where the Fourier coefficient $\hat{u}\left(k_{x,i}, k_{y,j}, k, t\right)$ is depending on the Fourier wave-numbers $k_{x,i}$ and $k_{y,j}$ and on the $k-th$ Chebyshev polynomial $T_k(z)e^{\iota\left(k_{x,i}x + k_{y,j}y\right)}$.

The x and y Fourier wave-numbers are then given by:

$$k_{x,i} = \frac{2\pi(i-1)}{L_x} \quad i = 1,\ldots,N_x/2+1 \tag{3.24a}$$

$$k_{y,j} = \begin{cases} \frac{2\pi(j-1)\pi}{L_y} & j = 1,\ldots,N_y/2+1 \\ -\frac{2\pi(N_y-j+1)}{L_y} & j = N_y/2+2,\ldots,N_y \end{cases}. \tag{3.24b}$$

It follows that derivatives in these two homogeneous directions can be immediatly

computed:

$$\frac{\partial f(x, y, z, t)}{\partial x} = \sum_{i=0}^{N_x/2} \sum_{j=-N_y/2+1}^{N_y/2} \sum_{k=0}^{N_z-1} \iota k_{x,i} \hat{f} T_k e^{\iota(k_{x,i}x + k_{y,j}y)}. \tag{3.25}$$

Instead, Chebyshev polynomials, and their derivatives, are obtained recursively:

$$
\begin{aligned}
T_0(z) &= 1 & \frac{\partial T_0(z)}{\partial z} &= 0 \\
T_1(z) &= z & \frac{\partial T_1(z)}{\partial z} &= 1 \\
&\vdots & &\vdots \\
T_n(z) &= 2z T_{n-1}(z) - T_{n-2}(z) & \frac{\partial T_n(z)}{\partial z} &= \frac{\partial T_{n-2}(z)}{\partial z} + 2n T_{n-1}.
\end{aligned}
\tag{3.26}
$$

The time-advancement is performed by an Implicit-Explicit scheme: the source term **S** is integrated explicitly by an Adam-Bashforth scheme (explicit Euler for the first time-step of any simulation), while the other terms are calculated according to the implicit Cranck-Nicolson, second order scheme. At the generic advancement in time, the discretized system of equations becomes:

$$\nabla \cdot \mathbf{u}^{n+1} = 0, \tag{3.27a}$$

$$\boldsymbol{\omega}^{n+1} \cdot \mathbf{n}_z = \left(\nabla \times \mathbf{u}^{n+1} \right) \cdot \mathbf{n}_z, \tag{3.27b}$$

$$
\frac{\nabla^2 \mathbf{u}^{n+1} - \nabla^2 \mathbf{u}^n}{\Delta t} \cdot \mathbf{n}_z = \left[\frac{3 \left[\nabla^2 \mathbf{S}^n - \nabla(\nabla \cdot \mathbf{S}^n) \right] - \left[\nabla^2 \mathbf{S}^{n-1} - \nabla \left(\nabla \cdot \mathbf{S}^{n-1} \right) \right]}{2} + \right.
$$
$$
\left. + \frac{1}{Re_\tau} \frac{\nabla^4 \mathbf{u}^{n+1} + \nabla^4 \mathbf{u}^n}{2} \right] \cdot \mathbf{n}_z, \tag{3.27c}
$$

$$
\frac{\boldsymbol{\omega}^{n+1} - \boldsymbol{\omega}^n}{\Delta t} \cdot \mathbf{n}_z = \left(\frac{3 \nabla \times \mathbf{S}^n - \nabla \times \mathbf{S}^{n-1}}{2} + \frac{1}{Re_\tau} \frac{\nabla^2 \boldsymbol{\omega}^{n+1} + \nabla^2 \boldsymbol{\omega}^n}{2} \right) \cdot \mathbf{n}_z. \tag{3.27d}
$$

Without going into further detail, this system is solved in modal space for the generic wave-numbers, given in equation 3.23, by means of the Chebyshev-Tau method. The method is applied to the fourth and second order equations for the velocity and the vorticity, given in equations 3.27. This reduces the problem to the solution of two Helmholtz-like equations, having split the fourth order velocity equation into two second order ones by means of an auxiliary variable. Eventually, this reduces to the application of the Gauss-Jordan elimination algorithm and a forward substitution method that allow the calculation of the vorticity vector and the wall-normal velocity. Finally, the stream-wise and span-wise velocity components are recovered through the continuity equation.

3.3.3. Boundary conditions

The Fourier discretization of the homogeneous directions imposes periodic boundary conditions for the x and y coordinates. The presence of the solid walls along the

wall-normal coordinate z requires a no-slip boundary conditions for this direction:

$$\mathbf{u}(x, y, z = \pm 1) = [u_w, v_w, 0] \ \text{and} \ \frac{\partial \omega}{\partial z}|_{z=\pm 1} = 0 \, . \tag{3.28}$$

By continuity, this implies a zero wall-normal component of the vorticity at the solid boundaries ($\omega_z(x, y, z = \pm 1) = 0$).

3.3.4. The fibres

The final system of equations that is going to be solved for each rod-element of a fibre is the following:

$$\mathbf{v}_n^{t+1} = \mathbf{K}_n^t + \bar{\mathbf{Q}}_n^t \left(\mathbf{X}_{n+1}^t - \mathbf{X}_n^t\right), \tag{3.29a}$$

$$\boldsymbol{\omega}_n^{t+1} = \mathbf{R}_n^t + \bar{\bar{\mathbf{S}}}_n^t \tilde{\mathbf{O}}_n^t \left(\mathbf{X}_{n+1}^t + \mathbf{X}_n^t\right), \tag{3.29b}$$

$$\mathbf{v}_n^{t+1} - \mathbf{v}_{n+1}^{t+1} + \lambda a \left(\boldsymbol{\omega}_n^{t+1} \times \mathbf{o}_n^t + \boldsymbol{\omega}_{n+1}^{t+1} \times \mathbf{o}_{n+1}^t\right) = \mathbf{0}, \tag{3.29c}$$

$$\mathbf{p}_n^{t+1} = \mathbf{p}_n^t + \Delta t \mathbf{v}_n^{t+1}, \tag{3.29d}$$

$$\mathbf{o}_n^{t+1} = \mathbf{o}_n^t + -\Delta t \mathbf{o}_r^t \times \omega_r^{t+1}, \tag{3.29e}$$

where:

$$\bar{\mathbf{O}}_n^t = \begin{bmatrix} 0 & -o_{z;r}^t & o_{y;r}^t \\ o_{z;r}^t & 0 & -o_{x;r}^t \\ -o_{y;r}^t & o_{x;r}^t & 0 \end{bmatrix} \implies \mathbf{o}_n^t \times \mathbf{a} = \tilde{\mathbf{O}}_n^t \mathbf{a} \quad \forall \mathbf{a}$$

$$\mathbf{K}_n^t = \left(\bar{\bar{\boldsymbol{\delta}}} + \frac{\Delta t}{m_p} \bar{\bar{\mathbf{A}}}_n^t\right)^{-1} \left(\mathbf{v}_n^t + \frac{\Delta t}{m_p} \bar{\bar{\mathbf{A}}}_n^t \mathbf{u}_n^t\right)$$

$$\bar{\bar{\mathbf{Q}}}_n^t = \left(\bar{\bar{\boldsymbol{\delta}}} + \frac{\Delta t}{m_p} \bar{\bar{\mathbf{A}}}_n^t\right)^{-1}$$

$$\mathbf{R}_n^t = \left[\bar{\mathbf{J}}_n^t + \Delta t \left(\dot{\bar{\mathbf{J}}}_n^t + \bar{\bar{\mathbf{C}}}_n^t\right)\right]^{-1} \left[\bar{\bar{\mathbf{J}}}_n^t \boldsymbol{\omega}_n^t + \Delta t \left(\bar{\bar{\mathbf{C}}}_n^t \Omega_n^t + \mathbf{H}_n^t + \mathbf{Y}_{n+1}^{b,n} - \mathbf{Y}_n^b\right)\right]$$

$$\bar{\bar{\mathbf{S}}}_n^t = \lambda a \left[\bar{\bar{\mathbf{J}}}_n^t + \Delta t \left(\dot{\bar{\mathbf{J}}}_n^t + \bar{\bar{\mathbf{C}}}_n^t\right)\right]^{-1} .$$

In all of these equations, the equivalence of shape between fibres and ellipsoidal particles is accounted for according to the semi-empirical correlation of Cox, 1971. As we have already seen in the experimental part of this manuscript, a fibre corresponds to a shorter ellipsoid if the diameter is the same. Here, instead, we invert Cox's formula to calculate the equivalent radius of our rod elements according to the following equation:

$$a = a_{ell} \cdot 1.24 / \sqrt{ln(r)}. \tag{3.31}$$

In this way, Cox's equivalence is enforced at imposed aspect ratio.

The expressions for the hydrodynamic drag force, hydrodynamic torque follow the

formulation of S. Kim and Karrila, 2013:

$$\mathbf{F}_n^D = \bar{\bar{\mathbf{A}}}_n(\mathbf{u}_n - \mathbf{v}_n) = 6\pi r a\mu[Y_n^A\bar{\bar{\delta}} + (X_n^A - Y_n^A)\mathbf{o}_n\mathbf{o}_n^T](\mathbf{u}_n - \mathbf{v}_n); \tag{3.32a}$$

$$\mathbf{T}_n^D = \bar{\bar{\mathbf{C}}}_n(\Omega_n - \omega_n) = 8\pi r^3 a^3 \mu[Y_n^C\bar{\bar{\delta}} + (X_n^C - Y_n^C)\mathbf{o}_n\mathbf{o}_n^T](\Omega_n - \omega_n); \tag{3.32b}$$

$$\mathbf{H}_n^D = -8\pi r^3 a^3 \mu Y_n^H(\bar{\bar{\epsilon}}\mathbf{o}_n) : (\bar{\bar{\gamma}}_n\mathbf{o}_n), \tag{3.32c}$$

where $\bar{\bar{\mathbf{A}}}$ is the resistance drag force tensor, $\bar{\bar{\mathbf{C}}}$ is the resistance drag torque tensor and $\bar{\bar{\mathbf{H}}}_n^D$ is the resistance drag torque tensor. In equation 3.32c:

$$(\bar{\bar{\epsilon}}\mathbf{o}_n) : (\bar{\bar{\gamma}}_n\mathbf{o}_n) = \epsilon_{ijk}(\dot{\gamma}_{jl;n}o_{j;n})o_{j;n}, \tag{3.33}$$

where the gradient tensor is:

$$\bar{\bar{\gamma}}_n = \frac{1}{2}(\frac{\partial u_i}{\partial x_j} + \frac{\partial u_j}{\partial x_i}), \tag{3.34}$$

and $\bar{\bar{\epsilon}}$ is the Levi-Civita third rank tensor.

Following the principles of the Lagrangian Particle Tracking, the flow velocity $\mathbf{u}_n$, the flow velocity gradient $d\mathbf{u}_n/dx_i$ and the flow vorticity Ω_n at the nth particle's position are calculated by fourth-order polynomial interpolation over the Eulerian grid representing the flow.

Finally, the coefficients $X_n^A, Y_n^A, X_n^C, Y_n^C$ and Y_n^H are defined in function of the parameter $e_{c,n} = \sqrt{(r^2 a^2 - a_{el}^2)/(r^2 a^2)}$ and correspond to the following expressions:

$$X_n^A = \frac{8e_{c,n}^3}{-6e_{c,n} + 3(1 + e_{c,n}^2)\log\frac{1+e_{c,n}}{1-e_{c,n}}} \tag{3.35a}$$

$$Y_n^A = \frac{16e_{c,n}^3}{6e_{c,n} + 3(e_{c,n}^3 - 1)\log\frac{1+e_{c,n}}{1-e_{c,n}}} \tag{3.35b}$$

$$X_n^C = \frac{4e_{c,n}^3(1 - e_{c,n}^2)}{6e_{c,n} - 3(1 - e_{c,n}^2)\log\frac{1+e_{c,n}}{1-e_{c,n}}} \tag{3.35c}$$

$$Y_n^A = \frac{4e_{c,n}^3(2 - e_{c,n}^2)}{-6e_{c,n} - 3(1 + e_{c,n}^2)\log\frac{1+e_{c,n}}{1-e_{c,n}}} \tag{3.35d}$$

$$Y_n^H = \frac{4e_{c,n}^5}{-6e_{c,n} + 3(1 + e_{c,n}^2)\log\frac{1+e_{c,n}}{1-e_{c,n}}} \tag{3.35e}$$

As previously mentioned, the equations for the carried phase are made dimensionless in terms of wall units. The final system of equations 3.29a:3.29e will now becom:

$$\mathbf{v}_n^{+,n+1} = \mathbf{K}_n^{+,n} + \bar{\bar{\mathbf{Q}}}_n^{+,n}\left(\mathbf{X}_{n+1}^{+,n} - \mathbf{X}_n^{+,n}\right) \tag{3.36a}$$

$$\boldsymbol{\omega}_n^{+,n+1} = \mathbf{R}_n^{+,n} + \bar{\bar{\mathbf{S}}}_n^{+,n}\tilde{\mathbf{O}}_n^t\left(\mathbf{X}_{n+1}^{+,n} + \mathbf{X}_n^{+,n}\right) \tag{3.36b}$$

$$\mathbf{o}_n^{t+1} = \mathbf{o}_n^t + \frac{1}{6}\left[\mathbf{k}_{rk1;n}^t + 2\left(\mathbf{k}_{rk2;n}^t + \mathbf{k}_{rk3;n}^t\right) + \mathbf{k}_{rk4;n}^t\right] \tag{3.36c}$$

$$\bar{\mathbf{M}}_{n+1}^t\mathbf{X}_{n+2}^{+,n} + \left(\bar{\mathbf{N}}_{n+1}^t + \bar{\mathbf{N}}_n^t\right)\mathbf{X}_{n+1}^{+,n} + \bar{\mathbf{M}}_n^t\mathbf{X}_n^{+,n} = \mathbf{K}_n^{tot,n} \tag{3.36d}$$

$$\mathbf{p}_n^{+,n+1} = \mathbf{p}_n^{+,n} + \Delta t^+\mathbf{v}_n^{+,n+1}, \tag{3.36e}$$

The constraint system is solved as a tridiagonal block-matrix one. Details about this method can be found in Dotto, Soldati, et al., 2020 and are not repeated for the sake of brevity. Equations 3.7 and the system 3.6 combine together to determine a tridiagonal block-matrix system. Its resolution requires the following steps, in order:

— an interpolation of the flow velocities and velocity gradients at the rod's position to determine the force and torques exerted by the fluid on the point-wise object, calculated by 4-th order polynomials;
— the resolution of the tridiagonal block-matrix system to determine the constraint forces $\mathbf{X}$ on each rod element of all the chains;
— time integration of the rod's kinematic equations according to a second order Adam-Bashford scheme to determine its linear position and orientation;
— verification of the quality of the time integration with special regards towards the accumulation of numerical error between constrained rod elements and correction.

The last step of the list is particularly important and comes from the discussion of Lindström and Uesaka, 2007 and Delmotte et al., 2015, and it is performed by fixing the position of the central rod element of the chain and translating around it the other rods, in order to reproduce the exact fiber length and avoid the accumulation of numerical errors. Each chain of rods must then meet a 1% maximum constraint error, which distinguishes between valid and failed solutions. This is why a sub-stepping procedure is introduced, in order to improve the stability of the model, particularly critical when simulating large values of Young's modulus E_Y or short rod elements.

Beyond stability issues, the time integration of the fibres is dominated by their shape and their density ratio with regard to the fluid. These two physical quantities are combined to determine the particle's response time, given here for a single rod (Dotto, Soldati, et al., 2020):

$$\tau_{p,n} = \frac{2a^2\rho_p r}{9\nu} \cdot \frac{\log\left(r + \sqrt{r^2 - 1}\right)}{\sqrt{r^2 - 1}}, \tag{3.37}$$

which will be the control parameter that determines the inertial nature of the simulated particles. Particles characterized by a low response time will behave as tracers in the flow, whereas for high values of this parameter rods will express a more ballistic behaviour. Note that no gravity is taken into account for these simulations so that the inertial behaviour of the particles will be purely hydrodynamic. Finally, while particles

interact with each other in a purely hydrodynamic way, particle-wall impacts are modelled as purely elastic collisions with a restitution coefficient equal to one. Therefore, when a fibre meets a solid boundary, it will be solidly bounced back according to the position of the rod element that is closest to the wall.

3.4. Implementation

3.4.1. A novel parallelization scheme for the solution of non-local Lagrangian tridiagonal block-matrix systems on an Eulerian grid.

As we have seen, the ERPP method naturally requires high-resolution grids, which must discretize a quasi-viscous length- scale in order to precisely capture the disturbance of the particles on the flow. For this reason, an implementation in a modern programming language is vital as well as making our solver suitable for High-Performance Computing. That is why the surf_gpu application is written in Fortran 90 while its core, the DNS+ERPP solver, is ported to CUDA C to run on Nvidia GPUs. Fourier and Chebyshev are performed relying on the cuFFT library for the solution, while the rest of the kernels are written in-house.

The main advantage of this operation is an exceptional performance of the solver, which can leverage modern Graphic Processing Units for accelerated simulations, as reported in figure 3.7 where the elapsed time per time-step of for the unladen flow calculations is displayed. The main disadvantage is determined by the difficulty of the software development and the lack of portability of CUDA C, which is compatible with the Nvidia GPUs only. Solutions to this issue would be represented by more generic compiler directives such as OpenACC and OpenMP.

Nevertheless, during the preparation of this manuscript we embraced the challenge and ported to CUDA C all the subroutines of the DNS+ERPP solver, as well as part of the LPT, the most challenging kernels being the non-homogeneous derivatives, the Gauss-Jordan elimination method and the fourth-order polynomial interpolation. As an example, the Gauss-Jordan CUDA C implementation is reported in Appendix B.

Instead, the rest of the LPT is kept in Fortran 90, given the complexity of the embedded communication phases, but multi-threading is enabled through OpenMP directives.

Essentially, the parallelization strategy is determined to ease the computational load of the DNS+ERPP solver and is based on a 1D domain decomposition to divide the workload among all the MPI tasks, each associated with one GPU. Asynchronous collective MPI AllToAll calls are deployed. The described parallelization scheme is maintained when rod elements are interfacing with the fluid by communicating flow halos for the interpolation of flow variables at the particle's positions and particle halos for the two-way coupling. In doing so, rods will be travelling through the distributed memory of the GPUs according to their physical position within the flow.

Instead, given the unpredictability of the memory accesses along each chain of

rods, we find it convenient to create a second copy of each rod, statically placed at the same distributed memory unit of all the elements of a given chain. These static addresses are chosen by balancing the load among all involved CPUs. Doing so, all the information is locally available for the resolution of the constraint equations that keep the chains of rods together, if two communication phases are considered, before and after these calculations, to update the sampled flow information and distribute the positions of the newly integrated rods. These communication steps are efficiently performed by Asynchronous MPI Send/Recv calls, having previously buffered the data, and are activated on-demand, so that the minimum number of messages is sent, as two MPI tasks will exchange data only if they share a chain of rods. Finally, I/O operations are performed using the MPI I/O subroutines from the MPI library, especially convenient when dealing with large files such as our flow and particle fields.

This computational approach is determined by the unique constraints of the studied problem and therefore required the development of an original proprietary code. The result is a scalable application, suitable for execution on large distributed computational architectures. Moreover, to the best of our knowledge, this is the first time that a similar algorithm is proposed for fibre-laden turbulent flows. The application has been tested and optimized on different Tier-0 GPU-accelerated clusters (e.g., Marconi100, Juwels-Booster, Piz Daint).

A measure of the quality of the proposed parallelization scheme is given by its scalability. By scalability, we indicate the ability of a system to handle an increasing quantity of computations by spawning them on a wider amount of resources. A strong scaling test is performed when the problem size is fixed and the number of computational resources systematically increased. This will return information about the parallelization overhead, intended as the time spent to synchronize distributed computing units, and its ratio with the time spent for calculations. Amdahl's law states that the theoretical speedup S_{th} of any application is limited by the fraction p of the execution time that can be parallelized divided by the number of computational resources s plus the fraction of the execution time $1 - p$ that cannot be executed in parallel (Gustafson, 1988):

$$S_{th} = \frac{1}{(1 - p) + \frac{p}{s}} \ .$$
(3.38)

Despite the non-ideal behaviour, the strong scaling test, reported in panel (a) of figure 3.7, shows the scalability and feasibility of our approach for the parallel resolution of such a demanding and constrained computational set-up. It is clearly that the communication phases are more and more important in determining the elapsed time per time-step as the number of GPUs is increased. By comparing the unladen solver performance (blue diamonds) and the fibre-laden one, we also appreciate the drawback determined by the extra computational load and the parallelisation scheme produced by the carried phase.

On the other hand, a weak scaling test is performed when both the problem size and the number of computational resources are increased to keep a constant workload per processor. An application showing good weak scaling will prefer communications
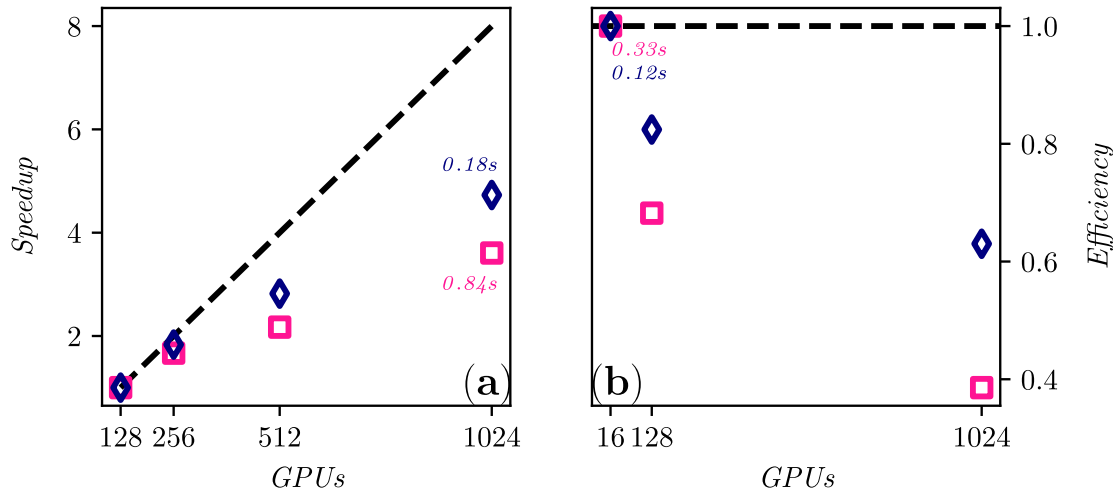
Figure 3.7. – Scalability tests of the flow solver (blue diamonds) and the fibre-laden flow solver (pink squares) on the Tier-0 PRACE system Marconi 100. Ideal behaviours are displayed as black dashed lines. Panels: (a) strong scaling test against the number of dedicated GPUs. Data were collected for a turbulent channel flow at shear Reynolds $Re_\tau = 600$ discretized on $2048 \times 1024 \times 1025$ grid points and laden with 20 million rods elements. (b) weak scaling test against the number of dedicated GPUs. Data were collected starting from a turbulent channel flow at shear Reynolds $Re_\tau = 150$ discretized on $512 \times 256 \times 257$ grid points and laden with 312500 rod elements. Both Eulerian and Lagrangian computational loads were then multiplied by a factor of 8 at each increment of computational resources. Elapsed times per time-step are also reported.

with the nearest neighbouring computational units in the topology of the system. This allows to solve smaller and larger computational problems in the same time, adjusting the number of computational resources accordingly. The weak scaling test, displayed in panel (b) of figure 3.7 highlights again the impact of including the fibres in our calculations, as the efficiency (pink squares) drops to 0.4 for the largest simulation. Note that already a pseudo-spectral algorithm is highly non-local, therefore even the unladen simulations (blue diamonds) show a drop of efficiency down to ∼ 0.6.

These two tests allow us to conclude that the surf_gpu application, already in the unladen case (blue diamonds) but especially for the laden simulations (pink squares), is strongly limited by the bandwidth of the communication network, crucial for the synchronization of the non-local memory addresses that represent the flow slabs as well as each rod element of the long and slender fibres. Nevertheless, this original solution is the only feasible approach to unprecedented simulations of fibre-laden turbulent flows.

3.5. Dimensional analysis

The suspension of fibres in a turbulent channel flow is characterized by nine quantities:

— the dynamic viscosity of the fluid $\mu \left[kg\ m^{-1}\ s^{-1} \right]$;
— the density of the fluid $\rho \left[kg\ m^{-3} \right]$;
— the size of the turbulent channel flow $h \left[m \right]$.
— the shear velocity of the flow $u_\tau \left[m\ s^{-1} \right]$;
— the density of the fibres $\rho_p \left[kg\ m^{-3} \right]$;
— the length of the fibres $2\ell \left[m \right]$;
— the diameter of the fibres $2a \left[m \right]$;
— the Young's modulus of the fibres $2a \left[kg\ m^{-1}\ s^{-2} \right]$;
— the number of dispersed fibres $N_p \left[- \right]$.

In the previous sections on this chapter we have already introduced the two dimensionless categories that are typically deployed in wall turbulence: the outer units and the wall units. Outer units, denoted using the superscript -, are obtained making physical units dimensionless with the typical scales of the flow, i.e., the channel half-height h and the shear velocity u_τ:

$$\mathbf{x}^- = \frac{\mathbf{x}}{h}, \quad \mathbf{u}^- = \frac{\mathbf{u}}{u_\tau}, \quad t^- = \frac{u_\tau}{h} t \ .$$

Wall units, denoted using the superscript+, rely on typical turbulence quantities to make physical quantities dimensionless, i.e., the shear velocity u_τ and the kinematic viscosity ν:

$$\mathbf{x}^+ = \frac{\mathbf{x} u_\tau}{\nu}, \quad \mathbf{u}^+ = \frac{\mathbf{u}}{u_\tau}, \quad t^+ = \frac{t u_\tau^2}{\nu} \ . \tag{3.39}$$

Typically, particle-related quantities are made dimensionless with regards to the wall units.

Following the Π theorem (Buckingham, 1914), we find $9 - 3 = 6$ dimensionless numbers that describe the physical system:

○ the shear Reynolds number $Re_\tau = \frac{u_\tau h}{\nu}$, which describes the ratio of turbulent scales that are considered in a given turbulent channel flow. In our simulations we will be limited to low values of this number, imposing $Re_\tau \in [150; 300]$;

○ the volume fraction of the fibres, Φ, which measures the ratio between the total volume of the dispersed particles and that of the turbulent channel flow, fixed to $(2\pi\ 2h \times \pi\ 2h \times 2h)$. In our simulations, we will consider dilute suspensions, exploring the range $\Phi \in \left[10^{-5}; 10^{-3} \right]$. Note that the volume fraction can be multiplied by the density ratio $\rho^+ = \rho_p/\rho$ to calculate the mass loading $\mathbb{M}$ of the suspension;

○ the aspect ratio of the fibres $r_{tot} = r \cdot n_{rods}$. This dimensionless number quantifies the slenderness of the chains of rods, calculated as the aspect ratio of one element times the number of elements in the chain of rods. In our simulations we typically consider rod elements of aspect ratio $r = 5$, which are combined to

determine fibres in the range $r_{tot} \in [50; 200]$. In addition, some calculations are performed with extremely slender chains with $r_{tot} = 1000$ ($r = 50$);

○ the length of the fibres $L^+ = \frac{L \cdot u_\tau}{\nu}$, that measures the ratio between the length of the particle and the viscous scale of the turbulent flow. In our simulations we will consider long fibres, fixing $L^+ \in [17; 71]$;

○ the Stokes number of the fibres

$$St^+_{fibre} = \frac{\tau_{p,n}}{\tau_f} = \frac{2a^{+2}}{9} \frac{\rho_p}{\rho} \cdot r_{tot} \cdot \frac{\log\left(r_{tot} + \sqrt{r_{tot}^2 - 1}\right)}{\sqrt{r_{tot}^2 - 1}} \ .$$

This dimensionless number measures the ratio between the characteristic times of the flow and is calculated for a fibre in its fully stretched configuration. A low value of the Stokes number describes fibres which will follow the streamlines of the flow, acting like a tracer. Instead, a high value of the Stokes number corresponds to an inertial particle, which will develop a ballistic behaviour within the flow. In our simulations we will look at fibres Stokes number in the range $St^+_{fibre} \in [0.1; 11]$. Note that inertial effects are modelled only for the particles' linear dynamics, ignoring the torque determined by flow and particle inertia (Einarsson, Candelier, et al., 2015b; Dabade et al., 2016);

○ the viscous-elasto number (Du Roure et al., 2019):

$$\mathbb{B} = \frac{8\pi r_{tot}^4 \cdot \left(\rho u_\tau^2\right)}{E_Y \cdot \pi/4} = \frac{32 \cdot r_{tot}^4}{E_Y^+} \ .$$

This number can be looked at as the typical ratio between the time-scale of the fibres' bending stiffness and that of the viscous scale of turbulence, so that at small $\mathbb{B}$ the fibres are very rigid whereas at large $\mathbb{B}$ the fibres become more flexible and might bend within the turbulence. The rod-chain model struggles to simulate rigid fibres, as a high value of the fibres Young's modulus, i.e., $\mathbb{B} \sim 0$, makes the calculations unstable and error-prone even when a sub-stepping procedure is deployed. Therefore, in our simulations we choose to consider completely stiff-less fibres and fibres with a finite but small bending stiffness. The corresponding values for the Young's modulus are $E_Y^+ = 0$ and $E_Y^+ = 10^4$, which determine respectively $\mathbb{B} = \infty$ for the first kind of chains, which are completely enslaved to turbulence, and $\mathbb{B} = [20000, 320000, 5120000]$ for fibres with aspect ratio $r = 50, 100, 200$, which are still remarkably flexible for the considered flows. Nevertheless, we will classify the $\mathbb{B} = \infty$ as stiff-less, whereas those with a finite value of the Young's modulus will be called stiff.
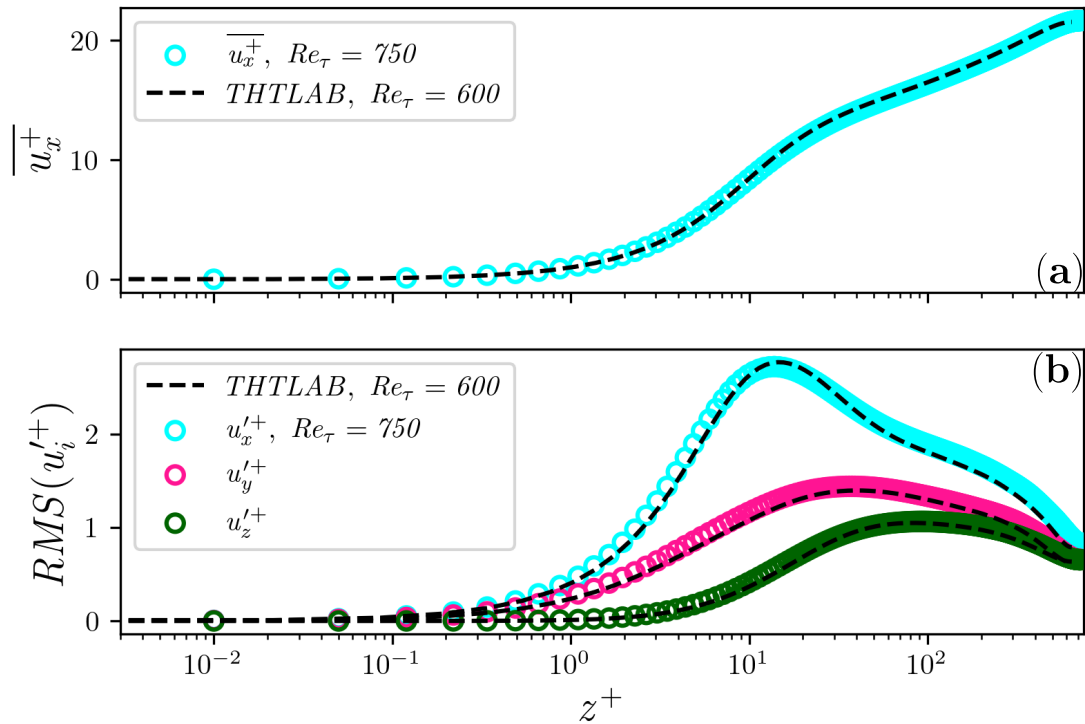
Figure 3.8. – Validation of the GPU-accelerated Turbulent Channel Flow DNS solver "surf_ gpu.exe" (coloured circles, shear Reynolds number $Re_\tau = 750$)) against the database of the University of Tokyo (black dashed lines, shear Reynolds number $Re_\tau = 600$, (Iwamoto et al., 2002)). Panels: (a) dimensionless stream-wise mean velocity profile against the wall-normal dimensionless coordinate z^+. (b) Root Mean Squared stream-wise (blue), span-wise (pink) and wall-normal (green) velocity fluctuations against the wall-normal dimensionless coordinate z^+.

3.6. Validation

3.6.1. Unladen flow

The GPU-accelerated flow solver is validated against the database of the University of Tokyo for the same geometry at a high shear Reynolds number $Re_\tau = 720$ (Iwamoto et al., 2002). Despite we will focus on fibre-laden turbulent channel flows at lower Re_τ, we look here for a robust test of the implemented flow-solver. Calculations are performed from an initial laminar velocity profile, perturbed by a sine function with random amplitude until a linear total axial momentum against the wall-normal coordinate is observed. Then, statistics are sampled every $18t^+$, over an averaging window of approximately $2000t^+$. As displayed in figure 3.8 for the mean velocity profile (panel (a)) and the turbulence intensities (panel (b)), good agreement is obtained, despite the slightly different shear Reynolds number.

3.6.2. Particle-laden turbulent channel flow

The current implementation of the ERPP method is validated against the work of Battista et al., 2019. These authors present the axial momentum balance for a particle-laden turbulent pipe flow at shear Reynolds number $Re_\tau = 180$, where particles are approximated as point-wise spheres modelled taking into account the Stokes Drag force with the Faxen correction term

$$\frac{d\mathbf{v}_p}{dt} = \frac{1}{St_p}\left(\mathbf{u}_p + \frac{d_p^2}{24}\nabla^2\mathbf{u}_p - \mathbf{v}_p\right). \tag{3.40}$$

In figure 3.9 the axial momentum balance for our implementation of the ERPP method is presented against their result. This is obtained by considering a minimal flow configuration, where the domain size was set to $(L_x, L_y, L_z) = (2\pi h, 2\pi h, 2h)$. Then, the grid is made of $(N_x, N_y, N_z) = (256, 256, 257)$ points, giving a maximum ratio of $\frac{dz_{max}^+}{\sigma_R}^+ = 1.2$ for the wall-normal coordinate and of $\frac{dx^+=dy^+}{\sigma_R}^+ = 2.45$.

As no detail about the effective regularization scale is given by Battista et al., 2019, we cannot compare the quality of the two simulations, despite we expect our study to be slightly more approximate, as they deploy a more refined grid for a practically similar flow volume. These considerations, together with the fact that we are indeed considering two analogous but yet different geometries, could explain the moderate differences in the intensity of the extra particle stresses displayed in figure 3.9, whereas there is still a good qualitative and quantitative agreement between the reference and our implementation to consider our implementation valid.

3.6.3. Jeffery orbits

The fibre solver is validated against the classical test case for axisymmetrical particles suspended in viscous shear flow. As we have seen, these particles will rotate according to the theory of Jeffery, 1922, enforcing an equivalence of shape between ellipsoids and cylinders so that fibres will always rotate like prolate ellipsoids with a lower particle aspect ratio r. Nevertheless, previous numerical studies have shown the importance of the local fluid acceleration determined by the particles in order to recover the correct period of rotation for the simulated fibres (Lindström and Uesaka, 2007; Delmotte et al., 2015).

Our results are reported in figure 3.10, where we look at the time evolution of the orientation of a fibre with aspect ratio $r = 15$ suspended in a viscous shear flow, given by the azimuthal angle ϕ. We see that the one-way coupled calculation (blue squares) recovers the qualitative behaviour, despite the rotation being clearly much slower than expected (blue dashed line). Once the ERPP is activated, a coarser grid will determine a delayed time-scale ϵ that is much larger than the time-step of the simulation, resulting in a slightly lower overestimation of the period of the Jeffery orbits for this fibre (green circles). Finally, a more refined grid determines a much shorter regularisation time scale, allowing a perfect match between the simulated fibre (orange diamonds) and
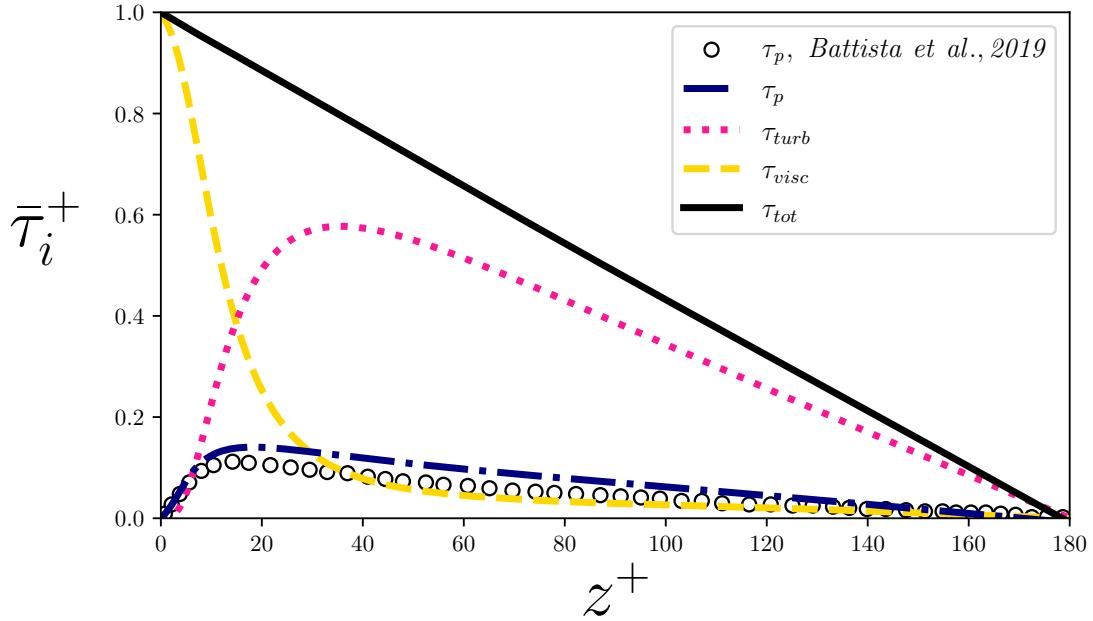
Figure 3.9. – Axial momentum balance for a turbulent channel flow at shear Reynolds $Re_\tau = 180$ against the result of Battista et al., 2019 in a turbulent pipe flow at $Re_\tau = 180$: particles have the same size ($St_p^+ = 80$) and density ratio with the fluid ($\rho^+ = 180$), and the mass loading is similar, fixed at approximately $\phi_m \simeq 0.4$. Note that in our work we do not consider the Faxen correction term, therefore relying only on the Stokes Drag force to couple the two phases. τ_{visc} identifies the viscous shear stress, $\tau_{turb} = \overline{u'w'}$ is the turbulent Reynolds stress and τ_p is the particles extra stress, calculated as a cumulative integral of the axial force $F_{2w,x}$ over the wall-normal coordinate z. In order to obtain a statistically steady state for the numerical simulations, the sum of these three terms must be a linear function of the wall-normal coordinate, as highlighted by the τ_{tot} term.

the experimentally validated theory.

Therefore, the two-way coupling is fundamental to obtaining a physically validated numerical simulation of a fibre suspended in a viscous shear flow, where the particle-induced flow acceleration clearly plays a key role. The ERPP two-way coupling method smoothly emulates the experiments, at the price of a more refined computational grid. Moreover, it allows us to bridge between the experimental and numerical investigations that were developed during the preparation of this manuscript, connecting simple experiments on the rotation of axisymmetrical particles in the viscous regime to complex numerical simulations of fibre-laden turbulence. This is a fundamental aspect when simulating cylindrical shapes, as we have discussed in Section 2.4.2 when comparing the shape equivalence between fibres and ellipsoids, and it will have deep consequences for their dynamics as well as for turbulence modulation and drag
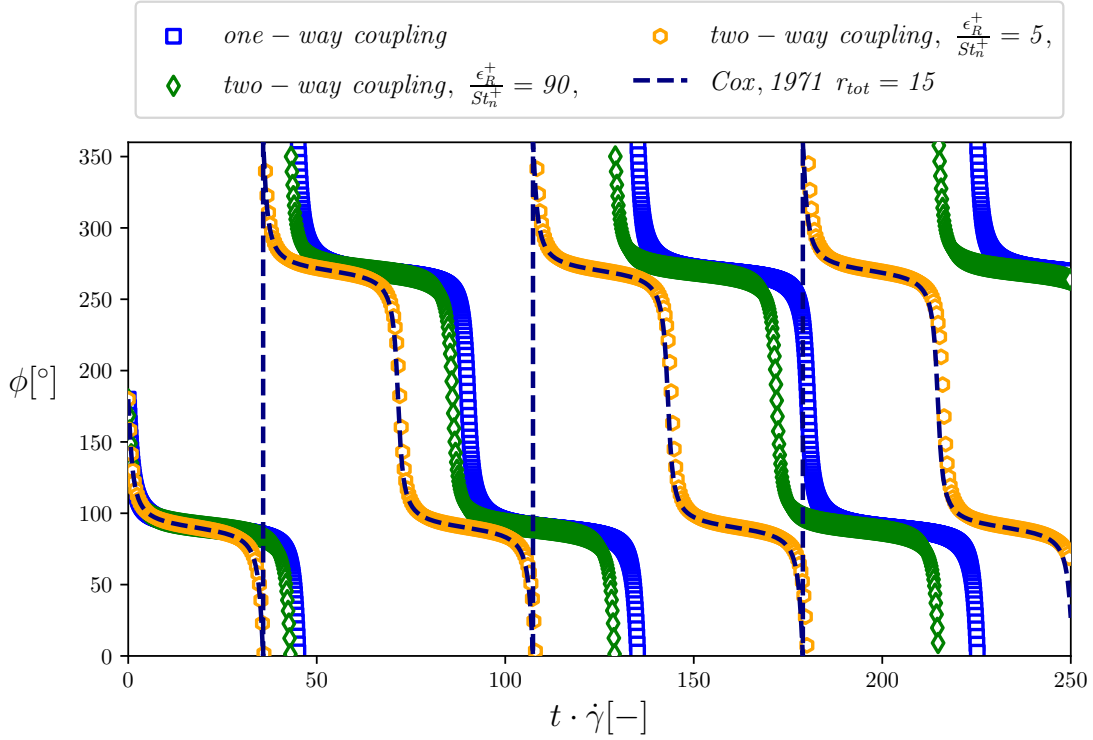
Figure 3.10. – Time evolution of the azimuthal angle ϕ of a numerically simulated rigid fibre suspended in a viscous shear flow. Here, the fibre is assembled as a chain of five rods of aspect ratio $r = 3$ so that the total aspect ratio is $r_{tot} = 15$, and bending is avoided by imposing a sufficient value for the Young's modulus. The dotted curves represent the obtained Jeffery orbits, calculated for progressively refined grids, while the dashed line is the effective analytical solution, obtained from Jeffery's theory (Jeffery, 1922) through the equivalence of shape of Cox, 1971. Note that, for the considered total aspect ratio $r_{tot} = 15$, the equivalence of shape of Harris and Pittman, 1975 would return the same result.

reduction (Z. Wang et al., 2021).

A comment is in order about the criterion behind the choice of the regularisation time-scale ϵ^+, which gives the best results when it is a small multiple of the time-step of the simulation and the particle response time. Clearly, it will not be possible to maintain the same accuracy when scaling up our calculations to the turbulent channel flow geometry, as the computational load would become unsustainable even for the modern High-Performance Computing infrastructures. Nevertheless, the analysis of the rod's response time, given by equation 3.37, shows a clear proportionality with the density and the size of the particle. Therefore, we speculate that inertial effects due to the particles' density will mitigate the inaccuracies due to the longer regularisation time-scales ϵ^+ estimated in our turbulent simulations.

3.7. Summary of the Simulations

We now present the results of a numerical investigation into the dynamics of fibres in turbulence at imposed shear Reynolds number $Re_\tau = 300$. The closed turbulent channel flow has dimensions $L_x \times L_y \times L_z = 4\pi h \times 2\pi h \times 2h$, which correspond to $L_x^+ \times L_y^+ \times L_z^+ = 3770 \times 1885 \times 600$ wall units. Simulations are performed in the two-way coupling regime, as the Exact Regularized Point Particle method is deployed to emulate the boundary conditions imposed by the point-wise rods on the flow. Therefore, we choose to resolve the computational domain on a grid made of $N_x \times N_y \times N_z = 1024 \times 512 \times 513$ points, much finer than those normally deployed for calculations in the one-way coupling regime. This corresponds to a grid resolution of ($dx^+ = d_y^+ \sim 3.7; d_{z,max}^+ \sim 1.8$), where the Chebychev polynomials allow for a much finely discretization near the walls. Therefore, we scale the two-way coupling regularization scale with regard to the coarser region of the grid, i.e. the bulk of the flow, setting the regularization scale to $\epsilon_R^+ = \sigma_R^{+2}/2 \sim 1.8^2/2 = 1.62$.

The time-step for the advancement of the flow equations in time is $\delta_t^+ = 0.015 \sim \tau_{k,w}^+/150$, where is the smallest relevant time-scale of the flow, i.e. the Kolmogorov's time-scale at the wall. The convergence condition is verified by verifying that the Courant number of the calculations is kept below 0.4 at all times. A comment is in order about the delay imposed by the ERPP two-way coupling method, which corresponds to $\epsilon^+/dt^+ = 108$ time-steps during which the particle disturbance information must be stored before being diffused to the computational grid. This choice is a compromise between the quality and the feasibility of our numerical simulations.

The dispersed fibres are built constraining together rod-like elements with fixed geometry, their diameter $2a^+ = 0.36$ wall units and their particle aspect ratio $r = 5$, so that their length $2\ell^+ = 1.79$ will be comparable to the smallest turbulent length-scale. This corresponds to a Stokes number of the rod equal to $St_{rod}^+ = 0.05$ which, combined with an imposed density ratio $\rho^+ = 3$, determines particles with low inertia and three times the density of the fluid, classified as tracer-like in the following pages. From the described rod element, chains are created with three different total lengths and aspect ratios, resulting in the total fibre Stokes numbers reported in table 3.1. For each different fibre length, a zero and a finite (10^4) value of Young's modulus are considered, to explore the influence of the bending stiffness. The influence of particle inertia is also studied. This is done by selecting the intermediate fibres ($L^+ = 35.81$, $r = 100$), both flexible and stiff, and increasing their rods' Stokes number and density ratio by two orders of magnitude ($St_{rod}^+ = 5, \rho^+ = 300$). The resulting inertial particles will have total Stokes number $St_{fibre}^+ = 11$ and produce a 100 times higher mass loading, as reported in the last two lines of table 3.1.

The rod motion equations are advanced in time at the same time-step as for the fluid but a one-tenth sub-stepping procedure is enabled, in order to maintain the error on the constraints below 1% as described at the end of Section 3.3.4. A final insight into the quality of the two-way coupling is given when we compare the characteristic fibre time-scale, given by their Stokes number St_{fibre}^+, to the regularization time-scale ϵ_R^+. Despite the computational effort, it is clear that the two-way coupling time-scale ($\epsilon_R^+ =$

run	$St_{fibre}\,(\rho^+)$	E_Y^+	r_{tot}	L^+	V_{frac}	$M_{frac}\%$
A	0.1 (3)	0	50	17.91	0.0001	0.032
B	0.1 (3)	10^4	50	17.91	0.0001	0.032
C	0.11 (3)	0	100	35.81	0.0001	0.032
D	0.11 (3)	10^4	100	35.81	0.0001	0.032
E	0.13 (3)	0	200	71.62	0.0001	0.032
F	0.13 (3)	10^4	200	71.62	0.0001	0.032
G	11 (300)	0	100	35.81	0.0001	3.2
H	11 (300)	10^4	100	35.81	0.0001	3.2

Table 3.1. – Report of the considered simulations with tracer-like fibres at different total particle lengths, showing the given values for the fibres' Stokes number St_{fibre}^+ and the corresponding density ratio ρ^+, the Young's modulus of the chains E_Y^+, the fibre aspect ratio r_{tot}, the total fibre's length L^+, the volume fraction and mass loading. The number of rods is fixed to 2.5 millions. Quantities are made dimensionless and presented in wall units. The Stokes number of each fibre is calculated in its fully stretched equilibrium configuration.

1.62) is small enough to correctly take into account the flow acceleration determined by the inertial rods only ($St_{fibre}^+ = 11$). Anyway, the imposed regularization time-scale is lower than the Kolmogorov time-scale at the wall ($\epsilon_R^+ = 1.62 < \tau_{k,w}^+ = 2.24$), allowing us to conclude that the interaction between fibres and turbulence will be accurately modelled even for the tracer-like chains of rods.

All the simulations start from a fully-developed turbulent flow condition. Fibres are injected into the flow as fully stretched and randomly dispersed, with initial orientation along the stream-wise direction. After injection, fibres evolve in time under the action of the turbulent flow and eventually forget about the initial condition imposed on their conformation, position, orientation and velocity. Then, statistics are collected every 15 t^+ over a time span of 1500 t^+, which corresponds to four times the eddy turnover time of the largest structures of the turbulent channel flow.

Calculations are performed on 64 Nvidia Tesla V100 cards of Marconi 100, hosted by CINECA (Italy). Thanks to the scalability properties of the computational solver, the simulations require an elapsed time per time-step of approximately 750 milliseconds.

3.8. Results

3.8.1. Visualisation of the fibre-laden turbulent channel flow

We begin the discussion of our results by looking at the flow visualisations in figures 3.11 and 3.12, where stiff-less and stiff fibres at all lengths are displayed respectively. In these figures, we consider a $L_x^+ = 975 \times L_y^+ = 840$ horizontal section of the turbulent channel at a given time, where the stream-wise direction x^+ increases from left to right

and the span-wise direction y^+ from bottom to top. The left panels show particles whose centre of mass lies within 30 wall units from the walls, whereas the right panels show those whose centre of mass lies within 30 wall units from the half-height of the turbulent channel flow. Left panels display also the stream-wise velocity u on a (x, y) plane at $z^+ = 10$, whereas right panels consider the same section but at $z^+ = 300$. We obtain a qualitative description of the fibre-laden flows from these two images. The characteristic velocity streaks are visible in the near-wall left panels, and at the given mass load no remarkable modification of their structure is measurable, which would be a typical sign of turbulence modulation (Z. Wang et al., 2021). On the other hand, the right panels display the more isotropic structure of the bulk of the flow. The real-scale rendering of the fibres allows us to appreciate the different particle lengths, which increase by a factor of 2 between each line of panels from the top to the bottom of the two figure. In general, fibres near the wall (left panels) prefer a flow-aligned configuration, whereas the orientation of the chains in the bulk of the flow appears more isotropic, The bending stiffness does not seem to play a role in the shortest chains, which look straight in all the panels. Instead, intermediate and long stiff fibres (panels (c), (d), (e) and (f) of figure 3.12) clearly appear more stretched than their stiff-less twins (panels (c), (d), (e) and (f) of figure 3.11).

3.8.2. Characterisation of the dynamic behaviour of the fibres

The instantaneous visualisation of the fibre-laden turbulent channel flows in figures 3.11 and 3.12 already reveals some features of the particle behaviour. Anyway, this description must be completed by considering the dynamic behaviour of the fibres. Within this scope, we find it convenient to average among all the rods of each chain and use the chain-averaged quantities to describe each fibre. Their position within the turbulent channel flow is that of their centre of mass:

$$\mathbf{p}_{cm} = \frac{\sum_{i=1}^{N} \mathbf{p}_i}{N} \, , \tag{3.41}$$

while their orientation is calculated as in Andrić et al., 2013:

$$\mathbf{n} = \frac{\sum_{i=1}^{N} \mathbf{o}_i}{|\sum_{i=1}^{N} \mathbf{o}_i|} \, , \tag{3.42}$$

and other averages will be calculated accordingly. Following in Byron et al., 2015, we decompose the rotation rate of an axisymmetrical particle among its tumbling and spinning components:

$$\textit{Tumbling rate} = |\dot{\mathbf{n}}| = |\omega \times \mathbf{n}| \, , \tag{3.43a}$$

$$\textit{Spinning rate} = |\mathbf{n} \cdot \omega| \, . \tag{3.43b}$$

The former measures the rotation of the fibres' axis of symmetry, while the latter the rotations around that axis. In a way, spinning and tumbling rates describe the particle
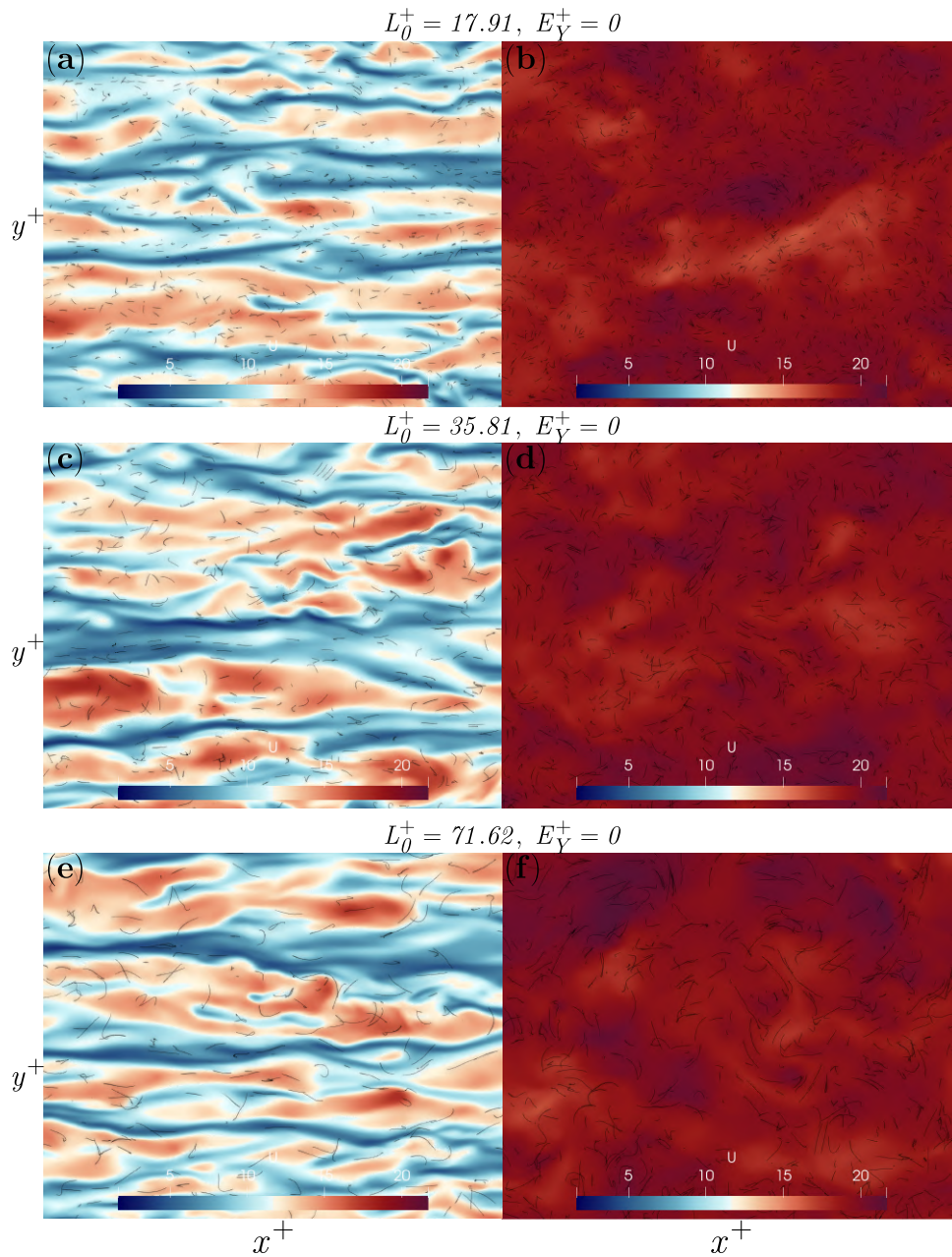
Figure 3.11. – Instantaneous visualisation of the fibre-laden turbulent channel flow for stiff-less ($E_Y^+ = 0$) fibres. Panels display fibres whose centre of mass lies within 30 w.u. from the wall (left) or the half-height of the channel (right). Panels are coloured according to the stream-wise velocity u measured on a plane at $z^+ = 10$ (left) or $z^+ = 300$ (right). The size of each panel is $L_x^+ = 975 \times L_y^+ = 840$ wall units. Panels: (a) and (b) short fibres ($L_0^+ = 17.91$); (c) and (d) intermediate fibres ($L_0^+ = 35.81$); (e) and (f) long fibres ($L_0^+ = 71.62$).
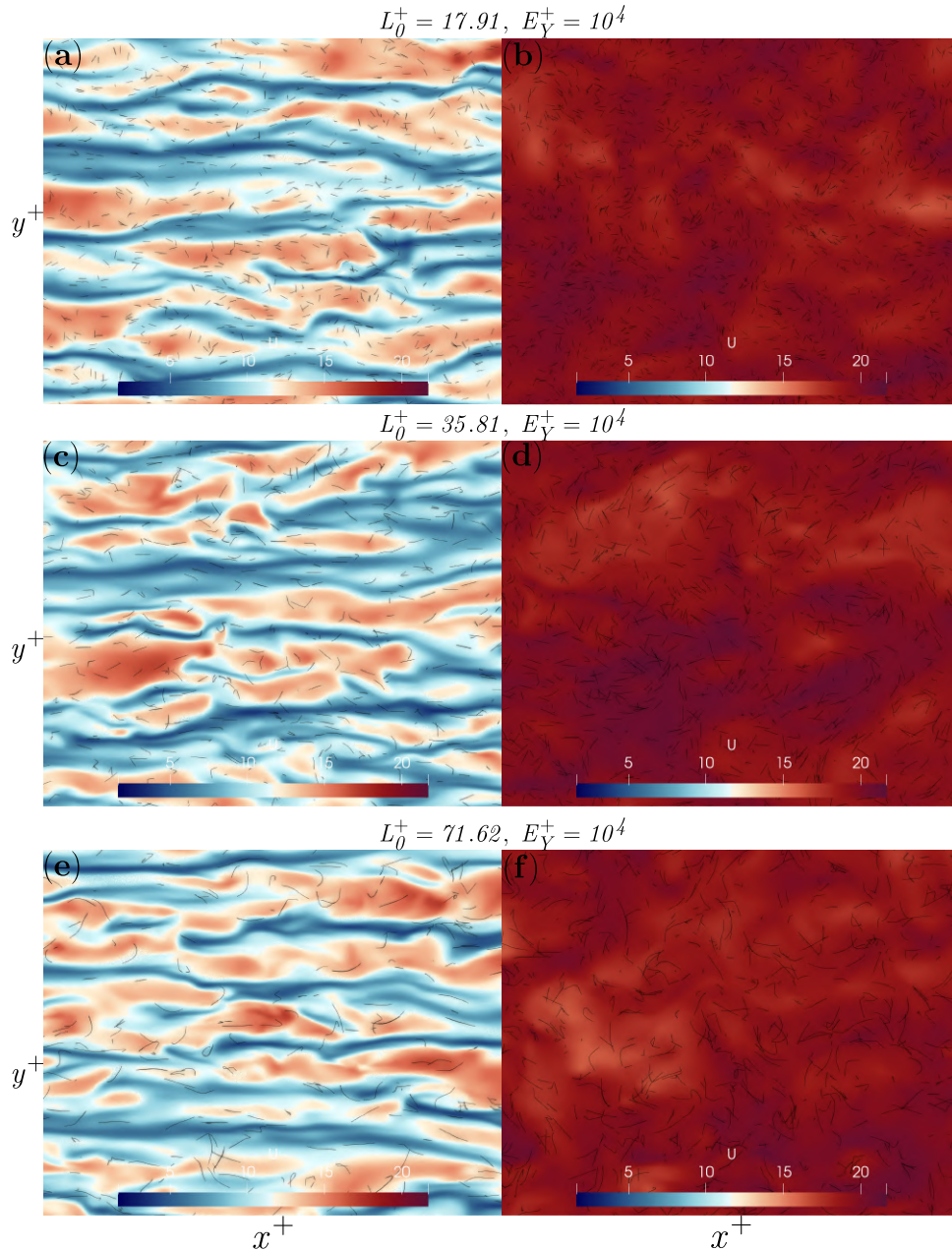
Figure 3.12. – Instantaneous visualisation of the fibre-laden turbulent channel flow for stiff ($E_Y^+ = 10^4$) fibres. Panels display fibres whose centre of mass lies within 30 w.u. from the wall (left) or the half-height of the channel (right). Panels are coloured according to the stream-wise velocity u measured on a plane at $z^+ = 10$ (left) or $z^+ = 300$ (right). The size of each panel is $L_x^+ = 975 \times L_y^+ = 840$ wall units. Panels: (a) and (b) short fibres ($L_0^+ = 17.91$); (c) and (d) intermediate fibres ($L_0^+ = 35.81$); (e) and (f) long fibres ($L_0^+ = 71.62$).
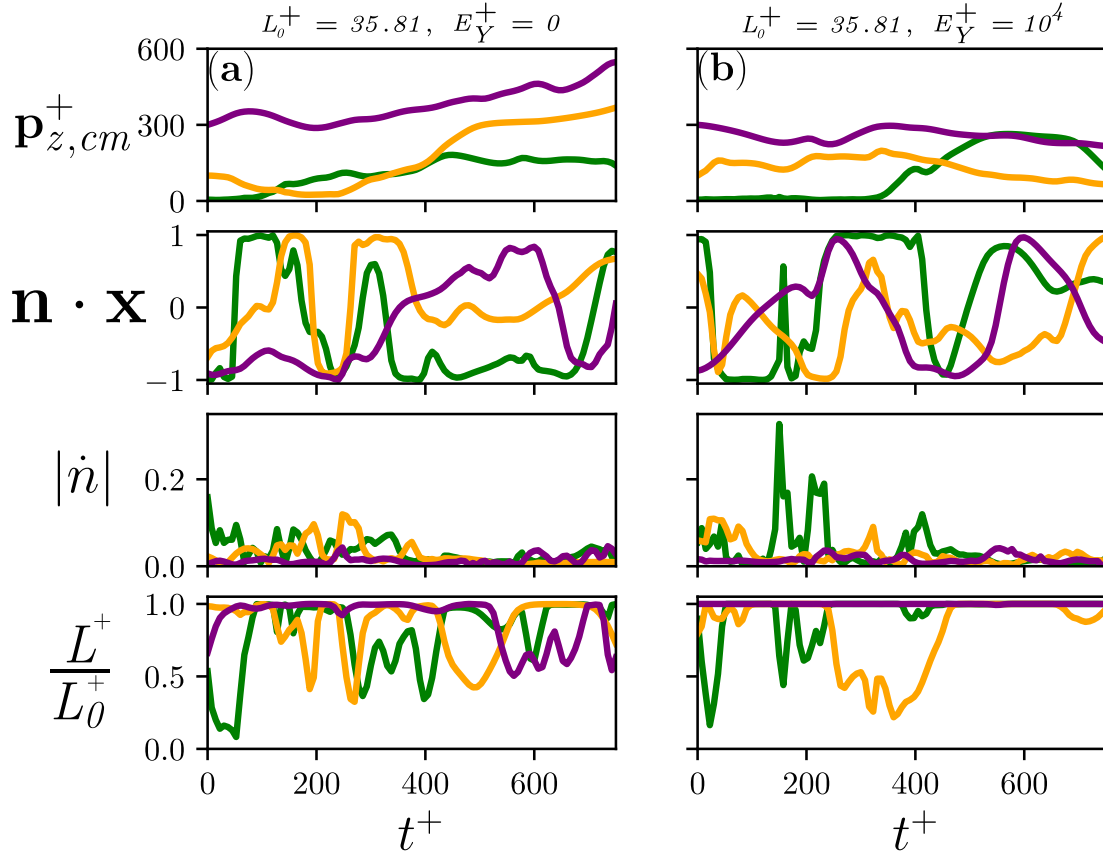
Figure 3.13. – Time-evolution of some fibres within the turbulent channel flow, at initial wall-normal position $z^+ = 5$ (green), $z^+ = 100$ (yellow) and $z^+ = 300$ (purple). For the selected particle, the wall-normal position of the centre of mass, the stream-wise component of the particle orientation vector, the module of the tumbling rate vector and the normalized effective end-to-end distance are displayed from top to bottom of each column. Averages are calculated on the whole chain of rods. Columns: (a) $St^+_{fibre} = 0.11, E^+_Y = 0, L^+_0 = 35.81, r = 100$; (b) $St^+_{fibre} = 0.11, E^+_Y = 10^4, L^+_0 = 35.81, r = 100$.

orientation within the local directions of strain and vorticity. Finally, we define the fibres' effective end-to-end distance as the module of the vector difference between the two free extremities of the chain:

$$L_e = \frac{L^+}{L^+_0} = \frac{\mathbf{p}_n + \mathbf{o}_n \cdot \ell - (\mathbf{p}_1 - \mathbf{o}_1 \cdot \ell)}{L^+_0} \ . \tag{3.44}$$

This observable describes, for values ≤ 1, the effective length that fibres adopt while being deformed by the flow.

We are finally able to look at the time-evolution of some meaningful fibres in fig-

ure 3.13, where the wall-normal position of the centre of mass z_{cm}^+, its alignment with the flow direction $n_x = \mathbf{n} \cdot \mathbf{1,0,0}$, the module of the tumbling rate $|\dot{n}|$ and the normalized effective end-to-end distance L^+/L_0^+ are plotted from top to bottom of the two columns. Stiff-less (column (a)) and stiff (column (b)) tracer-like chains are considered, being $L_0^+ = 35.81$ their stretched length and $r = 100$ their particle aspect ratio. From the first row of panels, we see that fibres will experience different flow conditions along the observation window, as they are either pushed towards or lifted from the solid boundaries. Therefore, the particle orientation in the flow does not correspond anymore to a periodic dynamical behaviour, such as was observed for axisymmetrical particles suspended in a viscous shear flow in the experimental part of this manuscript. As shown in the second row of panels, particles enjoy flow-aligned configurations only for brief times, being constantly reoriented by the action of eddies of proportional size (Shin and Koch, 2005). In any case, stiff and stiff-less fibres in the bulk seem more relaxed (purple lines), whereas these objects experience more frequent re-orientations as they get closer to the walls (green and yellow lines).

This is reflected in the third row of panels, where the tumbling rate is displayed against time. At first glance, it is clear that fibres near the walls experience stronger tumbling than those in the bulk of the flow, which reorient more softly. If one looks carefully, there is a correspondence between the tumbling rate events and the variations of particle orientation displayed in the second row. Finally, the analysis of the visco-elastic number $\mathbb{B}$ in Section 3.5 indicated that even the stiff fibres ($E_Y^+ = 10^4$) fall in the flexible regime. This is confirmed by looking at the effective end-to-end distance of the fibres, displayed in the fourth row of panels of figure 3.13. Comparing columns (a) and (b), we appreciate the influence of the finite bending stiffness (column (b)), which keeps fibres in the bulk remarkably stretched (purple line). Instead, stiff tracer fibres will experience rapid deformation events as they move closer to the walls (yellow and green lines). On the other hand, stiff-less chains of rods are deformed no matter their wall-normal position (columns (a)). In general, events in the bulk (purple lines) manifest themselves less frequently than those near the walls (yellow and green lines). Anyhow, turbulence eventually straightens the buckled chains, as the lowest effective lengths appear for relatively short times.

Forgacs and Mason, 1959 studied experimentally the Jeffery orbits of flexible fibres. These authors observed strong buckling deformations of their particles when rotating out of the flow-aligned stretched configuration into the compressing quadrant of a viscous shear flow. Interestingly, even our long fibres ($L^+ = 35.808$) suspended in turbulence exhibit similar behaviour, clearly displayed in column (b) by stiff tracer particles, where the correspondence between strong tumbling rate values and low effective particle lengths is appreciable. This physical mechanism was also observed for short sub-Kolmogorov flexible rods in HIT (Allende et al., 2018). Motivated by this analogy, in the following pages we will build a more quantitative discussion to try and understand the deformation of fibres in wall turbulence. This will be done by looking into their orientation, tumbling rate and effective shape before focusing on the dynamics of the deformations.

3.8.3. Orientation of fibres in wall turbulence

Figures 3.11 and 3.12 provided a nice perspective over the preferential orientation of fibres within the turbulent channel flow, highlighting the differences between the near-wall and the bulk regions. Moreover, having looked at figure 3.13 it is clear that the periodic rotations between flow-aligned configurations typical of the Jeffery orbits are definitely lost when fibres are suspended in turbulence. One could still obtain some insight into the orientation of slender fibres by looking at the probability distribution function of the components of the rods' orientation vector **o** in figure 3.14. We do so by splitting our particles according to the wall-normal position of their centre of mass, considering again either two near-wall regions of thickness 30 wall units ($p_{z,cm}^+ < 30$ or $p_{z,cm}^+ > 2Re_\tau - 30$, "near wall" panels), or a bulk region of thickness equal to 60 wall units ($Re_\tau - 30 < p_{z,cm}^+ < Re_\tau + 30$, "bulk" panels). Figure 3.14 shows that fibres near the walls express a strong preferential orientation in the stream-wise direction (o_1), determined by the mean shear that acts in this part of the channel (panels "Near wall"). This corresponds to a moderate anti-alignment with the span-wise direction (o_2) and an even stronger perpendicularity with the wall-normal orientation (o_3). These trends are much weaker but still observable for the fibres in the bulk of the flow ("Bulk" panels), which clearly lose the preferential alignment with the mean flow.

In general, the particle length alone does not influence these statistics, as one can appreciate by comparing panels on the same row. Only in the case of stiff tracer-like fibres near the wall, we can appreciate a reduction of the anti-alignment with the wall-normal direction as the length of the fibres is increased from left to right (panels (g), (h) and (i)). This could be related to geometrical constraints that the longer particles inevitably experience when closer to the solid boundaries. These observations hold even for the considered stiff and stiff-less inertial particles at intermediate particle length, which are not displayed here for the sake of brevity.

Yet, from the Introduction of this manuscript we know that axisymmetrical particles in HIT are not randomly oriented but instead preferentially sample the local strain rate according to their particle aspect ratio (Byron et al., 2015; Voth and Soldati, 2017). Therefore, one could expect that fibres in the bulk of a turbulent channel flow, the most isotropic region of this geometry, would behave in a similar way, even when longer than the smallest relevant flow-scale (Olivieri, Mazzino, et al., 2022). In order to answer this question, it is necessary to verify that the two-way coupling disturbance does not perturb the local flow conditions at the particles' positions, similar to what was done by Olivieri, Mazzino, et al., 2022 in HIT. This is done by looking at the alignment between vorticity and eigenvectors of the strain rate at the rods' centres of mass in figure 3.15, where stiff and stiff-less tracer-like and inertial fibres at intermediate particle length ($L_0^+ = 35.81$) are considered.

We find a good agreement with the literature, as the vorticity vector preferentially aligns with the intermediate eigenvector (pink lines) in the bulk of the flow (bottom panels). This corresponds to a well-understood phenomenology, where turbulent eddies follow not the first eigenvector (corresponding to the direction of maximal
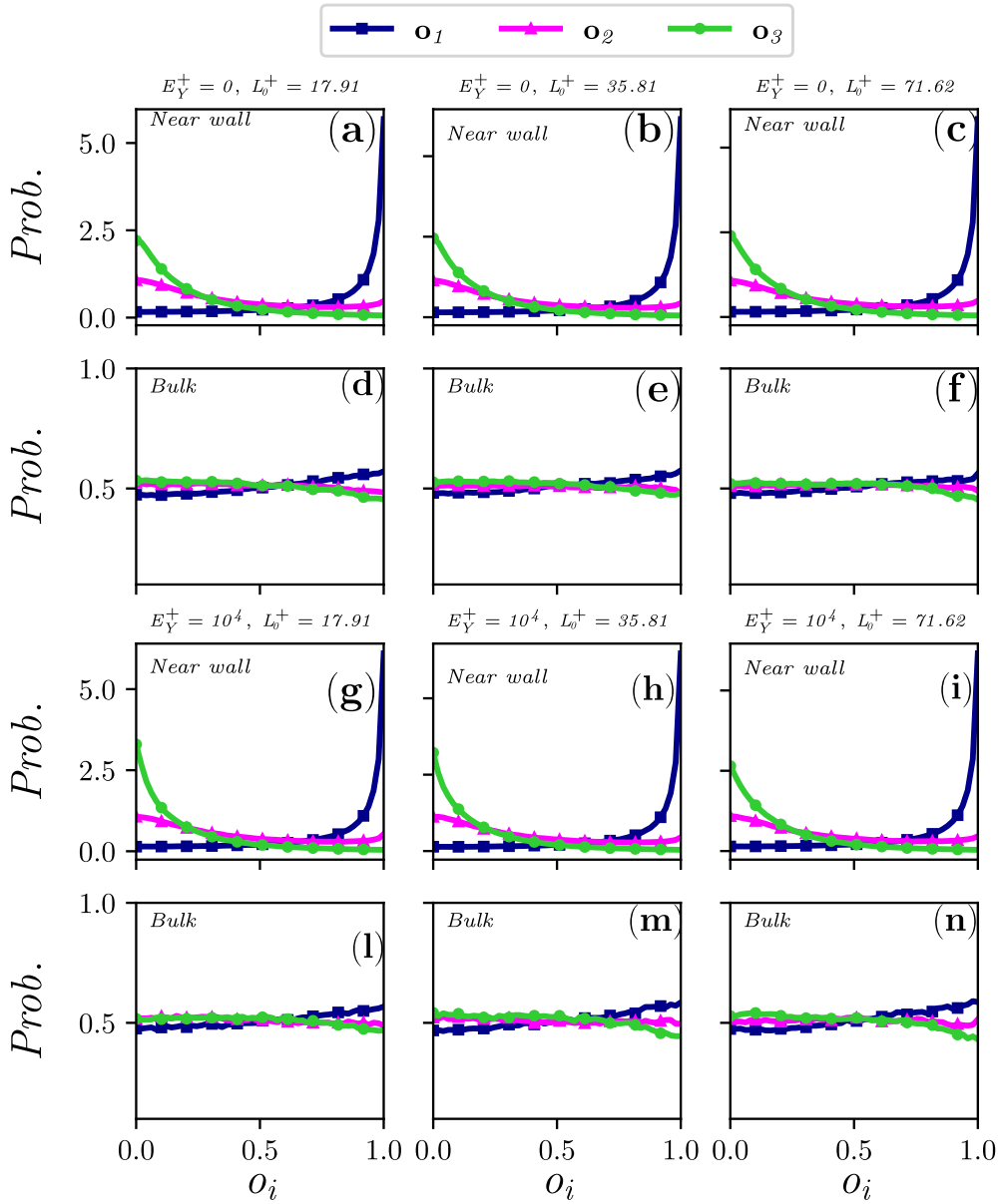
Figure 3.14. – P.d.f.s of the stream-wise (blue), span-wise (pink) and wall-normal (green) components of the rods' orientation vector **o**. "Near wall" panels on first and third rows: $p_{z,cm}^+ < 30$ *or* $p_{z,cm}^+ > 2Re_\tau - 30$; "Bulk" panels on second and fourth rows: $Re_\tau - 30 < p_{z,cm}^+ < Re_\tau + 30$. Panels: (a),(d) stiff-less short tracer-like fibres; (b),(e) stiff-less intermediate tracer-like fibres; (c),(f) stiff-less long tracer-like fibres; (g),(l) stiff short tracer-like fibres; (h),(m) stiff intermediate tracer-like fibres; (i),(n) stiff long tracer-like fibres.
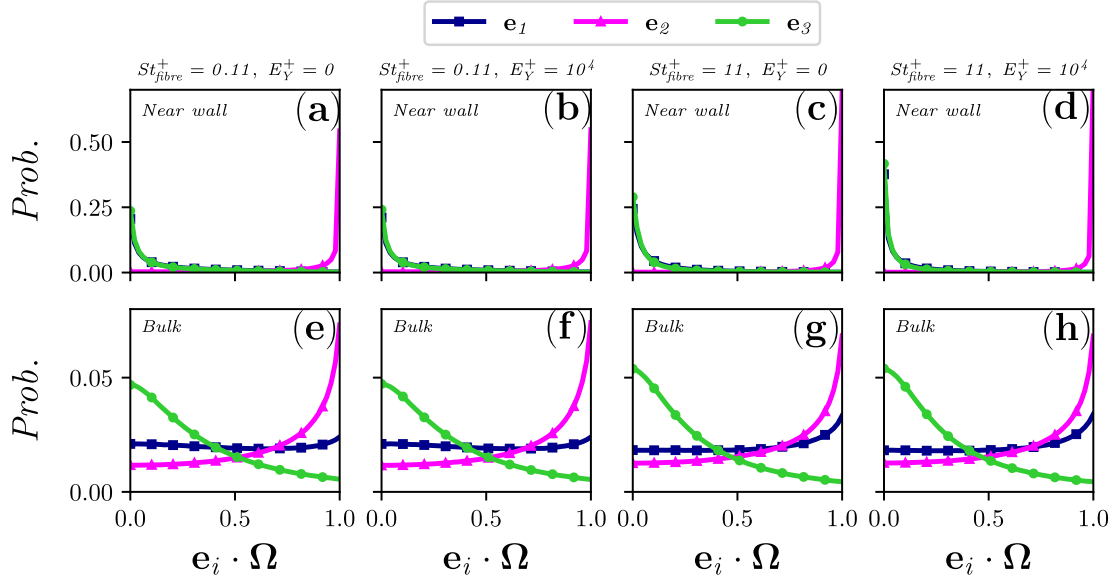
Figure 3.15. – P.d.f.s of the alignment between the flow vorticity and the eigenvectors **e** of the strain rate tensor at the rods' positions, sorted in descending eigenvalue order (**e**$_1$: blue, **e**$_2$: pink, **e**$_3$: green). Top panels: $p_{z,cm}^+ <$ 30 *or* $p_{z,cm}^+ > 2Re_\tau - 30$; Bottom panels: $Re_\tau - 30 < p_{z,cm}^+ < Re_\tau + 30$. Panels: (a),(e) stiff-less tracer-like intermediate fibres; (b),(f) stiff tracer-like intermediate fibres; (c),(g) stiff-less inertial intermediate fibres; (d),(h) stiff inertial intermediate fibres.

stretching) but the second one and, due to momentum conservation during vortex stretching, vorticity will align with this direction too (Voth and Soldati, 2017). Besides, the vorticity will feel a moderate alignment with the first eigenvector (blue lines) and a marked anti-alignment with the third one (green lines, corresponding to the maximal compression). Inertia slightly enhances the alignment with **e**$_1$, at the expense of that with **e**$_2$, in agreement with what was observed by Olivieri, Mazzino, et al., 2022. In addition, we extend this kind of measurement to the near-wall region of the flow (top panels of figure 3.15. This section of the channel is dominated by the strong shear so that the mean vorticity vector will follow the span-wise direction. The alignment between vorticity and the second eigenvector still persists, but a strong anti-alignment with the third and first ones emerges, in agreement with what was observed by L. Zhao and Andersson, 2016. Therefore, the consistency between our observation and the literature allows us to evaluate Eulerian strain and vorticity conditions at the Lagrangian positions of our fibres.

Finally, having evaluated the relative orientation between local strain rate and vorticity at the rods' positions, we possess sufficient insight into the flow structure to look at the particles' orientations in figure 3.16. Here probabilities of the alignment of the rods' orientation vector **o** with the vorticity vector Ω (black dashed lines) and with the eigenvectors of the strain-rate **e**$_i$ is displayed, the latter sorted following
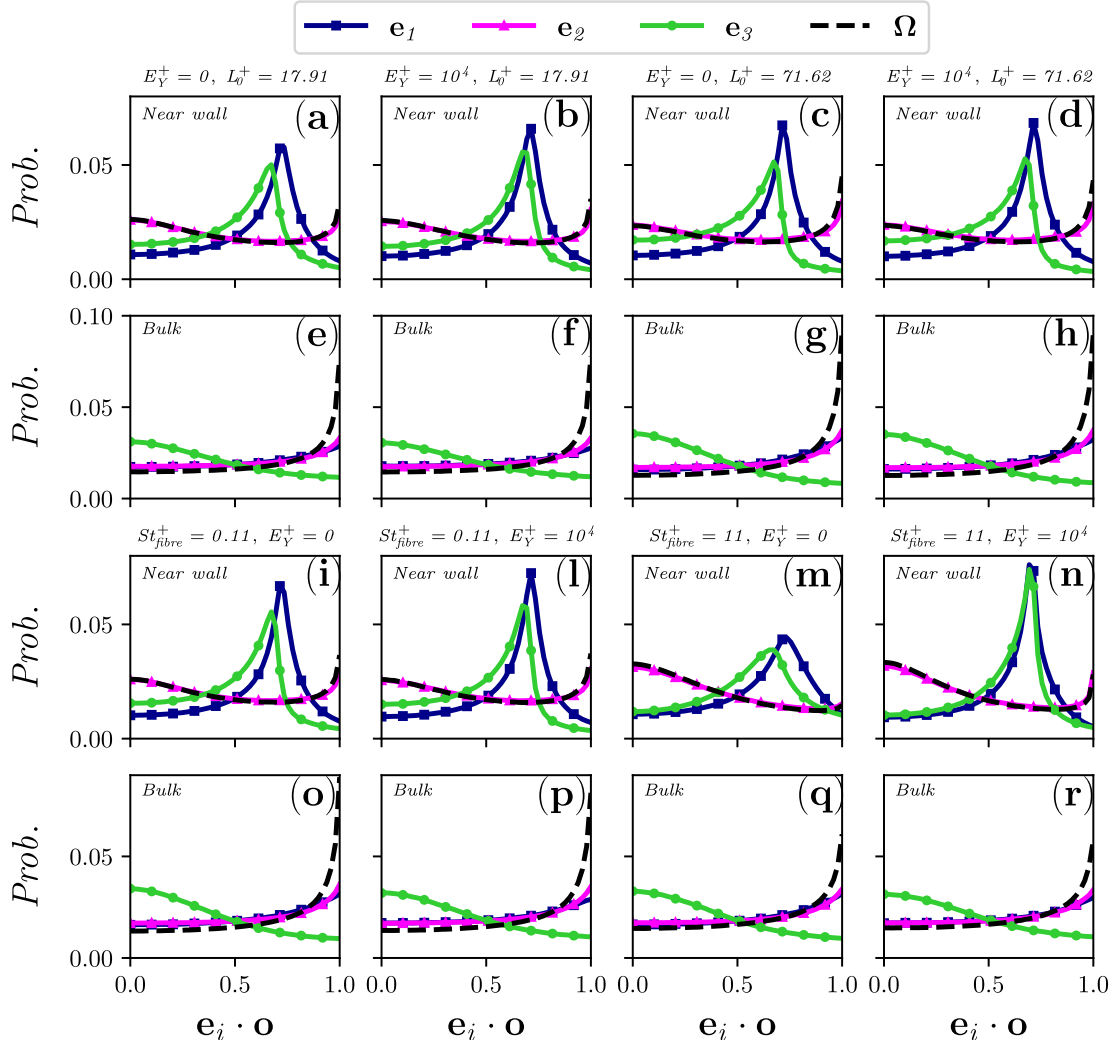
Figure 3.16. – P.d.f.s of the alignment between the rods' orientation and the eigenvectors **e** of the strain rate tensor, sorted in descending eigenvalue order (**e**$_1$: blue, **e**$_2$: pink, **e**$_3$: green). The p.d.f.s of the alignment between the rods' orientation and the vorticity are also displayed as black dashed lines. "Near wall" panels on first and third rows: $p_{z,cm}^+ < 30$ *or* $p_{z,cm}^+ > 2Re_\tau - 30$; "Bulk" panels on second and fourth rows: $Re_\tau - 30 < p_{z,cm}^+ < Re_\tau + 30$. Panels: (a),(e) stiff-less tracer-like short fibres; (b),(f) stiff tracer-like short fibres; (c),(g) stiff-less tracer-like long fibres; (d),(h) stiff tracer-like long fibres, (i),(p) stiff-less tracer-like intermediate fibres, (l),(p) stiff tracer-like intermediate fibres, (m),(q) stiff-less inertial intermediate fibres, (n),(r) stiff inertial intermediate fibres.

the intensity of the eigenvalues to separate between stretching and compressing events. Again, we separate between fibres whose centre of mass lies from 30 wall

117

units from a solid boundary ($p^+_{z,cm} < 30$ *or* $p^+_{z,cm} > 2Re_\tau - 30$, "Near wall" panels, first and third rows) or from the half-height ($z^+ = 300$) of the turbulent channel flow ($Re_\tau - 30 < p^+_{z,cm} < Re_\tau + 30$, "Bulk" panels, second and fourth rows). Short and long tracer-like fibres are considered in the first two lines, showing the results for the stiffless and stiff simulations. Intermediate fibres are displayed in the third and fourth lines of panels, where we explore the influence of bending stiffness and particle inertia as well.

Figure 3.16 shows that fibres of any length in the bulk of a turbulent channel flow (second and fourth rows of panels) align with the local stretching, with a slight preference for the second eigenvector of the local strain $\mathbf{e}_2$ over the first one $\mathbf{e}_1$. This has been recently observed in fibre-laden HIT, as suggests that long flexible fibres are being stretched inside tubular eddies of large dimension (Olivieri, Mazzino, et al., 2022; Picardo et al., 2020). As the local flow rotation is concurrently following the second eigenvector inside these stretched flow structures, all the considered fibres in the bulk of the flow are also strongly aligning with the local vorticity Ω, which has important consequences on their tumbling rate. On the other hand, a consistent anti-alignment is observed between all the rods and the third eigenvector of the local strain $\mathbf{e}_3$ in the bulk of the turbulent channel flow. Longer chains show a more marked tendency to follow the local vorticity than shorter ones (panels (e), (f), (g) and (h)). Instead, the bending stiffness of the particles has a limited influence on these statistics, whereas particle inertia slightly suppresses the observed alignment (panels (q) and (r)).

Interestingly, we observe different trends when considering the near-wall region, visualized in the first and third rows of panels of figure 3.16. First, all fibres show alignment and anti-alignment with the second eigenvector $\mathbf{e}_2$ and the vorticity vector Ω, where the former prevails for longer chains (panels (c) and (d)) and the latter is enhanced by particle inertia (panels (m) and (n)). Second, all particles show a sharp peak around a delayed alignment with the first and the third eigenvectors of the local strain, the latter always delayed with regard to the former. A finite bending stiffness gently brings together the two peaks, especially when considering the more inertial fibres (panels (m) and (n)).

The pinnacles of the $\mathbf{e}_1 \cdot \mathbf{o}$ probability indicate an ordinate value estimated to ~ 0.7. This is equivalent to an angle of $\sim 45°$ between the first eigenvector of the local strain and the fibres, which we have observed in the first and third rows of panels of figure 3.14 to prefer a flow-aligned and wall-perpendicular orientation in this region of the flow. Remarkably, this corresponds to the stream-wise inclination angle of large (20 times larger than the viscous scale) wall-attached coherent flow structures that extend up to the log-region of the flow (Yang and Pullin, 2011; Deshpande et al., 2019). In our simulations, the large size of the considered fibres seems to naturally allow for their sampling without losing the flow-aligned mean orientation. These structures are typical in the cycle of wall turbulence, therefore they could play an important role in the re-suspension and re-orientation of the long fibres that were considered in this study.

In conclusion, we have presented results on the orientation of long fibres suspended in a turbulent channel flow. Whereas near the solid boundaries, the particles follow

the mean flow, fibres in the bulk of the channel preferentially align with the local stretching and, coincidentally, with vorticity. This has deep consequences on their tumbling rate, as we will see in the following section of this manuscript.

3.8.4. Rotation of fibres in wall turbulence

In the previous section, the orientation of long slender fibres within a turbulent channel has been discussed, highlighting a stark similarity between particles in the bulk of the wall-bounded flow and previous studies with fibres suspended in HIT (Olivieri, Mazzino, et al., 2022). We expect this to deeply affect the rotational dynamics of the considered particles, therefore we look at the mean squared tumbling rate of the fibres in the bulk of the flow against the particle length in figure 3.17. Being the tumbling rate an inverse time scale, it is made dimensionless by the local squared Kolmogorov time scale τ_k^2, while the fibre length is normalized by local Kolmogorov length scale η_k.

Previous experiments with rigid fibres of different lengths in the HIT configuration reported that their tumbling rate approaches a $(L/\eta_k)^{-4/3}$ power law scaling above a certain ratio between the Kolmogorov length-scale and the particle length (~ 10) (Parsa and Voth, 2014; Oehmke et al., 2021). Interestingly, we report a good agreement with the previous studies, as the simulated tracer-like stiff and stiff-less fibres fall near the experiments with the shortest particles for all the different lengths. It is clear that we are limited by the anisotropy of the turbulent channel flow in considering longer fibres, being the most slender chains ($L_0^+ = 71.62$) already comparable to one-tenth of the total height of the computational domain (600 wall units). In all of this, the bending stiffness does not have a remarkable influence on the short and intermediate chains of rods, while a discrepancy is highlighted for the long flexible fibres, which rotate faster when more flexible. Instead, particle inertia appears to filter turbulent fluctuations, determining a lower mean squared tumbling rate (blue and pink dots). This is in qualitative agreement with the previous HIT experiments by Bounoua et al., 2018 and suggests that despite not modelling inertial effects on the flow-particle torque coupling, an inertial rod-chain representation still recovers a filtered rotational behaviour.

Encouraged by this preliminary agreement between our results and the data available in the literature, we now consider the probability distribution of the squared tumbling rate events in figure 3.18, normalising them by their mean value. Again, we separate fibres whose centre of mass lies within 30 wall units from the half-height of the flow in panel (a) or the two walls in panel (b). An amicable agreement is found between all the considered fibres in the bulk of the turbulent channel flow and those recorded in the HIT experiments by Parsa and Voth, 2014, showing a weak dependence of the tumbling rate events from the fibre length and aspect ratio.

Parsa and Voth, 2014 reported narrower tails for the longest fibres (black solid and empty exes), suggesting that the particle length influences the tumbling rate in the same way that the diameter of large spherical particles affects their acceleration statistics (Volk et al., 2011), suppressing their otherwise highly intermittent nature
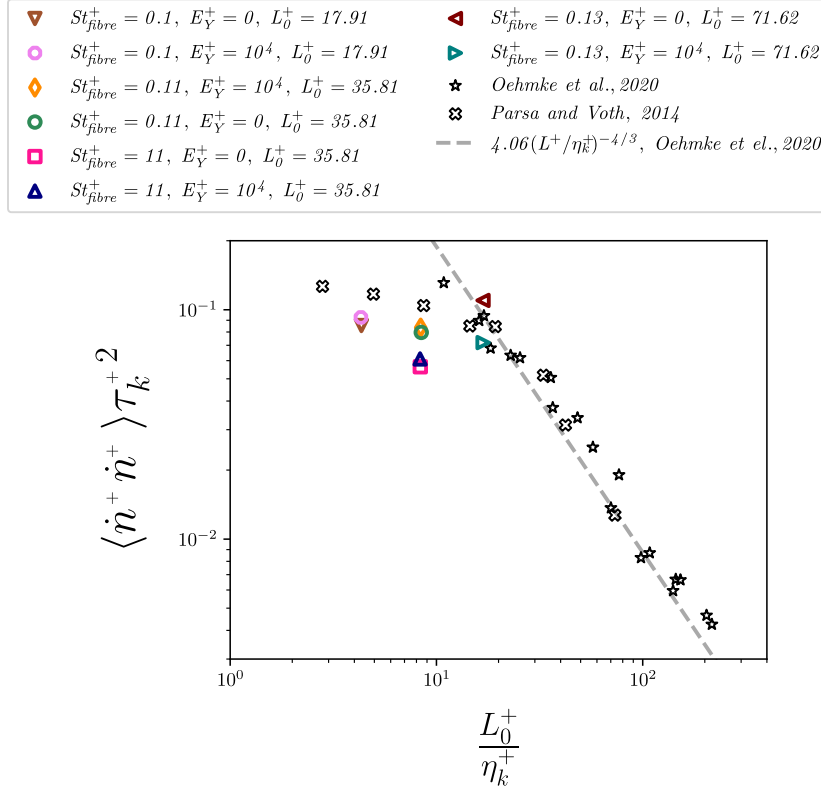
Figure 3.17. – Dimensionless mean squared tumbling rate against the dimensionless normalized fibre length. Averages are calculated on a ~ 30 wall units thick slab around the half-height of the turbulent channel flow.

(La Porta et al., 2001). Despite we did not consider long enough fibres to compare our results to those of Parsa and Voth, 2014, our simulations reveal an influence of particle inertia on the tails of the tumbling rate p.d.f.s. This effect is not remarkable in the bulk of the flow (panel (a) of figure 3.18), where the inertial fibres experience a weak suppression of extreme tumbling rate events. Considering fibres near the walls (panel (b) of figure 3.18), the local shear lifts the tails of the distributions, in qualitative agreement with the experiments of Alipour, De Paoli, Ghaemi, et al., 2021. As a consequence, the influence of inertia becomes clear for stiff (blue triangles) but especially stiff-less (pink squares) fibres, who see a strong shrinkage of their probability distributions. Extending the similitude between tumbling rate of fibres and acceleration of spheres, this effect is in agreement with what observed numerically for sub-Kolmogorov spheres in turbulent channel flow Zamansky et al., 2011.

Finally, we look at the dimensionless mean squared tumbling rate against the wall-normal coordinate z^+ in figure 3.19, averaging over the two half-widths of the domain according to the position of the centre of mass of the fibres. The first important result is that, in agreement with previous experiments by Shaik et al., 2020; Alipour, De Paoli, and Soldati, 2022, the tumbling rate increase as we move from the bulk of the flow to the walls for all the observed fibres. This is coherent with the previous trends for the

▽	$St^+_{fibre} = 0.1$, $E^+_Y = 0$, $L^+_0 = 4.32\eta^+_k$	◁	$St^+_{fibre} = 0.13$, $E^+_Y = 0$, $L^+_0 = 16.82\eta^+_k$
○	$St^+_{fibre} = 0.1$, $E^+_Y = 10^4$, $L^+_0 = 4.33\eta^+_k$	▷	$St^+_{fibre} = 0.13$, $E^+_Y = 10^4$, $L^+_0 = 16.83\eta^+_k$
○	$St^+_{fibre} = 0.11$, $E^+_Y = 0$, $L^+_0 = 8.44\eta^+_k$	★	*Parsa & Voth, 2014, $L = 2.8\eta$*
◇	$St^+_{fibre} = 0.11$, $E^+_Y = 10^4$, $L^+_0 = 8.38\eta^+_k$	✚	*Parsa & Voth, 2014, $L = 4.9\eta$*
☐	$St^+_{fibre} = 11$, $E^+_Y = 0$, $L^+_0 = 8.35\eta^+_k$	✖	*Parsa & Voth, 2014, $L = 32.8\eta$*
△	$St^+_{fibre} = 11$, $E^+_Y = 10^4$, $L^+_0 = 8.32\eta^+_k$	�	*Parsa & Voth, 2014, $L = 42.4\eta$*
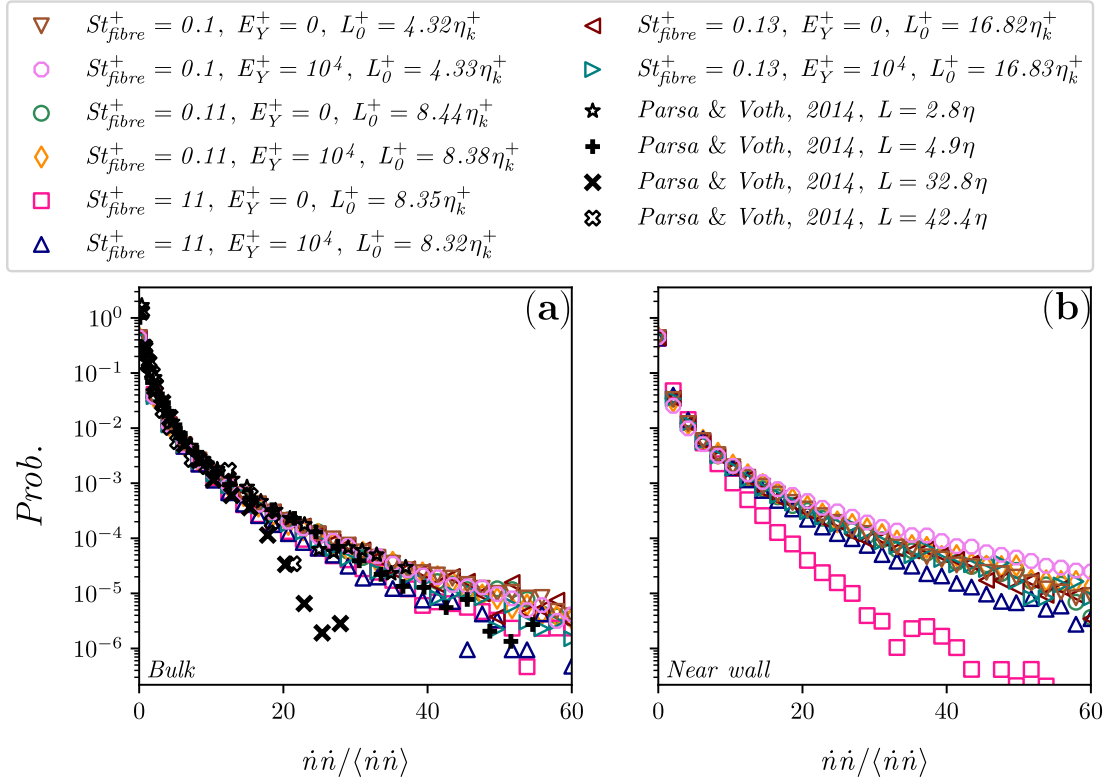
Figure 3.18. – Probability distribution of the squared tumbling rate normalized by its mean value. Panels: (a) particles whose centre of mass lies in a flow slab 60 wall units thick around the half-height of the channel; (b) particles whose centre of mass lies inside 30 wall units from one of the two walls. The length of the fibres is normalized by the Kolmogorov length scale of the corresponding two-way coupled simulation, calculated at the half-height of the channel. Therefore, slight variations are to be expected.

fibres' orientations, which showed that the slender particles lose their alignment with the local vorticity as they move from the bulk of the flow to the near-wall region. In the latter, the local shear determines span-wise mean vorticity, which will definitely contribute to the tumbling rate of the flow-aligned fibres, in a Jeffery-like scenario Marchioli, Fantoni, et al., 2010.

Shaik et al., 2020 observed that fibre's length determines higher tumbling rates, as longer particles interact with more energetic turbulent eddies. Nevertheless, our calculations do not report a remarkable influence of L^+_0 over the observed tumbling rates. On the other hand, we appreciate a more important effect of the bending stiffness as the fibres become longer. Indeed, just a slightly stronger tumbling rate is observed for completely flexible fibres in the viscous sub-layer at short and intermediate lengths (panels (a) and (b)). Instead, in panel (c) long stiff-less chains will tumble more than their stiff twins just to reach a plateau below ~ 20 wall units, where the latter take over.

The filtering effect of particle inertia on the tumbling rate is confirmed in panel (b)
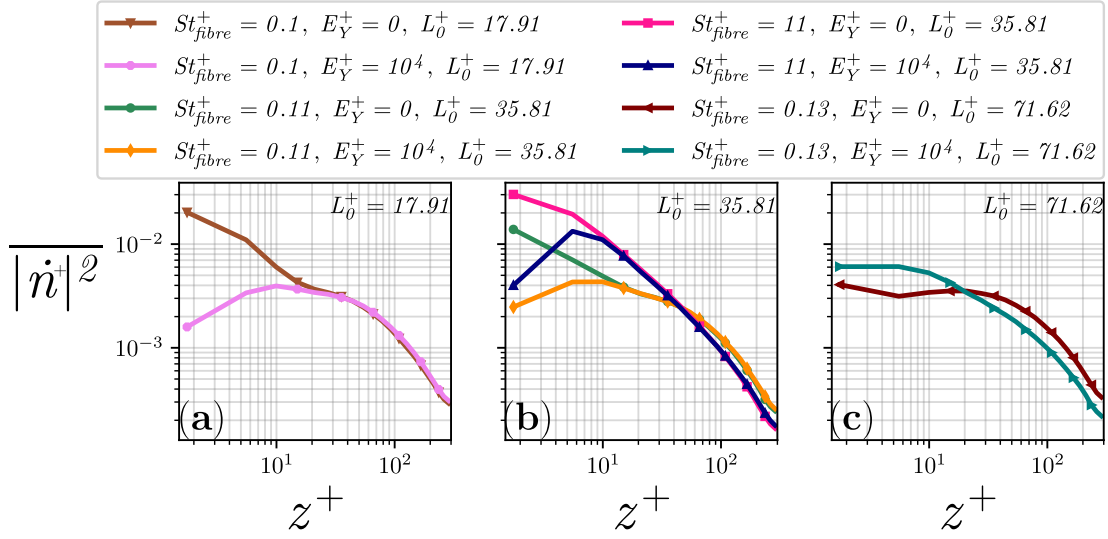
Figure 3.19. – Dimensionless mean squared tumbling rate against the wall-normal coordinate z^+. Panels: (a) tracer-like short fibres; (b) tracer-like and inertial intermediate fibres; (c) tracer-like long fibres.

of figure 3.19, where tracer-like and inertial, stiff and stiff-less fibres are compared at fixed particle geometry. It is possible to appreciate a reduced tumbling rate across the whole outer region of the turbulent channel flow ($50 < z^+ < 2Re_\tau - 50$) for the much denser particles. On the other hand, inertial particles near the wall will tumble more than the tracer-like fibres, and this is possibly due to the preferential sampling that the former display in this region. A zero Young's modulus seems to steam this effect in the viscous sub-layer for short and intermediate particles. Nevertheless, given the remarkable particle size, geometrical effects most probably play a relevant role in this section of the flow.

In conclusion, we have looked at the tumbling rate of flexible fibres in wall turbulence, to obtain some insight into the way these particles re-orient in response to the local strain and vorticity. The tumbling rate of the simulated chains in the bulk of the flow is comparable to previous experiments with rigid fibres in HIT (Parsa and Voth, 2014; Oehmke et al., 2021). Moving to the walls, the mean squared tumbling rate increases, in agreement with previous numerical and experimental studies Shaik et al., 2020; Alipour, De Paoli, and Soldati, 2022. This is consistent with the previous considerations on the particles' orientation within the flow in section 3.8.3: near the solid boundaries, fibres align with the mean flow but, as the local shear determines a strong vorticity along the span-wise direction, this will directly contribute to the rotation of the particles.
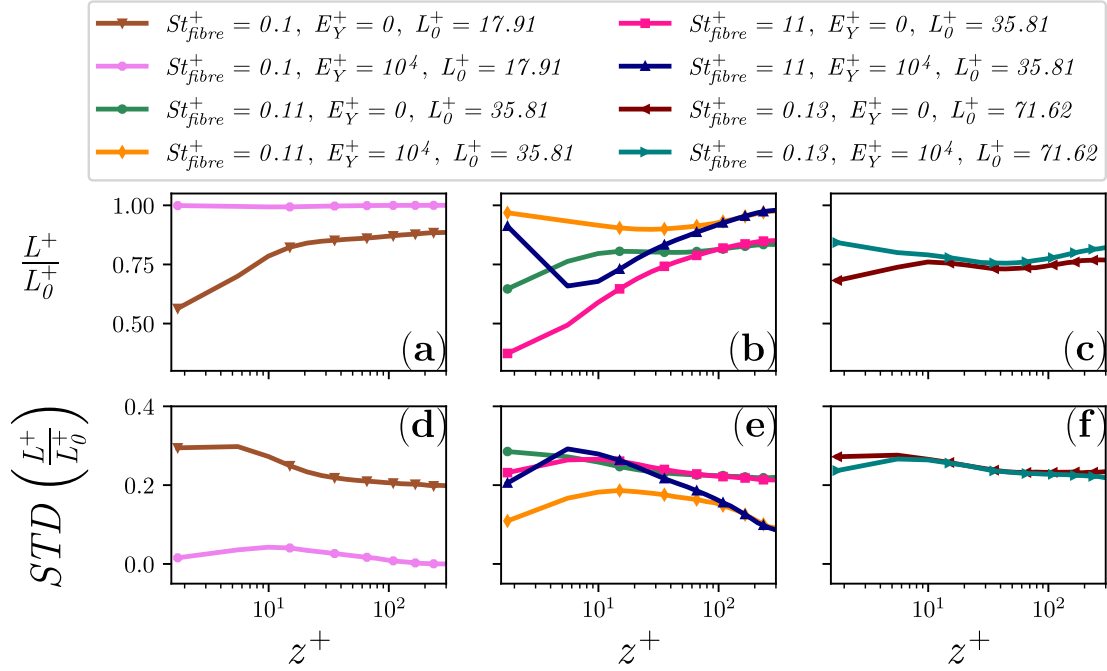
Figure 3.20. – Normalized effective end-to-end distance against the wall-normal coordinate z^+ for increasing fibre length from left to right. Data are sorted according to the wall-normal position of the centre of mass of each fibre and averaged over the full width, length and the two half-heights of the turbulent channel flow. Panels: (a) and (d) mean and standard deviation for stiff and stiff-less short tracer-like fibres; (b) and (e) mean and standard deviation for stiff and stiff-less intermediate tracer-like and inertial fibres; (c) and (f) mean and standard deviation for stiff and stiff-less long tracer-like fibres.

3.8.5. Deformation of fibres in turbulence

3.8.5.1. Classification of the deformed shapes

We now complete our study by evaluating the particle deformation within the turbulent channel flow. We start by looking at the normalised effective end-to-end distance L^+/L_0^+ of the fibres against the wall-normal position of their centre of mass in figure 3.20, again averaging over the two half-widths of the domain. Mean values are displayed in the top panels while its standard deviations are shown in the bottom panels, and the fibres' length is increasing from left to right.

Figure 3.20 highlights a clear dependence of the effective end-to-end distance L^+/L_0^+ on the fibres' bending stiffness and the fibres' total length L_0^+. As a matter of fact, short stiff fibres will always be stretched, while their stiff-less twins will deform across the whole channel, as their effective length rapidly decreases in the buffer layer (panel (a)). This picture holds for stiff and stiff-less tracer-like fibres at intermediate particle length (panel (b)), despite the latter being, on average, never completely stretched

but actually showing a non-monotone trend with a minimum just below the end of the outer layer. A clear difference is appreciable for the longest tracer-like fibres, as both stiff and stiff-less chains display a similar plateau at approximately $L/L_0 \sim 0.75$ in the bulk of the flow (panel (c)). This suggests that the particle bending stiffness is ineffective for very long chains.

The influence of particle inertia is also considered for the intermediate particle length in panel (b). Here, we can appreciate the fact that effective length in the bulk of the flow depends only on the bending stiffness of the chains, and not on the inertial nature of the chains. Instead, inertial effects consistently determine a lower end-to-end distance as these particles approach the wall, where their influence is remarkable below ~ 100 wall units. A comment is in order about the magnitude of the calculated standard deviations, which seem to include the fully stretched configuration practically everywhere.

The effective end-to-end distance is an intuitive observable that effectively describes the deformation of the flexible fibres within the flow. Even so, another parameter must be taken into account in order to completely classify all the possible shapes that the chains of rods can express when stretched and compressed by turbulence. Previous studies considered the mean curvature of the fibres (Allende et al., 2018). Given the discrete nature of our fibres, we find it natural to look at the radius of gyration, defined as the root mean squared distance between the rod elements and the centre of mass of the fibres (Brouzet et al., 2014):

$$\frac{R_g^+}{R_{g,0}^+} = \frac{\sqrt{\left(\sum_{i=1}^{N}(\mathbf{p}_i - \mathbf{p}_{cm})^2\right)/N}}{R_{g,0}^+} \, , \tag{3.45}$$

where the $R_{g,0}^+$ corresponds to a fully stretched chain and $R_g^+ = 0$ to a fully compressed chain, for which all rods lie on the same spot.

By combining the effective end-to-end distance and the radius of gyrations, a complete classification of the deformation of our fibres is possible. This is displayed in figure 3.21, where the bi-variate probability distribution of these two quantities is displayed for short (panels (a),(b),(e) and (f)) and long (panels (c),(d),(g) and (h)) tracer-like fibres near the wall (top panels) and in the bulk (bottom panels) of the turbulent channel flow. Moreover, meaningful values of the two-dimensional parameter space are explored by visualizing the corresponding particles in the small grey inserts, to provide a qualitative visualization of the possible configurations.

The first striking observation is that the most probable fibre configuration (blue colour) is the fully stretched one across all panels, no matter the particle length or bending stiffness. This is in qualitative agreement with what was observed by Picardo et al., 2020 for chains of beads in three-dimensional turbulence. Considering the mean values that were previously discussed in figure 3.20, we now understand that the probability distributions must be particularly skewed, as clearly suggested by the colours. More in detail, short stiff particles near the walls (panel (b)) and especially in the bulk (panel (f)) do not almost bend, whereas the same stiff-less shapes (panels

Figure 3.21. – Bi-variate probability of the normalized effective end-to-end distance and radius of gyration of the fibres. "Near wall" top panels: $p_{z,cm}^+ <$ 30 *or* $p_{z,cm}^+ > 2Re_\tau - 30$; "Bulk" bottom panels: $Re_\tau - 30 < p_{z,cm}^+ < Re_\tau + 30$. Panels: (a) Stiff-less tracer-like short fibres; (b) Stiff tracer-like short fibres; (c) Stiff-less tracer-like long fibres; (d) Stiff tracer-like long fibres; (e) Stiff-less tracer-like short fibres; (f) Stiff tracer-like short fibres; (g) Stiff-less tracer-like long fibres; (h) Stiff tracer-like long fibres. For each panel, one fibre is visualized in the small insert, whose shape corresponds to the black dot in the bi-variate space. For visualization purposes, fibres are not in scale.

(a) and (e)) can reach a wide variety of shapes, particularly when close to the solid boundaries.

From the dimensional analysis in Section 3.5 we know that the importance of elasticity $\mathbb{B} >> 1$ increases with the particle aspect ratio r_{tot} at an imposed Young's modulus E_Y^+. Therefore, we are not surprised to observe a lower influence of the bending stiffness as longer chains are considered, at the point that stiff and stiff-less long fibres cover a similar probability space, both near the walls (panels (c) and (d)) and in the bulk (panels (g) and (h)). This is also highlighted by the stark contrast between short and long stiff fibres, both near the walls (panels (b) and (d)) or in the bulk of the flow (panels (f) and (h)). These differences are slightly less important when comparing short and long stiff-less chains.

More insight into the deformation of the particles and the influence of the bending stiffness is given by looking at the rendered fibres in the grey inserts. For high values of effective end-to-end distance and radius of gyration, the particle conserves an almost straight shape (panel (f)). As the two quantities decrease, two main deformation

patterns appear, depending on their relative intensity with regard to the constraints of the particle geometry. If L^+/L_0^+ is much lower than $R_g^+/R_{g,0}^+$, fibres are bending like an eyelash, adopting a regular curvature while their extremities almost touch. This is more and more visible for both particle lengths moving from panel (b) to (c) (d) and finally (a), and corresponds to a yellow region of moderate probability clearly discernible in panels (a), (c), (d), (e), (g) and (h). On the other hand, if we move along the $L^+/L_0^+ \simeq R_g^+/R_{g,0}^+$ diagonal, fibres are being compressed along their axis. Therefore, either extreme curvatures are possible, like in panel (h) where the fibre is drawing a knot, or a teeth-saw configuration emerges, like in panel (g). Nevertheless, moving down to the left bottom of the bi-variate space, the chains of the rod will eventually collapse on themselves in an extremely buckled state (panel (e)).

Having classified the two main deformation patterns, we now understand that a finite bending stiffness suppresses the possibility of buckling along the chains' axis. Instead, the considered fibres will always bend like eyelashes, especially the longer tracer-like chains, whereas the shorter ones in the bulk of the flow can eventually maintain a straight shape. Nevertheless, deformed configurations are more rare than what is suggested by the mean values of the effective length in figure 3.20.

Finally, we evaluate the influence of inertia on the deformation of fibres, considering stiff and stiff-less, tracer-like and inertial chains at fixed particle length $L^+ = 35.81$ in figure 3.22, where the top and bottom panels display particles near the wall and in the bulk of the flow. Again, the most important finding is that the stretched configuration is the most probable shape for all the considered parameters. A finite bending stiffness suppresses the compression of the chains (panels (b), (f), (d) and (h)), allowing mostly for a regular eyelash-like bending. Instead, particle inertia is positively influencing the deformation, especially for stiff-less particles in the near-wall region (panel (c)). On the other hand, its importance in the bulk of the flow appears less relevant, as it emerges by comparing stiff-less (panels (e) and (g)) or stiff chains (panels (f) and (h)).

3.8.5.2. Characteristic deformation time

As we have seen, stiff and stiff-less fibres in wall turbulence seem to privilege a stretched configuration. Anyway, the presented statistics describe the steady state conformation of the particles. A natural question arises at this point, concerning the dynamics of the deformations: are we able to measure it and what is its characteristic time scale? Looking for its answer, we produce a dedicated data set for each of the considered simulations, with a particularly small sampling time of $0.75t^+$, which correspond to one-third of Kolmogorov time-scale at the wall, i.e. the smallest time-scale of the turbulent channel flow. In this way, finely resolved time-series of the fibres' dynamics are produced over a short window of $300t^+$, especially keeping track of their effective length L^+/L_0^+ and their tumbling rate $|\dot{n}|$. For the sake of simplicity, we will only consider tracer-like fibres, focusing on the influence of the particle length and the bending stiffness.

Inspired by the work of Allende et al., 2018, we define deformations events as the time span over which the effective end-to-end distance of the fibre is lower than 0.95.
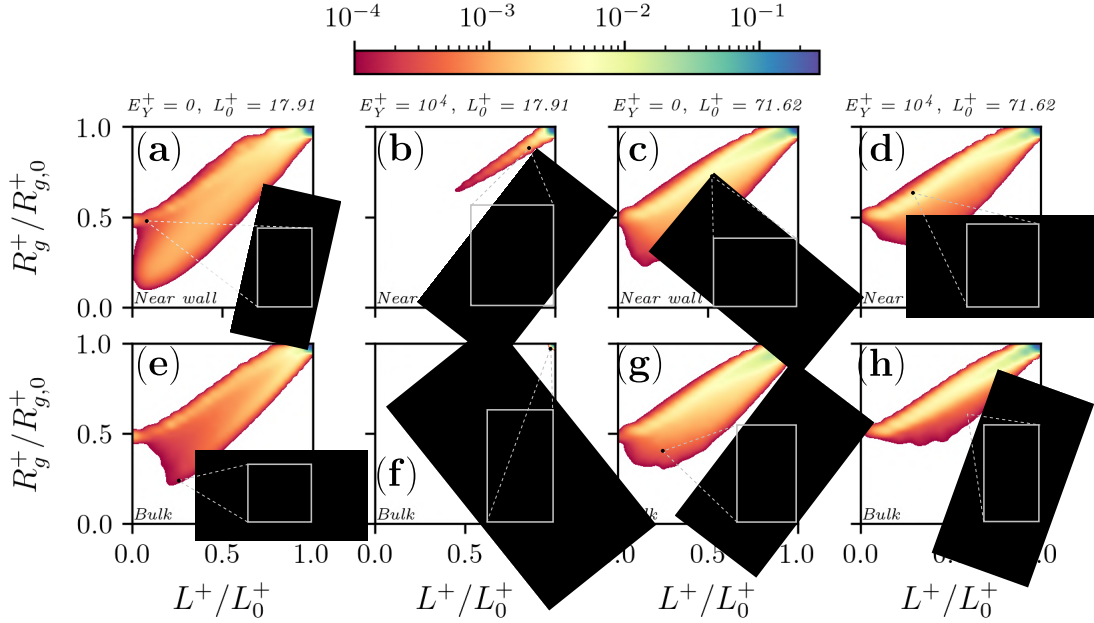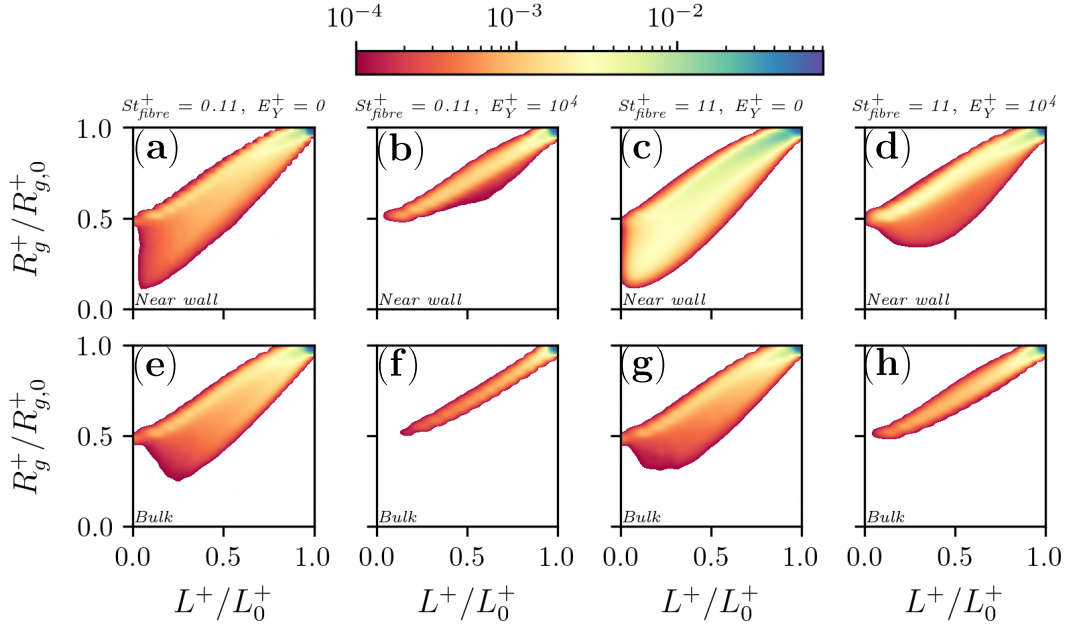
Figure 3.22. – Bi-variate probability of the normalized effective end-to-end distance and radius of gyration of fibres with total length $L^+ = 35.81$. "Near wall" top panels: $p^+_{z,cm} < 30$ *or* $p^+_{z,cm} > 2Re_\tau - 30$; "Bulk" bottom panels: $Re_\tau - 30 < p^+_{z,cm} < Re_\tau + 30$. Panels: (a) Stiff-less tracer-like fibres; (b) Stiff tracer-like fibres; (c) Stiff-less inertial fibres; (d) Stiff inertial fibres; (e) Stiff-less tracer-like fibres; (f) Stiff tracer-like fibres; (g) Stiff-less inertial fibres; (h) Stiff inertial fibres.

Not only do we measure the duration of the deformation events, but also we calculate their mean position, in order to segregate them accordingly within the turbulent channel flow. In addition, we keep track of their mean tumbling rate while the fibre is buckling. Indeed, this observable can be interpreted as the typical time-scale ($[|\dot{n}|] = 1/s$) of the rotation of the fibres. As displayed in figure 3.23 for stiff and stiff-les tracer-like fibres at intermediate particle length, this time-scale (symbols) does not correspond to the eddy turnover time evaluated at the fibre scale ($T_l = L_0^{2/3}\epsilon^{-1/3}$ (blue solid line)), where ϵ is the dissipation rate of turbulent kinetic energy. Anyway, it is also much longer than the Kolmogorov time scale (black dashed line), corresponding more to the time scale of a non-dissipating structure within the turbulent flow. Clearly, as we had already seen in figure 3.19, no remarkable difference is appreciable between stiff and stiff-less fibres at intermediate length away from the near-wall region.

Therefore, we decide to normalise the time span of the deformation events by the time scale identified by the mean tumbling rate recorded during each event. Given the remarkable size of our particles and the anisotropy of the turbulent channel flow, we reckon that this is an optimal solution, naturally taking into account the non-local nature of the flow around each chain of rods. This would have hardly been the case had we chosen to perform our analysis in dependence on the dissipation
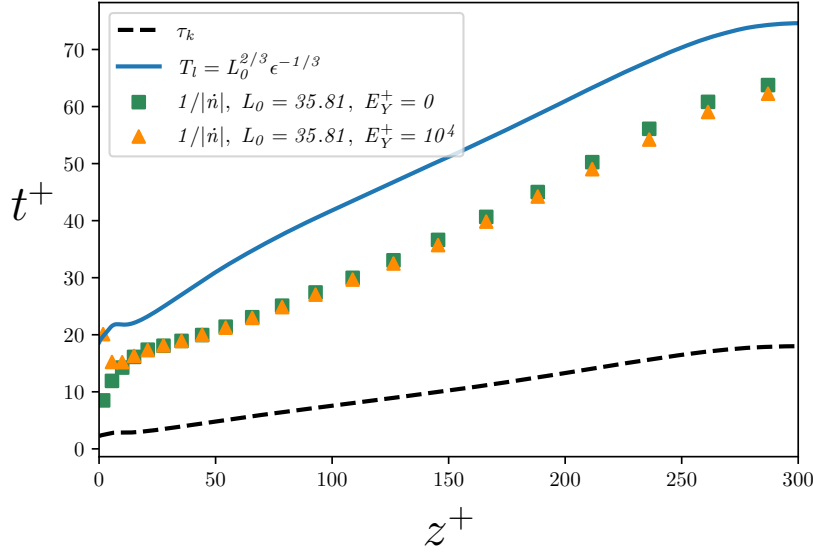
Figure 3.23. – Characteristic times-scales of a fibre-laden turbulent channel flow against the wall-normal coordinate z^+. Black dashed line: Kolmogorov time-scale; Blue solid line: turnover time of eddies of size equal to that of the fibres; Symbols: characteristic rotation time-scale, calculated as the inverse of the mean tumbling rate. We consider only stiff (orange triangles) and stiff-less (green squares) tracer-like fibres at intermediate lengths.

rate, using either the eddies turnover time or the Kolmogorov time scale. The results of these calculations are displayed in figure 3.24, where we look at the probability distribution of the normalised time duration of the deformation events (calculated by a Gaussian kernel density estimation by means of the gaussian_kde subroutine of the Scipy Python Library).

The first striking result is that the p.d.f.s of the normalised deformation time indicate a highly concentrated distribution of probability. This is clear for stiff-less and stiff chains of all lengths in the bulk of the flow (panels (c) and (d). Near the walls, the action of the mean shear seems to combine with the particle length to determine wider tails for the distributions (panels (a) and (b)). Nevertheless, short chains with finite bending stiffness(pink hexagons) display the same behaviour as what observed in the bulk of the flow.

In figure 3.24 we also show that the distribution of data is well approximated by a Gamma distribution (solid black line) with the following probability distribution function:

$$p.d.f.\left(\gamma\ dist.\right) = \frac{t^{\alpha-1}e^{-\beta t}\beta^\alpha}{(\alpha-1)!}\ . \tag{3.46}$$

where we fit the two shape parameter α and β over the measured distributions for the longest fibres ($L_0^+ = 71.62$). Estimations for the shape parameter α and the rate
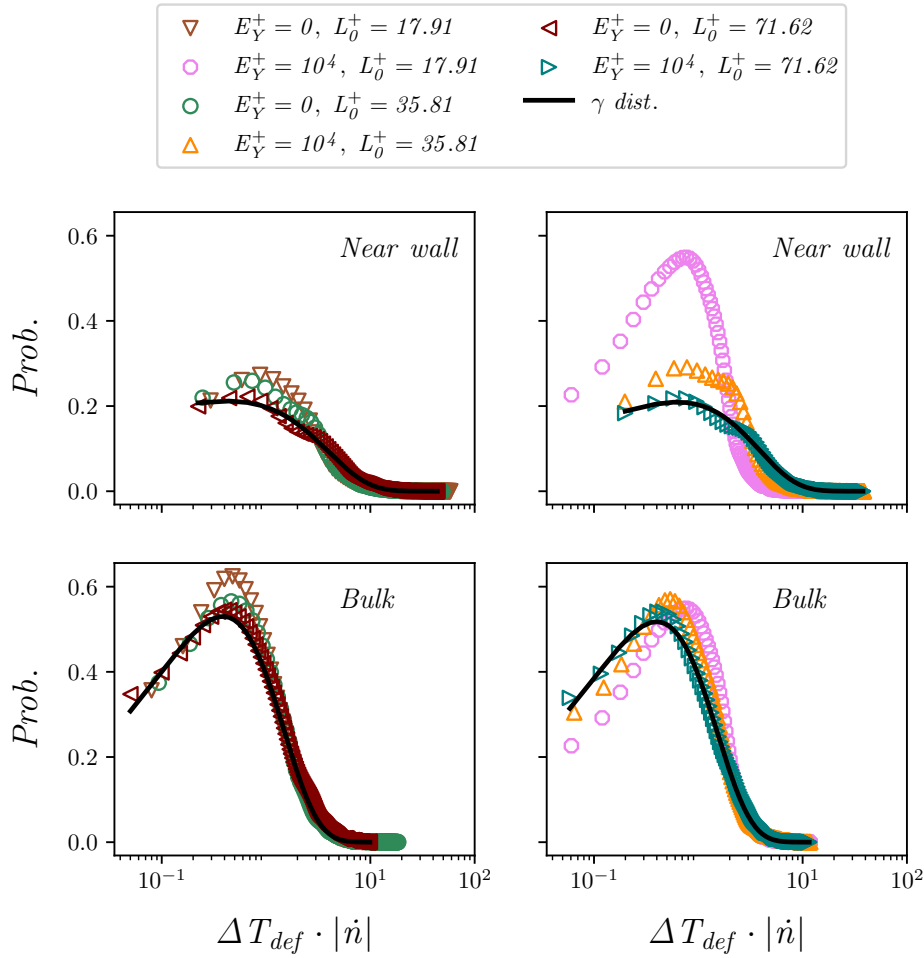
Figure 3.24. – P.d.f. of the deformation time normalized by the fibres rotational time-scale, calculated as the inverse of the mean tumbling rate during the corresponding deformation events. Panels: (a) Stiff-less tracer-like fibres of all lengths near the wall; (b) Stiff tracer-like fibres of all lengths near the wall; (c) Stiff-less tracer-like fibres of all lengths in the bulk; (d) Stiff tracer-like fibres of all lengths in the bulk.

parameter β set their value to ~ 1.5 and ~ 1.2 for both curves in the bulk of the channel (panes (c) and (d)), whereas the same estimations lead to $\alpha \sim 1.2$ and $\beta \sim 0.3$ in the near-wall region (panels (a) and (b)). These values confirm the concentration of data, especially in the bulk region, when compared to the typical shape parameter of a normal distribution, that is recovered for $\alpha > 100$ (Thom, 1958).

Hence, from figure 3.24 we are seeing that the deformation time that typically expires before a fibre reaches a stretched configuration is a fraction of the characteristic rotational time-scale of these particles in a turbulent channel flow. This is also confirmed by the small values of the fitted rate parameters β, which allows us to conclude what already guessed from the bi-variate probability plots of the deformed shapes
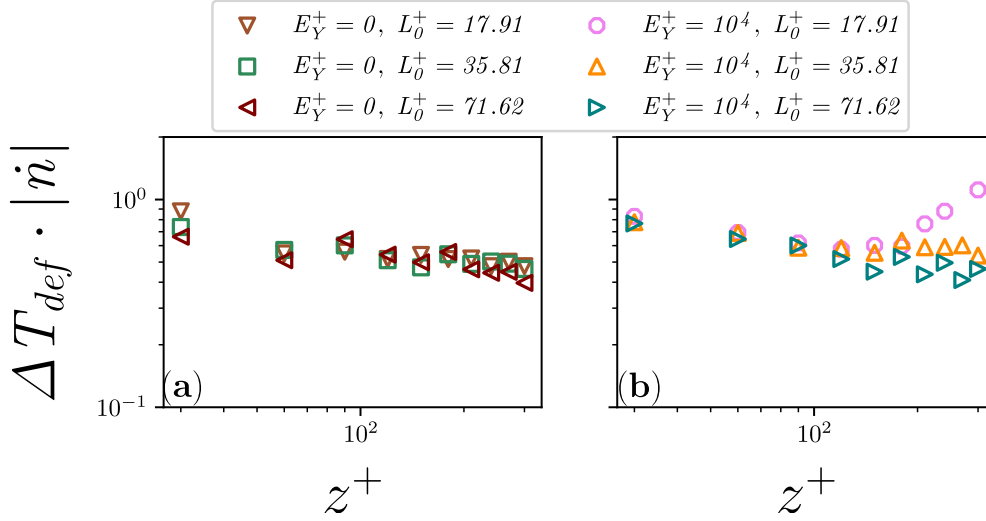
Figure 3.25. – Normalized characteristic time of deformation against the wall-normal coordinate z^+. Panels: (a) stiff-less tracers; (b) stiff tracers.

(figures 3.21 and 3.22): long flexible fibres in turbulence tend to a stretched configuration and deform for a short amount of time, which we are now able to estimate to a fraction of their characteristic rotation time. Our data suggest that the typical deformation time of long fibres in the bulk of the flow can be modelled according to a Gamma distribution. An interesting property of this kind of distribution is that it is not memory-less, i.e. the probability of a fibre leaving its buckled state decreases with the time the fibres has already spent in such configuration.

To conclude the discussion, we consider the scaling of the normalised deformation time against the wall-normal coordinate of the turbulent channel flow. This is returned by the most probable value of the p.d.f. of the deformation time, calculated by separating the fibres according to the mean wall-normal position during the deformation events, into 20 slabs of thickness 30 w.u. that completely span the wall-to-wall distance. Also, averages over the two half-heights are calculated.

The results of these calculations are displayed in figure 3.25 for stiff-less (panel (a)) and stiff (panel (b)) tracer-like fibres at all particle lengths. All curves collapse indicating that the deformation time is a fraction of the characteristic rotation time of the fibres independently from the considered particle length, except for the short stiff tracer-like chains (pink hexagons). Moreover, this seems to moderately increase from the bulk (~ 0.5) to the wall (~ 0.8), and such scaling holds for all the stiff-less chains as well as for the intermediate and long stiff fibres (yellow and green triangles of the panel (b)). This indicates that the deformation time corresponds on average to a temporal scale relatable to a small turbulent structure, between 2 and 3 times the Kolmogorov scales from the bulk to the wall of the turbulent channel flow. Therefore, we speculate that the long deformed fibres suspended in wall turbulence are stretched by turbulent structures with a short characteristic time-scale.

3.8.6. Turbulence modulation

Several simulations are conducted to study turbulence modulation by long and slender fibres, as reported in table 3.2. Calculations are performed at two shear Reynolds number of $Re_\tau = 150$ and $Re_\tau = 300$. The second value has the advantage of offering a wide ratio of scales in the turbulent channel flow, but it also implies an eight times larger domain, greatly increasing the computational load that is required to simulate a sufficient number of rods and attain remarkable volume fractions. Nevertheless, we focus on tracer-like and inertial stiff fibres of intermediate length ($L_0^+ = 35.81$, $r_{tot} = 100$) at volume fraction $\Phi \in [0.0001; 0.001]$ (runs A,B,C and D of table 3.2).

Anyway, to simulate more slender particles, we decrease the domain size by imposing a lower shear Reynolds number $Re_\tau = 150$. Doing so, we are able to explore turbulence modulation by more slender particles, exploring the influence of particle inertia at a twice as slender particle aspect ratio ($r_{tot} = 200$, runs E,F,G and H of table 3.2) and in the case of extremely slender chains of rods ($r_{tot} = 1000$, runs I,L,M and N of table 3.2). These simulations are performed on a computational grid made of $n_x = 1024 \times n_y = 512 \times n_z = 257$ points. This allows to set the dimensionless regularisation length-scale required by the ERPP method to $\sigma_R^+ = 1.8$, which gives a ratio $\sigma_R^+/dx^+ = \sigma_R^+/dy^+ \simeq \sigma_R^+/dz_{max}^+ = 1.02$, where d_i represents the grid spacing for the i_{th} direction. Eventually, this produces a delayed time-scale $\epsilon_R^+ = 108 \cdot dt^+ = 108 \cdot 1.5 \cdot 10^{-2} = 1.62$ wall time units. Then, fibres are modelled as chains of 40 rod elements with aspect ratio $r = 5$ and length $2\ell = 1.2$ in runs E,F,G and H, and as chains of 20 elements with $r = 50$ and length $2\ell = 1.8$ in runs I,L,M and N. A comment is order about the imposed density ratios, which can reach the extreme value of $\rho^+ = 3000$ in runs M and N. Despite one might argue about the realism of these simulations in which, by the way, gravitational forces are neglected, we find it interesting to push the exploration of the parameter space to its limits in order to appreciate the strongest possible influence of the mass loading on turbulence.

Before looking into the qualitative phenomenology of turbulence modulation, we appreciate that all simulations show a slight modification of the flow rate, which is calculated as following:

$$\Delta Q = \frac{Q_L - Q_U}{Q_U} \times 100 \,, \tag{3.47}$$

where Q is the flow-rate of the turbulent channel flow for the laden cases (L subscript) and unladen reference simulation (U subscript), calculated as the numerical integral of the dimensionless stream-wise velocity over the half-height of the channel. The modified flow-rates are displayed in the last column of table 3.2. In general, we do not appreciate a strong increment for the simulations at shear Reynolds $Re_\tau = 300$, where fibres with aspect ratio $r_{tot} = 100$ were considered (runs A,B,C and D). Instead, more slender chains ($r_{tot} = 200$, runs E,F,G and H) at shear Reynolds number $Re_{\tau=150}$ consistently display stronger variations of flow rate, both positive and negative, which become even more relevant when considering the most slender particles at the highest particle concentration ($r_{tot} = 1000$, runs I,L,K and N).

In the following, we are going to look into flow statistics to gather insights into the

run	Re_τ	St_{fibre} (ρ^+)	E_Y^+	r_{tot}	L^+	V_{frac}	$M_{frac}\%$	$\Delta Q\%$
A	300	0.11 (3)	10^4	100	35.81	0.0001	0.03	0.49
B	300	0.11 (3)	10^4	100	35.81	0.001	0.3	1.06
C	300	11 (300)	10^4	100	35.81	0.0001	3.2	-1.4
D	300	11 (300)	10^4	100	35.81	0.001	32.0	0.21
E	150	0.03 (1.3)	10^4	200	48.65	0.00002	0.003	1.76
F	150	0.03 (1.3)	10^4	200	48.65	0.0002	0.03	2.34
G	150	25 (1300)	10^4	200	48.65	0.00002	2.7	-1.76
H	150	25 (1300)	10^4	200	48.65	0.0002	27	1.68
I	150	0.2 (300)	0	1000	36.09	0.012	1	2.54
L	150	0.2 (300)	10^4	1000	36.09	0.012	1	4.09
M	150	2 (3000)	0	1000	36.09	0.012	10	-0.51
N	150	2 (3000)	10^4	1000	36.09	0.012	10	-0.25

Table 3.2. – Report of the considered simulations at shear Reynolds $Re_\tau = 150$ and $Re_\tau = 300$ with tracer-like and inertial, stiff and stiff-less fibres with different particle aspect ratios, total particle lengths, volume fractions and mass loads. The percentage flow rate increase is also displayed in the last column, calculated as in equation 3.47. Quantities are made dimensionless and presented in wall units. The Stokes number of each fibre is calculated in its fully stretched equilibrium configuration.

mechanism behind turbulence modulation by long fibres. First, we will focus on the runs E,F,G and H of table 3.2 at shear Reynolds $Re_\tau = 150$, discussing the modification of the first and second statistic moments of the flow as well as of its axial momentum balance. Finally, the non-Newtonian nature of the stresses induced by the fibres within the flow will be addressed. Then, we will switch to the runs A,B,C and D of table 3.2 to appreciate the multi-scale nature of the interaction between fibres and turbulence at a higher shear Reynolds number $Re_\tau = 300$. In the end, we will consider the runs I,L,M and N of table 3.2 with the most slender particles ($r_{tot} = 1000$), to discuss the influence of the carried phase on the turbulent kinetic energy budget and the mechanism behind drag reduction. Despite switching between data-sets, we believe that this is the most meaningful and insightful way to present our results, as we will focus on the best features that each simulation has to offer. This also underlines the consistency of the proposed numerical methodology, which gave coherent results at different shear Reynolds number and for multiple particle geometries.

3.8.6.1. Flow Visualization

A visual rendering of the modification of turbulence due to the presence of the fibres is provided in figures 3.26–3.29, each referring to a different simulation carried out in this study. For each figure, the Eulerian grid is horizontally cut at $z^+ = 10$ from the wall and the resulting slice is coloured according to the local value of the stream-wise fluid velocity. Fibres located within a distance of 20 wall units above the slice are also

Figure 3.26. – Top view of the stream-wise fluid velocity streaks in the near-wall region ($z^+ = 10$) and instantaneous fibre distribution. Reference simulation: run E, $St^+_{fibre} = 0.03, \rho^+ = 1.3, \Phi = 2.12 \cdot 10^{-5}$.

Figure 3.27. – Top view of the stream-wise fluid velocity streaks in the near-wall region ($z^+ = 10$) and instantaneous fibre distribution. Reference simulation: run G, $St^+_{fibre} = 25, \rho^+ = 1300, \Phi = 2.12 \cdot 10^{-5}$.

rendered. The actual fibre length is shown, whereas the fibre diameter is magnified by a factor of five for visualisation purposes.

The two cases at lower volume fraction (runs E and G), shown in figure 3.26 for the $St^+_{fibre} = 0.03$ fibres and in figure 3.27 for the $St^+_{fibre} = 25$ fibres respectively, already show some modification in the spatial distribution of the velocity streaks. These appear to be somehow weaker and characterised by a smoothing of the velocity field. Also, fibres seem to align along low speed streaks, in agreement with previous numerical studies (Dotto and Marchioli, 2019), but in disagreement with the experiments of Shaik et al., 2020.

As could be expected, the near-wall flow field modifications appear to be more

Figure 3.28. – Top view of the stream-wise fluid velocity streaks in the near-wall region ($z^+ = 10$) and instantaneous fibre distribution. Reference simulation: run H, $St^+_{fibre} = 0.03, \rho^+ = 1.3, \Phi = 2.12 \cdot 10^{-4}$.

evident at the higher volume fraction, as shown in figure 3.28 for the $St^+_{fibre} = 0.03$ (run F) fibres and in figure 3.29 for the $St^+_{fibre} = 25$ fibres (run H) respectively. The velocity streaks appear more regular and the spacing between them seems to increase, especially in the case of fibres with higher inertia, in accordance with numerical simulations of turbulence modulation by sub-Kolmogorov spheroids (Z. Wang et al., 2021). From a qualitative point of view, it can be observed again that fibres exhibit a preferential alignment in the low-speed streaks. This is especially visible in the case of inertial fibres, which are able to accumulate more efficiently than tracer-like fibres in the near-wall region by virtue of the turbophoretic mechanism that controls their wall-normal transport. In turn, this leads to an increase of the local (near-wall) volume and mass fractions, which generate a stronger feedback force from the fibres to the fluid.

3.8.6.2. Mean Velocity Profiles

The mean velocity profiles of the fibre-laden simulations are shown in figure 3.30, with small inserts enhancing the region $100 \le z^+ \le 150$ for a better visualisation of the modified curves. To correctly compare these profiles with those of the unladen case, the velocity is normalised by the shear velocity obtained from the actual mean wall shear stress of the two-way coupled simulation. Only the stream-wise velocity component u is plotted, as the other two components have zero mean. Our results indicates that there is a proportionality between the fibre volume fraction Φ and the attained flow rate increase, with a higher concentration of particles determining a stronger reduction of drag. This effect is more subtle for the inertial fibres. Apparently, an onset volume fraction is trespassed between the two simulations, which leads to a switch from drag increase in the low-Φ case to drag reduction in the high-Φ case. We can quantify these trends by defining the drag reduction percentage as done in
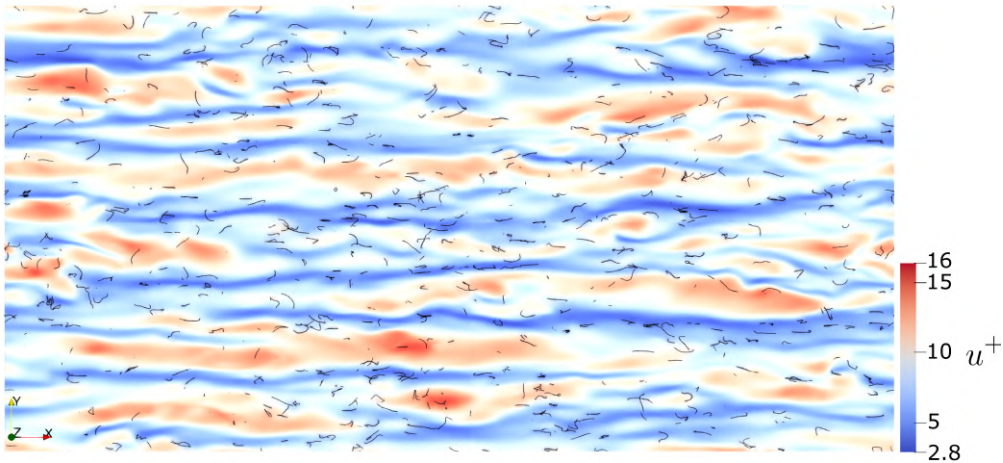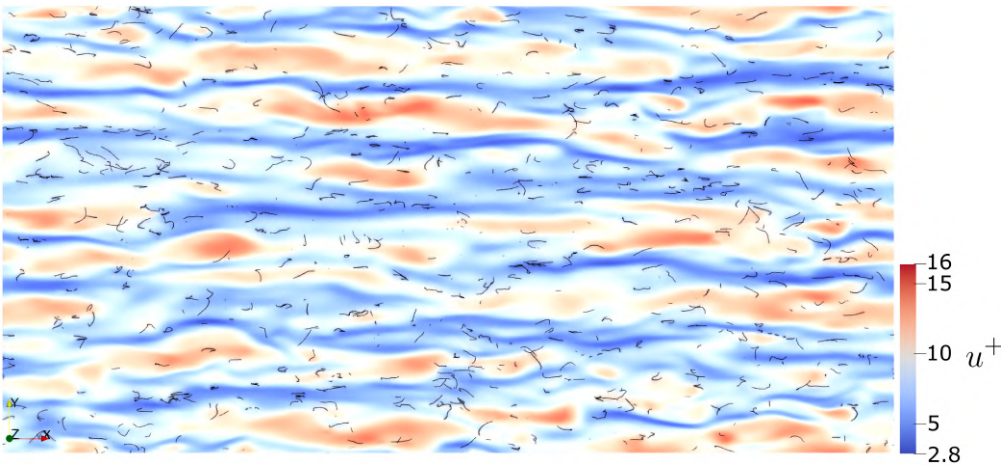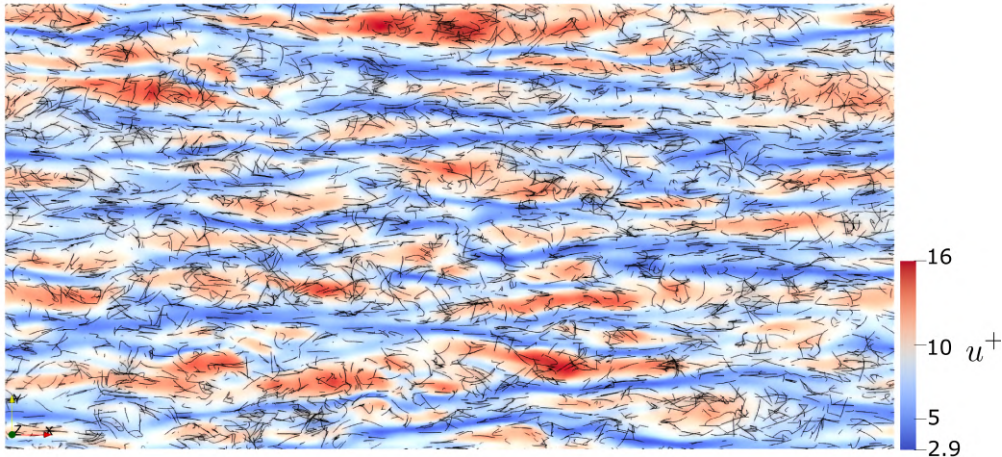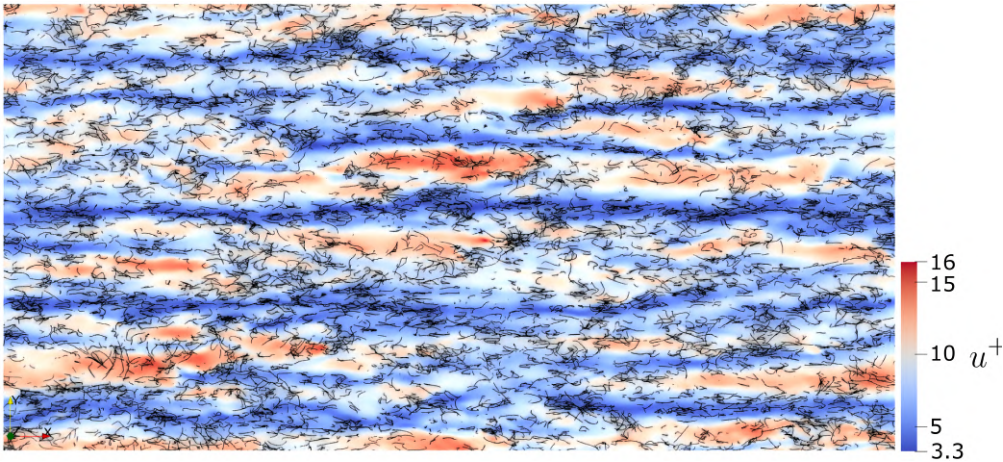
Figure 3.29. – Top view of the stream-wise fluid velocity streaks in the near-wall region ($z^+ = 10$) and instantaneous fibres distribution. Reference simulation: run F, $St^+_{fibre} = 25, \rho^+ = 1300, \Phi = 2.12 \cdot 10^{-4}$.

Paschkewitz et al., 2004:

$$\%DR = \left[1 - \left(\frac{u_\tau^L}{u_\tau^U} \right)^2 \right] \times 100, \tag{3.48}$$

where the superscript L indicates the friction velocity obtained in the two-way coupled simulations while the superscript U indicates the same quantity for the unladen flow. As reported in table 3.3, our results indicate a gentle drag reduction, except for one drag increase result. As a comparison, previous numerical investigations (Paschkewitz et al., 2004; Gillissen et al., 2008; Moosaie and Manhart, 2013; Z. Wang et al., 2021) reported a 10-times higher drag reduction percentage with a 10-times higher mass loading. The comparison with experiments is less satisfactory, as the measured drag reduction percentages reported in the literature are always larger than those reported in the table, even for the very low concentrations (Hoyt, 1972; Lee et al., 1974). These discrepancies, however, can be ascribed to several aspects of the present simulations, among which two emerge. The first aspect is the flexibility of the simulated fibres, which are not perfectly rigid as those considered in the experiments. Nevertheless, our analysis of the probability and of the life-time of the deformation events has highlighted that long fibres are continuously stretched by the turbulent flow, which could mitigate the issue. The second, and most relevant, aspect is the fibre aspect ratio, which was too large to be measured in the experiments, and therefore estimated to be several thousands (Hoyt, 1972). In our numerical study, we are limited to less slender fibres, in order to not be overwhelmed by an excessively high number of fibre elements (which would be necessary to maintain a volume fraction high enough to produce appreciable turbulence modulation). Anyway, an effort towards fibre-laden simulations with extremely slender fibres has been illustrated in table 3.2 and will be presented a following section.

Figure 3.30. – Mean stream-wise fluid velocity along the wall-normal coordinate. Panels: (a) $\Phi = 2.12 \cdot 10^{-5}$; (b) $\Phi = 2.12 \cdot 10^{-4}$. The curves of the unladen flow case is plotted in dashed black for reference. All cases are normalized according to the shear velocity yield by the corresponding simulation. The inserts zooms on the bulk of the flow, between 100 and 150 wall units.

Table 3.3. – Percentage of drag reduction, %DR (defined as in Equation (3.48)), for the different cases simulated in the (Φ, St_n^+) parameter space considered in this study. Drag increase is obtained when %$DR < 1$, whereas drag reduction is obtained when %$DR > 1$.

	$St_{fibre}^+ = 0.03$	$St_{fibre}^+ = 25$
$\Phi = 2.12 \cdot 10^{-5}$	1.44%	0.90%
$\Phi = 2.12 \cdot 10^{-4}$	1.48%	2.84%

3.8.6.3. Root Mean Square Profiles of the Velocities

The profiles of the root mean square (rms) of the fluid velocities allow more insight into the physical mechanism that controls drag modulation. The rms of the stream-wise fluid velocity is shown in figure 3.31 for all the simulated cases. Tracer-like fibres enhance the rms peak, in agreement with the previous simulations with inertialess spheroids (Z. Wang et al., 2021). This rms modulation effect reduces with the volume fraction. Inertial particles, instead, suppress this peak and, at higher Φ, produce a shift of the peak away from the wall. It can also be observed that all the simulations show a gentle increase of the rms profiles away from the wall. This corresponds to a suppression of turbulent activity and an enlargement of the buffer layer, in qualitative agreement with previous studies on polymer-induced drag reduction (Xi, 2019).

Considering the span-wise rms, shown in figure 3.32, tracer-like fibres determine a peak that is located further away from the wall with respect to the unladen case. In
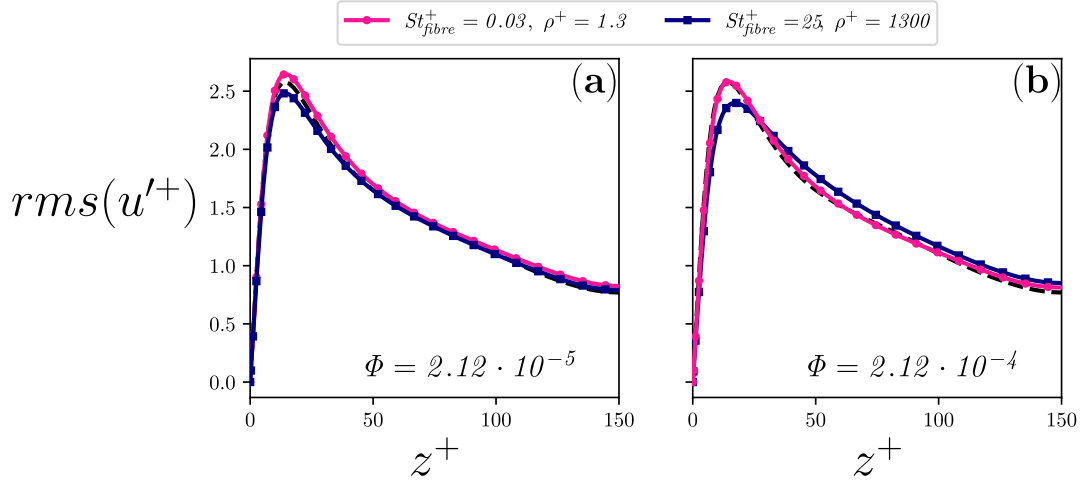
Figure 3.31. – Root mean square (rms) of the stream-wise fluid velocity along the wall-normal coordinate. Panels: (a) $\Phi = 2.12 \cdot 10^{-5}$; (b) $\Phi = 2.12 \cdot 10^{-4}$. The curve of the unladen flow case is plotted in dashed black for reference. All cases are normalized according to the shear velocity yield by the corresponding simulation.

addition, at low volume fraction, the mean profile is shifted upwards as one moves away from the wall. This is not observed with the inertial fibres, which appear to shift the profiles downward at increasing volume fraction.

Finally, the overall physical picture is coherent also for the wall-normal rms, shown in figure 3.33. In this case, all simulations show a gentle reduction, proportional to the volume fraction and to the inertia of the fibres, with the exception of the tracer fibres at low concentration, which seem to slightly detach the profile peak from the wall and increase its value in the center of the channel.

3.8.6.4. Axial Momentum Balance

In the flow configuration considered in this study, the mean axial momentum balance in the unladen case is determined solely by the viscous shear stress, $\tau_{visc} = \mu \partial \bar{u} / \partial z$, and the mixed axial-wall normal Reynolds stress, $\tau_{turb} = \rho \overline{u'w'}$. The sum of these two contributions provides the total shear stress, $\tau_{tot} = \frac{1}{2} (dp/dx) h$, which is a linear function of the wall-normal coordinate (Pope, 2000):

$$\underbrace{\mu \frac{\partial \bar{u}}{\partial z}}_{\tau_{visc}} - \underbrace{\rho \overline{u'w'}}_{\tau_{turb}} = \underbrace{\frac{1}{2} \frac{dp}{dx} \cdot h}_{\tau_{tot}} \qquad (3.49)$$

When a dispersed phase is added to the carrier fluid, an extra stress term must be accounted for in the balance. This extra stress is determined by the presence of the dispersed phase, and is generally referred to as *particle extra stress τ_{extra}* in the

137

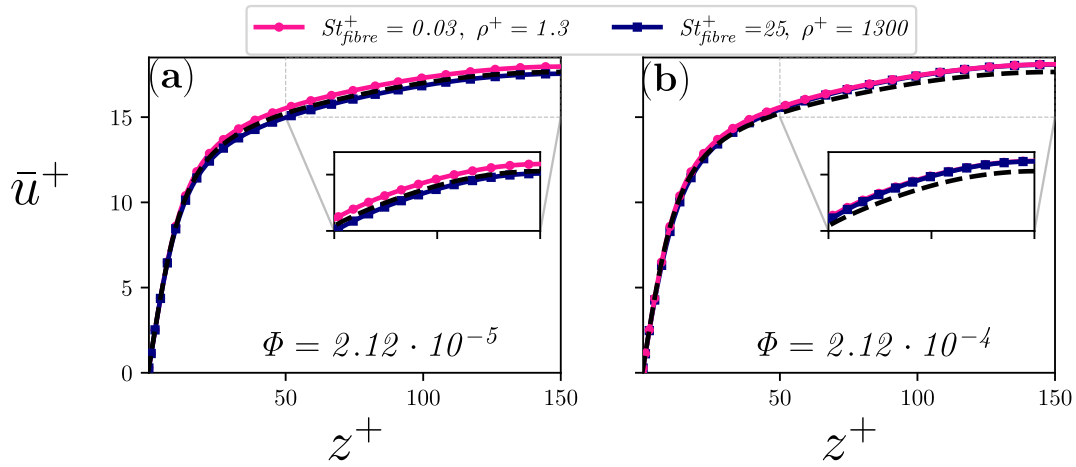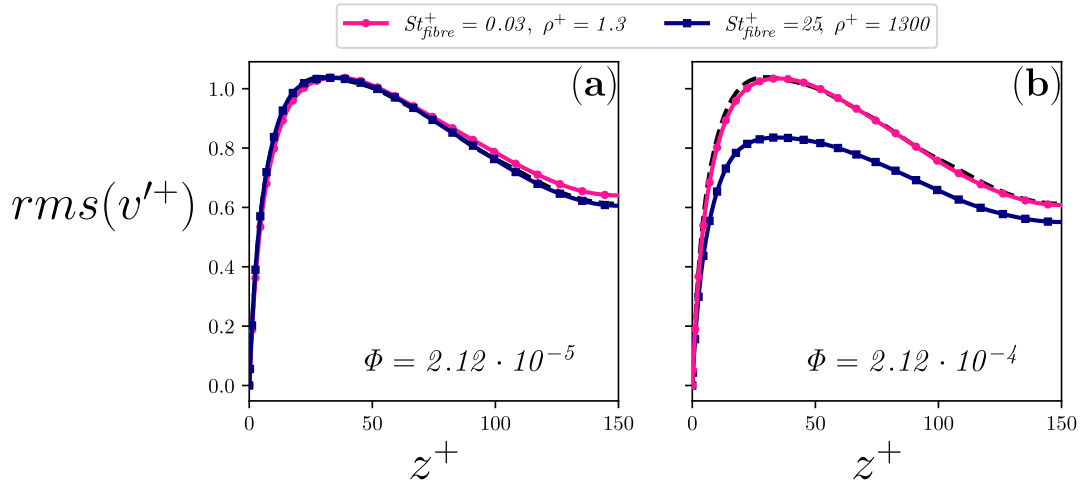Figure 3.32. – Root mean square (rms) of the span-wise fluid velocity along the wall-normal coordinate. Panels: (a) $\Phi = 2.12 \cdot 10^{-5}$; (b) $\Phi = 2.12 \cdot 10^{-4}$. The curve of the unladen flow case is plotted in dashed black for reference.
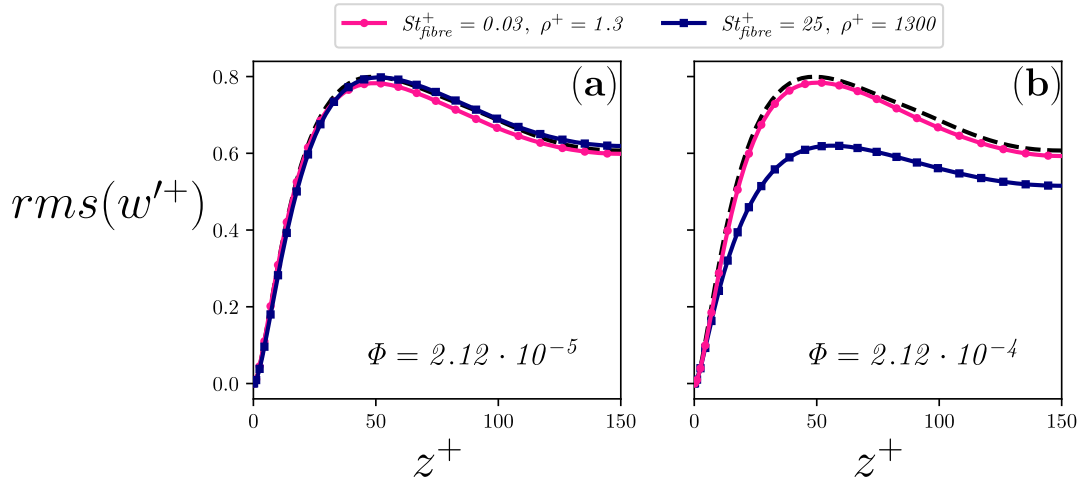
Figure 3.33. – Root mean square (rms) of the wall-normal fluid velocity along the wall-normal coordinate. Panels: (a) $\Phi = 2.12 \cdot 10^{-5}$; (b) $\Phi = 2.12 \cdot 10^{-4}$. The curve of the unladen flow case is plotted in dashed black for reference.

following. This term is calculated directly from the two-way coupling force, defined as in Equation (3.11), in the form of a cumulative integral over a given coordinate x_j:

$$\tau_{extra_{i,j}} = \frac{1}{L_j} \int_0^{L_j} F_{2w,i} dx_j. \tag{3.50}$$

138
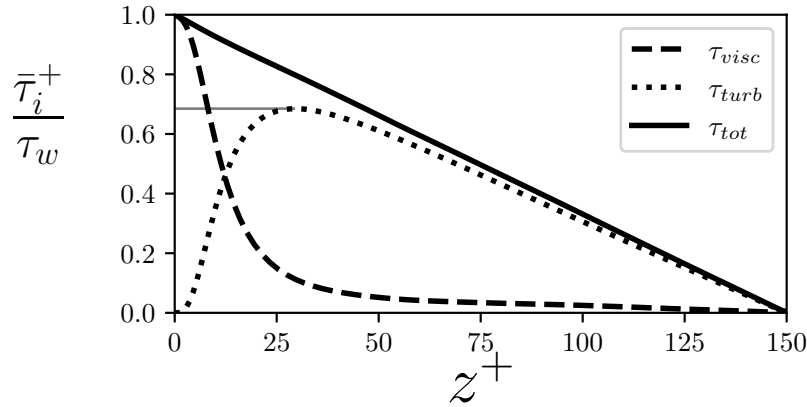
Figure 3.34. – Unladen-flow momentum balance along the wall-normal coordinate. The viscous shear stress dominates near the wall, while the Reynolds stress takes over away from it. The gray line indicates the maximum value of the Reynolds stress, which is used to compare present results with the fibre-laden ones.

The momentum balance given by Equation (3.49) then becomes:

$$\mu\frac{\partial \bar{u}}{\partial z} - \rho\overline{u'w'} + \tau_{extra_{x,z}} = \frac{1}{2}\frac{dp}{dx}\cdot h, \qquad (3.51)$$

where $\tau_{extra_{x,z}} = \frac{1}{h}\int_0^h F_x dz$ (simply referred to as τ_{extra} hereinafter, for ease of notation).

The different contributions to the total balance in the unladen flow case are shown in figure 3.34, whereas the contributions in the fibre-laden cases are shown in figures 3.35 and 3.36. Achieving a linear profile for the axial momentum balance is computationally intensive even in the unladen flow case, as statistics need to be calculated on very long averaging windows.

Figure 3.34 demonstrates that our simulations have reached a statistically steady state and ensures that the reported drag reduction is not depending on beneficial but temporary turbulent activity. For the two cases at the lower volume fraction, shown in figure 3.35, we can appreciate an effect of the mass loading on the intensity of the fibre extra (axial-normal) stress τ_{extra}. This stress is larger for the inertial fibres, while the disturbance given by the tracer-like fibres appears to determine an irrelevant contribution to the momentum balance of the flow (as it is reasonable to expect).

At higher volume fraction, as can be seen from figure 3.36, the effect of the mass loading is even more clear, as the inertial fibres determine a significant increase of τ_{extra}, which qualitatively behaves like a turbulent stress and directly feeds from the Reynolds stress τ_{turb}. Finally, we note that, even if the stress determined by the tracer-like fibres has slightly increased with the volume fraction, its contribution to the total momentum balance is still very small.
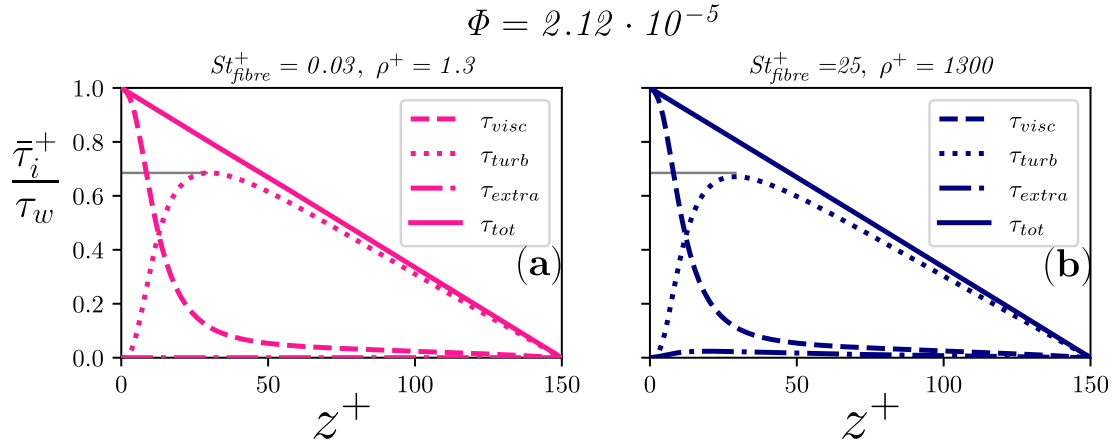
$$\Phi = 2.12 \cdot 10^{-5}$$

Figure 3.35. – Axial momentum balance at low volume fraction ($\Phi = 2.12 \cdot 10^{-5}$). Panels: (a) $St^+_{fibre} = 0.03$; (b) $St^+_{fibre} = 25$.
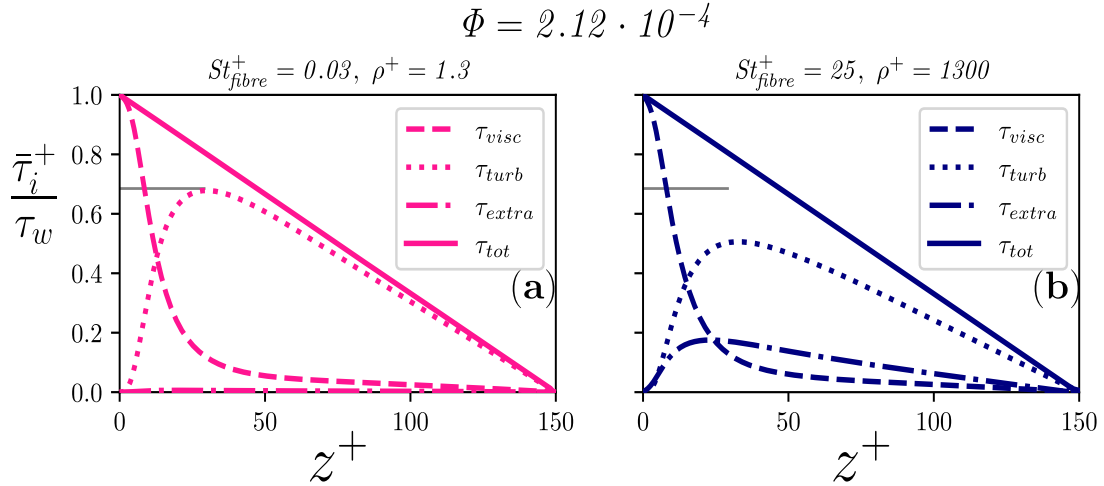
$$\Phi = 2.12 \cdot 10^{-4}$$

Figure 3.36. – Axial momentum balance at high volume fraction ($\Phi = 2.12 \cdot 10^{-4}$). Panels: (a) $St^+_{fibre} = 0.03$; (b) $St^+_{fibre} = 25$.

3.8.6.5. Particle Stresses

Equation (3.50) can be generalised to calculate the mean particle normal stresses, which reveal the non-Newtonian contribution of the dispersed fibres. Fibres introduce a dominant axial-normal stress $\tau_{x,z}$, that peaks close to the wall before decreasing and vanishing to zero at the center of the channel due to the symmetry of the flow configuration. The intensity of this profile is proportional to the local volume fraction of the dispersed fibres, as one would expect, but also to their inertia. This picture holds for the other non-zero normal stress, $\tau_{z,z}$, which is shown in Figure 3.37 and indeed shows a different profile. Starting from the wall, $\tau_{z,z}$ increases up to a distance of about 50 wall units and then maintains an almost constant value in the rest of the channel.
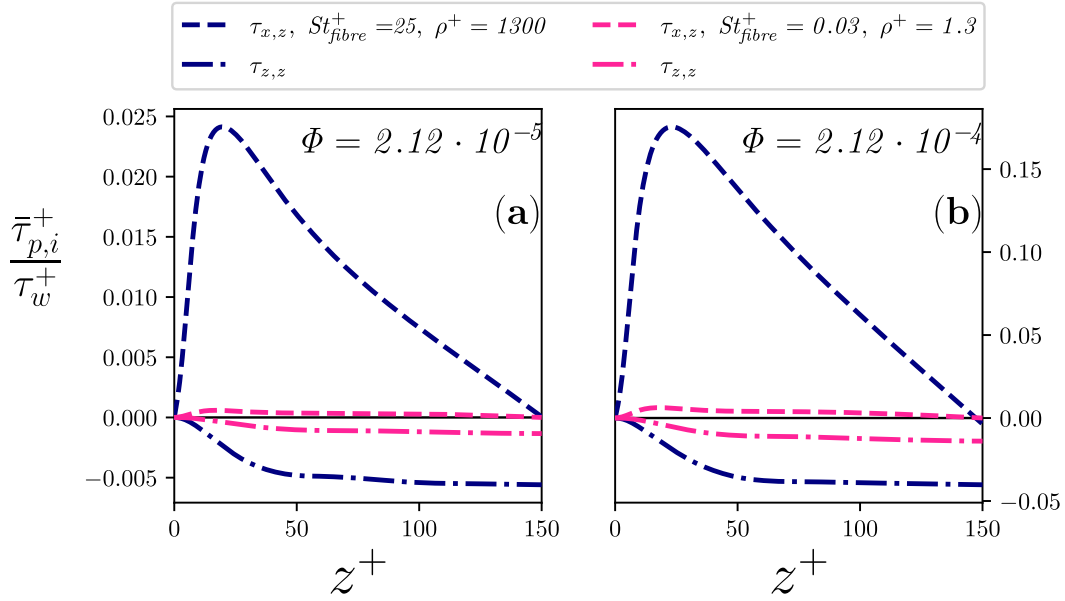
Figure 3.37. – Particle normal stresses. against the wall normal coordinate. Panels: (a) $\Phi = 2.12 \cdot 10^{-5}$; (b) $\Phi = 2.12 \cdot 10^{-4}$.

Another interesting feature is the fact that, away from the wall, the $\tau_{x,z}$ component is dominated by the $\tau_{z,z}$ component produced by the tracer-like fibres, whereas the situation is the opposite for the inertial cases. Compared with previous studies (Z. Wang et al., 2021), we can appreciate a difference related to the peak of $\tau_{x,z}$ and $\tau_{z,z}$, which appear to be less localised than previously observed (Z. Wang et al., 2021). We speculate that this is related to the size of the fibres considered in our study, much larger that the the typical ellipsoids and fibres simulated by means of the Lagrangian Particle Tracking (Paschkewitz et al., 2004; Z. Wang et al., 2021).

3.8.6.6. Turbulent kinetic energy spectra

The multi-scale nature of the interaction between slender fibres and turbulence is revealed when we look at the power spectra of the Turbulent Kinetic Energy (TKE). The TKE is defined as follows:

$$\mathbb{K} = \frac{1}{2} \left(u'u' + v'v' + w'w' \right) , \tag{3.52}$$

where the primes indicate fluctuating quantities. In Chapter 1, we have seen that the TKE identifies the kinetic energy associated with the different eddies within the turbulent flow, flowing from larger to smaller scales to be eventually dissipated by viscosity. Differently from spheres, when fibres interact with turbulence, they modulate it across a wide range of scales. Therefore, it is convenient to perform a scale-by-scale analysis by looking at the TKE spectra against the inverse length scale, i.e. the wave number.
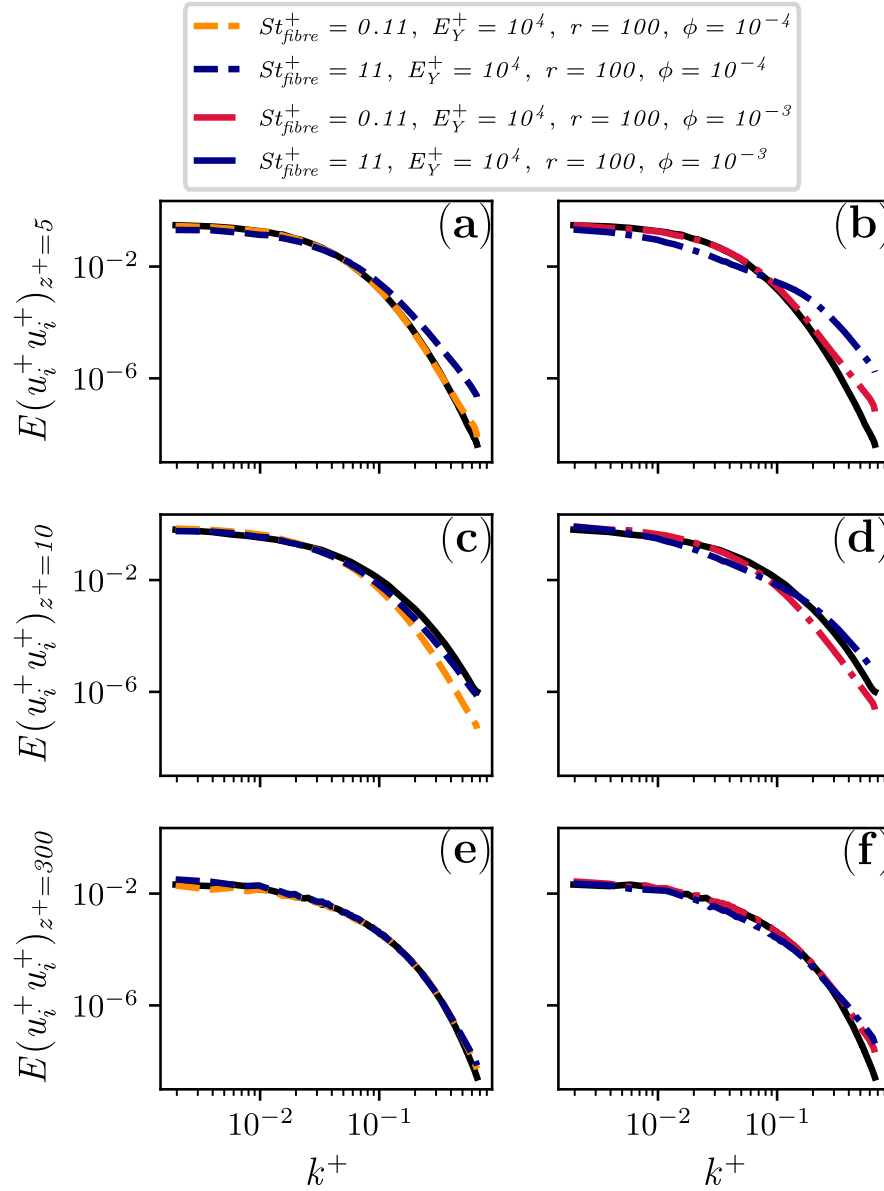
Figure 3.38. – Turbulent kinetic energy spectra against the dimensionless wavenumber k^+ at shear Reynolds number $Re_\tau = 300$. Panels: (a) $z^+ = 5$ wall units; (b) $z^+ = 10$ wall units; (c) $z^+ = 300$ wall units. The unladen cases are plotted as black solid lines.

To this purpose, we consider four simulations are shear Reynolds number $Re_\tau = 300$ where tracer-like ($St^+_{fibre} = 0.11$) and inertial ($St^+_{fibre} = 11$) stiff fibres of intermediate length ($L^+_0 = 35.81$) are dispersed in the turbulent channel flow. Two different concentrations of 10^{-4} and 10^{-3} are evaluated, produced by dispersing 125.000 and 1.250.000 chains of 20 rods respectively, to produce a total of four studies, identified as runs A,B,C and D in table 3.2.

The spectra of the turbulent kinetic energy are calculated by means of the Fast Fourier Transform implementation of the Numpy Python library. As displayed in figure 3.38, we will consider the flow-field on three different (x, y) planes parallel to the wall, situated at 5 (panels (a) and (b)), 10 (panels (c) and (d)) and 300 (panels (e) and (f)) wall units from the solid boundaries, while the volume fraction is increased from 10^{-4} in the left panels to 10^{-3} in the right panels.

Our results highlight typical features of fibre-laden turbulence. As we can see in panels (a) and (b), fibres near the wall distribute energy to the smallest scales, determining lifted tails for the spectra. This effect is proportional to the volume fraction but, most importantly, to the mass load of the suspension. Indeed, inertial fibres (blue curves) exhibit a clear bypass effect (Olivieri, Mazzino, et al., 2022), feeding from large and intermediate scales to redistribute at smaller ones, where the crossing point identifies a characteristic length scale that is smaller than that of the particles. Just a little further from the wall ($z^+ = 10$, panels (c) and (d)) and the scenario is modified. Tracer-like fibres (yellow and red curves) are now feeding from the smaller scales to slightly resonate at the larger ones. The crossing point suggests a typical length scale that is comparable to that of the particles ($k^{+*} \sim 0.03 \sim 1/L_0^+$). On the other hand, inertial fibres at higher concentrations (blue curve of the panel (d)) still show a gentle bypass effect, yet moderately resonate at the largest scales. The phenomenology is clearly weaker in the bulk of the flow (panels (e) and (f)). Here fibres seem to redistribute energy at both smaller and larger scales, as a gentle bypass effect emerges only for the inertial chains at higher volume fraction.

3.8.6.7. Turbulent kinetic energy budget

The mechanism behind drag reduction is revealed when one evaluates the budget of the Turbulent Kinetic Energy. This comprises the production, transport and dissipation of TKE over the whole height of the turbulent channel flow, and is given by the following equation:

$$\frac{\partial k}{\partial t} + \langle u_i \rangle \frac{\partial k}{\partial x_i} = \underbrace{- \left\langle u_i' u_j' \right\rangle \frac{\partial \langle u_i \rangle}{\partial x_j}}_{Production}$$

$$-\frac{\partial}{\partial x_j} \left(\overbrace{\frac{\left\langle p' u_j' \right\rangle}{\rho}}^{Pressure\ Diffusion} + \underbrace{\frac{\left\langle u_i' u_i' u_j' \right\rangle}{2}}_{Turbulent\ Transport} - \overbrace{\nu \frac{\partial k}{\partial x_j}}^{Viscous\ Transport} \right) \tag{3.53}$$

$$\underbrace{- \nu \left\langle \frac{\partial u_i'}{\partial x_j} \frac{\partial u_i'}{\partial x_j} \right\rangle}_{Dissipation} + \underbrace{\frac{1}{\rho} \left\langle f_i' u_i' \right\rangle}_{Particle\ Work} \quad .$$

When a statistically stationary state is attained, the production, dissipation and transport (turbulent, viscous and pressure transport) terms combine to completely describe the TKE budget.

From a quick overview of the literature about fibre-induced drag reduction, it is clear that previous numerical studies have evaluated particle aspect ratios of order $\mathbb{O}(10^2)$ (Z. Wang et al., 2021), whereas experiments would normally operate with much more slender fibres, having $r\mathbb{O}(10^3; 10^4)$ (Sharma, 1981). Motivated by this discrepancy, we decide to produce an extreme parameter study and simulate exceptionally slender fibres ($r = 1000$), corresponding to runs I,L,M and N of table 3.2 not only with consider the fibres with the largest particle aspect ratio but also we impose the highest particle concentration.

These chains are built from 20 rod elements with length $2\ell = 1.8$, diameter $2a = 0.036$ and aspect ratio $r = 50$, resulting in slender chains of total length $L_0^+ = 36.09$ and total aspect ratio $r_{tot} = 1000$. Ten million rods are considered for these simulations, dispersed in a turbulent channel flow at shear Reynolds number $Re_\tau = 150$ at a dilute concentration of $3.5 \cdot 10^{-5}$. The rod Stokes number and density ratio are combined at fixed geometry to produce two data sets, one with tracer-like chains ($St_{fibre}^+ = 0.2$)) and one with inertial fibres ($St_{fibre}^+ = 2.0$)). The influence of the bending stiffness is also explored by considering a zero and a finite ($E_Y^+ = 10^4$) value for the Young's modulus, which will determine a total of four simulations.

The TKE budget is displayed in figure 3.39, where the bending stiffness is increased from left to right and the inertial nature from top to bottom. When compared to the unladen budget (dotted black lines), fibre-laden simulations are characterised by a lower production peak (blue lines), indicating that the flow is loosing energy to the particles in this region, as observed by Pan et al., 2020 for inertial spheres. The transport and dissipation of TKE are also weakened, especially the viscous diffusion (red lines) and the viscous dissipation (purple lines) in the near-wall region. The influence of the mass loading does not look so remarkable, despite an even weaker peak of the production term being reported for the most inertial fibres (panel (d)).

At the same time, a novel source term appears in the TKE budget (brown lines), determined by the interaction between the particles and the flow and calculated as follows:

$$\mathbb{P} = \langle f_i' u_i' \rangle \,. \tag{3.54}$$

This corresponds to the work done by the particles on the fluid per mass and per time in all directions, which is displayed against the wall-normal coordinate in the top panel of figure 3.41. Despite its intensity is small, this term is fundamental in restoring the balance of the TKE budget of the fibre-laden turbulent channel flows. A positive sign indicates that the particles strengthen the flow and generate drag reduction, whereas a negative sign corresponds to drag increase. We can appreciate the fact that long and extremely slender fibres determine a not so remarkable positive contribution along a wide section of the bulk of the turbulent flow, whereas they more strongly drag the fluid in a narrow section just outside the buffer layer. The crossing point between these two regions moves away from the wall as particle inertia is increased. Therefore,

144
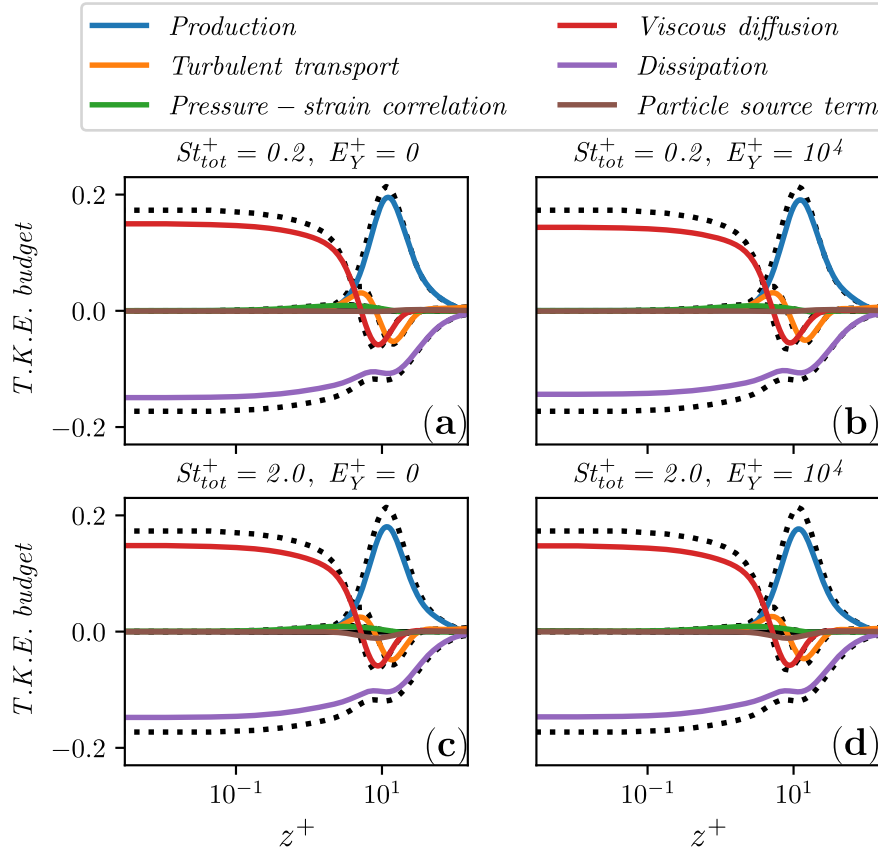
Figure 3.39. – Turbulent kinetic energy budget terms against the wall-normal dimen-
sionless coordinate z^+ at shear Reynolds number $Re_\tau = 150$. Panels: (a)
stiff-less tracer-like fibres; (b) stiff tracer-like fibres; (c) stiff-less inertial
fibres; (d) stiff inertial fibres. The unladen terms are plotted as black
dotted lines.

we can speculate that the considered fibres act to rearrange large scale structures of
the flow. Because of this, these large structures are more energetic and contribute in
a more effective way to the mean flow rate, determining a moderate drag reduction.
This consideration is in agreement with the resonance previously observed in the
spectra of the TKE 3.38 at shear Reynolds number $Re_\tau = 300$.

On the other hand, the TKE spectra suggested an enhancement of the energy content
of the smallest scales. At first this look in opposition with the reduced contribution of
the viscous diffusion and viscous dissipation in the near-wall region of the turbulent
channel flow, as displayed in the budgets of figure 3.39. Anyhow, we argue that the
particles play an intermediate role, inhibiting the production of turbulent TKE and its
transport from the large to small scales of the flow. As a consequence, we argue that
small turbulent scales energise themselves and become more coherent both in time
and in space. This is appreciable by looking at the visualisation of the flow for the stiff
tracer-like slender ($r = 1000$) fibres at shear Reynolds $Re_\tau = 150$ in figure 3.40, where
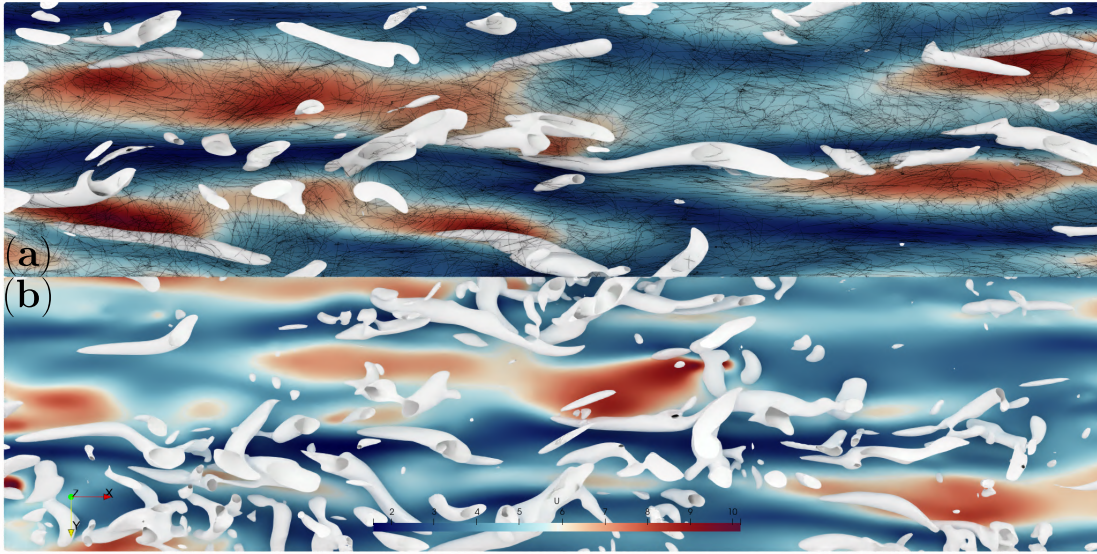
Figure 3.40. – Flow-visualisation of a $\pi Re_\tau/2 \times \pi Re_\tau/4$ wide section of a turbulent channel flow at shear Reynolds number $Re_\tau = 150$. The panels display the stream-wise velocity component on a section at $z\hat{I}^+ = 5$. Iso-surfaces of the second invariant Q of the fluid velocity gradient tensor are also displayed, being $Q = 0.02$ the selected value, corresponding to one tenth of the maximum value of Q obtained in the simulations). Panels: (a) fibre-laden flow simulation, where tracer-like stiff slender particles are considered. Fibres are enhanced by a factor 5 on their radius for visualization purposes. (b) un-laden flow simulation.

the panel displays the stream-wise velocity component u and the iso-surfaces of the second invariant Q of the fluid velocity gradient tensor are also displayed(Q = 0.02, corresponding to one tenth of the maximum value of Q obtained in the simulations) for the laden (top panel). The corresponding unladen flow is also displayed in the bottom panel and the comparison between the two confirms our speculation. Indeed, low and high speed velocity streaks are more homogeneously spaced in the fibre-laden flow and tend to assume a longer shape too. In addition, the flow structures are decimated and regularised by the presence of the fibres, whereas the iso-Q surfaces displays a forest of chaotic eddies in the unladen case. In conclusion, long slender fibres appear to act as drag reducing agents at intermediate flow-scales, acting to structurally rearrange the large structures in order to reduce the transport of TKE to the smallest scales which, as a consequence, rearrange themselves in a more coherent way. When comparing with previous studies on Drag Reduction with sub-Kolmogorov fibres, we understand that these fibres considered in this manuscript are much less efficient, underachieving by one order of magnitude (Paschkewitz et al., 2004; Z. Wang et al., 2021).

Nevertheless, long and slender fibres could be combined to shorter ones or polymers
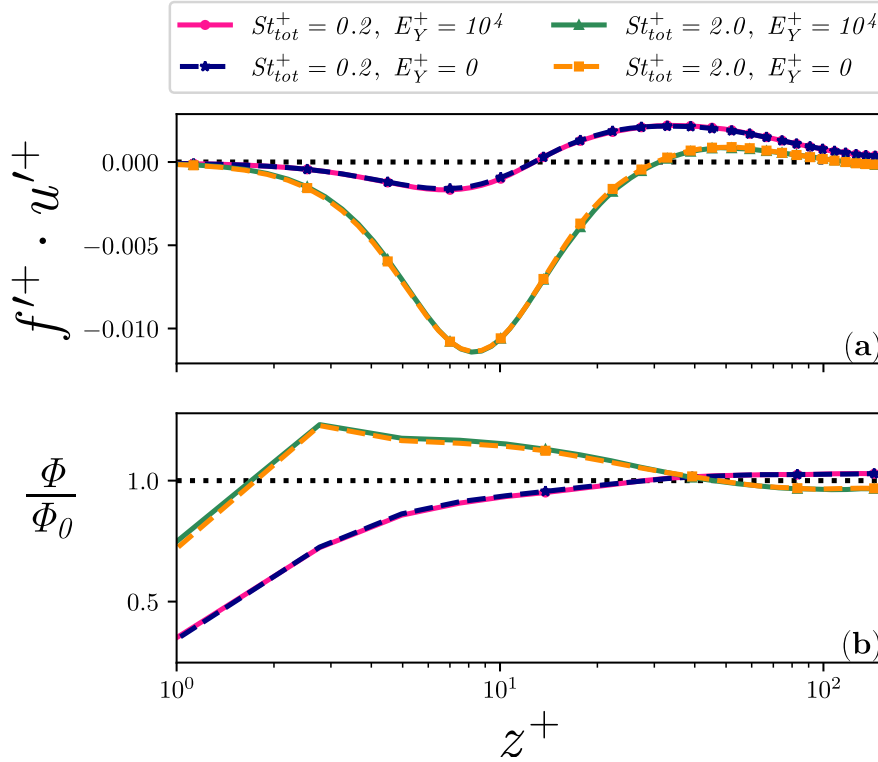
Figure 3.41. – Panels: (a) particle source term of the TKE budget against the wall-normal dimensionless coordinate z^+; (b) normalized particle volume fraction against the wall-normal dimensionless coordinate z^+.

to complement their near-wall effectiveness and extend drag reduction to the bulk of the flow (Marchioli and Campolo, 2021). This would be an effective solution as long as the fibres' inertia is small. To evaluate this statement we measure the effective steady state volume fraction Φ against the wall-normal coordinate, having normalized it by the initial concentration of particles, which is homogeneous along the channel height in the bottom panel of figure 3.41. Indeed, inertial particles tend to preferentially segregate in the near-wall region, and we speculate that this is the reason behind the marked negative particle work in that part of the flow, where this kind of particles are known preferentially segregate in high-speed streaks (Dotto and Marchioli, 2019). Instead, tracer-particles leave the walls and preferentially concentrate in the bulk of the flow, confirming that they could be successfully combined to smaller fibres or polymers to effectively reduce drag across the whole height a wall-bounded turbulent flow.

3.9. Conclusions

In this study, we have numerically explored the dynamics of long and flexible fibres in wall turbulence at moderate shear Reynolds number (Re_τ and Re_τ). Simulations

combine the Direct Numerical Simulation of the turbulent field with the Lagrangian Particle Tracking of sub-Kolmogorov rods constrained together to build long fibres following the rod-chain model.

Initially, we have focused on the dynamics of the fibres. The first important result is that, long and flexible fibres in the bulk of a turbulent channel flow orient with the local strain, coincidentally aligning with the vorticity, in agreement with the simulations of Olivieri, Mazzino, et al., 2022. Correspondingly, these particles experience a lower tumbling rate, comparable to what experimentally measured for rigid fibres in Homogeneous Isotropic Turbulence (Parsa and Voth, 2014; Oehmke et al., 2021).

This phenomenology is modified as we consider particles closer to the walls. Our results indicate that vorticity orients with the span-wise direction under the action of the mean shear determined by the solid boundaries, whereas flexible fibres align with the mean flow. This orthogonality determines a stronger contribution of the flow rotation to the tumbling rate of the observed particles, which moderately increases from the bulk to the near wall-region of the turbulent channel flow.

The second major finding is that the most probable configuration of a flexible fibre suspended in turbulence is the stretched one, in qualitative agreement with what observed numerically in Homogeneous Isotropic Turbulence (Picardo et al., 2020). Having classified the possible deformed shapes in a bi-variate probability space, our results suggest that the fibres deform following two typical deformation patterns, classified as 'eyelash' bending and 'compressing' buckling, where a finite yet moderate bending stiffness will suppress the latter.

This is in clear agreement with the observed dynamics of the deformations, as we find that flexible fibres in wall turbulence spend a short time in a bent state, before being stretched again by the flow. Our calculations indicate that this time is a fraction of their characteristic rotation time-scale and can be modelled as a gamma distribution, characterised by a stronger locality in the bulk of the flow than near the walls. Moreover, the typical deformation time moderately decreases with the wall normal coordinate for stiff-less fibres.

Overall, our results indicate that, from a dynamical perspective, flexible and rigid fibres in wall turbulence exhibit similar orientations and rotation rates. The reason behind this must be sought in the fact that the deformed fibres rapidly regain their stretched configuration, as their typical deformation time can be modelled by a highly local gamma distribution and most probably corresponds to the life span of small turbulent scales, i.e., between 2 and 3 time the Kolmogorov time-scale of the flow. This recalls the numerical investigation by Allende et al., 2018, who found that the inter-buckling time for sub-Kolmogorov flexible rods in Homogeneous Isotropic Turbulence was well predicted by a Weibull distribution.

Subsequently, we have focused on the modulation of turbulence by slender fibres. The general picture that emerges from a wide exploration of fibre-laden turbulent channel flows at different shear Reynolds number highlights the importance of the volume fraction highlights the importance of the volume fraction, which is the key parameter in determining the intensity of the drag reduction. The mass load is also an important parameter as, for inertial fibres, turbulence modulation generally leads to

drag increase.

Looking at the turbulence intensities, we appreciate two slightly different behaviours: one efficient case is determined by tracer fibres at low volume fraction, when they determine slightly stronger turbulence intensities, especially for the peak of the axial component and in the bulk of the flow. Instead, the three other simulations highlight a more classical picture, where the turbulence intensities are weakened proportionally with the inertia of the dispersed particles, especially for their peak (Xi, 2019). Keeping this is mind, we look at the axial momentum balance, where the non-Newtonian, axial-normal particle extra stress appears: from available theories on polymer-induced drag reduction, it is known that this term is limiting the possible amount of drag reduction, therefore it must be considered an undesired effect (Xi, 2019).

At the considered volume fractions, tracer-like fibres do not generate significant extra stresses, while inertial fibres do, feeding from the Reynolds stress proportionally to the mass load. However, tracer-like fibres are capable of introducing a more appreciable normal extra stress, of opposite sign. We speculate here that this stress acts to reduce the axis-wall normal momentum transfer, which can be thought of as the fundamental mechanism on which drag reduction is based (Xi, 2019). The effectiveness of the tracer-like fibres could be then related to their production of purely normal extra stresses without introducing a relevant particle stress in the momentum balance.

More insight into the mechanism behind turbulence modulation is obtained by looking at the spectra of the turbulent kinetic energy. Our results indicate typical features fibre-laden turbulence, in agreement with previous numerical studies (Olivieri, Mazzino, et al., 2022). The particles feed from the intermediate turbulent scales to vigorously distribute energy to the smaller ones but also modestly resonate in correspondence of the largest scales of the flow.

Traces of this mechanism are also found by looking at the budget of the turbulent kinetic energy. Long fibres act positively to affect the bulk of the turbulent channel flow. Despite their weak contribution, these particles modulate the production of turbulent kinetic energy which is more weakly transported to the smaller scales of the flow, where the viscous dissipation is also modulated.

In conclusion, our findings suggest that long and slender fibres could not so effectively replace smaller rods or polymers as Drag Reducing agents. Instead, it would be wiser to combine them together, as they typically influence a turbulent flow on different scales (Sharma, 1981).

4. General conclusions

The influence of inertia and flexibility on the dynamics of axisymmetrical particles suspended in viscous and turbulent flows were discussed in this manuscript.

Chapter 2 was devoted to an experimental study investigating the influence of small-inertia on the rotation of axisymmetrical particles suspended in a viscous shear flow. The first main finding is that the theory of Jeffery, 1922 is still valid to describe the periodic rotations of the particles in the explored inertial regime up to $Re_p \lesssim 1$. The second important result is that small-inertia modifies the stability of the orbits described by the rotating particles, determining the insurgence of attracting limiting cycles. Prolate particles eventually drift through consecutive rotations to the tumbling orbit in the plane of shear. Instead, oblate particles of any aspect ratio will either drift to the spinning orbit along the vorticity axis or the tumbling orbit in the plane of shear, depending only on their initial orientation.

The experimental methodology presented in this manuscript is rather flexible and therefore amenable to study the alignment of small particles of different shape in a viscous shear flow, opening for the following lines of future research:

- flexible fibres in viscous shear flows were studied experimentally by Forgacs and Mason, 1959. It would be of great interest to characterise the rotation and deformation of flexible prolate and oblate cylinders by means of the methodology proposed in this manuscript. First, the viscous regime could be fully characterised, before considering a weakly inertial one and its consequences on the particle deformation. Nevertheless, the particle reconstruction methods should be revisited to adapt them to flexible objects. Most probably, the optimal solution would be the direct deployment of the Neural Networks on the experimental images, despite this would require a precise and extensive training.

- the analytical model of Borker et al., 2018 highlighted the possibility of controlling the orientation of rings suspended in a viscous shear flow, which ultimately attained an aligned orientation in time when the fore-aft symmetry of the cross-section is broken. Preliminary experiments with 3D printed rings were performed during the preparation of this manuscript, qualitatively confirming the result of Borker et al., 2018 in the weakly inertial regime. As displayed in figure 4.1, depending on their section, donut rings rotate in a viscous shear flow at $Re_p = 0.35$ (top), whereas rings with fore-aft asymmetric section align with the flow at $Re_p = 0.44$ (bottom). This results are encouraging and justify a further exploration of the equivalence of shape between rings with different cross-sections and ellipsoids. Furthermore, these result open a perspective over the control of the rheology of suspensions by particle shape, which could have
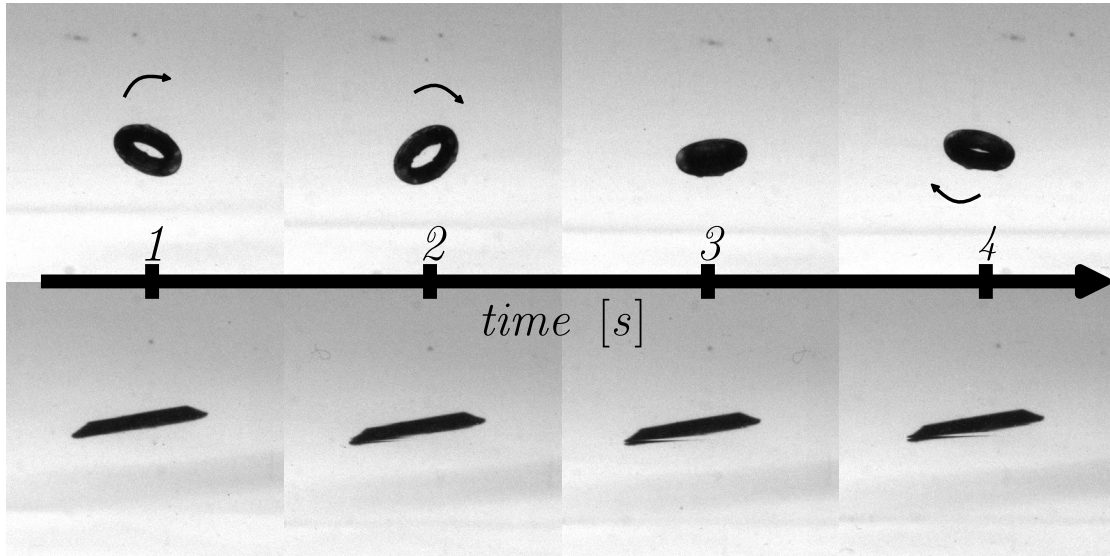
Figure 4.1. – Time-evolution of a fore-aft symmetric donut ring (top) and a fore-aft asymmetric ring with triangular section (bottom) suspended in a viscous shear flow. The viscosity of the fluid is $\mu = 25.7\,mPas$ and the shear rate is $\dot{\gamma} = 3.64$. The particle Reynolds number is estimated as $Re_p = \frac{\rho\dot{\gamma}a\zeta}{\mu}$, being ζ the equivalent radius of the cross section of the ring. This corresponds to a $Re_p = 0.35$ for the donut (top) and $Re_p = 0.44$ for the triangular ring (bottom). The time-line highlights the evolution of the experiment, from left to right. As displayed by the frames and highlighted by the arrows, while the donut rotates (top), the triangular ring maintains an aligned position in the viscous shear flow (bottom).

important applications in the field of process engineering.

In Chapter 3 we discussed the orientation, rotation and deformation of flexible fibres in a turbulent channel flow. Despite the embedded flexibility of the particles, our results indicate that fibres in wall turbulence deform for short times, preferring a stretched configuration. As a consequence, we observe that flexible fibres orient and rotate comparably to rigid ones in the bulk of a turbulent channel flow, whereas they align to the mean flow and experience stronger tumbling rates under the effect of the strong shear near the walls. Finally, by analysing the turbulence statistics of the fibre-laden flow, we find the proposed numerical approach recovers a moderate drag reduction, indicating that long and slender flexible fibres should be combined to smaller drag reducing agents to modulate turbulence all along the section of a pipe.

The numerical methodology is suitable to the investigation of numerous future developments:

- in this work, long and flexible fibres were modelled as chains of sub-Kolmogorov rods, while their rotational dynamics were calculated following the theory of Jeffery, 1922. Nevertheless, the experimental investigation over the influence of small-inertia on the Jeffery orbits highlighted its impact on their stability.

Therefore, a natural development would be to model the rods according to the equivalent theories of Einarsson, Candelier, et al., 2015b and Dabade et al., 2016. Not only this would produce numerical simulations of unprecedented accuracy, but, most importantly, it would allow us to assess the relative importance of small-inertia within a turbulent flow and its consequences on turbulence modulation.

○ the momentum exchange between fibres and turbulence could be modelled in a complete way, taking into account not only the linear terms, as done in this manuscript, but also the angular terms. Not only this is expected to modify the entity of the turbulence modulation, but it would also allow for a more realistic representation of the fibre bending dynamics.

○ in this manuscript we provided statistical evidence that the bending of flexible fibres is relatable to small turbulent scales. Therefore, in an effort to study the dependence of particle deformation of the flow Reynolds number, one could simulated flows at larger shear Reynolds number than what considered here ($Re_\tau = 300$), where stronger and more intermittent turbulent fluctuations are expected. Anyway, such a development would inevitably incur the computational load of such numerical simulations, which could be lifted by deploying modern computing infrastructures and relying on the novel algorithm discussed in Section 3.4.1.

Bibliography

[Aba+15]   M. Abadi et al. *TensorFlow: Large-Scale Machine Learning on Heterogeneous Systems*. Software available from tensorflow.org. 2015. URL: https://www.tensorflow.org/ (cit. on p. 58).

[AMR04]   M. D. Abràmoff, P. J. Magalhães, and S. J. Ram. "Image processing with ImageJ". In: *Biophot. Int.* 11.7 (2004), pp. 36–42 (cit. on p. 44).

[Ali+21]   M. Alipour, M. De Paoli, S. Ghaemi, and A. Soldati. "Long non-axisymmetric fibres in turbulent channel flow". In: *J. Fluid Mech.* 916 (2021) (cit. on pp. 43, 55, 120).

[ADS22]   M. Alipour, M. De Paoli, and A. Soldati. "Influence of Reynolds number on the dynamics of rigid, slender and non-axisymmetric fibres in channel flow turbulence". In: *J. Fluid Mech.* 934 (2022) (cit. on pp. 120, 122).

[AHB18]   S. Allende, C. Henry, and J. Bec. "Stretching and buckling of small elastic fibers in turbulence". In: *Phys. Rev. Lett.* 121.15 (2018), p. 154501 (cit. on pp. 37, 113, 124, 126, 148, 175).

[AM68a]   E. Anczurowski and S. G. Mason. "Particle motions in sheared suspensions. XXIV. Rotation of rigid spheroids and cylinders". In: *Trans. Soc. Rhe.* 12.2 (1968), pp. 209–215 (cit. on p. 30).

[AM68b]   E. Anczurowski and S. G. Mason. "Particle motions in sheared suspensions. XXIV. Rotation of rigid spheroids and cylinders". In: *Trans. Soc. Rhe.* 12.2 (1968), pp. 209–215 (cit. on pp. 31, 43, 47, 62, 63, 73, 74, 81).

[And+13]   J. Andrić, S. T. Fredriksson, S. B. Lindström, S. Sasic, and H. Nilsson. "A study of a flexible fiber model and its behavior in DNS of turbulent channel flow". In: *Acta Mec.* 224.10 (2013), pp. 2359–2374 (cit. on pp. 36, 84, 85, 109, 174).

[Ard+17]   M. N. Ardekani, P. Costa, W. P. Breugem, F. Picano, and L. Brandt. "Drag reduction in turbulent channel flow laden with finite-size oblate spheroids". In: *J. Fluid Mech.* 816 (2017), pp. 43–70 (cit. on p. 84).

[Aze20]   R. de Azevedo. *Smallest axis-aligned bounding box of hyper-ellipsoid.* https://math.stackexchange.com/questions/3926884/smallest-axis-aligned-bounding-box-of-hyper-ellipsoid. 2020 (cit. on p. 167).

[BC22]   L. J. Baker and F. Coletti. "Experimental investigation of inertial fibres and disks in a turbulent boundary layer". In: *J. Fluid Mech.* 943 (2022), A27 (cit. on pp. 43, 57).

[BFT20]   G. Basterretxea, J. S. Font-Munoz, and I. Tuval. "Phytoplankton orientation in a turbulent ocean: a microscale perspective". In: *Front. Marine Sci.* 7 (2020), p. 185 (cit. on pp. 20, 171).

[Bat47]   G. K. Batchelor. "Kolmogoroff's theory of locally isotropic turbulence". In: *Mat. Proc. Camb. Phil. Soc.* 43 (1947), pp. 533–559 (cit. on p. 24).

[BT49]   G. K. Batchelor and A. A. Townsend. "The nature of turbulent motion at large wave-number". In: *Proc. R. S. Q* 199 (1949) (cit. on p. 25).

[Bat+19]   F. Battista, J. P. Mollicone, P. Gualtieri, R. Messina, and C. M. Casciola. "Exact regularised point particle (ERPP) method for particle-laden wall-bounded flows in the two-way coupling regime". In: *J. Fluid Mech.* 878 (2019), pp. 420–444 (cit. on pp. 89, 104, 105).

[Ben+08]   R. Benzi, E. S. C. Ching, E. De Angelis, and I. Procaccia. "Comparison of theory and direct numerical simulations of drag reduction by rodlike polymers in turbulent channel flows". In: *Phys. Rev. E* 77.4 (2008), p. 046309 (cit. on p. 39).

[Bin39]   R. C. Binder. "The motion of cylindrical particles in viscous flow". In: *J. App. Phys.* 10.10 (1939), pp. 711–713 (cit. on p. 30).

[BSK18]   N. S. Borker, A. D. Stroock, and D. L. Koch. "Controlling rotation and migration of rings in a simple shear flow through geometric modifications". In: *J. Fluid Mech.* 840 (2018), pp. 379–407 (cit. on p. 150).

[BBV18]   S. Bounoua, G. Bouchet, and G. Verhille. "Tumbling of inertial fibers in turbulence". In: *Phys. Rev. Lett.* 121.12 (2018), p. 124502 (cit. on pp. 35, 119, 172).

[Bra00]   G. Bradski. "The OpenCV Library". In: *Dr. Dobb's J. Soft. Tools* (2000) (cit. on p. 55).

[BVL14]   C. Brouzet, G. Verhille, and P. Le Gal. "Flexible fiber in a turbulent flow: A macroscopic polymer". In: *Phys. Rev. Lett.* 112.7 (2014), p. 074501 (cit. on pp. 37, 55, 124).

[Buc14]   E. Buckingham. "On physically similar systems; illustrations of the use of dimensional equations". In: *Phys. Rev.* 4.4 (1914), p. 345 (cit. on pp. 65, 101).

[Bur38]   J. M. Burgers. "Second Report on Viscosity and Plasticity". In: 16 (1938), pp. 113–84 (cit. on pp. 30, 31, 62, 73, 74).

[Bur+18]   R. Burnett et al. "Global estimates of mortality associated with long-term exposure to outdoor fine particulate matter". In: *Proc. Nat. Acad. Sci.* 115.38 (2018), pp. 9592–9597 (cit. on pp. 20, 171).

[BM91]   D. M. Bushnell and K. J. Moore. "Drag reduction in nature". In: *Annu. Rev. Fluid Mech.* 23.1 (1991), pp. 65–79 (cit. on p. 37).

[Byr+15]   M. Byron, J. Einarsson, K. Gustavsson, G. A. Voth, B. Mehlig, and E. A. Variano. "Shape-dependence of particle rotation in isotropic turbulence". In: *Phys. Fluids* 27.3 (2015), p. 035101 (cit. on pp. 33, 34, 82, 109, 114, 172).

[CDC20]   C.D.C.P. "Social distancing: Keep a safe distance to slow the spread". In: *Retrieved July* 15 (2020), p. 2020 (cit. on pp. 20, 171).

[Can86]   J. Canny. "A computational approach to edge detection". In: *IEEE Trans. pattern analysis and machine intelligence* 6 (1986), pp. 679–698 (cit. on p. 55).

[Can+07]   C. Canuto, M. Y. Hussaini, Q. Quarteroni, and T. A. Zang. *Spectral methods: fundamentals in single domains.* Springer Science and Business Media, 2007 (cit. on p. 91).

[CR15]   A. Capone and G. P. Romano. "Interactions between fluid and fibers in a turbulent backward-facing step flow". In: *Phys. Fluids* 27.5 (2015), p. 053303 (cit. on p. 34).

[CZ15]   W. R. Chen and L. R. Zhao. "Review–volcanic ash and its influence on aircraft engine components". In: *Proc. Eng.* 99 (2015), pp. 795–803 (cit. on pp. 19, 171).

[Cox71]   R. G. Cox. "The motion of long slender bodies in a viscous fluid. Part 2. Shear flow". In: *J. Fluid Mech.* 45.4 (1971), pp. 625–657 (cit. on pp. 30, 31, 63, 73, 74, 95, 106).

[DMS16]   V. Dabade, N. K. Marath, and G. Subramanian. "The effect of inertia on the orientation dynamics of anisotropic particles in simple shear flow". In: *J. Fluid Mech.* 791 (2016), pp. 631–703 (cit. on pp. 18, 30–32, 40, 43, 64, 66, 68, 69, 78–82, 102, 152, 171, 173, 174).

[De 90]   P. G. De Gennes. *Introduction to polymer dynamics.* CUP Archive, 1990 (cit. on p. 39).

[DCP15]   B. Delmotte, E. Climent, and F. Plouraboué. "A general formulation of Bead Models applied to flexible fibers and active filaments at low Reynolds number". In: *J. Comp. Phys.* 286 (2015), pp. 14–37 (cit. on pp. 35, 84, 97, 104).

[DMM19]   R. Deshpande, J. P. Monty, and I. Marusic. "Streamwise inclination angle of large wall-attached structures in turbulent boundary layers". In: *J. Fluid Mech.* 877 (2019) (cit. on p. 118).

[DM19]   D. Dotto and C. Marchioli. "Orientation, distribution, and deformation of inertial flexible fibers in turbulent channel flow". In: *Acta Mec.* 230.2 (2019), pp. 597–621 (cit. on pp. 133, 147).

[DSM20]   D. Dotto, A. Soldati, and C. Marchioli. "Deformation of flexible fibers in turbulent channel flow". In: *Meccanica* 55.2 (2020), pp. 343–356 (cit. on pp. 37, 97).

[Du +19]   O. Du Roure, A. Lindner, E. N. Nazockdast, and M. J. Shelley. "Dynamics of flexible fibers in viscous flows and fluids". In: *Annu. Rev. Fluid Mech.* 51 (2019), pp. 539–572 (cit. on pp. 35, 44, 102).

[DSV12]   J. Dupire, M. Socol, and A. Viallat. "Full dynamics of a red blood cell in shear flow". In: *Proc. Nat. Acad. Sci.* 109.51 (2012), pp. 20808–20813 (cit. on p. 22).

[Ein+15a]   J. Einarsson, F. Candelier, F. Lundell, J. Angilella, and B. Mehlig. "Effect of weak fluid inertia upon Jeffery orbits". In: *Phys. Rev. E* 91.4 (2015), p. 041002 (cit. on pp. 31, 32, 43, 66, 67, 75–78, 81, 171, 173, 174).

[Ein+15b]   J. Einarsson, F. Candelier, F. Lundell, J. Angilella, and B. Mehlig. "Rotation of a spheroid in a simple shear at small Reynolds number". In: *Phys. Fluids* 27.6 (2015), p. 063301 (cit. on pp. 18, 31, 40, 66, 69, 102, 152, 171).

[Ein+16]   J. Einarsson, B. M. Mihiretie, A. Laas, S. Ankardal, J. Angilella, D. Hanstorp, and B. Mehlig. "Tumbling of asymmetric microrods in a microchannel flow". In: *Phys. Fluids* 28.1 (2016), p. 013302 (cit. on pp. 30, 55).

[Ein06]   A. Einstein. "Eine neue Bestimmung der Moleküldimensionen". In: *Ann. Physik* 19 (1906), pp. 289–306 (cit. on p. 30).

[FM59]   O. L. Forgacs and S. G. Mason. "Particle motions in sheared suspensions: X. Orbits of flexible threadlike particles". In: *J. Coll. Sci.* 14.5 (1959), pp. 473–491 (cit. on pp. 28, 30, 35, 36, 113, 150).

[FG31]   F. Forrest and G. A. Grierson. "Friction losses in cast iron pipe carrying paper stock". In: *Paper Trade J.* 92.22 (1931), pp. 39–41 (cit. on p. 37).

[FSN78]   U. Frisch, P. L. Sulem, and M. Nelkin. "A simple dynamical model of intermittent fully developed turbulence". In: *J. Fluid Mech.* 87.4 (1978), pp. 719–736 (cit. on p. 25).

[Gad65]   G. E. Gadd. "Turbulence damping and drag reduction produced by certain additives in water". In: *Nature* 206.4983 (1965) (cit. on p. 39).

[Gil+07]   J. J. J. Gillissen, B. J. Boersma, P. H. Mortensen, and H. I. Andersson. "On the performance of the moment approximation for the numerical computation of fiber stress in turbulent channel flow". In: *Phys. Fluids* 19.3 (2007), p. 035102 (cit. on p. 89).

[Gil+08]   J. J. J. Gillissen, B. J. Boersma, P. H. Mortensen, and H. I. Andersson. "Fibre-induced drag reduction". In: *J. Fluid Mech.* 602 (2008), pp. 209–218 (cit. on pp. 39, 135).

[Gle94]   P. Glendinning. "Stability, instability and chaos: an introduction to the theory of nonlinear differential equations". In: Cambridge university press, 1994, pp. 145, 158 (cit. on p. 68).

[Gol96]   H. L. Goldsmith. "The microrheology of dispersions: application to blood cells". In: *J. Jap. Soc. Biorhe.* 10.4 (1996), pp. 15–36 (cit. on pp. 22, 171).

[GM62a]   H. L. Goldsmith and S. G. Mason. "Particle motions in sheared suspensions XIII. The spin and rotation of disks". In: *J. Fluid Mech.* 12.1 (1962), pp. 88–96 (cit. on p. 30).

[GM62b]   H. L. Goldsmith and S. G. Mason. "The flow of suspensions through tubes. I. Single spheres, rods, and discs". In: *J. Coll. Sci.* 17.5 (1962), pp. 448–476 (cit. on p. 30).

[Gua+15]   P. Gualtieri, F. Picano, G. Sardina, and C. M. Casciola. "Exact regularized point particle method for multiphase flows in the two-way coupling regime". In: *J. Fluid Mech.* 773 (2015), pp. 520–561 (cit. on pp. 40, 85, 89, 90, 174).

[GRS12]   J. S. Guasto, R. Rusconi, and R. Stocker. "Fluid mechanics of planktonic microorganisms". In: *Annu. Rev. Fluid Mech.* 44 (2012), pp. 373–400 (cit. on pp. 20, 171).

[Gus88]   J. L. Gustafson. "Reevaluating Amdahl's law". In: *Comm. A.C.M.* 31.5 (1988), pp. 532–533 (cit. on p. 99).

[HB83]   J. Happel and H. Brenner. *Low Reynolds number hydrodynamics: with special applications to particulate media.* Vol. 1. Springer Science & Business Media, 1983 (cit. on p. 83).

[HP75]   J. B. Harris and J. F. T. Pittman. "Equivalent ellipsoidal axis ratios of slender rod-like particles". In: *J. Coll. Int. Sci.* 50.2 (1975), pp. 280–282 (cit. on pp. 30, 31, 62, 63, 73, 74, 81, 106).

[HA15]   F. Hoseini A. A .and Lundell and H. I. Andersson. "Finite-length effects on dynamical behavior of rod-like particles in wall-bounded turbulent flow". In: *Int. J. Mult Flow* 76 (2015), pp. 13–21 (cit. on p. 34).

[Hoy72]   J. W. Hoyt. *Turbulent flow of drag-reducing suspensions.* Tech. rep. NAVAL UNDERSEA CENTER SAN DIEGO CA, 1972 (cit. on pp. 21, 39, 135, 171).

[Hua+12]   H. Huang, X. Yang, M. Krafczyk, and X. Y. Lu. "Rotation of spheroidal particles in Couette flows". In: *J. Fluid Mech.* 692 (2012), pp. 369–394 (cit. on p. 32).

[ISK02]   K. Iwamoto, Y. Suzuki, and N. Kasagi. "Reynolds number effect on wall turbulence: toward effective feedback control". In: *Int. J. Heat Fluid Flow* 23.5 (2002), pp. 678–689 (cit. on p. 103).

[Jef22]   G. B. Jeffery. "The motion of ellipsoidal particles immersed in a viscous fluid". In: *Proc. R. Soc. Lond. A* 102.715 (1922), pp. 161–179 (cit. on pp. 18, 28, 30, 31, 33, 43, 61, 67, 73, 74, 84, 104, 106, 150, 151, 171, 173, 175).

[Jie+19]   Y. Jie, C. Xu, J. R. Dawson, H. I. Andersson, and L. Zhao. "Influence of the quiescent core on tracer spheroidal particle dynamics in turbulent channel flow". In: *J. Turb.* 20.7 (2019), pp. 424–438 (cit. on p. 35).

[Jim12]   J. Jiménez. "Cascades in wall-bounded turbulence". In: *Annu. Rev. Fluid Mech.* 44 (2012), pp. 27–45 (cit. on p. 27).

[KGM63]   A. Karnis, H. L. Goldsmith, and S. G. Mason. "Axial migration of particles in Poiseuille flow". In: *Nature* 200.4902 (1963), pp. 159–160 (cit. on p. 30).

[KGM66]   A. Karnis, H. L. Goldsmith, and S. G. Mason. "The flow of suspensions through tubes, V. Inertial Effects". In: *Can. J. Chem. Eng.* (1966) (cit. on p. 30).

[Kho+21]   S. Khomenko et al. "Premature mortality due to air pollution in European cities: a health impact assessment". In: *Lac. Plan. Health* 5.3 (2021), e121–e134 (cit. on pp. 20, 171).

[KMM87]   J. Kim, P. Moin, and R. Moser. "Turbulence statistics in fully developed channel flow at low Reynolds number". In: *J. Fluid Mech.* 177 (1987), pp. 133–166 (cit. on pp. 85, 92, 174).

[KK13]   S. Kim and S. J. Karrila. *Microhydrodynamics: principles and selected applications*. Courier Corporation, 2013 (cit. on p. 96).

[Kol41]   A. N. Kolmogorov. "The local structure of turbulence in incompressible viscous fluid for very large Reynolds numbers". In: *Cr Acad. Sci. URSS* 30 (1941), pp. 301–305 (cit. on p. 24).

[KSH19]   S. Kuperman, L. Sabban, and R. van Hout. "Inertial effects on the dynamics of rigid heavy fibers in isotropic turbulence". In: *Phys. Rev. Fluids* 4.6 (2019), p. 064301 (cit. on p. 35).

[La +01]   A. La Porta, G. A. Voth, A. M. Crawford, J. Alexander, and E. Bodenschatz. "Fluid particle accelerations in fully developed turbulence". In: *Nature* 409.6823 (2001), pp. 1017–1019 (cit. on p. 120).

[LVS21]   C. Le Ribault, I. Vinkovic, and S. Simoëns. "Large eddy simulation of particle transport and deposition over multiple 2D square obstacles in a turbulent boundary layer". In: *J. Geoph. Res. Atmo.* 126.16 (2021), e2020JD034461 (cit. on pp. 20, 28, 171).

[LH71]   L. G. Leal and E. J. Hinch. "The effect of weak Brownian rotations on particles in shear flow". In: *J. Fluid Mech.* 46.4 (1971), pp. 685–703 (cit. on p. 68).

[LVM74]   W. K. Lee, R. C. Vaseleski, and A. B. Metzner. "Turbulent drag reduction in polymeric solutions containing suspended fibers". In: *AIChE J.* 20.1 (1974), pp. 128–133 (cit. on p. 135).

[LU07]   S. B. Lindström and T. Uesaka. "Simulation of the motion of flexible fibers in viscous fluid flow". In: *Phys. Fluids* 19.11 (2007), p. 113307 (cit. on pp. 40, 84, 85, 88, 97, 104, 174).

[LG17]   D. Lopez and E. Guazzelli. "Inertial effects on fibers settling in a vortical flow". In: *Phys. Rev. Fluids* 2.2 (2017), p. 024306 (cit. on p. 27).

[Lum69]   J. L. Lumley. "Drag reduction by additives". In: *Annu. Rev. Fluid Mech.* 1.1 (1969), pp. 367–384 (cit. on p. 37).

[Lum73]   J. L. Lumley. "Drag reduction in turbulent flow by polymer additives". In: *J. Pol. Sci.* 7.1 (1973), pp. 263–290 (cit. on p. 39).

[LSA11]   F. Lundell, L. D. Söderberg, and P. H. Alfredsson. "Fluid mechanics of papermaking". In: *Annu. Rev. Fluid Mech.* 43 (2011), pp. 195–217 (cit. on pp. 21, 171).

[MA14]   W. Mao and A. Alexeev. "Motion of spheroid particles in shear flow with inertia". In: *J. Fluid Mech.* 749 (2014), pp. 145–166 (cit. on pp. 28, 32).

[MS17]   N. K. Marath and G. Subramanian. "The effect of inertia on the time period of rotation of an anisotropic particle in simple shear flow". In: *J. Fluid Mech.* 830 (2017), pp. 165–210 (cit. on pp. 31, 171).

[MS18]   N. K. Marath and G. Subramanian. "The inertial orientation dynamics of anisotropic particles in planar linear flows". In: *J. Fluid Mech.* 844 (2018), pp. 357–402 (cit. on pp. 31, 171).

[Mar+18] B. Marchetti, V. Raspa, A. Lindner, O. Du Roure, L. Bergougnoux, E. Guazzelli, and C. Duprat. "Deformation of a flexible fiber settling in a quiescent viscous fluid". In: *Phys. Rev. Fluids* 3.10 (2018), p. 104102 (cit. on p. 35).

[MC21]   C. Marchioli and M. Campolo. "Drag reduction in turbulent flows by polymer and fiber additives". In: *Pow. Part. J.* 38 (2021), pp. 64–81 (cit. on pp. 39, 147).

[MFS10]   C. Marchioli, M. Fantoni, and A. Soldati. "Orientation, distribution, and deposition of elongated, inertial fibers in turbulent channel flow". In: *Phys. Fluids* 22.3 (2010), p. 033301 (cit. on pp. 34, 84, 121).

[Mar+14] G. G. Marcus, S. Parsa, S. Kramel, R. Ni, and G. A. Voth. "Measurements of the solid-body rotation of anisotropic particles in 3D turbulence". In: *New journal of physics* 16.10 (2014), p. 102001 (cit. on p. 34).

[Mar09]   I. Marusic. "Unravelling turbulence near walls". In: *J. Fluid Mech.* 630 (2009), pp. 1–4 (cit. on pp. 23, 26).

[MM56]   S. G. Mason and R. S. J. Manley. "Particle motions in sheared suspensions: orientations and interactions of rigid rods". In: *Proc. R. S. A* 238.1212 (1956), pp. 117–131 (cit. on p. 47).

[MC81]   W. D. McComb and K. T. J. Chan. "Drag reduction in fibre suspension". In: *Nature* 292.5823 (1981), pp. 520–522 (cit. on pp. 38, 39, 172).

[McQ+19] A. McQuatters-Gollop et al. "Plankton lifeforms as a biodiversity indicator for regional-scale assessment of pelagic habitats for policy". In: *Eco. Ind.* 101 (2019), pp. 913–925 (cit. on pp. 20, 171).

[MB12]   B. Metzger and J. E. Butler. "Clouds of particles in a periodic shear flow". In: *Phys. Fluids* 24.2 (2012), p. 021703 (cit. on p. 47).

[MGB05]   B. Metzger, E. Guazzelli, and J. E. Butler. "Large-scale streamers in the sedimentation of a dilute fiber suspension". In: *Phys. Rev. Lett.* 95.16 (2005), p. 164506 (cit. on p. 27).

[MP64]   A. B. Metzner and M. G. Park. "Turbulent flow characteristics of viscoelastic fluids". In: *J. Fluid Mech.* 20.2 (1964), pp. 291–303 (cit. on p. 39).

[ML03]   P. Meunier and T. Leweke. "Analysis and treatment of errors due to high velocity gradients in particle image velocimetry". In: *Exp. Fluids* 35.5 (2003), pp. 408–421 (cit. on p. 50).

[Min+21] S. Minaee, Y. Y. Boykov, F. Porikli, A. J. Plaza, N. Kehtarnavaz, and D. Terzopoulos. "Image segmentation using deep learning: A survey". In: *IEEE Trans. Patt. An. Mach. Intel.* (2021) (cit. on pp. 53, 55).

[MM13]   A. Moosaie and M. Manhart. "Direct Monte Carlo simulation of turbulent drag reduction by rigid fibers in a channel flow". In: *Acta Mec.* 224.10 (2013), pp. 2385–2413 (cit. on pp. 39, 135).

[Mor+08] P. H. Mortensen, H. I. Andersson, J. J. J. Gillissen, and B. J. Boersma. "Dynamics of prolate ellipsoidal particles in a turbulent channel flow". In: *Phys. Fluids* 20.9 (2008), p. 093302 (cit. on p. 34).

[MAR01] K. B. Moses, S. G. Advani, and A. Reinhardt. "Investigation of fiber motion near solid boundaries in simple shear flow". In: *Rheo. Acta* 40.3 (2001), pp. 296–306 (cit. on pp. 30, 47).

[NS94]   L. Najman and M. Schmitt. "Watershed of a continuous function". In: *Signal Proc.* 38.1 (1994), pp. 99–112 (cit. on p. 54).

[NAS10] NASA. *Nasa Earth Observatory - Eruption of Eyjafjallajkull Volcano, Iceland.* https://earthobservatory.nasa.gov/images/43676/eruption-of-eyjafjallajokull-volcano-iceland. 2010 (cit. on p. 19).

[NAS14] NASA. *Nasa Earth Observatory - Haze over France.* https://earthobservatory.nasa.gov/images/83356/haze-over-france. 2014 (cit. on p. 19).

[NAS17] NASA. *Nasa Juno - Approaching Jupiter.* https://www.nasa.gov/image-feature/jpl/pia21390/approaching-jupiter. 2017 (cit. on p. 23).

[NAS22a] NASA. *Nasa Earth Observatory - A Burst of Saharan Dust.* https://earthobservatory.nasa.gov/images/149918/a-burst-of-saharan-dust. 2022 (cit. on p. 19).

[NAS22b] NASA. *Nasa Earth Observatory - Bristol Abloom.* https://earthobservatory.nasa.gov/images/149912/bristol-abloom. 2022 (cit. on p. 19).

[NAS22c] NASA. *Nasa Earth Observatory - Typhoon Hinnamnor.* https://earthobservatory.nasa.gov/images/150290/typhoon-hinnamnor. 2022 (cit. on p. 23).

[Ni+15]   R. Ni, S. Kramel, N. T. Ouellette, and G. A. Voth. "Measurements of the coupling between the tumbling of rods and the velocity gradient tensor in turbulence". In: *J. Fluid Mech.* 766 (2015), pp. 202–225 (cit. on pp. 33, 82, 172).

[Oeh+21] T. B. Oehmke, A. D. Bordoloi, E. A. Variano, and G. Verhille. "Spinning and tumbling of long fibers in isotropic turbulence". In: *Phys. Rev. Fluids* 6.4 (2021), p. 044610 (cit. on pp. 34, 119, 122, 148, 175).

[Oli+20]   S. Olivieri, L. Brandt, M. E. Rosti, and A. Mazzino. "Dispersed fibers change the classical energy budget of turbulence via nonlocal transfer". In: *Phys. Rev. Lett.* 125.11 (2020), p. 114501 (cit. on p. 39).

[OMR21]   S. Olivieri, A. Mazzino, and M. E. Rosti. "Universal flapping states of elastic fibers in modulated turbulence". In: *Phys. Fluids* 33.7 (2021), p. 071704 (cit. on p. 36).

[OMR22]   S. Olivieri, A. Mazzino, and M. E. Rosti. "On the fully coupled dynamics of flexible fibres dispersed in modulated turbulence". In: *J. Fluid Mech.* 946 (2022) (cit. on pp. 33, 35, 37, 39, 114, 116, 118, 119, 143, 148, 149, 172, 175, 176).

[Ots79]   N. Otsu. "A threshold selection method from gray-level histograms". In: *IEEE Trans. Syst. Man. Cybern.* 9.1 (1979), pp. 62–66 (cit. on p. 53).

[Ouc+18]   R. Ouchene, J. I. Polanco, I. Vinkovic, and S. Simoëns. "Acceleration statistics of prolate spheroidal particles in turbulent channel flow". In: *J. Turb.* 19.10 (2018), pp. 827–848 (cit. on p. 35).

[Pan+20]   A. Pan, H. Xiang, Z. Wang, H. I. Andersson, and L. Zhao. "Kinetic energy balance in turbulent particle-laden channel flow". In: *Phys. Fluids* 32.7 (2020), p. 073307 (cit. on p. 144).

[Par+12]   S. Parsa, E. Calzavarini, F. Toschi, and G. A. Voth. "Rotation rate of rods in turbulent fluid flow". In: *Phys. Rev. Lett.* 109.13 (2012), p. 134501 (cit. on pp. 33, 34, 172).

[PV14]   S. Parsa and G. A. Voth. "Inertial range scaling in rotations of long rods in turbulence". In: *Phys. Rev. Lett.* 112.2 (2014), p. 024501 (cit. on pp. 33, 119, 120, 122, 148, 172, 175).

[Pas+04]   J. Paschkewitz, Y. Dubief, C. Dimitropoulos, E. Shaqfeh, and P. Moin. "Numerical simulation of turbulent drag reduction using rigid fibres". In: *J. Fluid Mech.* 518 (2004), pp. 281–317 (cit. on pp. 38, 39, 135, 141, 146).

[PC82]   A. E. Perry and M. S. Chong. "On the mechanism of wall turbulence". In: *J. Fluid Mech.* 119 (1982), pp. 173–217 (cit. on p. 27).

[PXP00]   D. L. Pham, C. Xu, and J. L. Prince. "A survey of current methods in medical image segmentation". In: *Ann. Rev. Biomed. Eng.* 2.3 (2000), pp. 315–337 (cit. on p. 53).

[PBB15]   F. Picano, W. P. Breugem, and L. Brandt. "Turbulent channel flow of dense suspensions of neutrally buoyant spheres". In: *J. Fluid Mech.* 764 (2015), pp. 463–487 (cit. on p. 84).

[Pic+20]   J. R. Picardo, R. Singh, S. S. Ray, and D. Vincenzi. "Dynamics of a long chain in turbulent flows: impact of vortices". In: *Phil. Trans. R. Soc. A* 378.2175 (2020), p. 20190405 (cit. on pp. 37, 118, 124, 148, 172, 175).

[Pop00]   S. B. Pope. *Turbulent flows.* Cambridge university press, 2000 (cit. on pp. 23, 137).

[Pro15]   A. Prosperetti. "Life and death by boundary conditions". In: *J. Fluid Mech.* 768 (2015), pp. 1–4 (cit. on p. 89).

[PVV19]   N. Pujara, G. A. Voth, and E. A. Variano. "Scale-dependent alignment, tumbling and stretching of slender rods in isotropic turbulence". In: *J. Fluid Mech.* 860 (2019), pp. 465–486 (cit. on pp. 33, 172).

[PW11]   A. Pumir and M. Wilkinson. "Orientation statistics of small particles in turbulence". In: *N. J. Phys.* 13.9 (2011), p. 093030 (cit. on p. 33).

[QL03]   D. Qi and L. S. Luo. "Rotational and orientational behaviour of three-dimensional spheroidal particles in Couette flows". In: *J. Fluid Mech.* 477 (2003), pp. 201–213 (cit. on p. 32).

[Que+15]   N. Quennouz, M. J. Shelley, O. Du Roure, and A. Lindner. "Transport and buckling dynamics of an elastic fibre in a viscous cellular flow". In: *J. Fluid Mech.* 769 (2015), pp. 387–402 (cit. on p. 35).

[Qui16]   I. Quilez. *Cylinder - bounding box.* https://iquilezles.org/articles/diskbbox. 2016 (cit. on p. 57).

[Red+16]   J. Redmon, S. Divvala, R. Girshick, and A. Farhadi. "You only look once: Unified, real-time object detection". In: *Proc. IEEE Conf. Comp. Vis. Patt. Recog.* 2016, pp. 779–788 (cit. on p. 57).

[Ric20]   L. F. Richardson. "The supply of energy from and to atmospheric eddies". In: *Proc. R. S. A* 97 (1920), pp. 354–373 (cit. on p. 24).

[Ros+15]   T. Rosén, J. Einarsson, A. Nordmark, C. K. Aidun, F. Lundell, and B. Mehlig. "Numerical analysis of the angular motion of a neutrally buoyant spheroid in shear flow at small Reynolds numbers". In: *Phys. Rev. E* 92.6 (2015), p. 063022 (cit. on pp. 31, 32, 75).

[RLA14]   T. Rosén, F. Lundell, and C. K. Aidun. "Effect of fluid inertia on the dynamics and scaling of neutrally buoyant particles in shear flow". In: *J. Fluid Mech.* 738 (2014), pp. 563–590 (cit. on pp. 66, 83).

[Ros+21]   P. S. Ross et al. "Pervasive distribution of polyester fibres in the Arctic Ocean is driven by Atlantic inputs". In: *Nature communications* 12.1 (2021), pp. 1–9 (cit. on pp. 22, 171).

[Ros+18]   M. E. Rosti, A. A. Banaei, L. Brandt, and A. Mazzino. "Flexible fiber reveals the two-point statistical properties of turbulence". In: *Phys. Rev. Lett.* 121.4 (2018), p. 044501 (cit. on p. 35).

[Saf56]   P. G. Saffman. "On the motion of small spheroidal particles in a viscous liquid". In: *J. Fluid Mech.* 1.5 (1956), pp. 540–553 (cit. on p. 30).

[Sha+20]   S. Shaik, S. Kuperman, V. Rinsky, and R. van Hout. "Measurements of length effects on the dynamics of rigid fibers in a turbulent channel flow". In: *Phys. Rev. Fluids* 5.11 (2020), p. 114309 (cit. on pp. 35, 120–122, 133).

[Sha81]   R. S. Sharma. "Drag reduction by fibers". In: *Can. J. Chem. Eng.* 59.1 (1981), pp. 3–13 (cit. on pp. 39, 144, 149, 176).

[She+20] M. Z. Sheikh, K. Gustavsson, D. Lopez, E. Lévêque, B. Mehlig, A. Pumir, and A. Naso. "Importance of fluid inertia for the orientation of spheroids settling in turbulent flow". In: *J. Fluid Mech.* 886 (2020), A9. URL: doi: 10.1017/jfm.2019.1041 (cit. on pp. 27, 82).

[SK05a] M. Shin and D. L. Koch. "Rotational and translational dispersion of fibres in isotropic turbulent flows". In: *J. Fluid Mech.* 540 (2005), pp. 143–173 (cit. on pp. 33, 113, 172).

[Sno+14] B. Snook, L. M. Davidson, J. E. Butler, O. Pouliquen, and E. Guazzelli. "Normal stress differences in suspensions of rigid fibres". In: *J. Fluid Mech.* 758 (2014), pp. 486–507 (cit. on p. 28).

[SM09] A. Soldati and C. Marchioli. "Physics and modelling of turbulent particle deposition and entrainment: Review of a systematic study". In: *Int. J. Mult Flow* 35.9 (2009), pp. 827–839 (cit. on p. 34).

[SE90] K. D. Squires and J. K. Eaton. "Particle response and turbulence modification in isotropic turbulence". In: *Phys. Fluids* 2.7 (1990), pp. 1191–1203 (cit. on pp. 85, 89, 174).

[SC90] C. A. Stover and C. Cohen. "The motion of rodlike particles in the pressure-driven flow between two flat plates". In: *Rhe. Acta* 29.3 (1990), pp. 192–203 (cit. on pp. 30, 57).

[SK05b] G. Subramanian and D. L. Koch. "Inertial effects on fibre motion in simple shear flow". In: *J. Fluid Mech.* 535 (2005), pp. 383–414 (cit. on pp. 30, 171).

[SK06] G. Subramanian and D. L. Koch. "Inertial effects on the orientation of nearly spherical particles in simple shear flow". In: *J. Fluid Mech.* 557 (2006), pp. 257–296 (cit. on pp. 30, 171).

[Tay23] G. I. Taylor. "The Motion of Ellipsoidal Particles Immersed in a Viscous Fluid". In: *Proc. R. S. A* 103 (1923) (cit. on pp. 30, 47).

[Tho58] H. C. S. Thom. "A note on the gamma distribution". In: *Month. Weather Rev.* 86.4 (1958), pp. 117–122 (cit. on p. 129).

[Tom49] B. A. Toms. "Some observations on the flow of linear polymer solutions through straight tubes at large Reynolds numbers". In: *Proc. First Int. Cong. Rhe.* 2 (1949), pp. 135–141 (cit. on p. 37).

[TM51] B. J. Trevelyan and S. G. Mason. "Particle motions in sheared suspensions. I. Rotations". In: *J. Coll. Sci.* 6.4 (1951), pp. 354–367 (cit. on pp. 30, 42, 47, 56, 62, 63, 74).

[Ver22a] G. Verhille. "Deformability of discs in turbulence". In: *J. Fluid Mech.* 933 (2022) (cit. on p. 43).

[VB16] G. Verhille and A. Bartoli. "3D conformation of a flexible fiber in a turbulent flow". In: *Experiments in Fluids* 57.7 (2016), pp. 1–10 (cit. on p. 37).

[Ver22b] R. Verzicco. "Electro-fluid-mechanics of the heart". In: *J. Fluid Mech.* 941 (2022) (cit. on pp. 22, 23).

[VA14]   A. Viallat and M. Abkarian. "Red blood cell: from its mechanics to its motion in shear flow". In: *Int. J. Lab. Hem.* 36.3 (2014), pp. 237–243 (cit. on p. 23).

[Vir75]   P. S. Virk. "Drag reduction fundamentals". In: *AIChE J.* 21.4 (1975), pp. 625–656 (cit. on p. 39).

[Vol+11]   R. Volk, E. Calzavarini, E. Lévêque, and J. F. Pinton. "Dynamics of inertial particles in a turbulent von Kármán flow". In: *J. Fluid Mech.* 668 (2011), pp. 223–235 (cit. on p. 119).

[VS17]   G. A. Voth and A. Soldati. "Anisotropic particles in turbulence". In: *Annu. Rev. Fluid Mech* 49.1 (2017), pp. 249–276 (cit. on pp. 21, 27, 33, 34, 37, 39, 114, 116, 172).

[Wan+22]   J. Wang, F. Dalla Barba, A. Roccon, G. Sardina, A. Soldati, and F. Picano. "Modelling the direct virus exposure risk associated with respiratory events". In: *J. Roy. Soc. Int.* 19.186 (2022), p. 20210819 (cit. on pp. 20, 171).

[Wan+11]   Y. Wang, B. Yu, J. L. Zakin, and H. Shi. "Review on drag reduction and its heat transfer by additives". In: *Ad. Mech. Eng.* 3 (2011), p. 478749 (cit. on p. 37).

[WXZ21]   Z. Wang, C. Xu, and L. Zhao. "Turbulence modulations and drag reduction by inertialess spheroids in turbulent channel flow". In: *Phys. Fluids* 33.12 (2021), p. 123313 (cit. on pp. 38, 39, 82, 85, 106, 109, 134–136, 141, 144, 146).

[Wil+21]   J. B. Will, V. Mathai, S. G. Huisman, D. Lohse, C. Sun, and D. Krug. "Kinematics and dynamics of freely rising spheroids at high Reynolds numbers". In: *J. Fluid Mech.* 912 (2021) (cit. on pp. 43, 55, 57).

[Xi19]   L. Xi. "Turbulent drag reduction by polymer additives: Fundamentals and recent advances". In: *Phys. Fluids* 31.12 (2019), p. 121302 (cit. on pp. 136, 149, 176).

[YM93]   S. Yamamoto and T. Matsuoka. "A method for dynamic simulation of rigid and flexible fibers in a flow field". In: *J. Chem. Phys.* 98.1 (1993), pp. 644–650 (cit. on pp. 40, 84).

[YP11]   Y. Yang and D. I. Pullin. "Geometric study of Lagrangian and Eulerian structures in turbulent channel flow". In: *J. Fluid Mech.* 674 (2011), pp. 67–92 (cit. on p. 118).

[ZVG11]   R. Zamansky, I. Vinkovic, and M. Gorokhovski. "Acceleration statistics of solid particles in turbulent channel flow". In: *Phys. Fluids* 23.11 (2011), p. 113304 (cit. on p. 120).

[ZY01]   C. M. Zettner and M. Yoda. "Moderate-aspect-ratio elliptical cylinders in simple shear with inertia". In: *J. Fluid Mech.* 442 (2001), pp. 241–266 (cit. on pp. 32, 47, 65, 66).

[ZA16]   L. Zhao and H. I. Andersson. "Why spheroids orient preferentially in near-wall turbulence". In: *J. Fluid Mech.* 807 (2016), pp. 221–234 (cit. on pp. 34, 82, 116).

[Zha+15]   L. Zhao, N. R. Challabotla, H. I. Andersson, and E. A. Variano. "Rotation of nonspherical particles in turbulent channel flow". In: *Phys. Rev. Lett.* 115.24 (2015), p. 244501 (cit. on pp. 35, 84).

[Zha+19]   L. Zhao, N. R. Challabotla, H. I. Andersson, and E. A. Variano. "Mapping spheroid rotation modes in turbulent channel flow: effects of shear, turbulence and particle inertia". In: *J. Fluid Mech.* 876 (2019), pp. 19–54 (cit. on pp. 35, 84).

[Żuk+21]   P. J. Żuk, A. M. Słowicka, M. L. Ekiel-Jeżewska, and H. A. Stone. "Universal features of the shape of elastic fibres in shear flow". In: *J. Fluid Mech.* 914 (2021) (cit. on p. 28).

Appendices

A. Demonstration of the relation between the Axes-Aligned Bounding Box of an ellipsoid and the principal diagonal terms of its matrix of coefficients.

The following demonstration is freely inspired by Stack-Overflow answer (Azevedo, 2020).

Given a generic hyper-ellipsoid $\mathscr{E}$:

$$\mathscr{E} = \{x \in \mathbb{R}^n | (x - c)^T Q^{-1} (x - c) \leq 1\} \,, \tag{.1}$$

where $c \in \mathbb{R}^n$ is the vector of the centre of the solid and Q is a positive defined matrix of coefficients, write $g(x) = (x - c)^T Q^{-1} (x - c)$ to calculate the vector field orthogonal to the shell of the ellipsoid:

$$\nabla g(x) = 2Q^{-1}(x - c) \,. \tag{.2}$$

Given the $i^{th} \in n$ axis and its projection matrix $P_i = e_i e_i^T$, the orthogonal vector field $\nabla g(x)$ and its projection $P_i \nabla g(x)$ will touch in two points, that correspond to the minimum AABB, where:

$$\nabla g(x) = P_i \nabla g(x) \,, \tag{.3}$$

which is equivalent to:

$$(I_n - P_i) \underbrace{Q^{-1}(x - c)}_{y} = 0_n \,, \tag{.4}$$

where y_i will be the only non-zero value, i.e. $y = te_i$, or $x = c + tQe_i$.

Intersecting this line with the boundaries of the ellipsoid $\mathscr{E}$, we can find t:

$$t^2 = (e_i^T Q e_i)^{-1} = q_{ii}^{-1} \,, \tag{.5}$$

where q_{ii} is nothing but the ith entry of the inverse of the matrix of the coefficients of the ellipsoid Q^{-1}.

Therefore, the shell of the ith projection of the ellipsoid will touch the smallest AABB in the following two points:

$$x_i = c_i \pm \frac{1}{\sqrt{q_{ii}}} e_i^T Q e_i = c_i \pm \frac{q_{ii}}{\sqrt{q_{ii}}} = c_i \pm \sqrt{q_{ii}} \tag{.6}$$

B. Porting of the DNS+ERPP solver to CUDA C

The CUDA C version of the Gauss-Jordan elimination algorithm, described in section 3.3.2 is here displayed. We believe that this kind of solution is of great interest in the framework of software development for High-Performance Simulations of turbulent flows.

The code operates on the a,b,c,d and e coefficients of a matrix representing the linear system of equations that must be solved, storing the solution in the vector f. The main highlight of this implementation is the hidden periodicity of the arrays, given by the 'dim' dimension. Therefore, each thread out of the 'size' threads will independently assemble the solution vector by looping on its dimension nz. In this way, no synchronization between the CUDA threads is required.

```
__global__ void k_gauss_solver
(cufftDoubleComplex *f, double *a, double *b, double *c, double *d,
 ↪  double *e, int nz, int dim, int size)
//------------------------------------------
//     Subroutine for Gauss solver
//     Copyright Multiphase Flow Laboratory, University of Udine
//     authors - D. Di Giusto, March 2020
//------------------------------------------
{
  int index = blockIdx.x * blockDim.x + threadIdx.x; //from zero to
  ↪  spy*spx

  int j;
  double rc,rd,re;

  if (index < size)
  {
    for (j=nz-1;j>3;j--)
    {

      //cancel upper diagonal c
      rc = c[(j-4)*dim+index] / b[(j-2)*dim+index];
      b[(j-4)*dim+index] = b[(j-4)*dim+index] - a[(j-2)*dim+index]
      ↪  * rc;

      f[(j-2)*dim+index].x = f[(j-2)*dim+index].x - rc *
      ↪  f[j*dim+index].x;
      f[(j-2)*dim+index].y = f[(j-2)*dim+index].y - rc *
      ↪  f[j*dim+index].y;
```

```
  //cancel part of row d
  rd = d[j*dim+index] / b[(j-2)*dim+index];
  d[(j-2)*dim+index] = d[(j-2)*dim+index] -rd *
  ↪  a[(j-2)*dim+index];

  f[index].x = f[index].x - rd * f[j*dim+index].x;
  f[index].y = f[index].y - rd * f[j*dim+index].y;

  //cancel part of row e
  re = e[j*dim+index] / b[(j-2)*dim+index];
  e[(j-2)*dim+index] = e[(j-2)*dim+index] - re *
  ↪  a[(j-2)*dim+index];

  f[1*dim+index].x = f[1*dim+index].x - re * f[j*dim+index].x;
  f[1*dim+index].y = f[1*dim+index].y - re * f[j*dim+index].y;

}

for (j=3; j>=2;j--)
{
  //cancel part of row d
  rd = d[j*dim+index] / b[(j-2)*dim+index];
  d[(j-2)*dim+index] = d[(j-2)*dim+index] - rd *
  ↪  a[(j-2)*dim+index];

  f[index].x = f[index].x - rd * f[j*dim+index].x;
  f[index].y = f[index].y - rd * f[j*dim+index].y;

  //cancel part of row e
  re = e[j*dim+index] / b[(j-2)*dim+index];
  e[(j-2)*dim+index] = e[(j-2)*dim+index] - re *
  ↪  a[(j-2)*dim+index];

  f[1*dim+index].x = f[1*dim+index].x - re * f[j*dim+index].x;
  f[1*dim+index].y = f[1*dim+index].y - re * f[j*dim+index].y;
}

//remains only 2x2 array, diagonal and lower diagonal
//|d(1), d(2)|  |f(1)|
//|e(1), e(2)|  |f(2)|
//variable stored in f(1)
f[index].x =(f[index].x - f[1*dim+index].x * d[1*dim+index] /
↪  e[1*dim+index]) / (d[index] - e[index] * d[1*dim+index] /
↪  e[1*dim+index]);
```

```
      f[index].y =(f[index].y - f[1*dim+index].y * d[1*dim+index] /
      ↪  e[1*dim+index]) / (d[index] - e[index] * d[1*dim+index] /
      ↪  e[1*dim+index]);

      //variable stored in f(2)
      f[1*dim+index].x = (f[1*dim+index].x - f[index].x * e[index]) /
      ↪  e[1*dim+index];
      f[1*dim+index].y = (f[1*dim+index].y - f[index].y * e[index]) /
      ↪  e[1*dim+index];

      //forward-substitute variable from k=2,Nz
      //solution stored in f
      for (j=2; j<nz; j++)
      {
        f[j*dim+index].x = (f[j*dim+index].x - a[(j-2)*dim+index] *
        ↪  f[(j-2)*dim+index].x) / b[(j-2)*dim+index];
        f[j*dim+index].y = (f[j*dim+index].y - a[(j-2)*dim+index] *
        ↪  f[(j-2)*dim+index].y) / b[(j-2)*dim+index];
      }
    }

}//end kernel k_gauss_solver
```

C. Rèsumè complet

Une suspension est un système physique multi-phasique dans lequel des particules solides sont dispersées dans un fluide. Compte tenu de leur ubiquité, il est clair que leur compréhension est d'un intérêt absolu, nous permettant de faire face à des phénomènes complexes tels que les éruptions volcaniques, la pollution atmosphérique par des particules fines, la dynamique du plancton, les tempêtes de sable et les dispersions de patogènes (W. R. CHEN et L. R. ZHAO, 2015 ; KHOMENKO et al., 2021 ; BURNETT et al., 2018 ; MCQUATTERS-GOLLOP et al., 2019 ; GUASTO et al., 2012 ; BASTERRETXEA et al., 2020 ; C.D.C.P., 2020 ; J. WANG et al., 2022 ; LE RIBAULT et al., 2021).

Au-delà de l'approximation sphérique, de nombreux procédés naturels et industriels exploitent des particules axis-symétriques telles que les cylindres et les ellipsoïdes, c'est-à-dire des particules dont la forme n'est pas sphérique mais est obtenue par la rotation d'un rectangle ou d'une ellipse autour d'un de ses axes de symétrie. Du fait de leur forme, les particules axis-symétriques s'orientent préférentiellement dans l'écoulement, ce qui nous permet de modéliser la fabrication de matériaux complexes, la réduction de la traînée par les fibres dans les moteurs immergés et les oléoducs, mais aussi les pollutions par les micro-plastiques dans les eaux usées et l'hydrodynamique des globules rouges (LUNDELL et al., 2011 ; HOYT, 1972 ; ROSS et al., 2021 ; GOLDSMITH, 1996).

La dynamique des particules axis-symétriques dans un écoulement visqueux montre les propriétés fondamentales de ce système. Depuis les travaux précurseurs de JEFFERY, 1922, on sait qu'une seule particule axis-symétriques en suspension dans un écoulement visqueux cisaillé détermine un système dynamique périodique, et que son orientation change avec la vorticité de l'écoulement et une fraction de la déformation de l'écoulement, proportionnellement au rapport d'aspect r de la particule. En fin de compte, chaque extrémité de la particule décrit une orbite fermée parmi une infinité d'autres possibles, appelées orbites de Jeffery, qui ne dépendent que de la condition initiale. En conséquence, la viscosité d'une suspension de particules axis-symétriques est indéterminée, à moins que d'autres effets ne soient pris en compte pour déterminer les orbites de Jeffery préférentielles.

Les efforts théoriques récents de SUBRAMANIAN et KOCH, 2005 ; SUBRAMANIAN et KOCH, 2006 ; DABADE et al., 2016 ; MARATH et SUBRAMANIAN, 2017 ; MARATH et SUBRAMANIAN, 2018 et EINARSSON, CANDELIER et al., 2015a ; EINARSSON, CANDELIER et al., 2015b ont discuté de l'influence d'un petit effet inertiel sur les orbites de Jeffery de particules axis-symétriques. Ces auteurs ont trouvé que l'inertie du fluide et/ou des particules modifie les orbites de Jeffery, autrement stables, puisque les particules ellipsoïdales sont alors poussées vers une orbite stable limite au fur et à mesure de leurs rotations. Les ellipsoïdes 'prolate' sont poussés vers l'orbite dans le plan de cisaillement. La situation est plus complexe pour les ellipsoïdes 'oblate' qui sont attirés soit par la seule orbite de rotation, soit à la fois par l'orbite alignée sur la vorticité et l'orbite dans le plan de cisaillement, selon que leur rapport d'aspect est supérieur ou inférieur à une valeur critique d'environ 0, 14 (DABADE et al., 2016 ; EINARSSON, CANDELIER et al., 2015a).

La phénoménologie change radicalement lorsque des particules axis-symétriques sont transportées par un écoulement turbulent, la condition d'écoulement la plus courante pour ces suspensions dans les processus naturels et industriels. En raison de la structure multi-échelle et intermittente de la turbulence, les particules ne se comportent plus comme un système dynamique périodique, mais aussi des nombreux paramètres entrent en jeu, notamment la longueur, l'inertie et la flexibilité des particules. Les fibres (resp. cylindres) sub-Kolmogorov dans la turbulence isotrope homogène s'alignent avec (resp. perpendiculairement à) la déformation locale de l'écoulement turbulent ainsi que la vorticité locale des tourbillons étirés (VOTH et SOLDATI, 2017). En conséquence, cette dernière contribue faiblement à leur taux de rotation (resp. de filature), qui est jusqu'à trois fois plus faible que celui calculé par la théorie de Jeffery pour des particules orientées aléatoirement (SHIN et KOCH, 2005; PARSA, CALZAVARINI et al., 2012; BYRON et al., 2015; NI et al., 2015).

Si l'on considère des particules cylindriques allongées (fibres) proportionnelles aux structures inertielles de la turbulence, leur longueur non négligeable diminue la contribution des petits tourbillons (SHIN et KOCH, 2005), diminuant encore leur taux de rotation suivant une loi de puissance −4/3 (PARSA et VOTH, 2014; PUJARA et al., 2019). Ceci est également extensible aux effets d'inertie des particules déterminés par un décalage de densité entre les deux phases (BOUNOUA et al., 2018). En revanche, l'influence de la flexibilité sur la dynamique des fibres dans la turbulence est plus complexe. Les fibres flexibles se plient et s'étendent rapidement, étant étirées à l'intérieur de régions tourbillonnaires de taille comparable, ce qui suggère que la déformabilité des particules a un effet négligeable sur leur alignement dans la turbulence PICARDO et al., 2020; OLIVIERI, MAZZINO et al., 2022.

Enfin, on sait que les particules axis-symétriques interagissent avec la turbulence et, si elles sont dispersées en concentration suffisante, elles en modulent l'intensité, ce qui conduit à une phénoménologie macroscopique connue sous le nom de Réduction de la Traînée (VOTH et SOLDATI, 2017). Dans le cas des fibres, cela est déterminé par une modification structurelle de l'écoulement turbulent que les particules imposent aux tourbillons de taille comparable aux fibres. Cela détermine une interaction à toutes les échelles de la turbulence, où le rapport d'aspect et l'inertie des particules sont les paramètres les plus influents (MCCOMB et CHAN, 1981; OLIVIERI, MAZZINO et al., 2022).

Cette thèse porte sur l'étude de la dynamique des fibres dans les écoulements visqueux et turbulents. Pour mener à bien cette étude, deux spécialités ont été combinées dans le cadre d'une convention de co-tutelle entre l'Università degli Studi di Udine et l'Aix-Marseille Université. Des expériences ont été réalisées au Laboratoire IUSTI d'Aix-Marseille Université pour étudier l'influence de la petite inertie sur les rotations de particules axis-symétriques isolés et iso-denses dans un écoulement de cisaillement visqueux.

Dans le Chapitre Deux, nous présentons la partie expérimentale. Cette étude comprend la fabrication et la mesure de particules cylindriques et ellipsoïdales axis-symétriques faites sur mesure selon trois méthodes différentes pour lesquelles nous

avons combiné des connaissances de base en modélisation tridimensionnelle et des technologies de pointe dans le domaine du prototypage rapide. Les particules obtenues sont ensuite caractérisées par microscopie numérique pour déterminer statistiquement le rapport entre la longueur et le diamètre de la particule, c'est-à-dire le rapport d'aspect de la particule. Nous avons ainsi obtenu 16 particules axis-symétriques dans une large gamme de rapports d'aspect ($r \in [0.05; 20]$).

La préparation des fluides pour les expériences est donc expliquée en détail. Une solution d'eau pure, d'acide citrique et d'huile Ucon a été retenue. La concentration d'acide citrique permet de produire une condition d'iso-densité entre le fluide et les particules axis-symétriques données, répondant ainsi à l'exigence de la théorie de JEFFERY, 1922. Ensuite, la viscosité du fluide est proportionnelle à la concentration du Ucon, ce qui la rend facilement ajustable et offre un moyen simple de contrôler la nature inertielle des particules en suspension (DABADE et al., 2016 ; EINARSSON, CANDELIER et al., 2015a).

De plus, une cellule de cisaillement sur mesure est présentée. Elle est équipée de parois transparentes utilisé afin de permettre l'usage de un système d'enregistrement par deux caméras orthogonales. Le cisaillement du fluide est assuré par le déplacement continu d'une courroie, elle aussi, transparente, assuré par un moteur à courant continue. Les mesures de taux de cisaillement sont obtenues par Vélocimétrie par Image de Particules, effectuées avec des fluides à faible et forte viscosité. Le suivi de la particule, initialement placée au centre de la cellule, est assuré par deux caméras orthogonales qui enregistrent sa dynamique d'orientation au cours du temps. Ensuite, un algorithme de Vision par Ordinateur développé pendant la thèse est utilisé pour segmenter automatiquement la particule et mesurer l'orientation et la taille des deux projections des particules sur les deux cameras.

À ce stade, un problème fondamental émerge, étant donné que les deux particules projetées ne fournissent pas suffisamment d'informations pour estimer l'orientation tridimensionnelle des particules axis-symétriques données. Alors qu'une approche basée sur les deux projections pourrait résoudre le problème pour les formes cylindriques, à condition d'avoir une résolution suffisante sur la dimension mineure de la particule, ce n'est pas le cas pour les ellipsoïdes, qui manquent naturellement de bords nets. Par conséquent, nous tirons parti de la relation qui détermine le 'Axes Aligned Bounding Box' des ellipsoïdes et des cylindres, connue a priori étant une expression déterminée, pour entraîner un Neural Network sur la géométrie des particules axis-symétriques. Ensuite, après avoir combiné les informations recueillies par les deux caméras orthogonales, nous utilisons le Neural Network pour estimer leur pose sur la base de le 'Axes-Aligned Bounding Box' qui a été mesurée expérimentalement.

Nous examinons l'effet de l'inertie sur le comportement dynamique de ces particules en suspension jusqu'à un nombre de Reynolds des particules d'environ un, en modifiant systématiquement la viscosité du fluide. Qualitativement, pour un petit nombre de Reynolds des particules ($Re_p \sim \mathbb{O}(10^{-2})$) les orbites de Jeffery observées correspondent aux ellipses fermées décrites pour la première fois par Jeffery, alors qu'une dérive claire émerge pour une inertie plus élevé, les orbites s'étendent ou s'effondrent selon l'orientation initiale et le rapport d'aspect des particules.

Nos résultats montrent que la période de rotation des particules, quelque soit la forme, ne varie pas dans ce régime de faible inertie. Ceci étend la validité de la théorie de Jeffery jusqu'à un nombre de Reynolds des particules d'environ un. Nous trouvons une dérive systématique parmi plusieurs rotations vers des orbites stables limites. On constate que les particules 'prolate' dérivent vers l'orbite de rotation dans le plan de cisaillement, tandis que les particules 'oblate', quel que soit leur rapport d'aspect, sont entraînées soit vers l'orbite de rotation, soit vers l'orbite de rotation alignée sur la vorticité, en fonction de leur orientation initiale. Les résultats pour les particules allongées sont en bon accord avec les théories récentes de DABADE et al., 2016 ; EINARSSON, CANDELIER et al., 2015a. D'autre part, nos résultats suggèrent l'existence d'un bassin d'attraction plus large que prévu du cycle de rotation pour les particules aplaties dans la limite proche de la sphère , ainsi qu'une instabilité plus douce des orbites de Jeffery en général.

Le Chapitre Trois du manuscrit se concentre sur des simulations numériques très précises d'une suspension de fibres dans une turbulence de paroi, réalisées au Multiphase Flow Laboratory de l'Università degli Studi di Udine. Ces calculs visent à caractériser la dynamique et les déformations de fibres longues et flexibles suspendues dans un écoulement turbulent en canal, en reliant leur phénoménologie aux propriétés fondamentales de la turbulence.

Les simulations sont menées au moyen d'une approche de calcul Eulérienne-Lagrangienne. Nous effectuons des simulations numériques directes (DNS) d'un écoulement turbulent en canal imposé par pression, en discrétisant les équations de continuité et de Navier-Stokes selon une méthode pseudo-spectrale classique (J. KIM et al., 1987). Ensuite, les fibres sont modélisées selon le modèle rod-chain LINDSTRÖM et UESAKA, 2007 ; ANDRIĆ et al., 2013 : nous effectuons le suivi Lagrangian de particules (LPT) de tiges sub-Kolmogorov qui, étant assemblées en chaînes, modélisent des fibres qui s'étendent bien dans le domaine inertiel de la turbulence et sont naturellement enclines à la flexion. Cela signifie que les équations décrivant la dynamique linéaire et angulaire de chaque tige sont couplées dans un système matriciel tri-diagonal par la contrainte de non-glissement imposée au point de contact entre les deux extrémités de deux éléments consécutifs.

Enfin, nous évaluons la perturbation hydrodynamique des fibres sur l'écoulement en suivant la méthode de couplage bidirectionnel Exact Regularized Point Particle (ERPP) (GUALTIERI et al., 2015). Cette méthode normalise la perturbation des particules, par ailleurs singulière, sur la grille Eulérienne par le biais d'une échelle de temps retardée, qui est inversement proportionnelle à l'exactitude de la solution. Par conséquent, elle exige naturellement des grilles de calcul finement discrétisées, pénalisant la faisabilité des calculs. D'autre part, cela permette que l'intensité de l'interaction hydrodynamique calculée ne dépend pas de la fraction volumique locale comme dans d'autres schémas (SQUIRES et EATON, 1990).

La méthodologie décrite permet des simulations très précises de suspensions de fibres longues et flexibles dans la turbulence de paroi au prix de calculs intensifs. Nous présentons donc les principes d'un nouvel algorithme de parallélisation, dont l'exten-

sibilité est exploitée pour déployer un solveur accéléré par GPU (DNS+ERPP+LPT) sur l'infrastructure de calcul haute performance la plus moderne d'Europe.

Plus important encore, nous évaluons l'influence de la méthode de couplage bi-directionnel pour rétablir l'équivalence de forme correcte entre les fibres simulées et la théorie de JEFFERY, 1922. Cela nous permet de valider nos calculs, en trouvant une correspondance entre les expériences et les simulations présentées dans cette thèse, de sorte qu'un critère simple est déduit afin de garder la précision dans des simulations à grande échelle d'un écoulement turbulent.

Nous présentons des résultats à des nombres de Reynolds de cisaillement $Re_\tau = 300$ en dispersant des fibres courtes, intermédiaires et longues de type traceur et iner-tielles avec une rigidité en flexion nulle ou finie (10^{-4}). Les statistiques permettent de comprendre l'orientation préférentielle et le taux de rotation des particules. Nous constatons que dans le centre du cisaillement les fibres flexibles s'orientent et tournent comme s'il s'agissait de particules rigides en suspension dans une turbulence isotrope homogène, comme dans les expériences et les simulations numériques les plus ré-centes (PARSA et VOTH, 2014 ; OEHMKE et al., 2021 ; OLIVIERI, MAZZINO et al., 2022). Cependant, les mêmes fibres s'orientent avec l'écoulement moyen et connaissent des taux de rotation plus élevés lorsqu'elles se déplacent vers les parois, où le fort ci-saillement détermine l'orthogonalité entre la vorticité et la direction de l'écoulement, expliquant des rotations plus intenses des particules.

Ensuite, nous nous intéressons à la déformation des particules, en constatant que la configuration la plus probable d'une fibre flexible dans la turbulence est étirée à la fois dans le coeur de l'écoulement et près des parois, étirée comme ce qui est observé numériquement dans la turbulence isotrope homogène (PICARDO et al., 2020). Deux variables de forme, notamment la longueur effective et le rayon de giration, nous permet de classer toutes les formes déformées possibles, en constatant que les fibres se déforment selon deux schémas typiques, appelés flexion " en cils " et flambage " en compression ". Nous constatons qu'une rigidité finie mais modérée est suffisante pour supprimer le second mais seulement atténuer le premier.

Dans l'ensemble, nos résultats indiquent que, d'un point de vue dynamique, les fibres flexibles et rigides dans la turbulence des parois présentent des orientations et des taux de rotation similaires. Ceci s'explique par le fait que les fibres déformées retrouvent rapidement leur configuration étirée, car nous constatons que leur temps de déformation typique peut être modélisé par une distribution gamma très locale et correspond très probablement à la durée de vie des petites échelles turbulentes, c'est-à-dire entre 2 et 3 fois l'échelle de temps de Kolmogorov de l'écoulement. Ceci rappelle l'investigation numérique de ALLENDE et al., 2018, qui a trouvé que le temps d'inter-déformation pour des tiges flexibles sub-Kolmogorov dans une turbulence isotrope homogène était bien prédit par une distribution de Weibull.

Par la suite, nous nous sommes concentrés sur la modulation de la turbulence par les fibres. L'image générale qui se dégage d'un large nombre d'études des écoulements turbulents en canal chargés de fibres à différents nombres de Reynolds de cisaillement ($Re_\tau = 150$ and $Re_\tau = 300$) montre l'importance de la fraction volumique, qui est le paramètre clé pour déterminer l'intensité de la réduction de la traînée. La charge

massique est également un paramètre important car, pour les fibres inertielles, la modulation de la turbulence entraîne généralement une augmentation de la traînée.

En regardant les intensités de turbulence, nous apprécions deux comportements légèrement différents : un cas efficace est déterminé par les fibres iso-denses à faible fraction volumique, lorsqu'elles déterminent des intensités de turbulence légèrement plus fortes, en particulier pour le pic de la composante axiale et dans la masse de l'écoulement. Au contraire, les trois autres simulations mettent en évidence une image plus classique, où les intensités de turbulence sont affaiblies proportionnellement à l'inertie des particules dispersées, en particulier pour leur pic (XI, 2019). En gardant cela à l'esprit, nous examinons le bilan du moment axial, où apparaît la contrainte supplémentaire non-Newtonienne, axiale-normale des particules : d'après les théories disponibles sur la réduction de la traînée induite par les polymères, il est connu que ce terme limite la quantité possible de réduction de la traînée, il doit donc être considéré comme un effet indésirable (XI, 2019).

Aux fractions volumiques considérées, les fibres iso-denses ne génèrent pas de contraintes supplémentaires significatives, alors que les fibres inertielles le font, alimentant la contrainte de Reynolds proportionnellement à la charge de masse. Cependant, les fibres traçantes sont capables d'introduire une contrainte supplémentaire normale plus appréciable, de signe opposé. Nous supposons ici que cette contrainte agit pour réduire le transfert de moment normal axe-paroi, qui peut être considéré comme le mécanisme fondamental sur lequel la réduction de la traînée est basée (XI, 2019). L'efficacité des fibres iso-denses pourrait alors être liée à leur production de contraintes supplémentaires purement normales sans perturber l'équilibre axial de la quantité de mouvement.

L'examen des spectres de l'énergie cinétique turbulente permet de mieux comprendre le mécanisme de la modulation de la turbulence. Nos résultats indiquent des caractéristiques typiques de la turbulence chargée de fibres, en accord avec des études numériques antérieures (OLIVIERI, MAZZINO et al., 2022). Les particules se nourrissent des échelles turbulentes intermédiaires pour distribuer l'énergie aux plus petites, mais résonnent aussi modestement en correspondance des plus grandes échelles de l'écoulement.

On trouve également des traces de ce mécanisme en examinant le bilan de l'énergie cinétique turbulente. Les fibres longues agissent positivement pour affecter la masse de l'écoulement turbulent du canal. Malgré leur faible contribution, ces particules modulent la production d'énergie cinétique turbulente qui est plus faiblement transportée aux plus petites échelles de l'écoulement, où la dissipation visqueuse est également modulée. Nos résultats suggèrent que les fibres longues et minces ($L_0^+ \sim 30$ *w.u.* and $r = 1000$) ne pourraient pas remplacer aussi efficacement les tiges plus petites ou les polymères comme agents de réduction de la traînée. Il serait plutôt plus judicieux de les combiner ensemble, car ils influencent généralement un écoulement turbulent à différentes échelles (SHARMA, 1981).

En conclusion, le travail présenté ici tente de répondre à des questions fondamentales concernant la dynamique des fibres en suspension dans des écoulements visqueux et turbulents, lorsque l'inertie et la flexibilité jouent un rôle important. Cette

étude a été menée en combinant des expériences et des simulations numériques, tout en validant ces dernières sur les résultats des premières. Il en résulte deux lignes de recherche complémentaires, qui ont permis d'explorer les suspensions de particules axis-symétriques à de multiples échelles.